

## Copyright Undertaking

This thesis is protected by copyright, with all rights reserved.

**By reading and using the thesis, the reader understands and agrees to the following terms:**

1. The reader will abide by the rules and legal ordinances governing copyright regarding the use of the thesis.
2. The reader will use the thesis for the purpose of research or private study only and not for distribution or further reproduction or any other purpose.
3. The reader agrees to indemnify and hold the University harmless from and against any loss, damage, cost, liability or expenses arising from copyright infringement or unauthorized usage.

If you have reasons to believe that any materials in this thesis are deemed not suitable to be distributed in this form, or a copyright owner having difficulty with the material being included in our database, please contact [lbsys@polyu.edu.hk](mailto:lbsys@polyu.edu.hk) providing details. The Library will look into your claim and consider taking remedial action upon receipt of the written requests.

**Laser Surface Modification of Copper Alloy  
for Enhancing Cavitation Erosion Resistance  
and Corrosion Resistance**

Submitted by  
**Tam Kam Fai**

For the Degree of  
**Master of Philosophy in Physics**

**The Hong Kong Polytechnic University**

August 2000



Pao Yue-Kong Library  
PolyU • Hong Kong

## Abstract

**Abstract of thesis entitled “Laser Surface Modification of Copper Alloys for Enhancing Cavitation Erosion Resistance and Corrosion Resistance”.**

**submitted by Tam Kam Fai**

**for the degree of Master of Philosophy in Physics**

**at The Hong Kong Polytechnic University**

**August 2000**

.....

Copper alloys are widely used as engineering parts in marine applications because of the combination of good corrosion resistance, strength, and machinability. Among these, bronze (CuSn) and brass (CuZn) have the lowest cost, but are less resistant to cavitation erosion than the more expensive copper alloys such as cupro-nickel, aluminium bronze and beryllium copper. Laser surface modification is a well-known technique to produce unique surface properties for enhancing wear and corrosion resistance. However, the high reflectivity and high thermal conductivity of copper alloys pose a problem for laser surfacing. It is thus the aim of the present project to investigate the feasibility of enhancing the cavitation erosion resistance  $R_e$  of bronze and brass by laser surface modification.

Laser surface modification of bronze (Cu8%Sn) and brass (Cu38%Zn) were achieved by a 2 kW continuous wave Nd-YAG laser. Two groups of alloying / cladding materials were employed in the present study: (i) nickel-based alloy powder (Ni-Cr-Si-B, Ni-Cr-Al-Mo) and (ii) nickel-based alloy-ceramic powder (Ni-Al<sub>2</sub>O<sub>3</sub>, Ni-Cr-Si-B-WC and Ni-Cr-Fe-WC). Varying degrees of enhancement in the cavitation erosion

resistance were achieved in standard cavitation erosion test (ultrasonic vibration at 20 kHz, 60  $\mu\text{m}$  peak-to-peak amplitude). Under optimal processing conditions, improvement in the cavitation erosion resistance  $R_e$  by a factor of 9 could be achieved by laser surface modification using Ni-Cr-Fe-WC or Ni-Cr-Si-B-WC or Ni-Cr-Si-B. On the other hand, the best improvement in  $R_e$  that could be obtained in specimens Ni- $\text{Al}_2\text{O}_3$ /bronze and Ni-Cr-Al-Mo/brass was 5 times and 4 times that of the substrate respectively. The improvement of  $R_e$  was attributed to the formation of intermetallic phase, metal carbides and borides, or to the increase in hardness of the modified surface layer. In general, the improvement of  $R_e$  increased as the laser scanning speed increased, or as the preplaced coating thickness increased or as the power density decreased, with two exceptions. In Ni- $\text{Al}_2\text{O}_3$ /bronze specimens,  $R_e$  increased as the power density increased since  $\text{Al}_2\text{O}_3$  decomposed and reacted with Ni to form the Ni-rich intermetallic phase  $\text{Ni}_3\text{Al}$ . In the case of Ni-Cr-Al-Mo/bronze,  $R_e$  decreased as the coating thickness increased owing to violent heating, leading to loss of alloying materials.

The effect of laser surface modification on the corrosion resistance varied, and was less pronounced than on the cavitation erosion resistance even when the effect was positive. The corrosion current density was reduced in all the specimens except in those modified with Ni- $\text{Al}_2\text{O}_3$  owing to the formation of  $\text{Ni}_3\text{Al}$  precipitates. In terms of passivation and pitting, only the specimens modified with Ni-Cr-Si-B exhibited passivity and a substantial noble shift of the pitting potential to -112 mV (Epit of brass : -173 mV) in the best case, owing to the increase in Ni, Cr content, and to a more homogeneous microstructure and composition. [Part of the results of the present project was presented in 2000 MRS (Materials Research Society) Spring Meeting, April 2000



(Session J3.2) and the 45<sup>th</sup> International SAMPE (Society for the Advancement of Material and Processing Engineering) Symposium and Exhibition, May 2000 (Session 3B) and published in the corresponding proceedings]\*

- \* • Tam, K. F., Cheng, F. T. and Man, H. C. "Improvement of cavitation erosion resistance and corrosion resistance of brass by laser surface modification". *Materials Research Society Symposium 2000*, San Francisco, CA., USA., 24-28 April, 2000, Vol. 617, pp. J3.2.1-J3.2.6
- Tam, K. F., Cheng, F. T. and Man, H. C. "Laser surface alloying of brass with NiCrSiB for improving cavitation erosion resistance and corrosion resistance". *Proceedings of the 45<sup>th</sup> International Symposium and Exhibition of the SAMPE*, Long Beach, CA., USA., 21-25 May, 2000, pp. 635-644

## Acknowledgements

I would like to express my sincere gratitude to my supervisor, Dr. F. T. Cheng, for his patient guidance and genuine support. He is knowledgeable and experienced in the field of the present study. Not only did he provide me with valuable recommendations, but also, more importantly, he provided tireless encouragement throughout the course of the present study.

My gratitude also goes to the co-supervisor of the present project, Dr. H.C. Man. He is also knowledgeable and experienced in the field of the present study. His comments and suggestions helped me to solve many problems.

I am indebted to Dr. C. T. Kwok for his support. He shared his experiences with me and I have learnt much from him. Besides, he provided me with some advice that was very helpful for my experimental analysis.

I wish to thank Mr. T. W. Chan in the laser laboratory for their precious advice and technical support, Mr. K. H. Ho for the work on the preparation of specimen for cavitation testing and Mr. Hui for buying the spraying alloy powder from China.

I wish to thank Mr. M. N. Yeung and Mr. C. S. Lo in the laboratory for their help in SEM work.

Finally, my thankfulness goes to my family members and my friends, Miss Jasmine Lam, Miss Manliza Chan, Mr. L. S. Tai and Mr. Mendel Wong for their continual encouragement and unfailing support.

# Table of contents

<b>Abstract.....</b>	<b>I</b>
<b>Acknowledgement .....</b>	<b>IV</b>
<b>Table of contents.....</b>	<b>V</b>
<b>1. Introduction.....</b>	<b>1</b>
1.1 Motivation .....	1
1.2 Objectives .....	2
1.3 Scope of study .....	3
<b>2. Theoretical aspects and backgrounds .....</b>	<b>4</b>
2.1 Cavitation erosion and cavitation corrosion .....	4
2.1.1 Cavitation .....	4
2.1.2 Vaporous cavitation .....	5
2.1.3 Gaseous cavitation.....	5
2.1.4 Cavitation erosion .....	5
2.1.5 Effect of synergistic interaction between cavitation erosion and corrosion.....	7
2.1.6 Effect of corrosion on the cavitation process .....	8
2.1.7 Effect of cavitation on the corrosion process .....	8
2.1.8 Effect of viscosity .....	11
2.2 Evaluation of cavitation erosion and cavitation corrosion resistance .....	11
2.2.1 Vibration-induced cavitation devices .....	12
2.2.2 Effect of separation in unattachment method .....	13
2.2.3 Effect of temperature .....	15
2.2.4 Influence of amplitude.....	15
2.2.5 Influence of frequency.....	16
2.2.6 Cavitation erosion rate against time .....	16

<b>2.3 Cavitation erosion related to mechanical properties .....</b>	<b>20</b>
2.3.1 Cavitation erosion resistance of metals and alloys.....	21
<b>2.4 Combating of cavitation erosion .....</b>	<b>23</b>
2.4.1 System design.....	23
2.4.2 Materials selection and development .....	23
2.4.3 Surface modification .....	23
<b>2.5 Surface modification technologies .....</b>	<b>24</b>
2.5.1 Thermal spraying .....	24
2.5.2 Plasma spraying .....	25
2.5.3 Chemical vapour deposition (CVD) .....	26
2.5.4 Ion implantation.....	26
2.5.5 Laser surface modification .....	27
<b>2.6 Types of laser surface modifications.....</b>	<b>27</b>
2.6.1 Laser surface melting (LSM).....	28
2.6.2 Laser surface alloying (LSA).....	29
2.6.3 Laser cladding (LC).....	30
2.6.4 Three basic bead profiles.....	31
2.6.5 Metallurgical and physical aspects.....	32
 <b>3. Literature review .....</b>	 <b>34</b>
<b>3.1 Copper and Copper-based alloys.....</b>	<b>34</b>
<b>3.2 Corrosion of pure copper, tin bronze and brass .....</b>	<b>37</b>
3.2.1 Copper .....	37
3.2.2 Brass.....	37
3.2.3 Tin bronze.....	38
<b>3.3 Cavitation Erosion on Copper and Copper-based alloys .....</b>	<b>38</b>
<b>3.4 Surface modification of Copper and Copper-based alloys.....</b>	<b>39</b>
3.4.1 Laser surface Melting of Copper alloys .....	39
3.4.2 Surface modification by Chromium Cr.....	40
3.4.3 Surface modification by Nickel Ni.....	41
3.4.4 Surface modification by Boron B.....	41
3.4.5 Surface modification by Aluminium Al.....	42
3.4.6 Surface modification by Ni-based alloys.....	42
3.4.7 Laser surface modification of Copper and Copper based alloys ...	43

---

<b>4. Experimental details .....</b>	<b>49</b>
<b>4.1 Substrate materials.....</b>	<b>49</b>
4.1.1 Compositions.....	49
4.1.2 Specimen preparations .....	49
<b>4.2 Alloy powder .....</b>	<b>51</b>
4.2.1 Physical properties .....	51
4.2.2 Compositions.....	51
<b>4.3 Preplacement of powder .....</b>	<b>52</b>
4.3.1 Flame spraying .....	52
<b>4.4 Laser surface modification .....</b>	<b>55</b>
4.4.1 Nd-YAG laser system .....	55
4.4.2 Laser emission head arrangement .....	58
4.4.3 Co-axial gas shielding .....	59
4.4.4 Determination the focal distance.....	61
4.4.5 Measurement of effective laser power and beam size.....	62
4.4.6 Laser surface alloying / cladding .....	63
<b>4.5 Microstructural and metallographic analysis.....</b>	<b>64</b>
4.5.1 Optical microscopy (OM) .....	64
4.5.2 Scanning electron microscopy (SEM).....	64
4.5.3 Energy dispersive X-ray spectroscopy (EDX).....	65
4.5.4 X-ray diffractometry (XRD).....	65
<b>4.6 Cavitation erosion testing .....</b>	<b>67</b>
4.6.1 Ultrasonic induced vibratory tester .....	67
4.6.2 Cavitating medium .....	70
4.6.3 Evaluation of cavitation erosion resistance .....	70
<b>4.7 Electrochemical corrosion testing .....</b>	<b>71</b>
4.7.1 Potentiodynamic polarization.....	71

## 5. Results and discussions –

### Laser surface modification of bronze (Cu8%Sn)

#### with Ni-Al<sub>2</sub>O<sub>3</sub> .....76

5.1	Introduction .....	76
5.2	Materials and laser processing parameters .....	77
5.2.1	Materials.....	77
5.2.2	Laser processing parameters.....	78
5.3	Microstructural and metallographic analysis.....	79
5.3.1	X-ray diffraction analysis of Ni-Al <sub>2</sub> O <sub>3</sub> /bronze .....	86
5.4	Composition profiles of Ni-Al <sub>2</sub> O <sub>3</sub> /bronze.....	89
5.5	Hardness profiles of Ni-Al <sub>2</sub> O <sub>3</sub> /bronze .....	91
5.6	Cavitation erosion of Ni-Al <sub>2</sub> O <sub>3</sub> /bronze .....	93
5.7	Electrochemical corrosion of Ni-Al <sub>2</sub> O <sub>3</sub> /bronze.....	99
5.8	Cavitation damage mechanism of Ni-Al <sub>2</sub> O <sub>3</sub> /bronze .....	101

## 6. Results and discussions –

### Laser surface modification of brass (Cu38%Zn)

#### with Ni-Cr-Al-Mo .....103

6.1	Introduction .....	103
6.2	Materials and laser processing parameters .....	104
6.2.1	Materials.....	104
6.2.2	Laser processing parameters.....	104
6.3	Microstructural and micrograph analysis .....	106
6.3.1	X-ray diffraction analysis of Ni-Cr-Al-Mo/brass .....	113
6.4	Compositional profiles of Ni-Cr-Al-Mo/brass .....	116
6.5	Hardness profiles of Ni-Cr-Al-Mo/brass.....	120
6.6	Cavitation erosion of Ni-Cr-Al-Mo/brass.....	123
6.7	Electrochemical corrosion of Ni-Cr-Al-Mo/brass .....	126

<b>6.8 Cavitation damage mechanism of Ni-Cr-Al-Mo/brass.....</b>	<b>128</b>
------------------------------------------------------------------	------------

## **7. Results and discussions –**

### **Laser surface modification of brass (Cu38%Zn)**

#### **with Ni-Cr-Si-B .....130**

<b>7.1 Introduction .....</b>	<b>130</b>
<b>7.2 Materials and laser processing parameters .....</b>	<b>130</b>
<b>7.3 Effect of power density .....</b>	<b>132</b>
7.3.1 Microstructural and micrograph analysis .....	132
7.3.2 X-ray diffraction analysis of Ni-Cr-Si-B/brass.....	138
7.3.3 Hardness profiles of Ni-Cr-Si-B/brass .....	140
7.3.4 Composition profiles of Ni-Cr-Si-B/brass .....	141
7.3.5 Cavitation erosion of Ni-Cr-Si-B /brass .....	143
7.3.6 Electrochemical corrosion of Ni-Cr-Si-B /brass .....	144
7.3.7 Cavitation damage mechanism of Ni-Cr-Si-B/brass .....	145
<b>7.4 Effect of coating thickness .....</b>	<b>146</b>
7.4.1 Microstructural and micrograph analysis .....	147
7.4.2 X-ray diffraction analysis of Ni-Cr-Si-B/brass.....	149
7.4.3 Hardness profiles of Ni-Cr-Si-B/brass .....	150
7.4.4 Composition profiles of Ni-Cr-Si-B/brass .....	151
7.4.5 Cavitation erosion of Ni-Cr-Si-B/brass.....	154
7.4.6 Electrochemical corrosion of Ni-Cr-Si-B/brass .....	156

## **8. Results and discussions –**

### **Laser surface modification of Brass (Cu38%Zn)**

#### **with Ni-Cr-Fe-WC and Ni-Cr-Si-B-WC alloy.158**

<b>8.1 Introduction .....</b>	<b>158</b>
<b>8.2 Brass (Cu38%Zn) laser surface modified with</b>	
<b>Ni-Cr-Si-B-35%WC .....</b>	<b>159</b>

8.2.1 Materials and laser processing parameters .....	159
8.2.2 Microstructural and micrograph analysis .....	160
8.2.3 X- ray diffraction analysis of Ni-Cr-Si-B-WC/brass.....	168
8.2.4 Composition profiles of Ni-Cr-Si-B-WC/brass.....	172
8.2.5 Hardness profiles of Ni-Cr-Si-B-WC/brass .....	177
8.2.6 Cavitation erosion of Ni-Cr-Si-B-WC/brass .....	179
8.2.7 Electrochemical corrosion of Ni-Cr-Si-B-WC/brass .....	182
8.2.8 Cavitation damage mechanism of Ni-Cr-Si-B-WC/brass .....	186
 <b>8.3 Brass (Cu38%Zn) laser surface modified with</b>	
<b>Ni-Cr-Fe-20%WC .....</b>	<b>187</b>
8.3.1 Materials and laser processing parameters .....	187
8.3.2 Microstructural and metallographic analysis.....	188
8.3.3 X-ray diffraction analysis of Ni-Cr-Fe-WC/brass .....	195
8.3.4 Composition profiles of Ni-Cr-Fe-WC/brass.....	199
8.3.5 Hardness profiles of Ni-Cr-Fe-WC/brass.....	204
8.3.6 Cavitation erosion of Ni-Cr-Fe-WC/brass .....	205
8.3.7 Electrochemical corrosion of Ni-Cr-Fe-WC/brass.....	207
8.3.8 Cavitation damage mechanism of Ni-Cr-Fe-WC/brass.....	211
 <b>9. Conclusions .....</b>	<b>215</b>
9.1 Concluding remarks.....	215
9.2 Limitations of the present study and suggestions for further work.....	219
 <b>References .....</b>	<b>222</b>



# 1 Introduction

## 1.1 Motivation

Cavitation erosion is primarily a wearing-away of material by erosion resulting from repeated impact blows produced by the growth and collapse of vapour cavities within a rapidly flowing and vibrating fluid due to the fluctuations of the local pressure. During the collapse of the cavities, a large pulse of stress is generated. The repeated stress pluses would induce localized fatigue failure and subsequent material removal by mechanical erosion. Cavitation erosion is a common phenomenon in high speed hydrodynamic systems such pump impellers and casing, throttling valves, propellers, turbines, hydrofoils, pipelines, and ultrasonic mixers in the food and pharmaceutical industries. In a corrosive environment, the effects may be greatly magnified, owing to the synergistic effect of erosion (mechanical effect) and corrosion (electrochemical effect).

Copper alloys are commonly employed as water pump castings and propellers, and as other engineering parts which are in contact with high velocity fluids. Thus attack due to cavitation erosion and corrosion is common, leading to reduction in efficiency and shortening of service life.

The problem of degradation of copper alloy parts due to cavitation erosion can of course be solved by the optimisation of hydrodynamic profiles or replacing the copper alloys with more resistant materials such as super duplex stainless steels, but at a high cost. A more practical and economical way is to modify the surface of the copper

alloys, since cavitation erosion and corrosion are surface phenomena which are unrelated to the bulk properties. Among the various methods available for surface modification, laser treatments are relatively new and possess a number of advantages in relation to processing and quality, the most attractive one being the possibility of producing novel surface alloys or structures not attainable by other methods.

Laser surface modification may be divided into three main types, heating, shocking and melting. Heating is used in transformation hardening process in order to obtain a desired phase. Shocking is employed for shock hardening. Melting includes processes such as, laser surface melting (LSM), laser surface alloying (LSA) and laser cladding (LC), depending on the presence and interaction of the preplaced materials on the substrate.

## **1.2 Objectives**

- (1.) To modify the surface of common copper alloys for enhancing the cavitation erosion and corrosion resistance by using laser surface treatments.
- (2.) To evaluate the cavitation erosion resistance and corrosion resistance of laser treated specimens.
- (3.) To relate the change in surface properties with the microstructure of the laser modified surface layer.

### 1.3 Scope of study

Laser surface alloying and laser surface cladding have shown a prospective potential in the production of resistant coatings since both the chemical composition and the microstructure of the surface of the substrates are modified simultaneously, without deterioration of the mechanical properties of the bulk substrates in most cases.

In fact, owing to the high reflectivity and thermal conductivity, laser treatments on copper alloys present certain degree of difficulty and reports in this respect are relatively scarce in the literature. Reports on the effect of laser surface treatments on the cavitation erosion resistance of copper alloys are even more scarce. The success of the process and the performance of the modified surface depend on a judicious combination of the pretreatment of the substrate, the nature of the preplaced materials, and the parameters of the laser process. It is the theme of the present project to identify such an optimal combination.

## **2 Theoretical aspects and backgrounds**

### **2.1 Cavitation erosion and cavitation corrosion**

#### **2.1.1 Cavitation**

Cavitation is defined as the repeated nucleation, growth and collapse of bubbles inside a liquid caused by the sudden local pressure fluctuation due to high flow velocity or vibration.

According to Bernoulli's equation:

$$P + \rho gy + \frac{1}{2} \rho v^2 = \text{constant}$$

The variation of the velocity of a flowing liquid greatly affects the pressure at constant ambient temperature. This is the reason why cavitation tends to be associated with components driven at high velocities through a liquid. If the liquid pressure suddenly falls below the vapour pressure, vapour-filled cavities will grow at the numerous small solid and gaseous cavitation nucleation sites present in liquid. When these cavities are subjected to a higher pressure, they collapse violently. The collapse of cavities imposes stress pulses capable of causing plastic deformation on material surfaces nearby, leading to damage. In general, cavitation may occur in hydrodynamic systems, turbomachines, pumps, marine propellers, hydraulic turbines and hydrofoils, and also in liquid-handling systems and ultrasonic cleaning systems. Thus cavitation attack will cause modification in hydrodynamic properties of flow, breakdown in performance of the systems, generation of vibration and noise, material degradation and erosion. Moreover, cavitation erosion of materials also occurs in a stationary liquid system when it is subjected to vibrational pressure fluctuations. In general, vaporous

cavitation and gaseous cavitation are two main types of cavitation occurring in vibrational or high velocity flowing liquids.

### **2.1.2 Vaporous cavitation**

When the hydrostatic pressure is below the vapour pressure, vapour-filled cavities are formed. The cavities collapse very rapidly (of the order of  $\mu\text{s}$ ) on reaching a region of high hydrostatic pressure thus generating stress pulses with high pressure. The vapour condense almost instantaneously because the damping effect of the bubble collapse is relatively little. Hence, the damage of the cavities generated by vaporous cavitation is more serious.

### **2.1.3 Gaseous cavitation**

Gaseous cavitation usually occurs in the region where the hydrostatic pressure is above the vapour pressure of the liquid and also involves the growth of bubbles which contain gas coming out from the liquid. These cavities collapse relatively slowly under compressive condition because the gas pressure in the bubbles damps the cavity collapse, sometimes taking a period of several seconds. Therefore, stress pulses generated are relatively less intense, and thus the damage due to gas-filled bubbles on the surface of a material is less severe than in vaporous cavitation.

### **2.1.4 Cavitation erosion**

Cavitation erosion is a complex phenomenon involving the interaction of hydrodynamical, mechanical, metallurgical and chemical factors that results in the removal of material. Cavities repeatedly nucleate, grow and collapse inside the liquid

either at or near the surface of a metal. During the implosion of the cavities, the presence of a large stress pulse, which may exceed the elastic limit of the metal, deforms the surface. The deformed surface provides better nucleation sites for the formation of new cavities due to the roughening of the surface.

Furthermore, the effects of surface tension and viscosity on the collapse of a cavity are relatively insignificant in a liquid of high fluidity. The compressibility of the liquid, vapour, and any trapped gases have an intense effect on the final stage of the collapse, which will reduce the cavitation erosion effect of the single cavity by acting as a cushion. It is because the driving force for the cavity collapse is the difference between the hydrostatic pressure ( $P_{\text{hydro}}$ ) and the pressure ( $P_v$ ) inside the cavity [Karimi and martin, 1986].

The collapse of cavities or bubbles will exert stress pulses on a solid surface nearby by two mechanisms. When the collapse of a cavity is asymmetrical, a microjet of liquid is generated. When the collapse is symmetrical, a shock wave is generated. Both the microjet and the shock wave will exert an intense stress pulse (of the order of 1 GPa) on the solid surface because the pulse is very localized. In the case of microjets, the jet diameter is of the order of  $\mu\text{m}$  while shock waves from a single cavity are of greater spatial dimensions, of the order of tens of  $\mu\text{m}$ . When a cluster of cavities collapse, they tend to do so in a concerted manner, thus increasing the spatial dimension of the shock waves generated. The repeated stresses promote the accumulation of fatigue-like hardening in materials. The pulses are hardening the material continuously and the local internal stress may become sufficient to initiate fracture. Finally, these repeated impact stresses lead to removal of material from the bulk solid, known as erosion. The microjets generated from single cavities tend to form small pits when they

reach a solid surface. On the other hand, shock waves from cavity clusters will form craters of larger dimensions.

Hydrostatic pressure, cavity cluster size, distance of the individual cavities from the solid surface, cavity size distribution, and the temperature and density of liquid all play a role in the erosive effect of the cavity cluster. The total inherent energy of the cavity cluster is absorbed, or dissipated by the solid material or reflected as shock waves in the near liquid. The energy absorbed accumulates inside the solid material to cause elastic deformation, plastic deformation and fracture failure by material removal. Therefore, a solid material which can absorb more elastic deformation energy has a higher resistance against cavitation erosion.

#### **2.1.5 Effect of synergistic interaction between cavitation erosion and corrosion**

Judging from the fact that there is a higher weight loss of alloys induced by cavitation in seawater than in fresh water, one may infer that the damage mechanism is a combined action of mechanical and chemical factors in the former case. In marine environments, the widely used engineering materials are subjected to both cavitation erosion and corrosion simultaneously, a process known as cavitation erosion-corrosion. For example, propellers, pump impellers and valves, which serve in seawater or corrosive environments suffer such combined damage. Cavitation erosion is a mechanical degradation and defined as the loss of material related to fatigue processes occurring in the surface of bulk material. However, corrosion arises from electrochemical dissolution or oxidation of metallic materials. The passive film or corrosion product may be removed by cavitation and the rate of corrosion is increased.

The importance of the corrosion factor depends on the dominated damage mechanism of the employed materials. Materials subjected to high intensity cavitation or have low cavitation resistance are less affected by corrosion factor, while materials subjected to low intensity cavitation and have high cavitation resistance are more affected [Tomlinson *et al.*, 1988]. For environments which contain chloride, or sulphide or have extreme pH values, the corrosion factor might be predominant in cavitation erosion-corrosion.

The damage mechanism of cavitation erosion-corrosion is a synergism of mechanical and electrochemical processes, which may lead to enhancement or reduction in material removal.

#### **2.1.6 Effect of corrosion on the cavitation process**

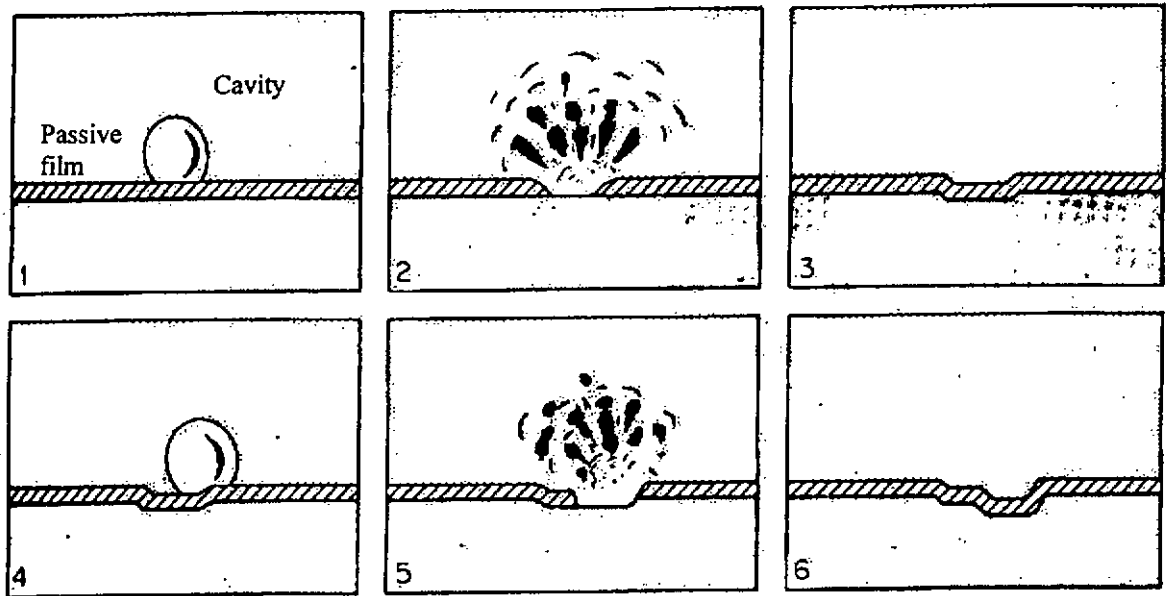
In the cathodic reaction in corrosion, hydrogen bubbles may be generated and act as cushions for the implosion of the cavities to reduce the erosion damage. On the other hand, the corroded products may act as nuclei for the formation of cavities to enhance the onset of cavitation [Auret *et al.*, 1993].

#### **2.1.7 Effect of cavitation on the corrosion process**

In a corrosive environment, the metals and alloys may produce a protective oxide layer or passive film, which covers the material itself. The degree of the protection depends on the resistance of the film against mechanical erosion and the time taken for formation of a new film once it is broken. A hard, dense, adherent and continuous passive film is much preferred. The growth of a loose or brittle film may be destroyed by the repeated impact stress and exposes a newly fresh surface to oxidize again at the



initial rate. Therefore, the metal loss is accelerated by this repetitive action. The schematic diagram of the growth and removal of passive film in a corrosive environment by cavitation erosion-corrosion is shown in Fig. 2.1 [Fontana, 1987].



- (1) A cavity forms on the protective film of a metal.
- (2) The cavity collapses and destroys the film.
- (3) The newly exposed metal surface corroded and the film is reformed.
- (4) A new cavity forms on the same site.
- (5) The cavity collapses and destroys the film.
- (6) The exposed area is corroded and the film is reformed. The repetition of cavitation erosion results in deep crater.

Figure 2. 1 Schematic representation of steps in cavitation erosion.

Tomlinson and Talks stated that the damage (in terms of weight loss) of cast irons in various metallurgical conditions in 3% NaCl solution at 50°C was raised by 5% due to electrochemical corrosion and 70-85% of material loss was due to corrosion-induced erosion [Tomlinson and Talks, 1991].

Owing to erosion of the passive films or corrosion products, cavitation can affect the open-circuit potential (OCP) or corrosion potential of a metal or alloy, such as Cu-

Mg-Al alloy [Trethewey *et al.*, 1988], Ni-Al bronze [Al-Hashem *et al.*, 1995] and duplex stainless steel [Shalaby *et al.*, 1996] in seawater. For Cu-Mg-Al alloy, the OCP shifted in the noble direction by 120 mV (from -540 mV to -420 mV) in the presence of cavitation, which was attributed to the increase in the supply of oxygen. For Ni-Al bronze and duplex stainless steel, the OCP shifted in the active direction by 140 mV (from -200 to -340mV) and 70 mV, (from -250 mV to -320 mV) respectively in a cavitation test with a vibratory amplitude of 25  $\mu\text{m}$ . In cavitation erosion-corrosion process, there is a competition of the mechanical destruction of the passive film or corrosion product and the ability of repassivation. Copper-based alloys do not passivate in 3.5 % NaCl solution, and the effect of chloride ion is smaller than in stainless steels alloy. Consequently, corrosion was found to play a minor role in the overall cavitation erosion-corrosion (0.1 % - 1.8 %) for copper-based alloys [Man *et al.*, 1997].

The factors of the enhancement of corrosion by cavitation erosion is summarized as follows:

- (i) removal protective passive film or corrosion reaction products from the metal surface;
- (ii) chemical changes in the environment caused by local streaming of the liquid around a cavity leading to change in the kinetics of reactions;
- (iii) diffusion of dissolved gas into the cavity and the formation of reactive species in the liquid; and
- (iv) creation of active sites due to localised stress of imploding bubbles.

### 2.1.8 Effect of viscosity

During one-quarter of a cycle of the oscillation, the cavitation bubbles grow and collapse within  $12.5\mu\text{s}$  corresponding to a frequency of  $20\text{kHz}$ . The viscosity of the liquid medium alter the pressure at the bubble wall, and hence the difference of the effective pressure was reduced resulting in a decrease in the rate of either cavitation growth and collapse [Rao and Buckley, 1984]. The pressure at the bubble wall during collapse can be expressed as

$$P(R) = P_1(R) - \frac{2S}{R} + \frac{4\mu U}{R}$$

where  $P_1(R)$  is the total vapour and gas pressure in the bubble  
 $R$  is the bubble radius  
 $S$  is the surface tension of the liquid  
 $\mu$  is the viscosity of the liquid  
 $U = dR/dT$  is the bubble wall collapse velocity  
 $T$  is the time

In general, viscosity has a negligibly small role in the cavity collapse in water.

## 2.2 Evaluation of cavitation erosion and cavitation corrosion resistance

The fracture failure of engineering materials with cavitation erosion damage may be a long-term process in real environments. The investigation of the cavitation erosion properties of engineering materials in the real cavitating environment is very time consuming, and hence very costly, and remedial action cannot be taken immediately. Therefore, a technique employing high cavitation intensities in a reasonable testing time to simulate the damage of materials is needed. Consequently, accelerated laboratory tests have been developed to ensure that the cavitation erosion properties of materials

can be evaluated more economically. The cavitation testing instrument can be mainly divided into two types: flow-induced cavitation device and vibration-induced cavitation device.

Rotating disk devices, Venturi devices and Cavitating jet devices are three common apparatus used for the flow-induced cavitation devices. In the present study, the cavitation erosion test employs an ultrasonic vibratory cavitation tester which is a vibration-induced cavitation device.

### **2.2.1 Vibration-induced cavitation devices**

One of the common ways in the generation of cavitation in the laboratory is to use a vibratory device, which is simple and economical. The size of the apparatus and specimens, and the power consumption for this method are smaller than those for other methods. The quantity of the cavitating liquid needed for test is also small that tests in molten salt can be carried out relatively easily. Therefore, this method has been widely used as an accelerated test for solid material, and has been documented as an ASTM Standard [ASTM G32-92].

The vibration-induced cavitation device consists of a piezoelectric or magnetostrictive device with a horn oscillating in the kilohertz frequency range with an amplitude up to 100  $\mu\text{m}$ . The test specimen is attached to the horn or placed stationary under the horn tip.

During the testing process, the horn tip of the vibration-induced cavitation device is immersed in the testing liquid/solution at just below the liquid level. In the upward stroke of the horn tip, a low pressure region is created immediately below it and results in the nucleation and growth of cavity cluster below the horn tip. In the subsequent

downward stroke the local pressure increases and the cavities collapse, generating stress pulses on the specimen surface.

For a direct attachment the tested specimen must be machined and threaded as a stud to be screwed into the vibration-induced cavitation device. This method of attachment is only suitable for some metallic materials, such as stainless steel. Ceramics, polymers and many hard metal cannot be machined as a threaded stud, but may be soldered to the threaded part, which can then be screwed into the device. Alternatively, the unattachment method may be employed. The test specimen is secured stationary below the vibrating horn tip which is made of a cavitation erosion resistant material, such as Stellite or super duplex stainless steel. The tip has to be replaced from time to time because itself is eroded, though at a lower rate, so as to maintain a constant cavitation intensity. The schematic diagram of the direct attachment and unattachment cavitation erosion setup is shown in Fig. 2. 2 (a) and (b).

### **2.2.2 Effect of separation in unattachment method**

In the vibratory cavitation test, the energy emitted by the vibration specimen screwed to the horn. The horn tip transfers the energy to the cavitating liquid, and then from the cavitating liquid to the specimen under test, by the cavitation field. The weight loss of the test specimen is inversely proportional to the separation range from 0.127 to 6.069 mm between [Kikuchi and Hammitt, 1985]. However, the weight loss of both vibratory and stationary specimens depends substantially on the material tested. In most cases, the energy also causes a significant temperature increase of the cavitating liquid in the region between the vibratory the stationary tested specimens. As the separation increases, the temperature rises of the cavitating liquid decreases.

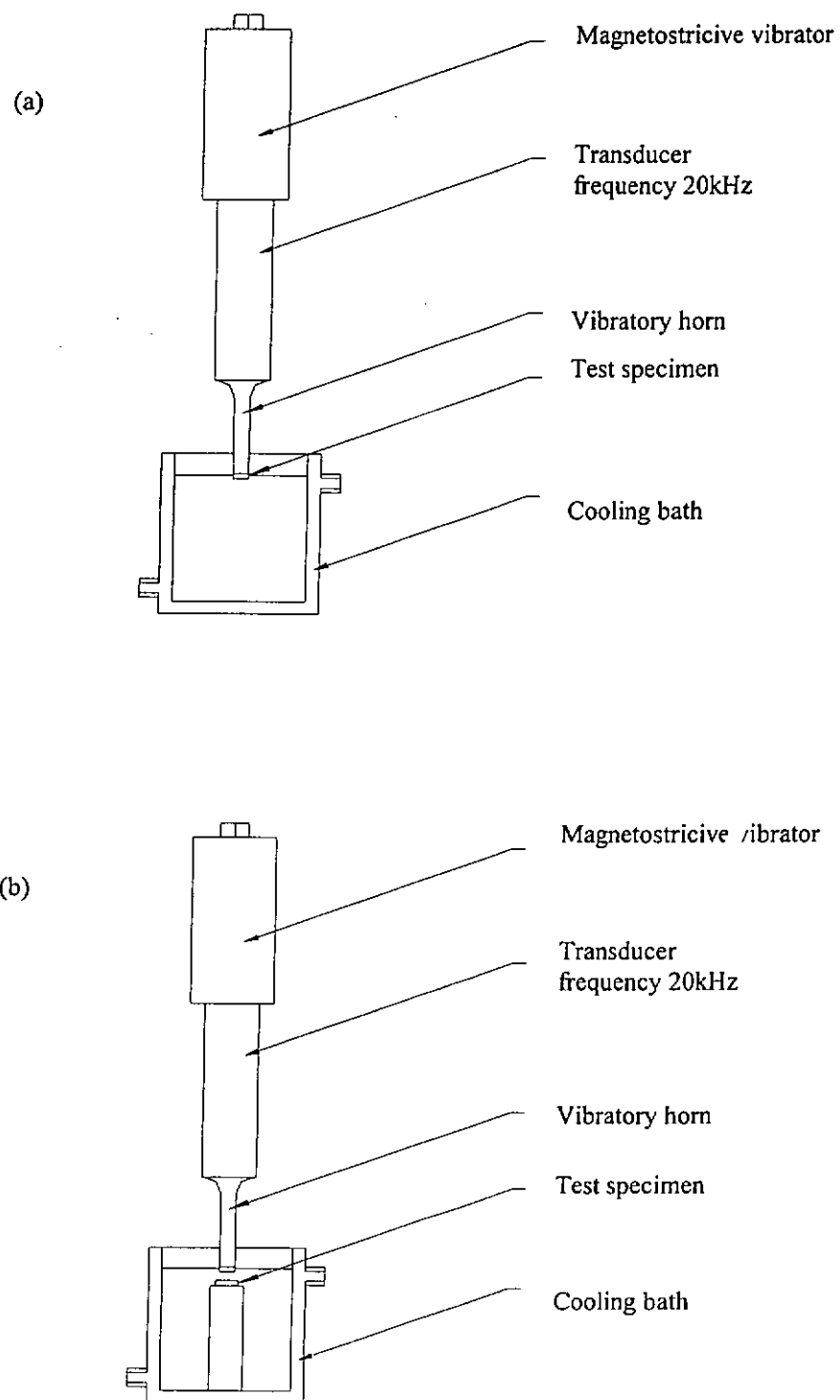


Figure 2. 2 Vibration-induced cavitation device (a) direct attachment and (b) unattachment method.

### **2.2.3 Effect of temperature**

The variation in temperature of the cavitating liquid leads to several factors that affect the erosion rate, such as:

- i) Changes in viscosity, vapour pressure, surface tension and density of the liquid
- ii) Thermodynamic effects on bubble growth and collapse
- iii) Changes in the dissolved gas content of the fluid and
- iv) Changes in the properties of the solid material

As the temperature of the cavitating liquid increases, the rate of the erosion damage increases, and passes through a maximum point. The cavitating liquid has a relatively high viscosity and surface tension at low temperatures, which result in lower erosion rate. Consequently, the erosion damage rate rises to a maximum level when the temperature increases to a certain value. Eventually, the cavitating fluid reaches its boiling point; the erosion rate reduces to a lower level or negligible weight loss. The reduction of erosion rate is generally considered to be due to the increase in vapour pressure. Therefore, bubble growth and collapse are then significantly inhibited as thermal restraints become dominant. The maximum bubble diameter and collapse violence is reduced.

### **2.2.4 Influence of amplitude**

The amplitude greatly affects the rate of damage. Since, the increase of amplitude means an increase of the pressure differential produced in the cavitating liquid below the horn. Consequently, the size of induced bubbles increases, and a higher collapse pressure follows. The surface of solid material is thus subjected to a higher erosion rate.

### 2.2.5 Influence of frequency

Similarly, as the frequency decreases, the bubbles have enough time to grow to a much bigger size. Therefore, the magnitude of the pressure pulse increases and results in a higher pressure. Nevertheless, the rate of bubble generation, and hence the rate of pulses, is reduced.

### 2.2.6 Cavitation erosion rate against time

Cavitation erosion is a complex phenomenon and results in a form of material removal. Hence a quantitative method to characterize the resistance against erosion of a material is by measuring the weight loss or volume loss. Since different materials are significantly different in density, the erosion rate should be presented in terms of the mean depth of penetration rate (MDPR) as follow:

$$\text{MDPR} = \frac{\Delta W}{\rho A \Delta t}$$

where  $\Delta W$  is the weight loss in each time interval of test experiment  
 $\Delta t$  is the time interval  
 $A$  is the area of damaged surface of the specimen and  
 $\rho$  is the density of the material

Beside material removal, the surface is also roughened by cavitation attack. Therefore, it can be assessed by measuring the surface roughness of the eroded specimens [Haferkamp *et al.*, 1987].

In general, the relationship between the erosion rate of the surface of material and time is nonlinear. In the past, most of the erosion tests were performed using the vibration cavitation technique.



The erosion-time and erosion rate-time curves can be roughly divided into five stages, namely (A) incubation period, (B) acceleration period, (C) steady-state period, (D) deceleration period and (E) terminal period.

**(A) Incubation period**

Incubation period is the initial stage of the cavitation erosion process. At this stage the surface of the material is subjected to deformation, roughening and metallurgical changes. However, the surface suffers little or no material loss. Although this is a common observation in most erosion situation, it may be very short under high cavitation intensity conditions or with low cavitation erosion resistance material.

**(B) Acceleration period**

The erosion rate tends to increase to a maximum level in this period. The surface is subjected to superficial hardening, crater or crack development and removal of erosion fragments by fatigue failure mechanism. In this period, the erosion damage expands over the whole area of the specimen.

**(C) Steady state period**

During the steady state period, the erosion rate remains constant or nearly so and has the greatest value in the cavitation erosion process, which is the result of cavitation attack of a homogeneously work-hardened surface. This period may be long or short.

**(D) Deceleration period**

The erosion damage rate is reduced in this period. Consequently, the weight loss of erosion decreases either smoothly or exhibits little fluctuations. This decline is associated with reduction of cavitation collapse pressure of cavities in the vicinity of the rough surface, and with the cushioning effect of liquid trapped in the pockets and crevices of the eroded surface.

**(E) Terminal period**

It is the period in which the erosion damage rate remains constant at a relatively low value. Nevertheless, some tests do not show terminal period, and the erosion rate either continues to decline or goes into a series of fluctuations. For some brittle materials or coatings, the rate can increase rapidly, which is called a “catastrophic period”.

Fig. 2. 3 and Fig. 2. 4 show some commonly used parameters in the erosion-time curve, including the nominal incubation period (NIP), the slope representing maximum erosion rate (ER<sub>max</sub>), the slope representing terminal erosion rate (ER<sub>ter</sub>), the y intercept of terminal erosion rate line (ER1), and the y intercept of maximum erosion rate line (ER2) [ASTM G73-93] The maximum erosion rate (ER<sub>max</sub>) is the most predictable by empirical relationships.

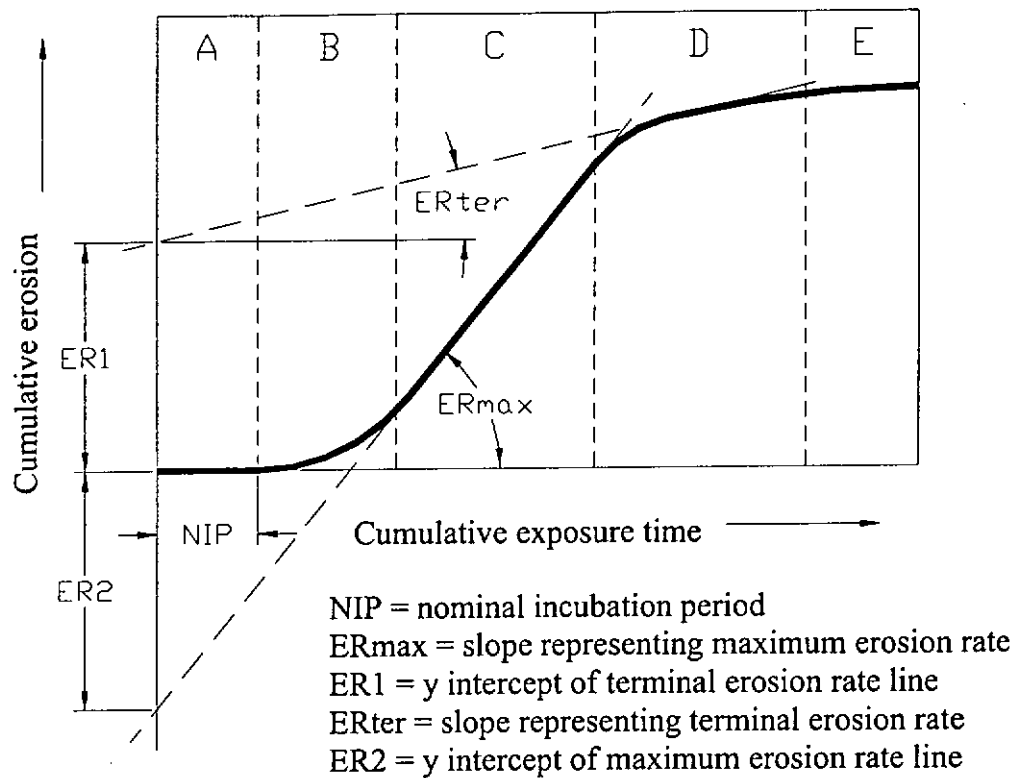
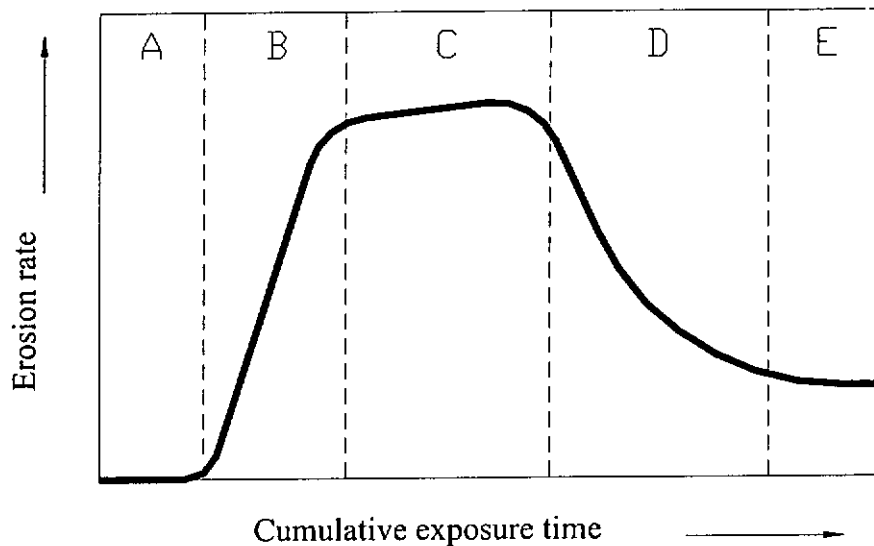


Figure 2.3 Cumulative erosion (mass or volume loss) vs. exposure time.



(A : incubation period; B : acceleration period; C : steady-state period; D : deceleration period; E : terminal period)

Figure 2.4 Corresponding instantaneous erosion rate vs. exposure time obtained by differentiating curve Figure 2.3

## 2.3 Cavitation erosion related to mechanical properties

Many investigators found that hardness, tensile strength, engineering strain energy, ultimate resilience and product of fatigue strength coefficient and cyclic strain-hardening exponent were correlated with cavitation erosion resistance.

### i) Hardness

Similar materials usually show a fairly consistent increase in erosion resistance with a power of hardness. Hence, hardness has traditionally been considered as a good index to cavitation erosion resistance. This is not too unexpected as hardness is a measure of the resistance to plastic deformation. However, correlation of cavitation erosion resistance with hardness is poor across different groups of materials.

### ii) Strain energy

Strain energy to fracture is defined as the area under a tensile stress-strain curve up to fracture. This strain energy indicates the ability of a material to absorb energy of deformation to fracture.

### iii) Ultimate resilience

Ultimate resilience represents the failure energy if rupture is in the brittle mode, defined as  $U_r = \frac{\sigma_u^2}{2E}$ , where  $\sigma_u$  is the strength and  $E$  the modulus of elasticity. As a result, the ultimate resilience seems preferable for brittle materials and the strain energy parameter should be adequate for very ductile materials. Obviously, materials with higher fatigue resistance and higher elastic resilience materials are more cavitation erosion resistant.

In fact, as a material is exposed to a cavitating liquid, it is subjected to a localized loading, which is dynamic, and compressive in nature. The material is deformed locally. Therefore, the deformation of material is not as a bulk, but occurs only at one grain or one phase within a grain and is not influenced by the behaviour of the surrounding grains or phases. This mechanism is different from the material deformed under uniform stress acting on bulk volume. Consequently, universal correlation between cavitation erosion resistance and quasi-static mechanical properties has not been observed. On the other hand, the ability of materials against cavitation erosion should also be investigated in relation to their microstructure, phase transformability and stacking fault energy.

### **2.3.1 Cavitation erosion resistance of metals and alloys**

In general, cavitation erosion resistance is related to binding energy, crystal structure and phase transformability of materials. For single phase metals, those which have high binding energy, low stacking fault energy and high corrosion resistance, possess the highest cavitation erosion resistance, such as W, Cr and Co.

The crystal structure and strain-rate sensitivity highly affect the deformation and failure mechanisms of both metals and alloys. Furthermore, the phase transformability and the stacking fault energy indicate the ability of a material to absorb the energy of shock loading without macroscopic deformation, and hence greater resistance to fatigue failure. The response of different lattice structures to cavitation attack is discussed below:

(i) Face-centered cubic

Face-centered cubic (fcc) metals and alloys, which are isotropic and are less sensitive to strain rate among the three common lattice structures, can absorb more energy of attack cavitation. As a result, the fcc materials are highly ductile, and fail by a void growth and coalescence mechanism [Preece *et al.*, 1979], i.e. by a ductile rupture mechanism. Their response to cavitation attack is similar to their quasi-static mechanical behaviour. The deformation mechanisms are indicated by indentation, slip, cross-slip, twinning, void formation, grain boundary delineation and strain-induced transformation etc.

(ii) Body-centered cubic

Deformation of body-centered cubic (bcc) metals and alloys are highly strain-rate sensitive although they are usually also isotropic. Under cavitation attack, the deformation is a competition between flow and fracture. When the temperature decreases or the strain rate increases, flow becomes more difficult. Consequently, the bcc materials tend to fail by brittle fracture.

(iii) Hexagonal close-packed

Hexagonal close-packed (hcp) metals are anisotropic to varying different degree. Depending on the axial ratio of the unit cell, it can be either strain-rate sensitive or not. If a material is anisotropic and highly strain-rate sensitive, it has poor cavitation erosion resistance.

For multiphase alloys, the situation is complex and there is no general rule to obtain the overall erosion resistance from the resistance of the individual phases. Only in the simplest case the rule of mixture applies. In other cases, in particular, the interfacial bonding between the second-phase particles and the matrix plays a crucial

role. The volume fraction, size, and dispersion of the second phase all play a role. For instance, in  $\alpha+\beta$  brass [Hammit, 1980] [Han and Zhao, 1988] [Kowk *et al.*, 1998], the fcc  $\alpha$  phase peels off more easily than the bcc  $\beta$  phase, since  $\alpha$  phase is more ductile and soft.

## **2.4 Combating of cavitation erosion**

### **2.4.1 System design**

The most direct method is to modify and optimize the hydrodynamic profiles in order to reduce or eliminate cavitation attack. Also, the component geometry should be improved to minimize the pressure fluctuation in the flowing liquid and eliminate the vibrations of the system to reduce cavitation.

### **2.4.2 Materials selection and development**

According to the deformation mechanism and the localised nature of a material in cavitation erosion, the selected material should possess high ability of absorbing impact energy by a non-destructive strain mechanism, such as twinning, stacking deformation or strain-induced martensitic transformation.

### **2.4.3 Surface modification**

Since cavitation erosion is a surface phenomenon, improving the surface properties of a material can meet the demand of increasing the cavitation erosion resistance. There are many surface modification techniques that can be applied to improve the cavitation erosion resistance of conventional materials.

## **2.5 Surface modification technologies**

Surface modification is a process which can alter the surface structure or composition, or provide a surface layer with the aim of modifying the surface properties, such as erosion and corrosion resistance, of a material.

Surface modification is attractive because it only consumes a small amount of additional material and it retains the properties of the bulk material . It provides an unlimited number of combinations of surface and bulk properties.

The more traditional surface modification techniques are electroplating, weld overlay surfacing, thermal spraying and thermochemical treatments (carburising & nitriding). In recent years, there are many new surface modification techniques, such as physical and chemical vapour deposition (PVD & CVD), ion implantation, plasma thermochemical diffusion treatment and laser surface modification.

### **2.5.1 Thermal spraying**

Thermal spraying process uses a torch as heat source which mixes fuel gas and oxygen for combustion. The heat source gives sufficient thermal energy to heat the spray materials to an advanced plastic state. The spray materials can be in the form of wire or powder and fed into the heat source. The near-molten particles is rapidly accelerated by the pressure of the combustion gas flow and forced onto a desired target. During collision of particle and target, a splat is formed which cools rapidly and adheres to the substrate. Consequently, the particles build up and form a discrete coating.

One of the common thermal spraying processes is flame powder spraying. The spray material is used in powder form and the combustion flame from a mixture of fuel gas and oxygen, which is produced by a torch, is employed as a heat source. The



temperature of the flame can reach about 3000°C and can melt the most refractory metals. The schematic diagram of flame powder spraying is shown in Fig. 2. 5.

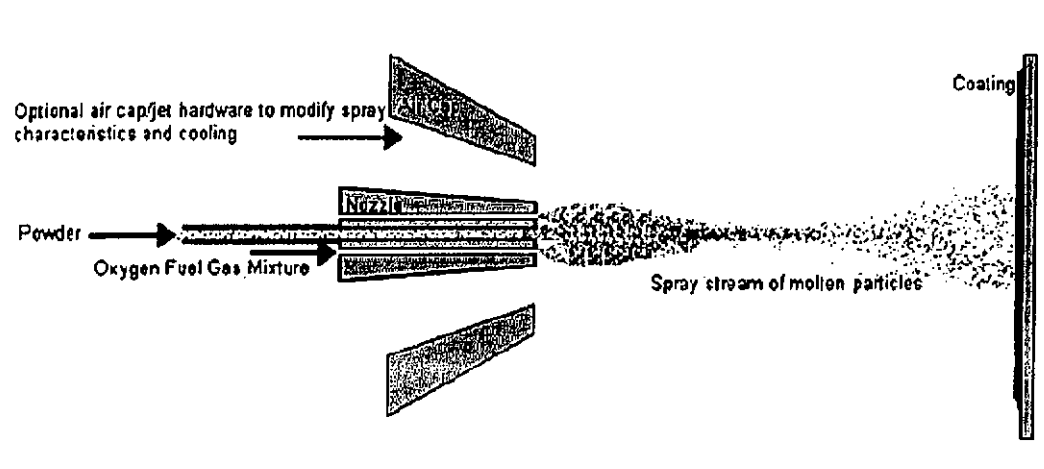


Figure 2. 5 Schematic diagram of flame powder spraying

Some conventional methods of flame spraying which deposit the coatings in air may introduce defects such as oxides and pores. This lead to limitations of their applications in both cavitating condition and corrosive environments. Post-treatment of flame sprayed coatings to remove these defects can be implemented by laser surface melting which will further improve their protective properties against cavitation erosion and corrosion.

### 2.5.2 Plasma spraying

Plasma spraying uses Ar or He gas to pass through an electric arc to generate an extremely hot plasma. The spraying temperature can be up to 16650°C, which can spray high melting point refractory metals and ceramics. Although plasma spraying is a high temperature process, substrate distortion is low due to rapid quenching. Oxide and porosity in the coating may be introduced by air plasma spraying (APS) because it is

done in atmospheric environment. However, it can be overcome by vacuum plasma spraying (VPS), which is done in a vacuum chamber with the presence of some argon.

### **2.5.3 Chemical vapour deposition (CVD)**

This is a process where a solid reaction product nucleates and grows on a substrate, due to a gas phase reaction. Heat, plasma or UV light can enable it. Many factors affect a good CVD coating such as gas reactant composition, flow rate, Reynolds number, substrate temperature and total gas pressure. Some advantages of CVD are:

- (i) it is versatile and gives some coatings not easily obtained by other techniques;
- (ii) it can be done on powders and complicated shapes;
- (iii) relatively simple equipment;
- (iv) deposition is possible over a wide range of pressures and temperatures; and
- (v) composition, structure and grain size of coating can be controlled.

### **2.5.4 Ion implantation**

The ion implantation technique consists of introducing the substrate material into the implanter vacuum chamber, which is in a moderate vacuum (1 mPa), and ionizing the implant species. After that, the atomic species are electrostatically accelerated in a field of 10 to 1000 keV into the target. Ion penetration is only about 0.2  $\mu\text{m}$  but the surface properties of the substrate material are greatly altered. Ion beam sputtering, ion beam mixing, plasma ion deposition and ion beam assisted deposition, which improve the effect of ion implantation when applied alone, are also classified into this type of surface modification. The advantages of ion implantation include:

- (i) no sacrifice of bulk properties
- (ii) solid-solubility limit can be exceeded
- (iii) alloy preparation is independent of diffusion constants
- (iv) no significant change in sample dimensions
- (v) precise location of implanted area

The disadvantages of ion-implantation include:

- (i) expensive capital investment .
- (ii) the ion-beam modified layer is shallow, and therefore may be removed easily.

### **2.5.5 Laser surface modification**

Laser surface cladding and laser surface alloying have shown a prospective potential in the production of corrosion resistant coatings since both the chemical composition and the microstructure of the surface of the substrates are modified simultaneously, without deterioration of the mechanical properties of the bulk substrates in most cases. Compared with the other processes mentioned above, laser surface modification does not require a vacuum, and is thus especially attractive when large engineering parts are to be treated.

## **2.6 Types of laser surface modifications**

One of the classification methods of laser surface treatment was proposed by Gnanamuthu [Gnanamuthu, 1979] who suggested three treatment regimes, namely, heating, melting and shocking as illustrated in Fig. 2. 6.

Alternatively, the laser surface treatment can be simply divided into those involving metallurgical change – such as transformation, hardening, annealing, grain

refining, glazing and shocking – and those involving modification of the surface by the addition of new material such as alloying and cladding. The present study will mainly focus on laser surface melting, alloying and cladding.

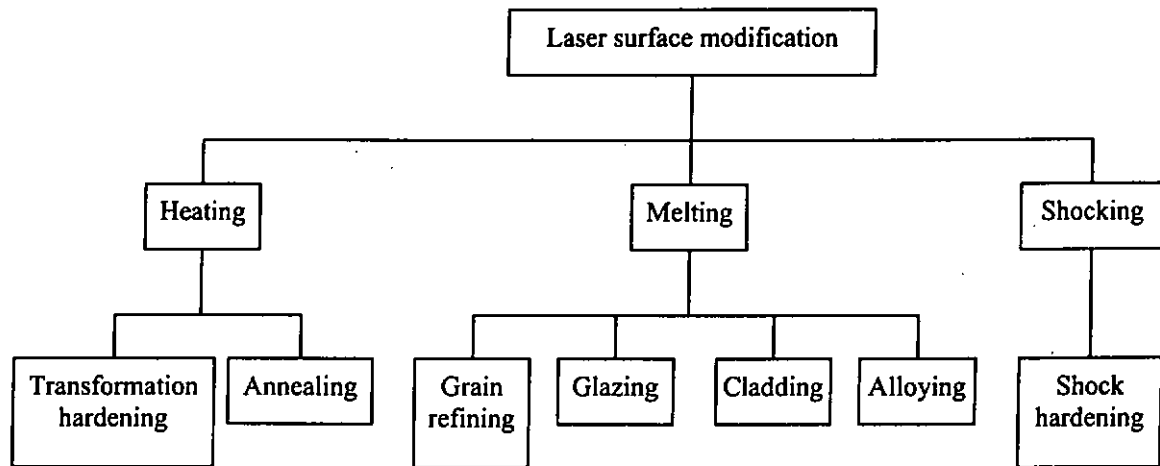


Figure 2. 6 Methods of laser surface treatment of materials.

### 2.6.1 Laser surface melting (LSM)

Laser surface melting employs a high intensity laser beam to scan across the surface of a metal substrate, often in a shielding gas atmosphere. The high power energy is absorbed by the metal substrate and yields a shallow molten metal pool by rapid melting. After the irradiation, subsequent rapid quenching produces a track which has a refined and homogenized microstructure. This effect can improve surface hardness, corrosion and wear resistance.

Draper *et al.* investigated the effect of laser melting on the corrosion behaviour of Fe-containing aluminum bronzes [Javadpour *et al.*, 1982] (C61400) and tin-modified copper-nickel alloy [Draper and Sharma, 1984] (C72500). In aluminum bronze, the laser melting is to homogenize the two-phase microstructure into a single phase devoid

of iron-rich precipitates. This effect reduced the rate of anodic dissolution in 0.5M  $\text{H}_2\text{SO}_4$  and also increased the cavitation erosion resistance in distilled water. In copper-nickel alloy, laser melting significantly decreased the thickness of the corrosion film in humid atmospheres containing  $\text{H}_2\text{S}$  or  $\text{Cl}_2$  pollutants, indicating a decrease of corrosion rate.

Laser glazing is one type of laser surface melting processes, which is carried out at high processing speed. Therefore, the cooling rate can be achieved to the order of  $10^4$ - $10^6$ °C. At this cooling rate, the formation of metallic glass is possible if the alloy composition has a high glass forming tendency [Lindner *et al.*, 1980].

### **2.6.2 Laser surface alloying (LSA)**

Laser surface alloying melts a preplaced alloy layer into a portion of the underlying substrate to yield an alloyed surface layer with desired composition by controlling the thickness of coating and laser melting penetration. The schematic diagram of different stages involved in laser surface alloying from the arrival of laser pulse to complete resolidification is shown in Fig. 2. 7.

There are many different methods used to deposit the alloy layer onto the substrate before laser beam scanning. Preplacing a layer of the alloying elements can be achieved by electroplating, vapour deposition, ion implantation, thermal spraying or painting.

Laser surface melting of the substrate can also be carried out in a controlled atmosphere of gas such as  $\text{N}_2$ . Such a process is known as Laser Gas Alloying.

The ideal predeposited layer should be uniform thickness, low in porosity, have good adherence, possess a clean interface between coated layer and substrate, and have optically clean surface.

The alloying material, in the form of powder, can also be introduced simultaneously with laser beam scanning. This method, which makes use of a powder feeder, is a one-step process in contrast to the two-step process in which the alloying material is preplaced.

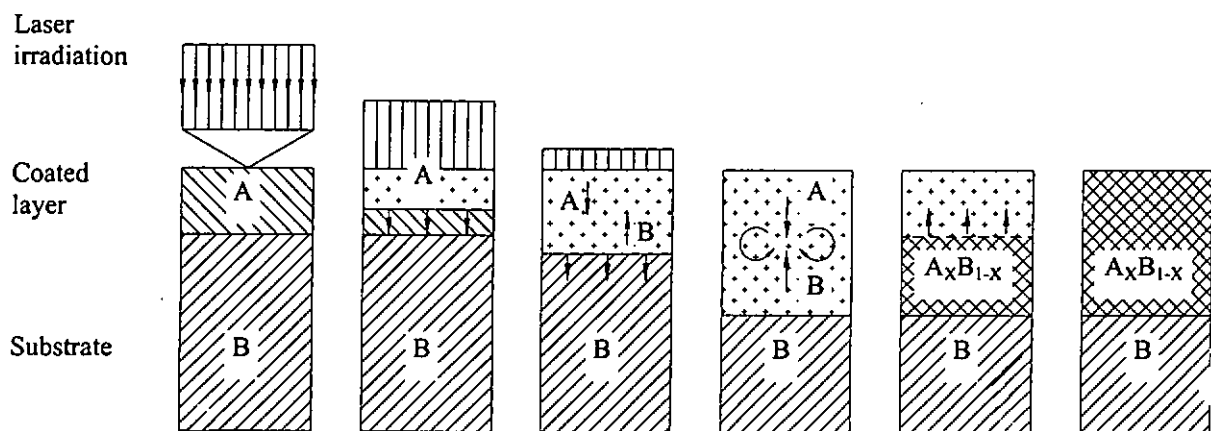


Figure 2.7 Stages involved in laser surface alloying from arrival of laser pulse to complete resolidification [Draper and Ewing, 1984]

### 2.6.3 Laser cladding (LC)

In laser cladding, the beam melts the material preplaced or injected onto the substrate and a thin layer of the substrate, and yields an interface by fusion bonding with minimum dilution of the cladding. The preplaced methods of laser cladding are similar to those in laser surface alloying.

For preplacement of powder, the laser sends a wave and is absorbed by the powder layer. Since this layer has low thermal conductivity, the melt pool is thermally

insulated and the process may be regarded as adiabatic. When the molten alloy reaches the substrate surface, it will freeze back. Consequently, a relatively weak liquid/solid bonding is formed. This resolidified material will be remelted by continuous heating and form a fusion bonding with the substrate. The two important requirements in laser cladding, are (i) formation of a fusion bond (ii) low dilution. So, the optimal process parameters for a success cladding lie in a relatively small range. The schematic diagram of different stages involved in laser cladding from the arrival of the laser pulse to complete resolidification is shown in Fig. 2. 8.

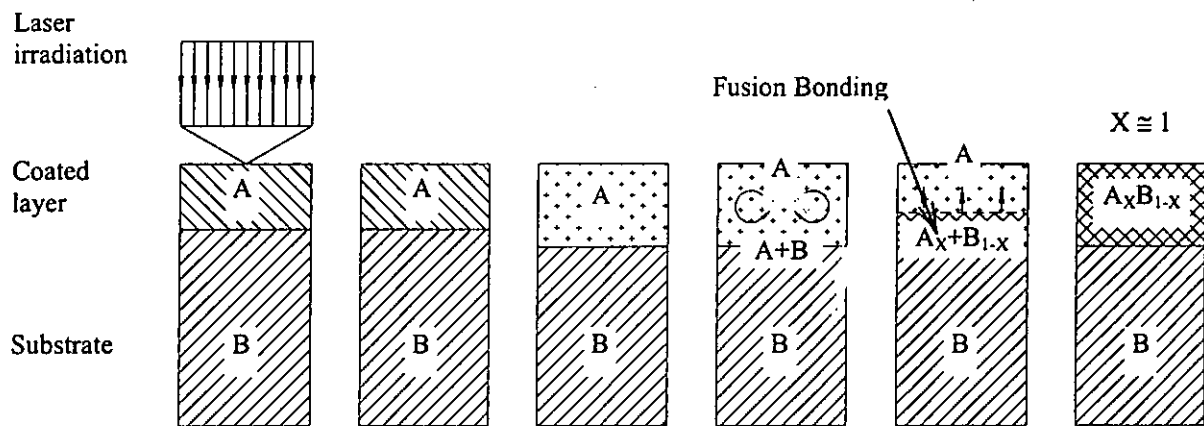


Figure 2. 8 Stages involved in laser cladding from arrival of laser pulse to complete resolidification

#### 2.6.4 Three basic bead profiles

During laser cladding, three basic types of melt profiles can be formed on the substrate, as shown in Fig. 2. 9. (a) In “balling”, the melt track is formed with several small sphere droplets on the substrate. It is either because the coated layer is too thick or insufficient laser power density is used or wetting of the substrate with the liquid

metal is poor. The interface of the clad layer and the substrate is not a fusion bond, the adhesion is very poor. Also the multiple-track clad layer will have poor surface finish and heavy porosity. (b) If the power density is too high, the powder layer will be melted into the substrate. The dilution of laser clad layer will become too high. (c) The preferred profile for low dilution cladding is a melt track profile with an obtuse angle. Overlapping of this profile will produce a multiple-track clad layer with good surface finish, minimum or no porosity and minimum dilution.

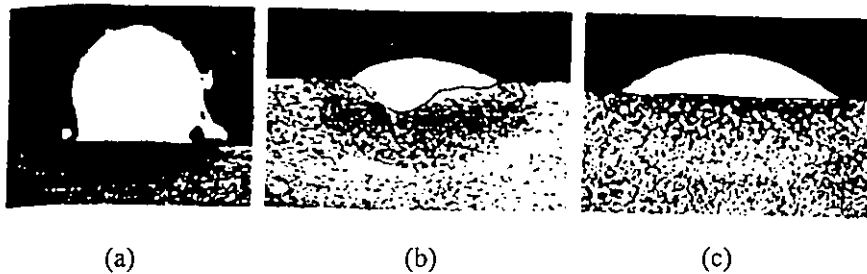


Figure 2. 9 Three basic single track bead profiles

### 2.6.5 Metallurgical and physical aspects

#### i) Surface finish

The entire area of the alloyed clad layer is formed by overlapping of single clad tracks. The surface finish is characterized by the “peak and valley” morphology, which can be quantified by the surface roughness  $R_a$ .

#### ii) Porosity

Cavities between two overlapped tracks and solidification cavities and / or gas evolution are the origins of porosity during laser processing.



**iii) Residual stress and plate distortion**

Laser melted and resolidified layer has high tensile stress but plate distortion is very small.

**iv) Microstructure**

The microstructure of alloyed or clad layers consists of dendrites and dendrite size is much finer than traditional processes due to the extremely high cooling rate.

**v) Cracking**

Cracking is related to the hardness of the alloyed or clad layer. Sometimes, laser processing with high speed and high power densities will yield interdendritic cracking. Crack-free layers may be produced by lower power densities and lower speeds.

**vi) Chemical composition (dilution)**

Dilution of laser clad layer should be low.

$$\text{Dilution ratio DR} = \left( 1 - \frac{\text{Coating thickness } t}{\text{Melt depth } d} \right) \times 100\%$$

An ideal cladding is one which consists of a top layer of 100% cladding material fused bonded by a thin interfacial layer to the substrate, and dilution only occurs in this interfacial layer.

### 3 Literature review

#### 3.1 Copper and Copper-based alloys

Copper has the highest thermal and electrical conductivity of all the commercial metals, and the effect of oxygen on these properties is slight. Phosphorus is a cheap and convenient deoxidant for copper and the relatively poor machinability of copper can be overcome by the addition of 0.3-0.7% tellurium. However, phosphorus diminishes the conductivity of copper and while tellurium would scarcely affect this property.

Tin bronze Cu-Sn (or phosphor bronze) has high corrosion resistance and moderate strength, which is always used in casting because of its low hot ductility. In some case, lead is added for lubrication and for better machinability, and  $\text{Cu}_3\text{P}$  can increase the wear resistance and stiffness of tin bronze.

Brass Cu-Zn probably forms the most important series of copper alloys because of its wide range of properties, which are highly dependent on the content of zinc. Brass has moderately good mechanical properties and corrosion resistance. When the zinc content is below 35%, brass appears as a single-phase alloy. The stability and quantity of the presence of  $\beta$  phase increases as the concentration of zinc increases. This  $\beta$  phase strengthens and lowers the ductility of the brass. Sometimes, lead is also added for improving the machinability of the alloys.

Cupro-nickel Cu-Ni, is a single-phase solid solution with any combination of the two elements since, copper and nickel are completely soluble in both liquid and solid

states. This alloy has excellent corrosion resistance, and coupled with good strength and ductility even at moderately elevated temperature.

Chromium copper Cu-Cr has high conductivity and retention of good mechanical strength at temperature up to approximately 400°C after the fully heat-treated condition. The solid solubility of chromium reduces as the temperature falls during solidification. Consequently, the alloys are hardened by chromium particles, known as precipitation hardening.

Aluminium bronze Cu-Al is a copper aluminium alloy rich in copper and is a multi-phase alloy when the content of aluminium exceeds 8%. The corrosion resistance of aluminium bronze is excellent, coupled with high strength, even at moderately elevated temperature. Usually, iron and nickel are added in small amount, maximum 3%, for strengthening the alloy and without significantly reducing the ductility. Iron and nickel also stabilize the  $\beta$  phase by minimizing the likelihood of the less ductile  $\alpha+\gamma_2$  eutectoid forming on slow cooling. The presence of this eutectoid highly reduces the corrosion resistance of the alloys.

Beryllium copper is the hardest and strongest of the common structural copper alloys. The microstructure of beryllium copper consists of small spherical  $\beta$  particles in a fine-grained  $\alpha$  matrix. This precipitation hardening phenomenon, which results from the decrease in solid solubility of beryllium in copper as temperature falls, is similar to chromium copper.

## Typical properties of common engineering copper alloys

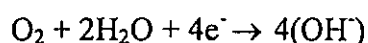
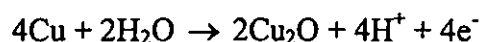
Material	Vickers Hardness (Hv)	Tensile Strength (Tons/sq.in.)	Elongation (%)	Electrical Conductivity (%IACS)*
Tough-Pitch Copper Hot-worked	45	14	55	100
Tough-Pitch Tellurium Copper Hot-worked	50	15	50	95
Deoxidised Copper Hot-worked	45	14	60	80
95/5 Phosphor Bronze Cold-worked	225	50	5	18
95/5 Phosphor Bronze Cold-worked and annealed	75	22	65	18
90/10 Phosphor Bronze Sand cast	90	17	10	10
70/30 Brass Sand cast	55	18	35	27
70/30 Brass Cold-worked and annealed	65	21	70	27
60/40 Brass Sand cast	80	18	25	25
Leaded 60/40 Brass Hot-worked	90	25	45	25
High Tensile Brass Sand cast	160	42	18	15
Aluminium Bronze Sand cast	115	34	25	13
Aluminium Bronze Hot-worked	185	40	25	10
70/30 Cupro-Nickel Hot-worked	80	23	45	5
Chromium Copper Sand cast, Solution-treated	55	13	40	40
Chromium Copper Sand cast, Solution-treated and precipitation hardened	125	22	20	80
Beryllium Copper Wrought, Solution-treated	110	33	45	16
Beryllium Copper Wrought, Solution-treated and precipitation-hardened	270	75	5	30
Beryllium Copper Wrought, Solution-treated, cold-worked and precipitation-hardened	420	90	3	25

\* IACS: International Annealed Copper Standard (pure annealed copper with a resistivity of 1.7241 mΩ-cm, at 20°C is taken as 100%)

## 3.2 Corrosion of pure copper, tin bronze and brass

### 3.2.1 Copper

Copper and copper alloys are in general corrosive resistance in aqueous environments because of the formation of  $\text{Cu}_2\text{O}$ , which is adherent and only semiconducting, according to the equations:



In practice, alloying elements such as Al, Zn, Sn, Fe and Ni will modify this semiconducting film and may reduce the corrosion rate, in addition to improvement of mechanical or processing properties.

All copper alloys are susceptible to pitting corrosion in a chloride-containing medium. The corrosion behaviour of copper alloys in NaCl solutions is, however, not so simple as expected. The mechanism of anodic products depend on the electrode potential and are in general very complicated [Bjorndahl and Nobe, 1984] [Milosev and Metikos-Hukovic, 1992] [Pynn and Chun, 1996].

### 3.2.2 Brass

In addition to pitting corrosion, brasses are susceptible to three types of corrosion, namely, dezincification, stress corrosion cracking and impingement erosion, which arises from liquid flow. The degree of susceptibility depends on the amount of zinc present. Dezincification does not occur in the Zn content is less than 15%. Resistance

to stress corrosion cracking also decreases as the zinc content decreases. The addition of tin greatly improves its resistance to dezincification.

### **3.2.3 Tin bronze**

Bronze containing 8 to 10% of Sn shows good resistance to impingement attack and is also more corrosion resistant to seawater and to most nonoxidizing acids than brass [Jones, 1996].

## **3.3 Cavitation erosion on Copper and Copper-based alloys**

Owing to the localized and dynamic nature of cavitation attack, the resistance to cavitation erosion of a material is related in a complex manner to its mechanical properties [Karimi and Martin, 1986]. With the same group of materials, hardness may play an important role. Therefore, the cavitation erosion resistance of bronze is higher than brass. The cavitation erosion behaviour of bronze depends on a great degree of deformation mode and microstructure, which are strongly influenced by chemical composition and heat treatment.

Of the copper alloys, aluminum bronzes have received the most attention because of their extensive use in marine applications and their better erosion resistance. Aluminium-nickel bronzes are also well known to have high cavitation erosion resistance, this is especially true of bronzes containing 11 - 14% Al. For single phase, the erosion mechanism of aluminium bronze alloys is governed essentially by hardening of a phase which depends on stacking fault energy. The multiphase aluminium bronze

alloys (Cu-Al-Ni, Cu-Al-Fe, Cu-Al-Ni-Fe, Cu-Al-Co, Cu-Al-Si) erosion resistance results both from hardening of a phase and from the percentage and the distribution of intermetallic precipitates [Heuze and Karimi 1991]. Furthermore, Tsvetkov and Pogodaev have tried to alloy bronzes with titanium and this titanium alloyed bronzes have improved the cavitation erosion resistance with a substantial amount [Tsvetkov *et al.*, 1994].

Study of cavitation corrosion field and laboratory of nickel-aluminium bronze in seawater, also investigated the cavitation erosion behaviour of NiAl bronze and identified the erosion mechanism to the selective removal of the  $\alpha$ -phase at its interface with intermetallic precipitate [Shaluby *et al.*, 1995].

### **3.4 Surface modification of Copper and Copper-based alloys**

#### **3.4.1 Laser surface melting of Copper alloys**

Laser surface modification provides an unique, fast and economic method for improvement of the surface properties of the bulk material. This process induces a rapid quenching rate. Laser surface melting of copper alloys improve its microstructure by rapid solidification, including refined grain sizes, homogenization [Draper and Sharma, 1981], segregation reduction, solid solution extension, and metastable phase formation [Draper, 1981]. The microstructural changes enhance surface sensitive properties such as, resistance to cavitation erosion, corrosion [Draper *et al.*, 1980] [Toivanen and Hirvonen, 1989] and wear. Due to the low melting point elements in tin bronze and brass, laser surface modification induced preferential loss of high vapour

pressure elements, as results in surface roughness [Panagopoulos and Michaelides, 1992], cracking, porosity and presents difficulties to modify high zinc alloys [Draper, 1981]. In addition, the cracking tendency increases with increasing lead content and increasing laser power [Hyatt and Mackay, 1993].

### **3.4.2 Surface modification by Chromium Cr**

Chromium is a high corrosion resistant element and provides improvement of hardness in alloying. In decoration usage, corrosion and wear resistant chromium coatings on copper alloys substrate is commonly used for protection. This kind of application can be produced by electroplating, physical vapour deposition (PVD) [Koch and Ebersbach, 1997] etc. The chromium coatings need to provide lower porosity and compact nature, because of its higher corrosion resistance. Hence, the degree of the corrosion protection of the chromium coatings depends on the percentage of the pores in the coatings.

Chromium as an alloying element in copper gives a well known excellent anticorrosive and mechanical characteristics even at high temperatures, without appreciably reducing its thermal and electrical conductivity. The solid solubility of chromium in copper is limited, maximum 0.89 atomic % at 1350 K [Massalski (Ed), 1990], with traditional alloying methods. The characteristic of laser surface alloying causes a rapid solidification after irradiation. Consequently, the chromium particles crystallize and are finely dispersed in the modified layer upon rapid cooling accompanied with increasing in hardness [Hirose and Kobayashi, 1994] and wear resistance [Manna, 1996]. The percentage of chromium content can be extended up to



20% - 40% [Galantucci *et al.*, 1989]. In the laser surface alloying of copper with chromium, the problem need to overcome is the high reflectivity of both copper and chromium.

### **3.4.3 Surface modification by Nickel Ni**

Copper and nickel form a complete solid solution in any compositional proportion. Unfortunately, electroplated pure nickel layer cannot be laser modified on pure copper substrate due to the high reflectivity of the nickel coating combined with high thermal conductivity of the copper substrate. However, the improvement of hardness and corrosion resistance of bronze can be achieved by laser surface melting. For additional chromium layer plated on the nickel coating, laser surface modification can be applied [Pelletier *et al.*, 1993].

### **3.4.4 Surface modification by Boron B**

Laser boronizing is the laser alloying process with boron powder as an alloying element to produce hardened layers [Selvan *et al.*, 1999]. In conventional boronizing processes, the hardened layer is rather thin, less than several tens of micro-meters even with long treatment times at high temperature 850°C [Nakata *et al.*, 1995, 1996]. The hardened layer is attributed to a uniform dispersion of hard boron particles and hard boride phases, which improve the wear resistance significantly.

Furthermore, the cavitation erosion of a metal is significantly influenced by the composition, structure and state of stress in surface. Consequently, the implantation of foreign ions, which introduces a composition change, structural defects and generally, a

compressive stress in the surface. Boron ions implanted on 99.999% copper for improvement of cavitation erosion resistance has been attempted by Preece and Kaufmann [Preece and Kaufmann, 1982].

#### **3.4.5 Surface modification by Aluminium Al**

The addition of aluminium in copper can significantly reduce the stacking fault energy and leads to the larger changes in deformation feature. Aluminium bronze can be further improved by laser cladding with a welding wire of composition C-9.0Al-4.6-Ni-3.9Fe-1.2Mn for increasing corrosion- and cavitation-erosion resistance of the surface [Hyatt *et al.*, 1998].

#### **3.4.6 Surface modification by Ni-based alloys**

Ni-based alloys, such as, COI MONOY, INCOLOY and HASTELLOY, have an excellent oxidation corrosion resistance, wear resistance and attractive mechanical properties. For surface engineering, the Ni-based alloy powder is a common kind of powder used for the formation of hardfacing coating for enhancing mechanical properties [Qian *et al.*, 1997] [Vannes *et al.*, 1998] [Hidouci *et al.*, 2000], cavitation erosion resistance [Sang and Li, 1995] [Kwok *et al.*, 1998], wear resistance [Dehm *et al.*, 1999]. Furthermore, the Ni-based alloys compose with additional element and/or ceramic, such as Mo [Luperi *et al.*, 1998], WC [Qian *et al.*, 1998] [Li *et al.*, 1999 a], TiC [Li *et al.*, 1999 b]. However, there is very little information about the surface modification on copper-based substrate.

### 3.4.7 Laser surface modification of Copper and Copper-based alloys

Owing to high reflectivity and high thermal conductivity, laser surface modification of copper and copper alloys presents some degree of difficulties. As a consequence reports on such investigation are relatively scarce compare with those on other structural materials like steel and aluminium alloys. The number of publications related to the laser surface modification of copper and copper alloys only amounts to about 20 over the past two decades (METADEX). The results of these investigations are summarized in the table below. A number of points can be readily conducted from an analysis of this summary.

- i) Up to the present moment, most of the work is concentrated to laser surface melting (LSM) and laser surface alloying (LSA). Laser cladding (LC) is extremely rare, probably because of the high reflectivity and high thermal conductivity of copper and its alloys.
- ii) Most of the studies were aimed at the improvement of hardness and corrosion resistance. Only one study reported the investigation of wear resistance [Nataka *et al.*, 1996] and only one was devoted to cavitation erosion [Draper *et al.*, 1982, 1984].
- iii) Most of the studies employing LSM dealt with alloy system Cu-Al-Fe (studied by Draper' group), probably because this ternary system does not contain a particularly high vapour pressure element. In view of this, brass is more difficult to treat using LSM as it contains zinc, a high vapour pressure element.

- iv) The enhancement in properties after LSM were attributed to (a) homogenization of the constituents in the alloy, (b) refinement of structure, and (c) formation of metastable phases, as in laser treatment of other alloys.
- v) Most of the studies on the LSA of copper employed chromium as the alloying element. Chromium enhanced the corrosion resistance and also increased the hardness by the presence of finely dispersed Cr particles.
- vi) The paper by Nataka *et al.* (1996), which reported their work on the LSA of Cu-Ni using boron powder, is particularly interesting. Very large increase in hardness and wear resistance was achieved owing to the presence of hard boron particles and nickel boride in the alloyed layer.
- vii) Investigation of LC on copper and copper alloys is only at the initial stage. The preliminary work by Weisheit and Mordiki (1997) belongs to such an attempt in this direction.

Table 3.1 Summaries of laser surface modification of copper and copper alloys

Laser Process	Substrate	Alloying element	Results	Author	Year
Laser surface melting	Cu-Al-Fe (aluminium bronze)	--	-Depletion of the highest vapour pressure element in central area of track	Draper <i>et al.</i>	1980
	Cu-Ni-Sn				
	Cu-Al-Fe	--	-Enhanced corrosion resistance to acidic NaCl solution, attributed to the homogenizing effect of laser processing	Draper <i>et al.</i>	1980
	Cu-Al-Fe	--	-Laser melted region of 10µm deep obtained homogenization achieved	Draper <i>et al.</i>	1981
	Cu-Al-Fe	--	-Erosion rate lower for laser treated sample -Incubation period longer for laser treated sample	Draper <i>et al.</i>	1982
			-Corrosion behaviour (in deaerated CH <sub>3</sub> COONa + CH <sub>3</sub> COOH, pH 7 solution with or without NaCl) improved -Both improvement in erosion and corrosion resistance due to the highly supersaturated and chemically homogeneous single phase alloy structure		
	Cu-Al-Fe	--	-Both cavitation erosion and corrosion resistance improved -In particular, the incubation period increased by 10x -Extended solution metastable crystalline and martensite phases observed over tens of µm	Draper <i>et al.</i>	1984

Cu-Ni-Sn	--	-Corrosion resistance to gaseous H <sub>2</sub> S, Cl <sub>2</sub> improved, attributed to homogenization of treated layer	Draper <i>et al.</i>	1984
Cu-Al-Fe	--	-Corrosion resistance increased, as measured by polarization studies in deaerated 5% H <sub>2</sub> SO <sub>4</sub> , attributed to homogenizing	Javadpour <i>et al.</i>	1982
Cu-Al-Fe	--	-Microstructure studied by glancing-angle XRD	Vandenberg and Draper	1984
Cu-35%Zn	--	-Improved resistance to nitric acid -Selective corrosion at the boundaries of resolidified cells	Toivanen, Hivenen	1989
Cu	--	-Only corrosion potential was measured, therefore no conclusion on the corrosion rate could be drawn	Panagopoulos, Michaelide	1992
Brass	--	-Pores and cracks were present in the treated layer. -Pores were due to presence of high vapour pressure element and dissolved gas	Hyatt and Mackay	1993
Cu coating on cold rolled Cu	--	-Corrosion resistance between extension and electrical conductivity increased by laser treatment	Gurkovsky, Stoychev	1994
Laser surface alloying	Cu, Cr, Ni	-Cu-Cr-Ni metallic glass formed, called 'stainless coppers' -Excellent resistance to HS -Low contact resistance -Stable over long period, and through 10 <sup>4</sup> electronic dial switching cycle	Draper <i>et al.</i>	1987

Cu	Cr	-Ten of $\mu\text{m}$ alloying depths obtained Cr% ranged from 20% to 40%	Galentucci <i>et al.</i>	1989
Cu	Ni	-Surface alloys formed, except in the case of Ni on pure copper	Pelletier <i>et al.</i>	1993
Cu-4%Sn	Ni, Cr	-Hardness almost doubled		
Cu-9%Sn		-Surface very ductile, could withstand very large plastic deformation		
		-Corrosion resistance increased in NaCl, but decreased in $\text{H}_2\text{SO}_4$		
Cu	Cr	-Hardness at room temperature increased from 60-70Hv to 120Hv	Hirose, Kobayashi	1994
		-Hardness at 873K of the surface alloy was 3-4 times pure Cu		
		-Increase in hardness due to strengthening by finely dispersed Cr particles		
Cu	Cr electrode- posited	-Hardness in the alloying zone 1.3-3 times that of substrate	Manna <i>et al.</i>	1996
		-Alloying zone contained Cr 2-8%, with 1-3.5% at solid solution, the rest as Cr precipitates		
		-Increase in hardness due to dispersion hardening		
Cu-Al	Fe	-A laser treated zone of $\sim 200\mu\text{m}$ depth was obtained, with relatively uniform alloyed Fe concentration and a fine-scaled structure	Palumbo <i>et al.</i>	1989
		-Hardness enhanced		
		-Corrosion resistance in acidified 3% NaCl solution improved		

Cu-Ni	B	<ul style="list-style-type: none"> <li>-Alloyed layer consisted of hard boron particles, hard Ni-B, and a soft Cu-Ni solid solution phase</li> <li>-Hardness of alloyed layer increased to 400-500Hv</li> <li>-Wear resistance improved to 40 times that of Cu-Ni alloy</li> </ul>	Nakata <i>et al.</i>	1996
Laser cladding	Cu	<ul style="list-style-type: none"> <li>Cu-Al-Fe -Layers of 0.5-2mm were produced</li> <li>-Hard Fe-rich particles were embedded in the ductile Cu-rich matrix</li> <li>-These particles were undesirably big</li> <li>-Will be conducted</li> </ul>	Weisheit, Mordike	1997



## 4 Experimental details

### 4.1 Substrate materials

#### 4.1.1 Compositions

The substrate materials included the as-received Bronze (Cu8%Sn) and Brass (Cu38%Zn). Bronze was in the form of round bar and brass was in the form of rectangular bar. Table 4. 1 shows the compositions of the alloys which were obtained by energy dispersive X-ray spectroscopy (EDX).

Table 4. 1 Analytical chemical compositions of various steels.

Element (wt %)	Cu	Sn	Zn	Pb
Bronze	Bal.	8		4
Brass	Bal.		38	1.5

#### 4.1.2 Specimen preparations

As-received bronze was cut into disc 5mm in thickness and 20mm in diameter. For the rectangular bar of brass, the bar was machined to a size about 15mm × 30mm × 8mm (Fig. 4. 1) for laser surface modification. The surface of the specimens for flame spraying and laser surface treatment was sand-blasted to provide better adhesion for flame spraying and to reduce reflectivity for laser surface treatment.

Subsequent to laser surface treatment, the laser modified specimens were cut into two, one for cavitation erosion test and the other for potentiodynamic test. The surface of the laser modified specimens was rough and oxidised. In order to keep a constant surface roughness, the surface of the specimens was mechanically polished to 1  $\mu\text{m}$

diamond finish. Then the specimens were cleaned, degreased, dried and weighed before and after each subsequent ultrasonic vibratory cavitation erosion test.

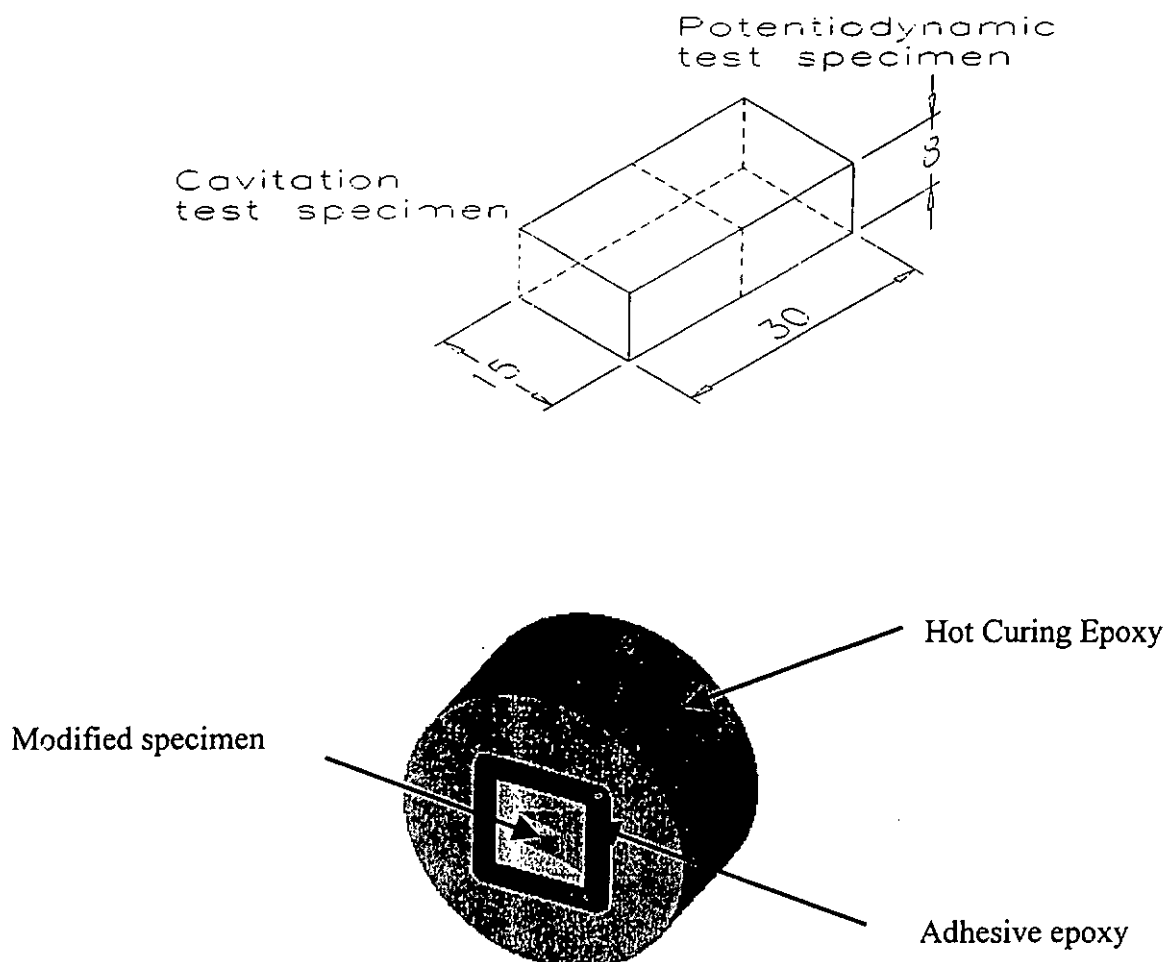


Figure 4. 1 Dimensions of the substrate specimen and specimen mounted for cyclic polarisation studies

For cyclic polarisation studies, the surface of the specimens was also mechanically polished to a 1  $\mu\text{m}$  diamond finish and, cleaned, degreased with ethanol alcohol and ultrasonic cleaner. The specimens were mounted in a hot-curing epoxy holder and the interface edge between the specimen and holder was sealed with

adhesive epoxy to prevent crevice corrosion and any other adverse effect. The mounted specimens were drilled and threaded for the connecting rod to screw into the holder, which provided an electrical conduction path for the working electrode.

## 4.2 Alloy powder

### 4.2.1 Physical properties

Powder materials for LSA and LSC consist of alloys and alloy-ceramics shown in Table 4. 2:

Table 4. 2 Melting point and particle size of powder materials

Powders materials	Melting point (°C)	Particle size
<b>Alloys</b>		
Ni-Cr-Si-B	~ 1050	~ -140 to +350 mesh ( <105 $\mu\text{m}$ and > 40 $\mu\text{m}$ )
Ni-Cr-Al-Mo		~ -140 to +350 mesh ( <105 $\mu\text{m}$ and > 40 $\mu\text{m}$ )
<b>Alloys-Ceramics</b>		
Ni-Cr-Si-B-35%WC	WC : ~ 2800	~ -140 to +350 mesh ( <105 $\mu\text{m}$ and > 40 $\mu\text{m}$ )
Ni-Al <sub>2</sub> O <sub>3</sub> (20%-80%)	Al <sub>2</sub> O <sub>3</sub> : ~ 2050	~ -140 to +350 mesh ( <105 $\mu\text{m}$ and > 40 $\mu\text{m}$ )
Ni-Cr-Fe-20%WC	WC : ~ 2800	~ -140 to +350 mesh ( <105 $\mu\text{m}$ and > 40 $\mu\text{m}$ )

### 4.2.2 Compositions

The nominal compositions of various alloy and alloy-ceramic powders are given in Table 4. 3:

Table 4.3 Nominal chemical compositions (wt %) of various alloys and alloy-ceramics powders.

Powders	Ni	Cr	Si	B	Fe	Al	Mo	W	C
<b>Alloys</b>									
NiCrSiB	Bal.	16.5	3.5	3.5	16				< 1
NiCrAlMo Alloy	Bal.	10		1	5	7	5		
<b>Alloys-Ceramics</b>									
NiCrSiB-35%WC	Bal.	16.5	3.5	3.5	16			30-35	< 1
Ni-Al <sub>2</sub> O <sub>3</sub> (20%-80%)	Bal.								
NiCrFe-20%WC	Bal.	10			10			15-20	

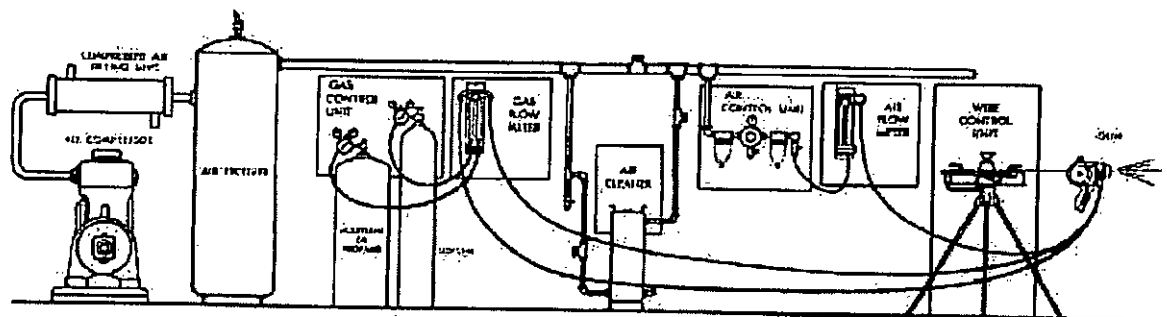
### 4.3 Preplacement of powder

#### 4.3.1 Flame spraying

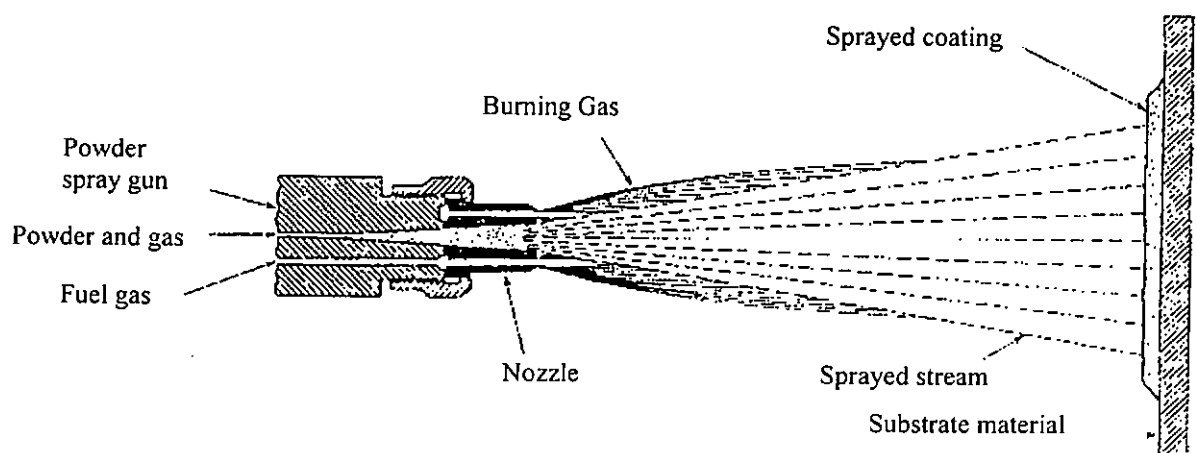
Prior to laser surface treatment, powders of self-fluxing alloy Ni-Cr-Si-B, Ni-Cr-Al-Mo, Ni-Al<sub>2</sub>O<sub>3</sub>, NiCrSiB-WC and Ni-Cr-Fe-WC (particle size ~ -140 to +350 mesh, i.e. -105  $\mu\text{m}$  to +40  $\mu\text{m}$ ) were preplaced on the substrate by flame spraying. Since flame sprayed layer adhered to the substrate surface primarily by mechanical bonding, the substrate surface was roughened by sand blasting and then degreased and cleaned before flame spraying.

A gravity-feed powder spray gun (Shanghai Welding & Cutting Tool Works, Model SPH-2/h) was used to achieve flame spraying of the powders on the substrate. Fig. 4.2 (a) illustrates the spray gun system. The major components include a fuel gas-control unit, which consists of two regulators to supply acetylene (C<sub>2</sub>H<sub>2</sub>) and oxygen (O<sub>2</sub>), respectively, a flow meter for measuring the flow rate of aspirating gas, a canister for containing powder and a nozzle with a diameter of 1.9 mm. Fig. 4.2 (b) illustrates

the operational principle of the spray gun. Powder falls through a metering valve in the bottom of the canister into a stream of aspirating gas, which propels it to a stream of fuel gas that is diverted through a valving system in the spray gun. The flow rate of the powder is manipulated by the size of the metering valve and the amount of aspirating gas through the nozzle.



(a)



(b)

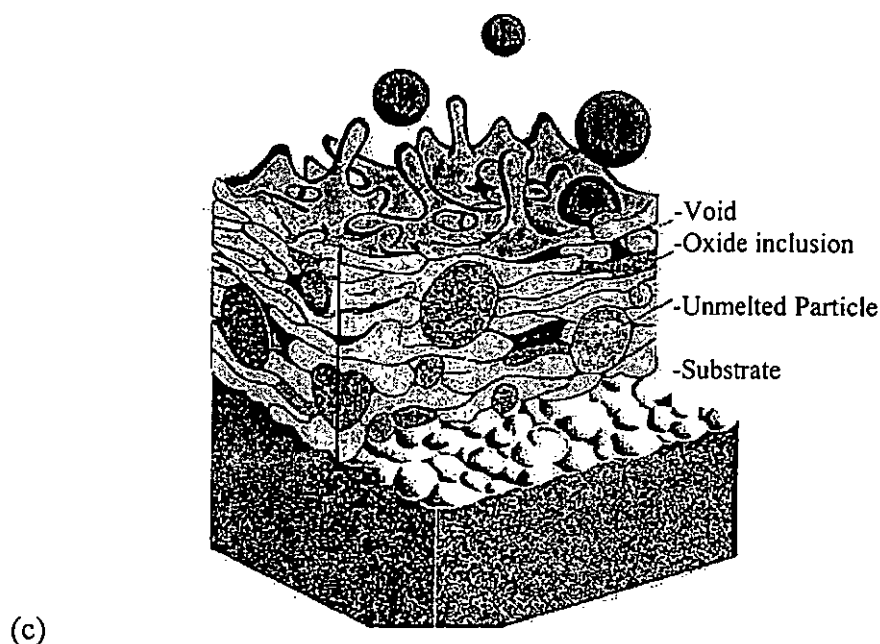


Figure 4. 2 (a) Main components of spray gun system and (b) operational principle of spray gun and (c) Schematic diagram of flame spray metal coating

The pressure and flow rate of oxygen ( $O_2$ ) and acetylene ( $C_2H_2$ ) are given in Table 4. 4. The ratio of  $O_2 / C_2H_2$  was controlled at 1 to 1.2 approximately with an aim to avoid oxidation of the metal powder. Hence, a neutral flame was produced which could be visually identified with a pale blue core and an orange / yellow outer part. Acetylene was burnt completely in air. The equation is given as follows:



Table 4. 4 The parameters of gas for flame spraying.

Gas	Pressure (kPa)	Flow rate ( $m^3 h^{-1}$ )
Acetylene	0.8	0.8
Oxygen	0.35	0.06

In order to vaporise the moisture and activate the substrate, the specimens in the form of disc and plate were placed on a steel plate holder and preheated evenly to 300 to 400°C. Then the specimens were placed under the nozzle of the spray gun with a distance kept at 80 mm and with a spraying angle kept at 45° to the specimens. Throughout the flame spraying process, the spray gun was moved continuously across the surface of specimens in the way that each consecutive pass overlapped the previous one. The powders sprayed from the nozzle were bright red hot. After the surface of specimens was completely coated, succeeding passes to increase thickness at right angles to those used for initial coverage were carried out. This procedure was repeated until the required thickness was achieved. A digital micrometer was employed to measure the average thickness of the flame sprayed layer. Subsequent laser surface melting of the sprayed layer was conducted in the as-sprayed condition.

## **4.4 Laser surface modification**

### **4.4.1 Nd-YAG laser system**

A Nd-YAG laser (Lumonics, MW2000) was employed for laser surface treatment. The laser can achieve a maximum mean output power of 2 kW in continuous wave (CW) mode. The main parts of the laser system are shown in Fig. 4. 3. The laser system comprises of a single enclosure housing of top-mount laser head, with power and control electronics modules and the cooling system equipment underneath. Laser output is delivered by a single fibre optic cable which exits through an output connector on the laser head lid.

The laser beam path is illustrated in Fig. 4. 4. Laser radiation is generated essentially by four pumping chambers, forming a single oscillator, and rear mirror M1 and front mirror M2, forming the resonator. Each pumping chamber houses a cylinder of crystalline Nd-YAG (laser rod) and two quartz tubes (flashlamp). Cooling water is pumped through the chamber to dissipate the heat generated during excitation of the laser rod. The rear mirror M1 is totally reflective and is fitted with tilt controls. Laser output beam passes through a partially reflective mirror which is mounted in a machined cell. A silicon photodiode power monitor PM1, which is mounted adjacent to the front mirror M2, monitors the laser output beam and displays it as a mean laser power value.

A shutter enclosure located at the resonator output houses a shutter / beam turning mechanism M3, a motor, a beam turning mirror M4 and lens assembly L1. A water-cooled beam dump is secured to the outside of the shutter enclosure. Under the condition of zero laser output, the resonator output beam is directed to the beam dump which absorbs the generated power. In case an output is required, M3 is driven into the beam path to turn the beam through 90° and direct the oscillator output beam to M4. The beam is turned through 90° by M4 and directed via lens assembly L1. From the lens assembly the beam enters the fibre input connector which houses a focusing lens L2 to focus the beam to the end of the fibre-optics. From the fibre input connect, the fibre optic cable, carrying the output beam, exists the laser head via output connector.



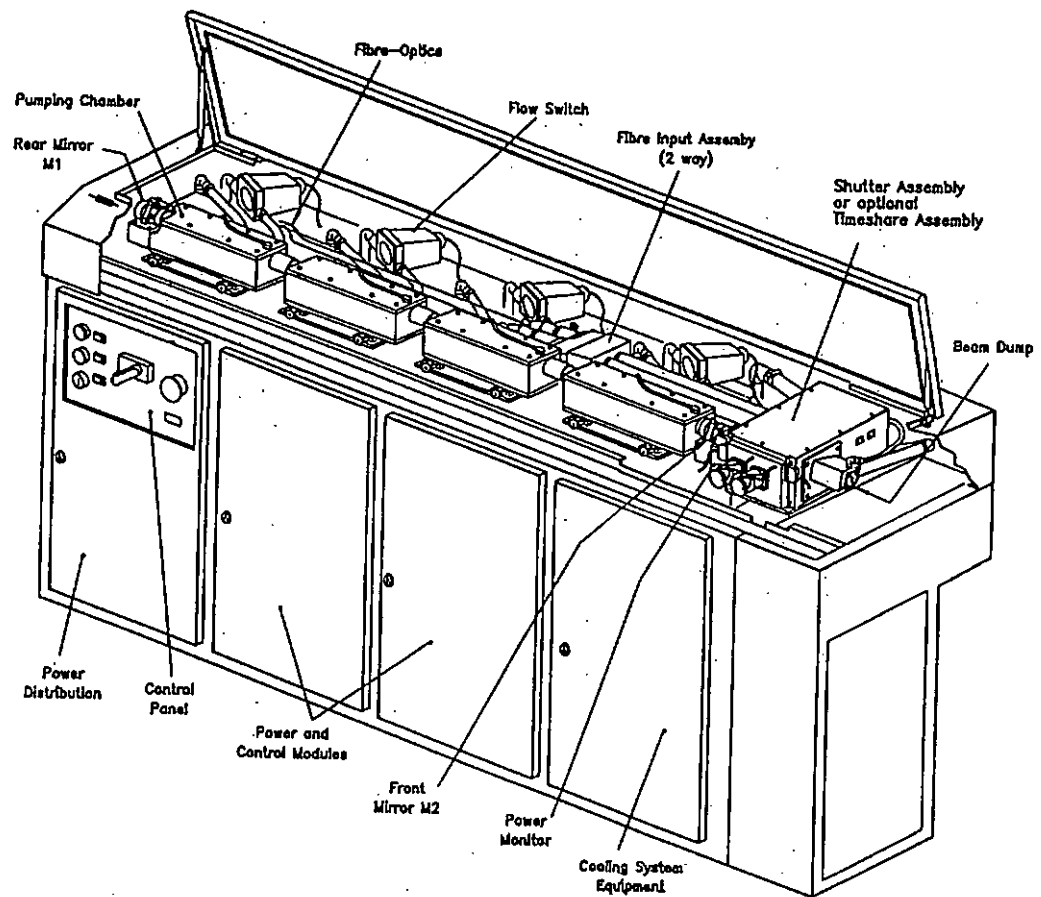


Figure 4. 3 Major components of the 2 kW Nd-YAG laser systems

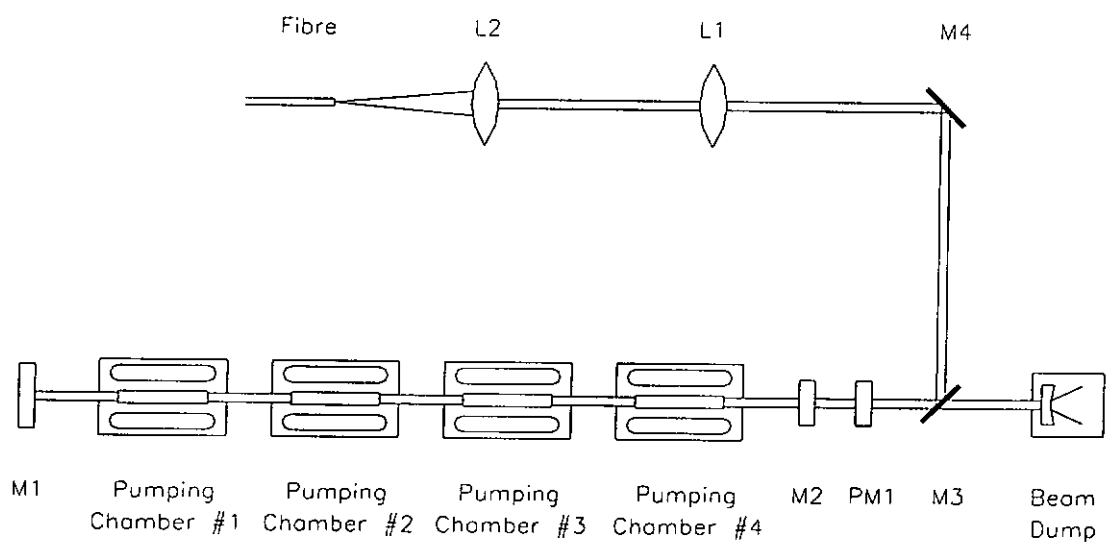


Figure 4. 4 Laser beam path of the 2 kW Nd-YAG laser systems.

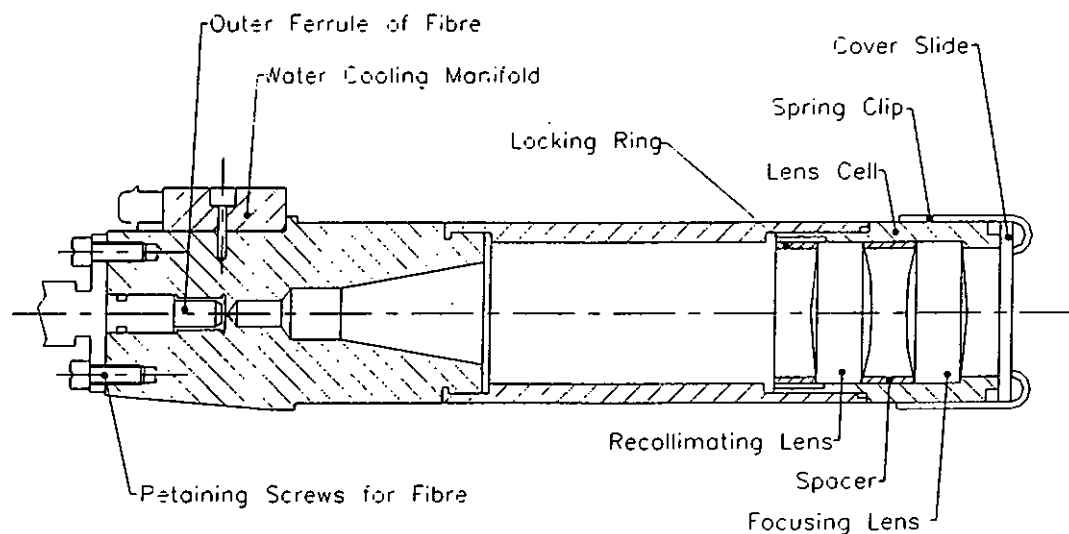


Figure 4. 5 Sectional drawing of the focusing head showing relative position of recollimating and focusing lens.

#### 4.4.2 Laser emission head arrangement

The laser beam was equipped with a recollimating lens of 200 mm focal length and a focus lens of 100 mm focal length to achieve a minimum spot size of 0.5 mm in diameter as shown in Fig. 4. 5. The laser beam was transmitted by optical fibre and focused onto the specimen by a zinc selenide (ZnSe) lens. The smaller the beam size, the higher the mean power density of laser. Back reflections from the workpiece were prevented to avoid the damage of the optical system. It was achieved by tilting the focusing head at  $10^\circ$  relative to the workpiece normal. The diagram of the tilting is shown in Fig. 4. 6. The movement of the focusing head was controlled by a computerised X-Y-Z table.

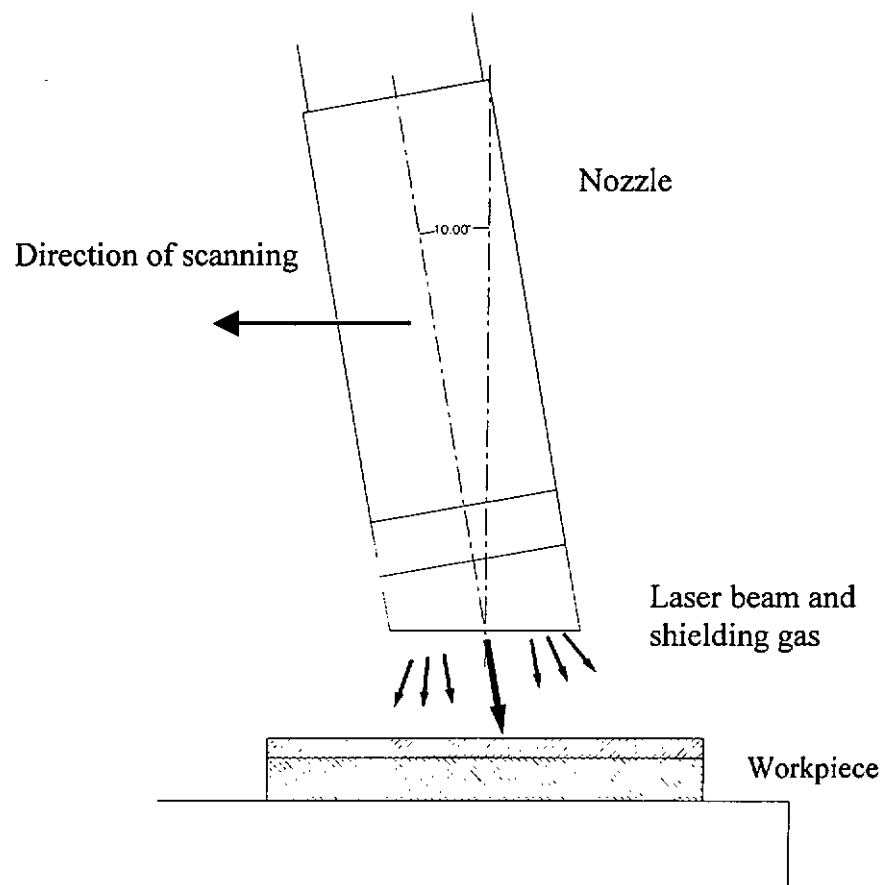


Figure 4. 6 Schematic showing the tilt angle of focusing head, position of gas shielding feed pipe and surface treatment of specimens.

#### 4.4.3 Co-axial gas shielding

In order to avoid oxidation during laser surface treatment, argon gas was applied to shield the specimens. The co-axial shielding nozzle employed for the laser surface modification was shown in Fig. 4. 7. The gas flow rate was about 15 - 20 l / min.

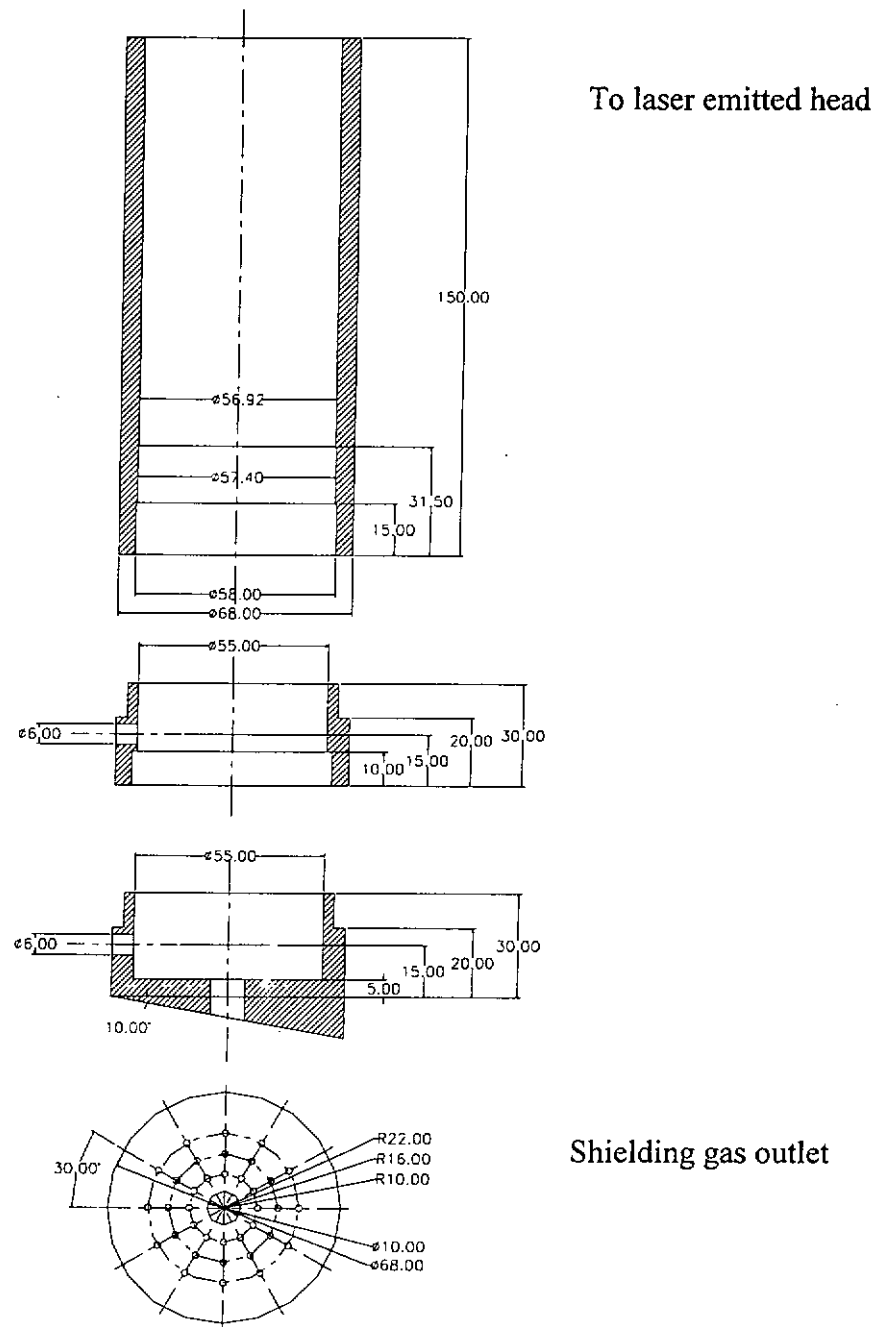
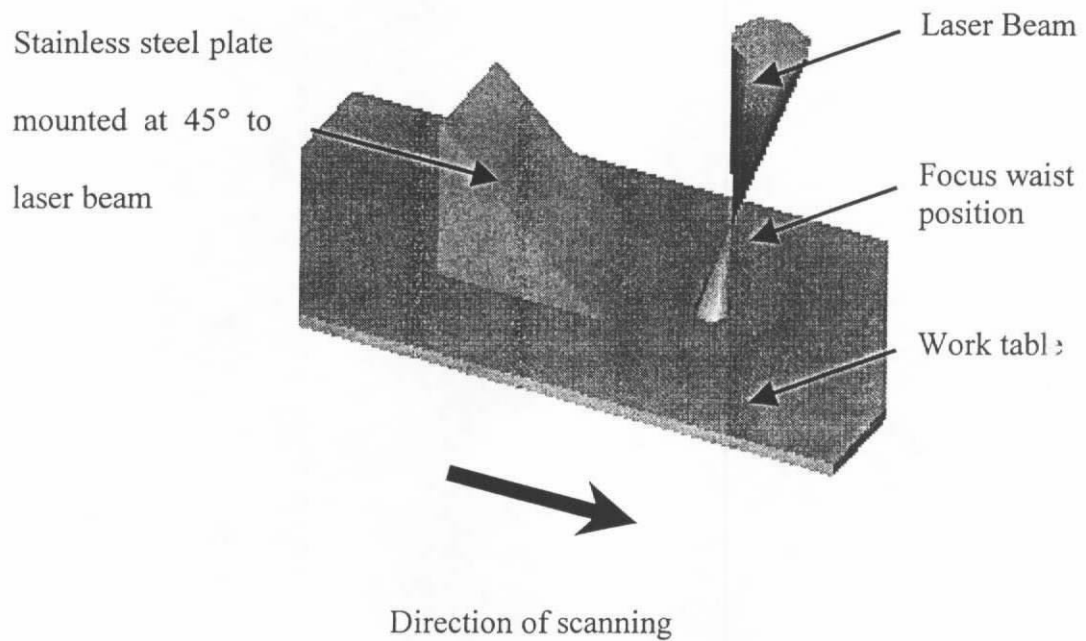


Figure 4. 7 Detailed drawing of the co-axial shielding nozzle

#### 4.4.4 Determination the focal distance

The position of the beam waist was established by the blue flash technique shown in Fig. 4. 8. A focus beam print was made on a small stainless steel plate which was tilted at an angle of  $45^\circ$ . The power of the laser used was set at 1.1 kW and the scanning speed was set at 25 mm/s. The waist position was 150 mm below the focusing head.



(a)

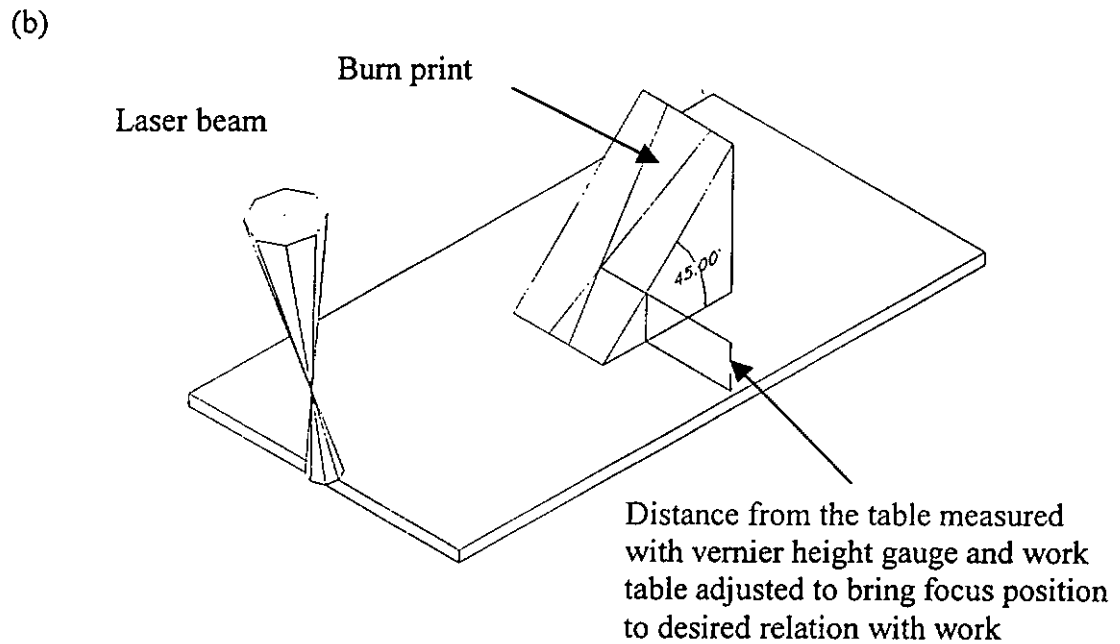


Figure 4. 8 Principle for establishing the beam waist position by using a stainless steel plate: (a) before beam print; (b) after beam print.

#### 4.4.5 Measurement of effective laser power and beam size

The effective power of the laser beam on the workpiece was measured by a laser power probe (Macken Instruments, Inc., P2000Y) as the power of laser will diminish through the fibre. The major components of the laser power probe include an absorbing head, a temperature measuring mechanism, a zeroing knob and a readout dial. The absorbing head is exposed to the laser beam for 20 seconds and the average laser power can be read out on the dial.

The defocused laser beam was used for laser surface treatment, and the working distance was defocused for 5 - 12.5 mm from the substrate. The beam size was measured by a photographic film, and the diameter was 2 - 5 mm approximately.

#### 4.4.6 Laser surface alloying / cladding

Laser surface alloying and cladding of preplaced material on substrate were performed using a laser beam with spot size 2 - 5 mm in diameter. Various beam scanning speeds and laser power densities were used. The laser processing parameters were able to produce an effective melt track with appropriate width to depth ratio (at least  $> 2$ ). An optical microscope at a magnification of 50 times was employed to observe the melt depth (D) of the specimen and captured a picture by a CCD camera (JVC). The melt depth was measured at ten different locations of the captured picture of melt zone and the average value was obtained. Image analysis would achieve a more accurate value of the average melt depth. The ratio of the cross-sectional area of the melt zone to the track width would also achieve a more accurate value for the average melt depth. The melt surface was obtained by scanning of parallel tracks each of 50% overlapping (unless otherwise specified) with the preceding one. The degree of overlapping (OL) was calculated by equation 4.1 as below:

$$OL = \frac{a - x}{a} \times 100\% \quad \dots\dots\dots (4.1)$$

where  $a$  is the width of a single track and

$x$  is the displacement between two successive tracks.

As given in equation 4.2, the dilution ratio (DR) of the laser modified layer was defined as the ratio of the thickness of the sprayed coating layer ( $t$ ) to the laser melt depth ( $d$ ).

$$DR = \left( 1 - \frac{t}{d} \right) \times 100\% \quad \dots\dots\dots (4.2)$$

After laser surface remelting of the preplaced material on the substrate was accomplished, the surface of the specimens was then polished to a consistent surface roughness by 1  $\mu\text{m}$  diamond paste. Then the specimens were cleaned, degreased, and dried before the corrosion test and also weighed before and after each cavitation test.

## **4.5 Microstructural and metallographic analysis**

### **4.5.1 Optical microscopy (OM)**

The laser treated specimens were sectioned, polished and etched slightly by a solution of acidic ferric chloride solution (25 g  $\text{FeCl}_3$ , 25 ml  $\text{HCl}$  and 100 ml  $\text{H}_2\text{O}$ ) for 5 - 30 seconds. Then the specimens were observed by optical microscopy with a magnification from 50 to 800 times (Nikon, Microphot-FXA). The microstructures of laser treated specimens were analysed and the melt depth of the specimens was measured by using CCD camera (JVC).

### **4.5.2 Scanning electron microscopy (SEM)**

SEM, which can give a higher magnification up to 10,000 times (Cambridge, Model S250), was used as a supplement to OM for the study of the microstructures of laser treated specimens. The mounted specimens were gold-coated for electrical conduction in the study of SEM. Moreover, surface morphology of eroded specimens after cavitation and the corroded specimens were studied by SEM.



### 4.5.3 Energy dispersive X-ray spectroscopy (EDX)

When the high energy electrons produced in SEM interacting with the atoms within the top few  $\mu\text{m}$  of the specimen surface, X-rays are generated with an energy characteristic of the atom that produces them. The intensity of such X-ray is proportional to the mass fraction of that element in the specimen. Therefore, the chemical compositions of specimens can be found by the energy dispersive X-ray spectroscopy (EDX) together with SEM. The elements with atomic weight higher than sodium (Na) can be studied. The light elements (atomic weight lower than Na) such as B and C can be analysed with a windowless detector. The average chemical compositions of laser treated specimens were taken at three to seven fields (depending on the melt depth) from top to bottom of melt zone of  $20\ \mu\text{m} \times 20\ \mu\text{m}$  in area.

### 4.5.4 X-ray diffractometry (XRD)

When an incident X-ray beam of wavelength  $\lambda$  strikes a polycrystalline specimen at an angle  $\theta$ , grains with interplanar spacing  $d$  diffract the radiation at the same angle according to Bragg's law given by equation 4.3:

$$\lambda = 2d \sin \theta \dots\dots\dots(4.3)$$

If the wavelength  $\lambda$  and the incident angle  $\theta$  of X-ray are known, then the plane distance  $d$  can be computed. Since line position depends upon unit cell size, and line intensity depends upon the type of atoms present and on their arrangement in the crystal, each crystalline substance has a unique X-ray diffraction pattern. The unique

diffraction pattern of particular substance can be identified by the Powder Diffraction Files (PDF) from Joint Committee on Powder Diffraction Standards (JCPDS). As illustrated in Fig. 4. 9, the structures and phases of the laser treated and cavitated specimens were analysed by an X-ray diffractometer (Philips, Model PW3710).

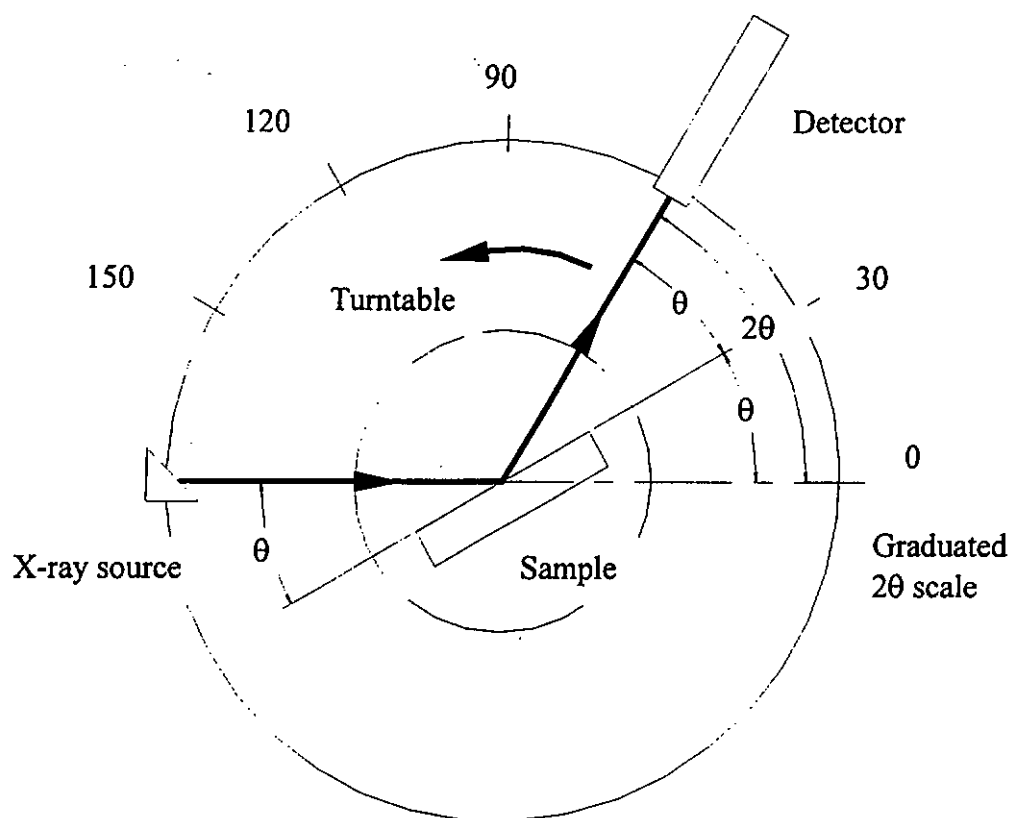


Figure 4. 9 Layout of powder diffractometer.

The radiation source Cu  $K\alpha$  with monochromatic nickel filter, generated at 40 kV and 35 mA, was used for the study of XRD. The scan rate was  $0.04^\circ / \text{s}$ . The longer Cu  $K\alpha$  wavelength (0.15406 nm) was chosen for the purpose of maintaining a thin layer about  $10 \mu\text{m}$  in diffracting (i.e shallow penetration).

## 4.6 Cavitation erosion testing

### 4.6.1 Ultrasonic induced vibratory tester

An ultrasonic induced vibratory cavitation facility (Heat System Inc. U.S.A. Sonicator Ultrasonic Liquid Processor Model XL2020, 550 W) was employed to carry out the cavitation erosion experiments. As shown in Fig. 4. 11, the cavitation erosion tester consists of a power supply, a converter and a disrupter horn. The power supply converts conventional 50 or 60 Hz alternating current to 20 kHz electrical energy fed to the converter, which transforms the electrical energy to mechanical energy. Hence the vibratory frequency applied for the cavitation erosion study was 20 kHz.

The cavitation erosion test was performed conforming to the ASTM Standard G32-92 [ASTM G32-92], with minor modification of the method of mounting the specimen. Instead of mounting the specimen directly to the ultrasonic horn, it was held stationary at a distance 1 mm below the horn. Such a method has also been used by some other researchers [Vyas and Hansson, 1990]. The vibratory studs were made of super duplex stainless steel S32760 (Fig. 4. 10) and the setup was shown in Fig. 4. 11. The vibratory stud was screwed into the tip of the vibratory horn and the dial indicator with scale division of 1  $\mu\text{m}$  was mounted under the surface of vibratory stud. Readings were taken with the apparatus stationary and with it turned on. Since the dial indicator could not pursue the vibrations of the horn tip, it took on a position corresponding to the peak displacement, with peak to peak amplitude at 60  $\mu\text{m}$  (the dial reading in 30  $\mu\text{m}$ ). The test solution was contained in an open container of 1000 ml. In order to keep the solution in a constant temperature of 23°C, a circulation system with controllable temperature water bath (Cole and Pamer, Polystat) was used. The screwed vibratory stud was immersed in the test solution with an immersion depth of 10 mm. During the

upward stroke of the horn, when the lower portion of the vibratory horn was immersed in the operating solution, a low pressure region was created instantly below it and led to the nucleation and growth of a cloud of bubbles. During its downward stroke, a higher pressure region was created and the bubbles collapsed, induced impact pressure pulses attacking the test. Therefore the vibratory device was used to simulate the cavitating environment occurring in flow systems of hydraulic machineries, or in vibrating systems.

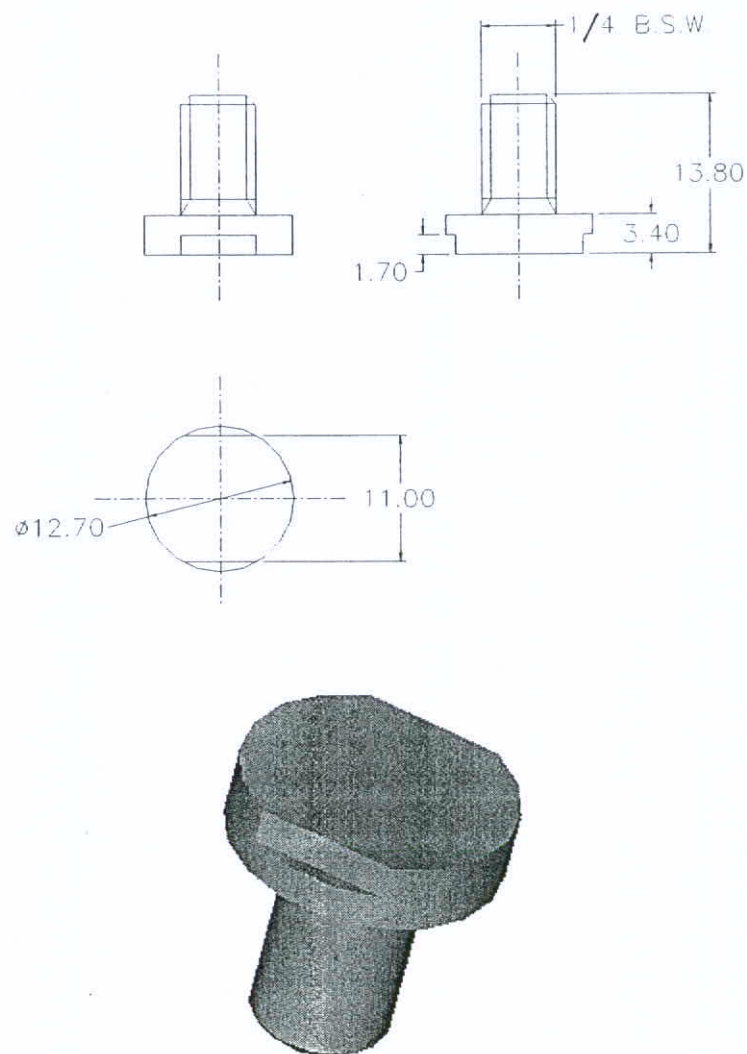


Figure 4. 10 Dimensions drawing and 3-D view of the vibratory stud for cavitation erosion test

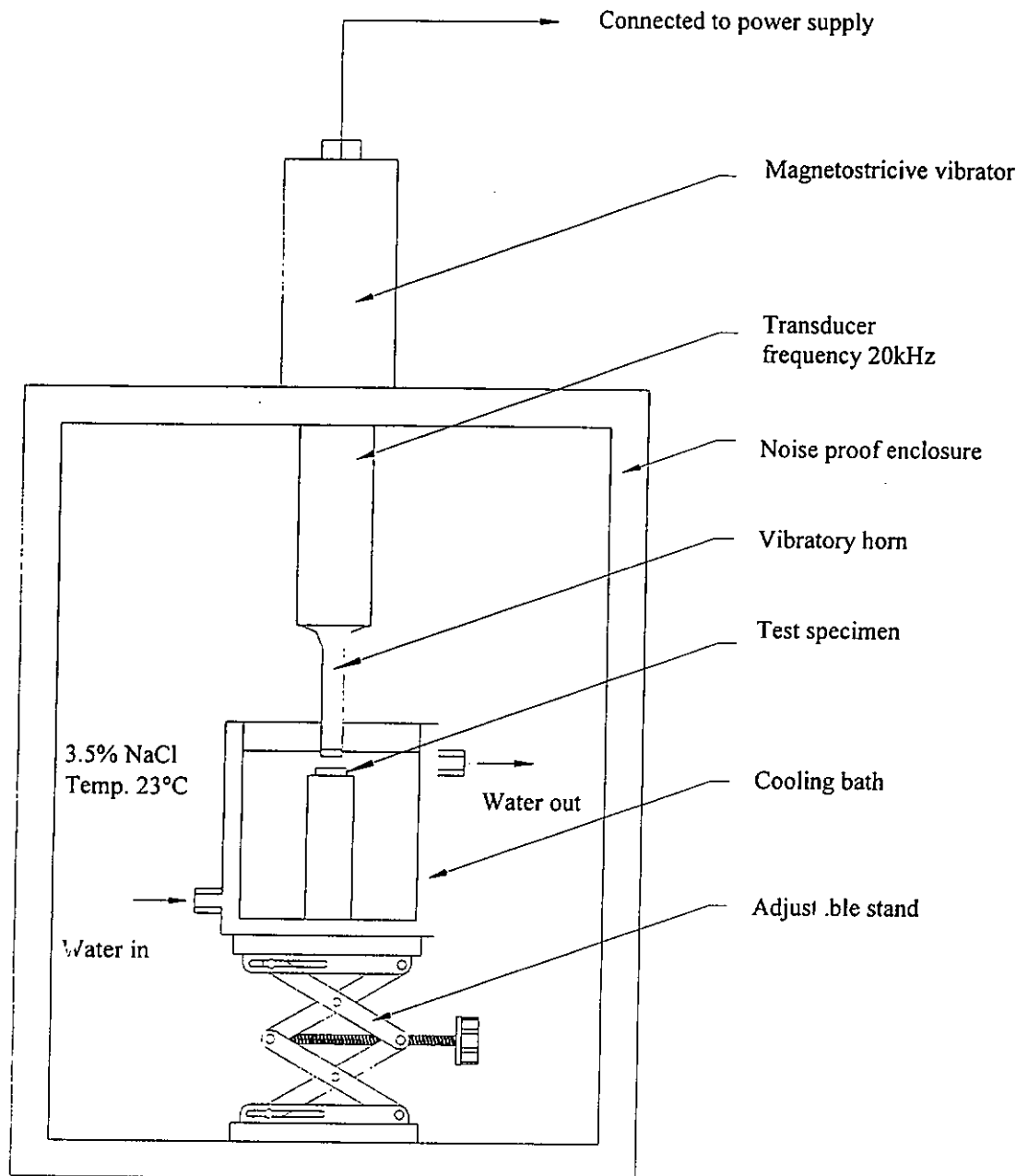


Figure 4. 11 Schematic of vibratory of cavitation erosion tester (unattachment method).

### 4.5.2 Cavitating medium

The cavitation medium was made of deionised water and reagent grade sodium chloride to give 3.5 wt % NaCl solution by dissolving 35 g NaCl solid into 965 ml deionised water. The temperature was controlled at  $23 \pm 1^\circ\text{C}$ .

### 4.5.3 Evaluation of cavitation erosion resistance

Subsequent to the cavitation test, the specimens were cleaned, degreased, dried and weighed at each interval of the test. Weight loss at each time interval was obtained by weighing the specimens using an electronic balance with accuracy of  $\pm 0.1$  mg (METTER AT balance). The erosion loss of materials was expressed in terms of the mean depth of penetration (MDP) and the mean depth of penetration rate (MDPR) as calculated by the following equations:

$$\text{MDP } (\mu\text{m}) = \frac{\Delta W}{10\rho A} \dots\dots\dots (4.4)$$

and

$$\text{MDPR } (\mu\text{m/h}) = \frac{\Delta W}{10\rho A \Delta t} \dots\dots\dots (4.5)$$

where  $\Delta W$  is the weight loss at each time interval in mg,

$\Delta t$  is the time interval in hour,

$A$  is the surface area of the specimen in  $\text{cm}^2$  and

$\rho$  is the density of the modified melt layer in  $\text{g cm}^{-3}$ .

The cumulative MDP versus time curve could then be calculated. In addition, the cavitation erosion resistance  $R_e$  is defined as the reciprocal of the mean depth of penetration rate.

$$R_e \text{ (h/}\mu\text{m)} = (\text{MDPR})^{-1} \dots\dots\dots (4.6)$$

## **4.7 Electrochemical corrosion testing**

### **4.7.1 Potentiodynamic polarisation**

The main purpose of cyclic potentiodynamic polarisation scans was to investigate into the pitting corrosion behaviour of laser surface modified and as-received specimens according to the ASTM Standard G5-94 [ASTM G5-94]. The polarisation scans were conducted using an EG&G PARC 273 corrosion system. The cell and apparatus for polarization study are demonstrated in Fig. 4. 12. The 3.5 wt % NaCl solution was kept at  $23 \pm 1^\circ\text{C}$ . A saturated calomel electrode (SCE, 0.244V versus SHE at  $25^\circ\text{C}$ ) was used as the reference electrode and two parallel graphite rods served as the counter electrode for current measurement.

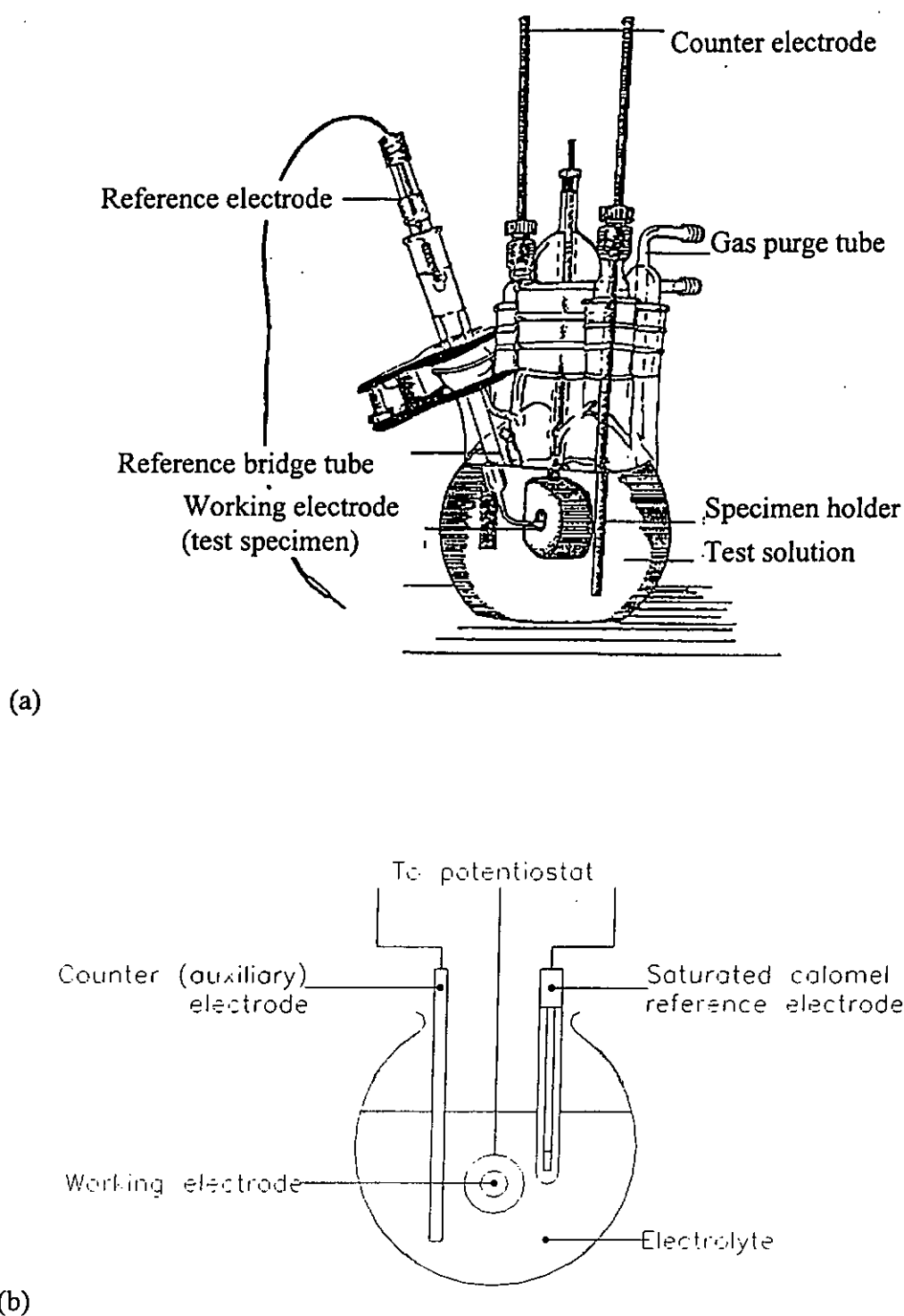


Figure 4. 12 The cell and apparatus for polarization study: (a) The three-electrode cell; (b) connection of the cell to the potentiostat. (EG&G Princeton Applied Research Inc.)



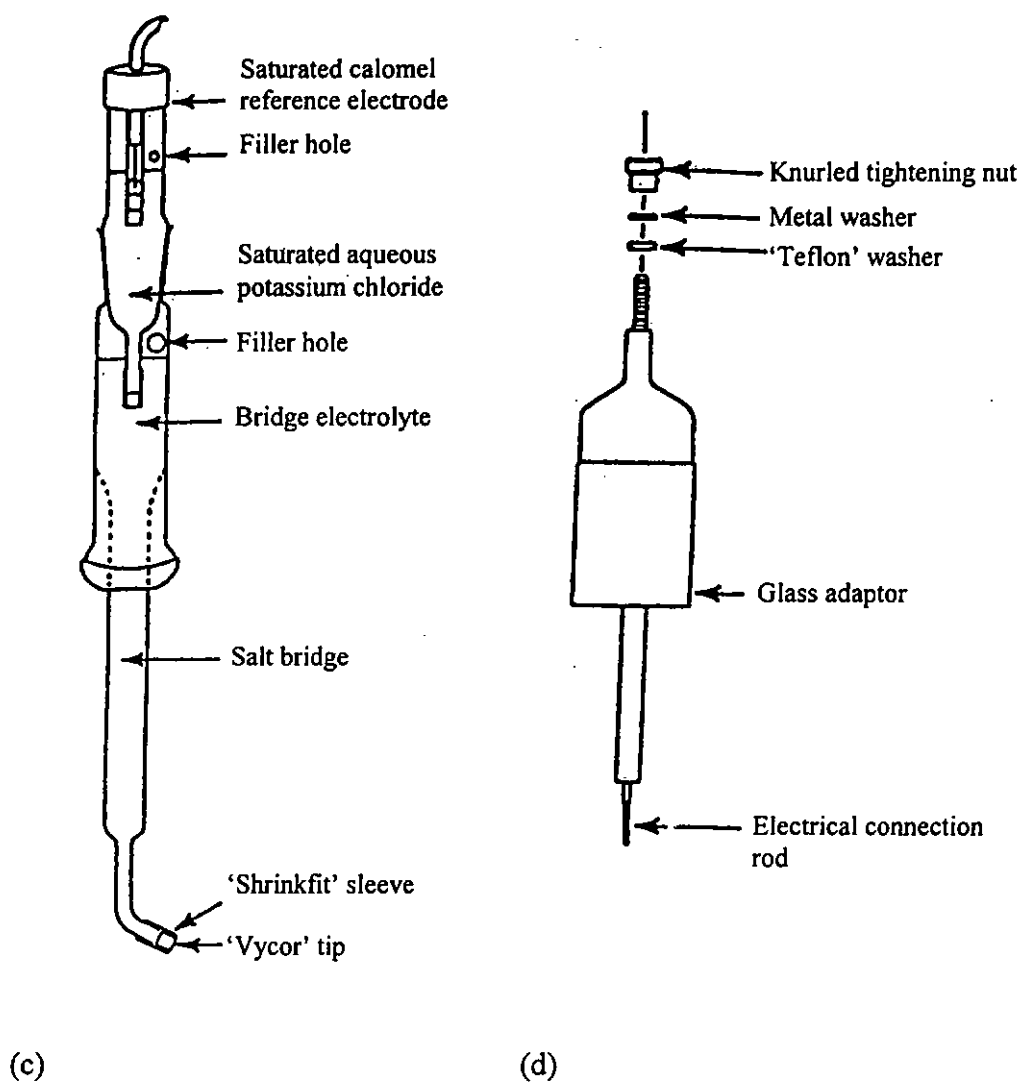


Fig. 4.12 The cell and apparatus for polarization study: (c) special design of glass salt bridge with ball-and-socket ground glass joint (d) working electrode. (EG&G Princeton Applied Research Inc.)

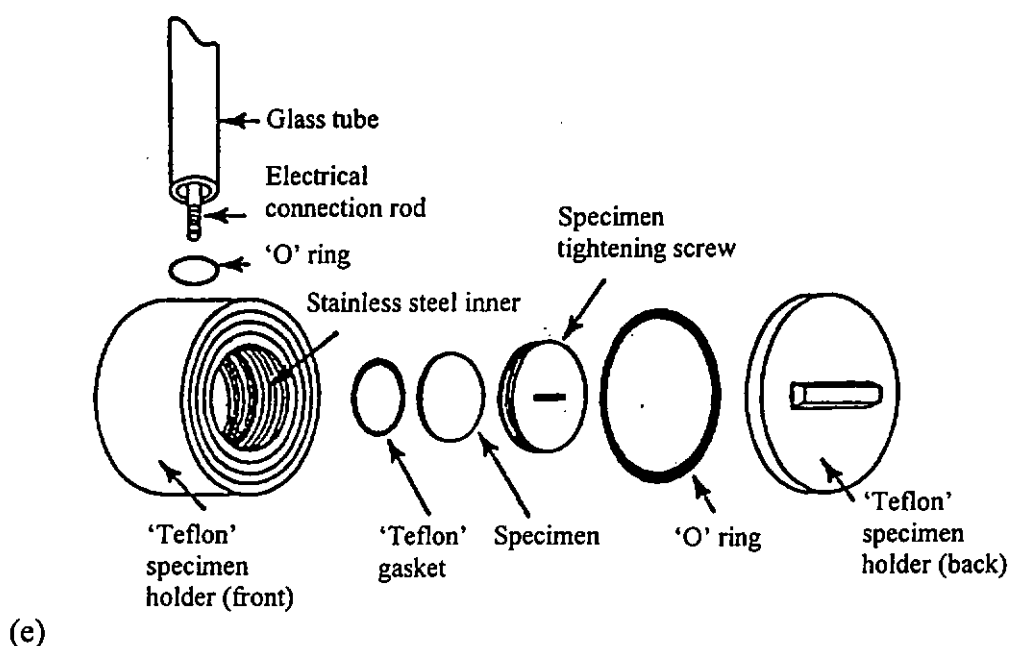
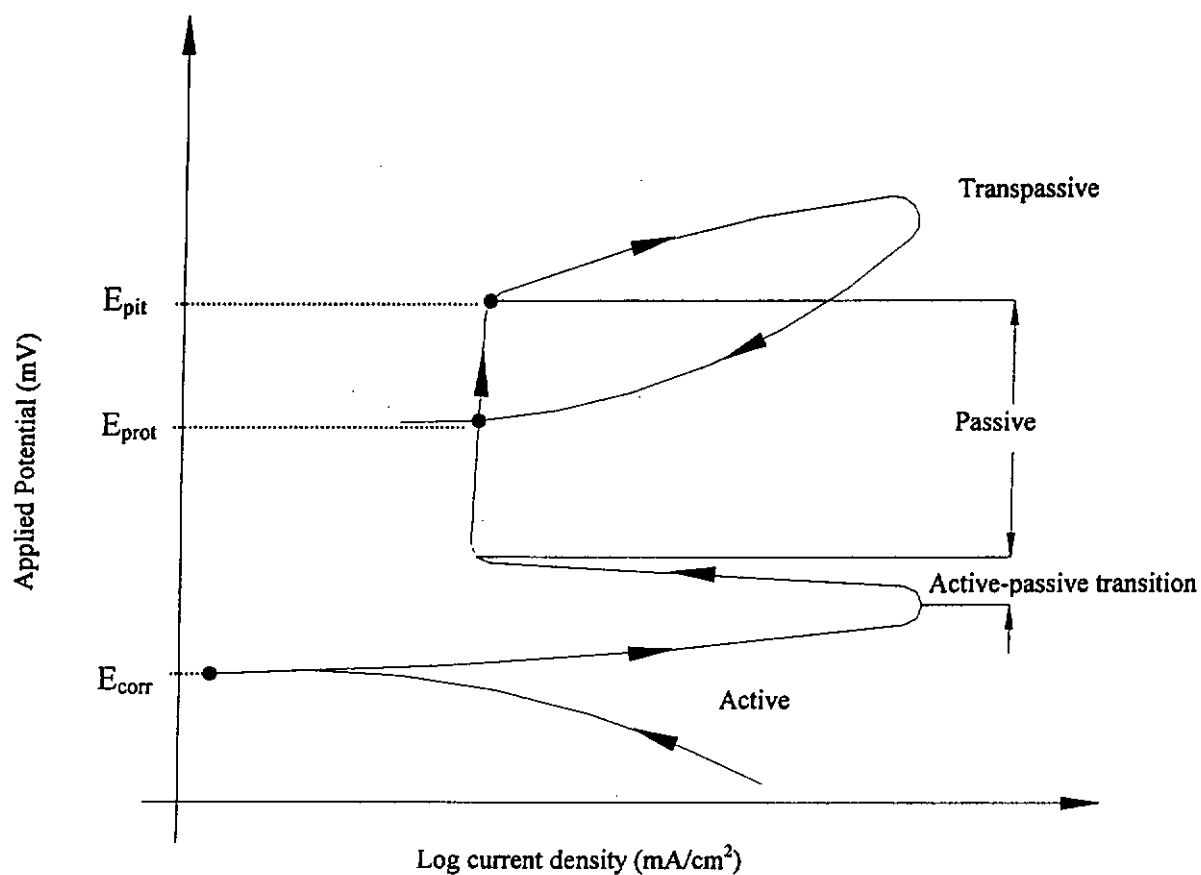


Fig. 4.12 The cell and apparatus for polarization study: (e) specimen and its holder. (EG&G Princeton Applied Research Inc.)

All data were recorded after waiting for an initial delay of 10 minutes to let the specimen to become steady. The potential was increased from 100 mV below the corrosion potential in the anodic direction at a scan rate of  $1 \text{ mV s}^{-1}$ . The scanning direction was then reversed when an anodic current density of  $5 \text{ mA cm}^{-2}$  was reached until the loop closed at the protection potential ( $E_{\text{prot}}$ , the potential below which the pre-existing pits repassivate and stop growing). The pitting potential ( $E_{\text{pit}}$ ) is the parameter in assessing the pitting resistance of material which the protection potential is a measure of the capability of repassivation. A typical cyclic polarisation curve in 3.5% NaCl solution is given in Fig. 4. 13.



$E_{\text{pit}}$  = Pitting potential;  $E_{\text{prot}}$  = Protection potential;  $E_{\text{corr}}$  = Corrosion potential;

Figure 4. 13 A typical cyclic polarisation curve for austenitic stainless steel in 3.5% NaCl solution.

## **5 Results and discussions – Laser surface modification of tin bronze (Cu8%Sn) with Ni-Al<sub>2</sub>O<sub>3</sub>**

### **5.1 Introduction**

Tin bronze (Cu8%Sn) has moderate strength, good machinability and high corrosion resistance but low cavitation erosion resistance. Surface modification can provide an engineering solution to components employed in erosive environment with the appropriate composition and microstructure of the modified surface layer. Damage in copper-based alloy is usually initiated at the grain boundaries and propagates into the interior of the grain. This crack propagation can be blocked by adjacent grains or hard phases. Therefore, a multicomponent system, which is composed of a hard ceramic phase in a ductile matrix may resist the attack of the microjet or shock wave in cavitation erosion.

Single-phase ductile copper is damaged by plastic deformation and ductile rupture while single-phase brittle materials are thought to be damaged by the generation and propagation of subsurface lateral cracks. Therefore, a multicomponent system composed of a ductile matrix containing hard ceramic particles is expected to be strong and tough enough to resist cavitation erosion.

In fact bulk Cu based composites have been fabricated by powder metallurgy [Tjong and Lau, 2000] [Ma and Tjong, 2000] and composite coatings have also been achieved by electrodeposition [Selvan *et al.*, 2000]. In the present study a surface MMC layer of Ni-Al<sub>2</sub>O<sub>3</sub> will be fabricated by laser surfacing technique.

## 5.2 Materials and laser processing parameters

### 5.2.1 Materials

The substrate tin bronze was received in the form of a round bar and machined to specimens 5 mm in thickness and 20 mm in diameter. The specimens were sand blasted prior to flame spraying in order to increase the adhesion effect between the sprayed particles and the substrate. The thickness of the substrate and the sprayed coating layer was measured before and after the flame spraying process by a digital micrometer. The nominal compositions of the tin bronze specimen and the Ni-Al<sub>2</sub>O<sub>3</sub> powder are shown in Table 5. 1 and the general physical and mechanical properties of the tin bronze specimen and Ni and Al<sub>2</sub>O<sub>3</sub> are shown in Table 5. 2

Table 5. 1 Nominal compositions (wt %) of tin bronze and Ni-Al<sub>2</sub>O<sub>3</sub> power

Material	Cu	Sn	Pb	Ni	Al <sub>2</sub> O <sub>3</sub>	Particle size
Tin bronze	Bal.	8	4			
Ni-Al <sub>2</sub> O <sub>3</sub>				25-80	Bal.	~ -140 to +350 mesh (<105 $\mu$ m and > 40 $\mu$ m)

Table 5. 2 General physical and mechanical properties of tin bronze and Ni-Al<sub>2</sub>O<sub>3</sub> powder

Material	Melting temp. (°C)	Density (g/cc)	Yield strength (MPa)	Tensile strength (MPa)	Elastic modulus (GPa)	Elongation (%)
Tin bronze	1060	8.78	350	455	110	68
Ni	1453	8.88	59	317	207	30
Al <sub>2</sub> O <sub>3</sub>	2015	3.96	3790 compressive	310	366	\

### 5.2.2 Laser processing parameters

After the flame spraying process, the specimens were measured by a digital micrometer to evaluate the sprayed coating thickness. The coating thickness of the sprayed specimens was in the range 200  $\mu\text{m}$  - 250  $\mu\text{m}$ .

In order to investigate the effect of the laser processing parameters, the laser power density was set as a varying parameter from 95 to 119  $\text{W}/\text{mm}^2$  at a constant scanning speed of 10  $\text{mm}/\text{s}$ . The processing parameters, including the laser power density, scanning speed, coating thickness and flow rate of the shielding gas, are summarized and shown in Table 5. 3.

Table 5. 3 The summary of laser power density, scanning speed, coating thickness and flow rate of the shielding gas

Specimen	Laser power density	Scanning speed	Coating thickness	Shielding gas flow rate
Ni-Al <sub>2</sub> O <sub>3</sub> -1	95 $\text{W}/\text{mm}^2$	10 $\text{mm}/\text{s}$	~ 200 $\mu\text{m}$	Argon 15 l/min
Ni-Al <sub>2</sub> O <sub>3</sub> -2a	103 $\text{W}/\text{mm}^2$	10 $\text{mm}/\text{s}$	~ 250 $\mu\text{m}$	Argon 15 l/min
Ni-Al <sub>2</sub> O <sub>3</sub> -3a	111 $\text{W}/\text{mm}^2$	10 $\text{mm}/\text{s}$	~ 250 $\mu\text{m}$	Argon 15 l/min
Ni-Al <sub>2</sub> O <sub>3</sub> -4a	119 $\text{W}/\text{mm}^2$	10 $\text{mm}/\text{s}$	~ 250 $\mu\text{m}$	Argon 15 l/min

After laser irradiation, the laser modified specimens were cross sectioned and polished to measure the melt depth and calculate the dilution ratio (DR) in the surface layer. The calculated DR is listed in Table 5. 4.

Table 5. 4 Melt depth and estimated dilution ratio of laser modified layer

Specimen	Coating thickness (t)	Melt depth (d)	Dilution ratio (DR)*
Ni-Al <sub>2</sub> O <sub>3</sub> -1	~ 200 $\mu\text{m}$	not evaluated	not evaluated
Ni-Al <sub>2</sub> O <sub>3</sub> -2a	~ 250 $\mu\text{m}$	610 $\mu\text{m}$	59%
Ni-Al <sub>2</sub> O <sub>3</sub> -3a	~ 250 $\mu\text{m}$	714 $\mu\text{m}$	65%
Ni-Al <sub>2</sub> O <sub>3</sub> -4a	~ 250 $\mu\text{m}$	781 $\mu\text{m}$	68%

$$* \text{ Dilution ratio (DR)} = \left( 1 - \frac{t}{d} \right) \times 100\%$$

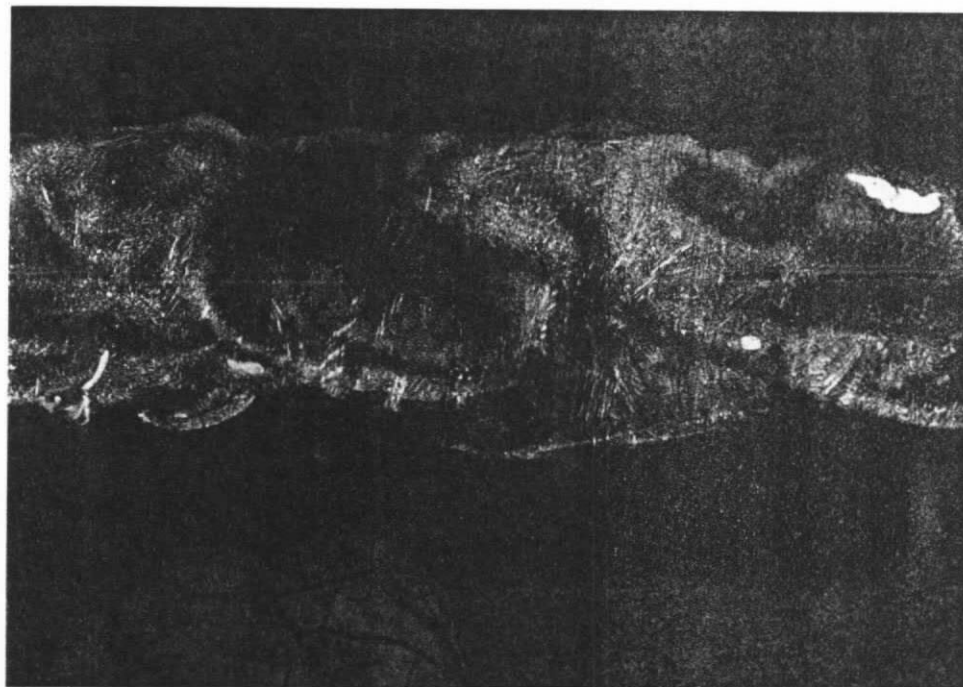
### 5.3 Microstructural and metallographic analysis


The micrograph of specimens modified with Ni-Al<sub>2</sub>O<sub>3</sub> is shown in Fig. 5. 1, Fig. 5. 2 and Fig. 5. 3. The laser modified layer had a dendritic microstructure. The dendrite grew from the interface between the melt track and tin bronze substrate towards the center of the melt zone. Due to relatively cold substrate, the heat energy absorbed from the laser irradiation was transferred from the melt pool to the bulk substrate. As a result the growth of dendrite was in the direction towards the center of the melt pool.

In the cross sectioned specimens, the precipitated secondary phases were found in the melt layer. The percentage of secondary phases increased as the power density increased.

The optical micrographs of the microstructure of the laser surface modified specimens revealed a white region in the melt layer. According to the EDX analysis, the white particles were not the preplaced alumina. The alumina powders were expelled from the melt pool because of the poor wetting between molten Cu and alumina. Some alumina had already dissociated during laser irradiation due the high power laser. Some of the aluminium combined with nickel to form an intermetallic nickel aluminide (Ni<sub>3</sub>Al) [La *et al.*, 1999], which precipitated in the laser melted layer. The hardness measured at the intermetallic was found to be 437 Hv<sub>0.2</sub> and decreased drastically to a low value of 150 Hv<sub>0.2</sub> in the matrix. For specimen Ni-Al<sub>2</sub>O<sub>3</sub>-4a, micro-cracks were induced in the laser modified layer and also in the nickel rich intermetallic phases. It also occurred in specimens processed with higher laser power density. Consequently, laser power density higher than 111 W/mm<sup>2</sup> would produce cracks in the treated surface.


(a)



200  $\mu\text{m}$  

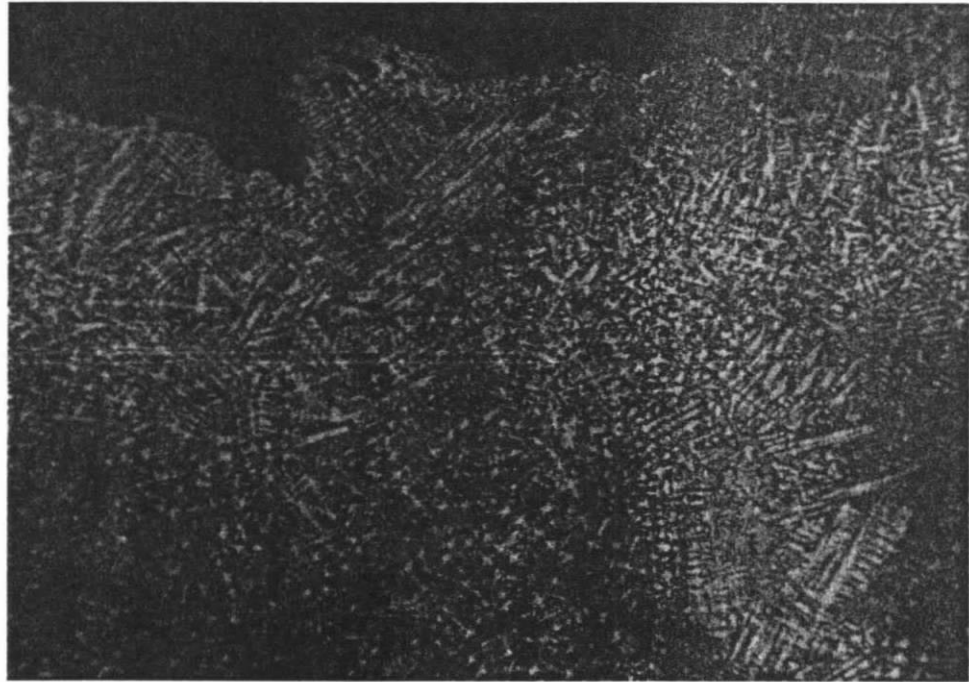
(b)



50  $\mu\text{m}$  

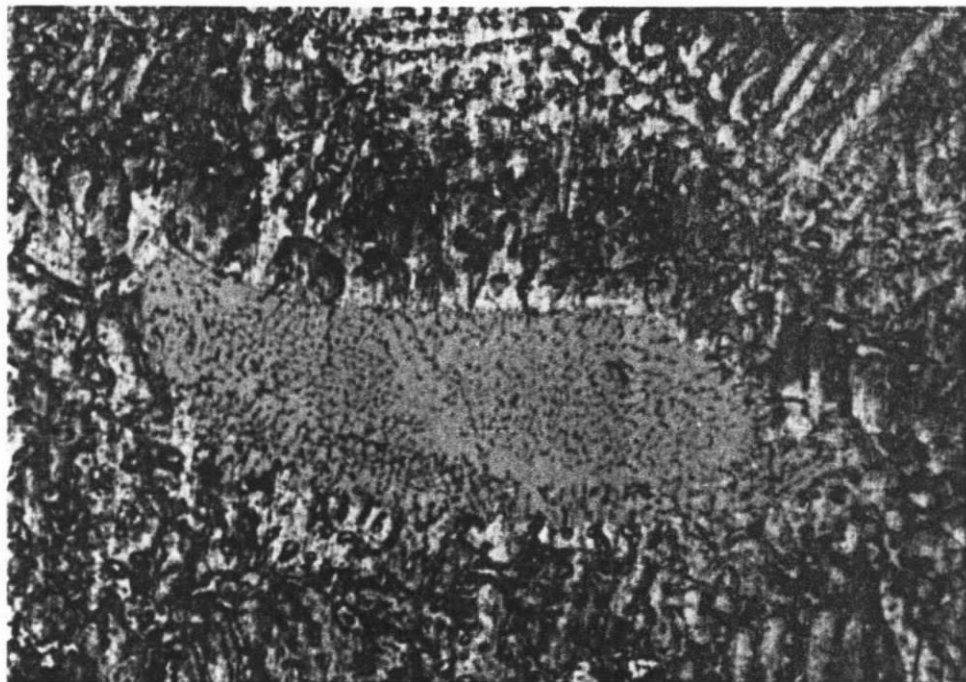


(c)



20  $\mu\text{m}$  —

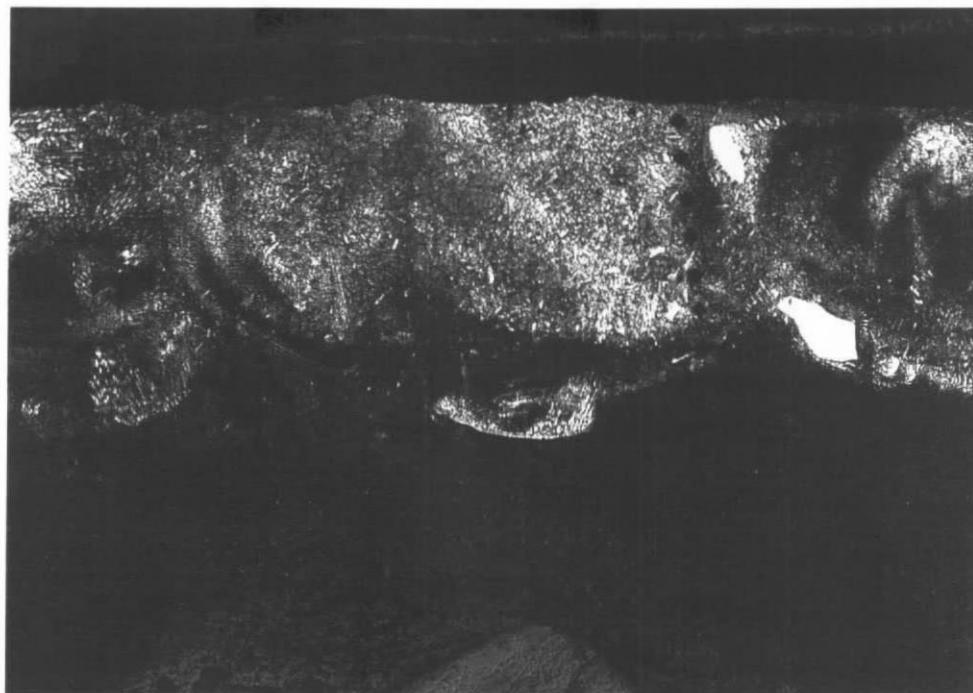
(d)



10  $\mu\text{m}$  —

Figure 5. 1 Microstructure of Ni-Al<sub>2</sub>O<sub>3</sub>-2a (a) melt layer 50 $\times$ , (b) interface 200 $\times$ , (c) surface 400 $\times$  and (d) nickel rich intermetallic phase 800 $\times$

(a)



200 μm ———

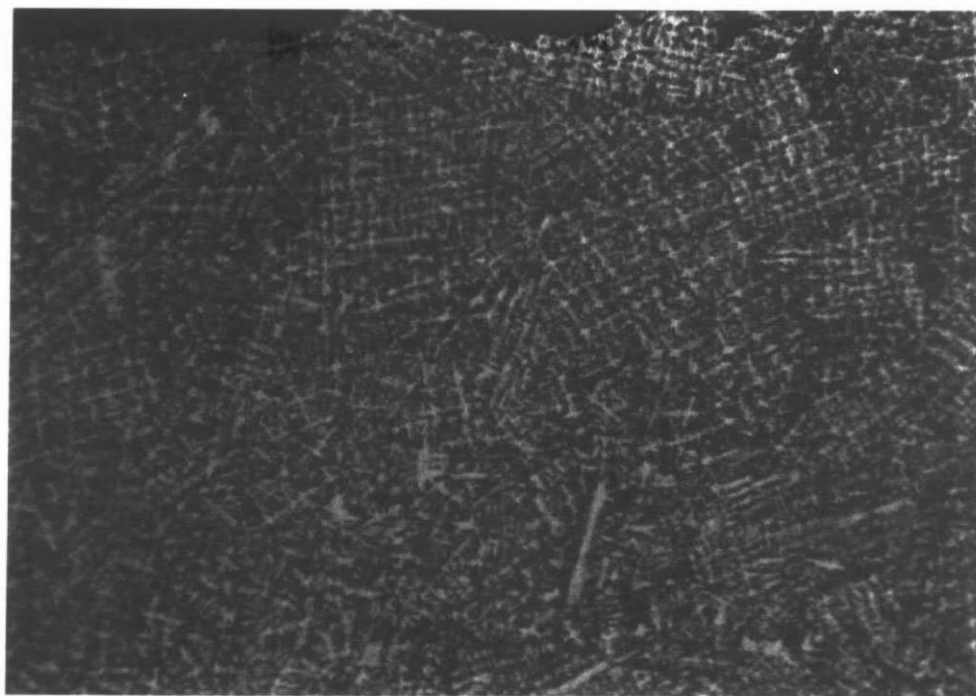
(b)



50 μm ———

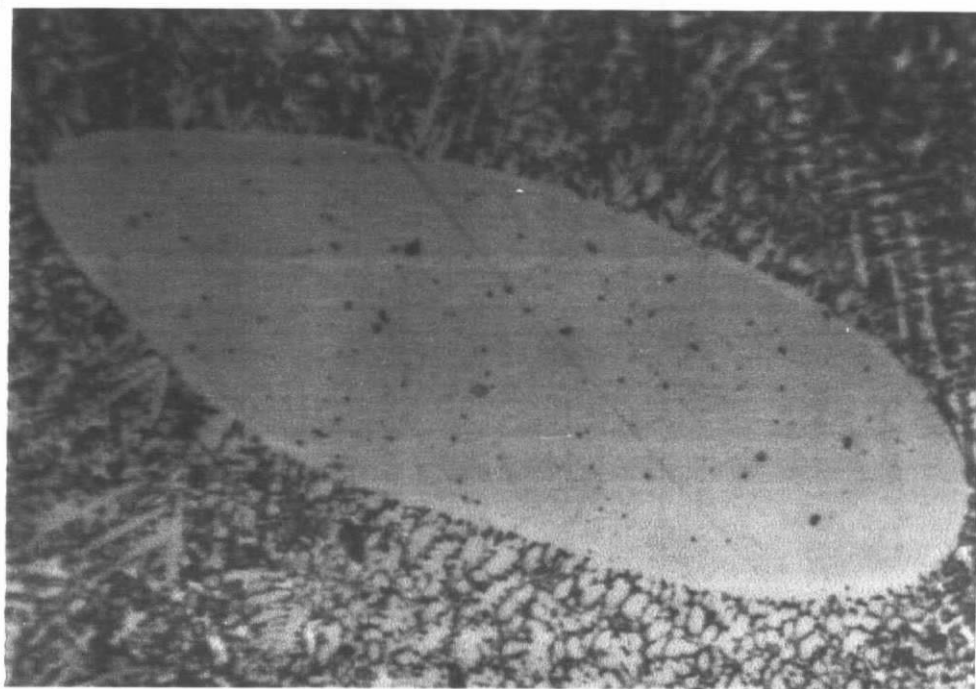


(c)



20  $\mu\text{m}$  

(d)



10  $\mu\text{m}$  

(e)

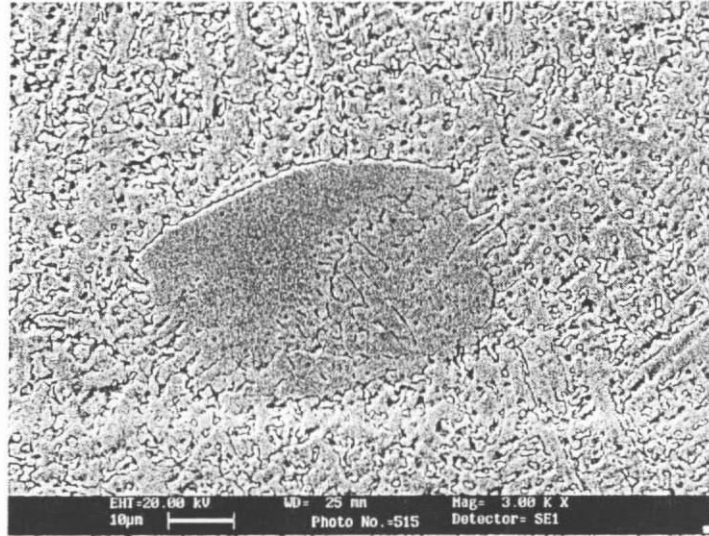


Figure 5. 2 Microstructure of Ni-Al<sub>2</sub>O<sub>3</sub>-3a (a) melt layer 50×, (b) interface 200×, (c) surface 400×, (d) nickel rich intermetallic phase 800× and (e) nickel rich intermetallic phase (SEM)

(a)



200 µm



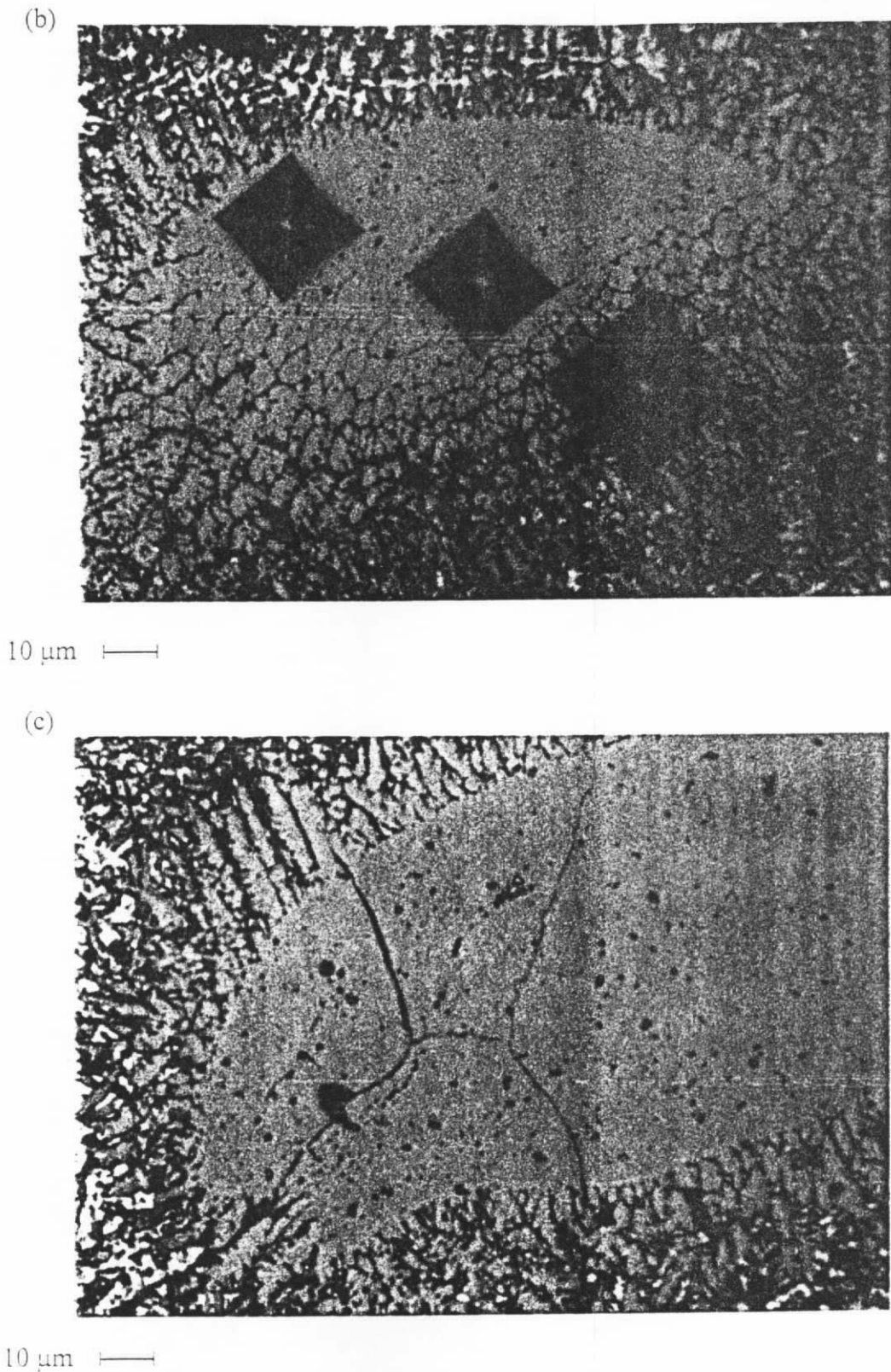
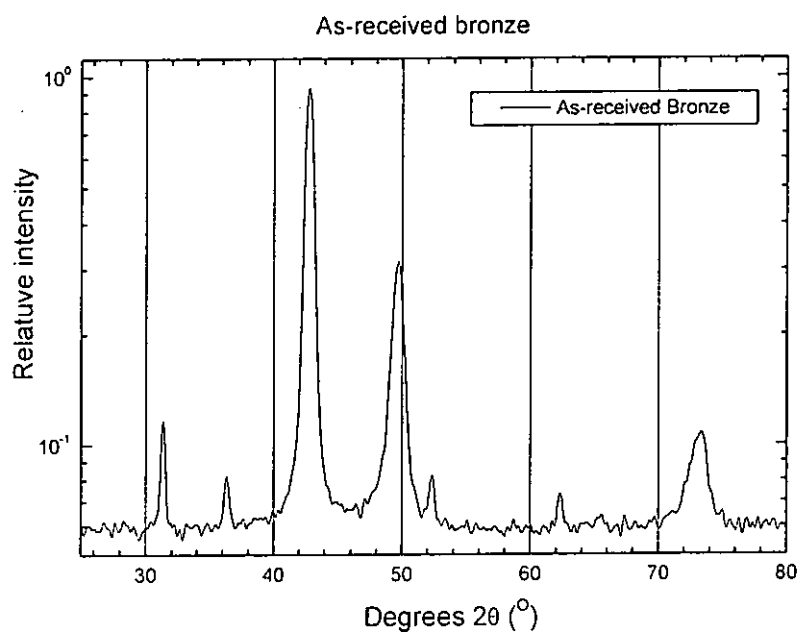


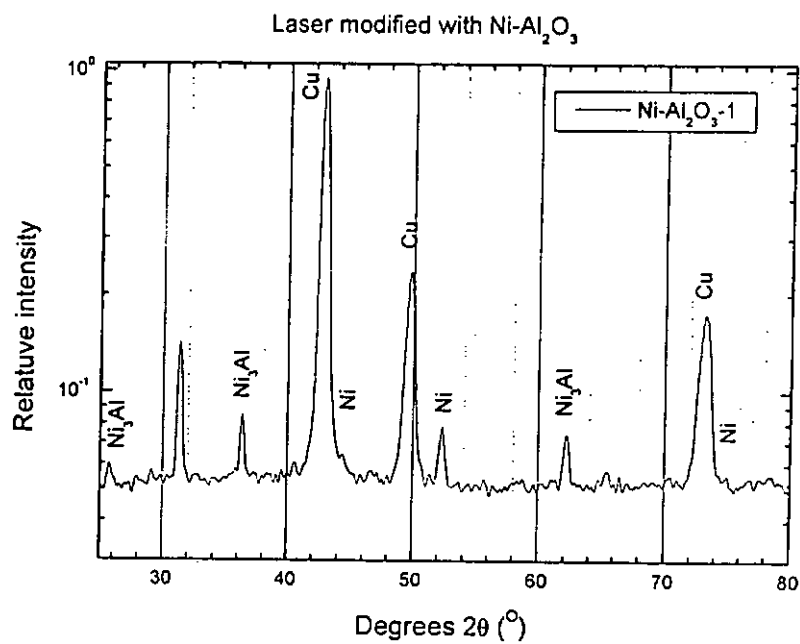
Figure 5. 3 Microstructure of Ni-Al<sub>2</sub>O<sub>3</sub>-4a (a) crack induced in the laser surface modified layer 50×, (b) indentations on the nickel rich intermetallic phase 800× and (c) crack induced in the nickel rich intermetallic phase 800×

### 5.3.1 X-ray diffraction analysis of Ni-Al<sub>2</sub>O<sub>3</sub>/bronze

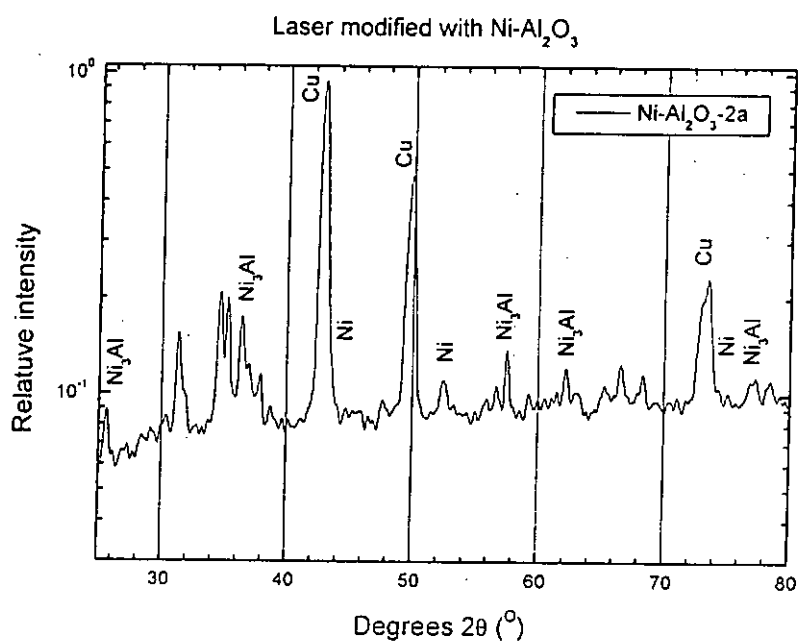
The corresponding X-ray spectra of the tin bronze substrate and the laser surface modified specimens are shown as Fig. 5. 4



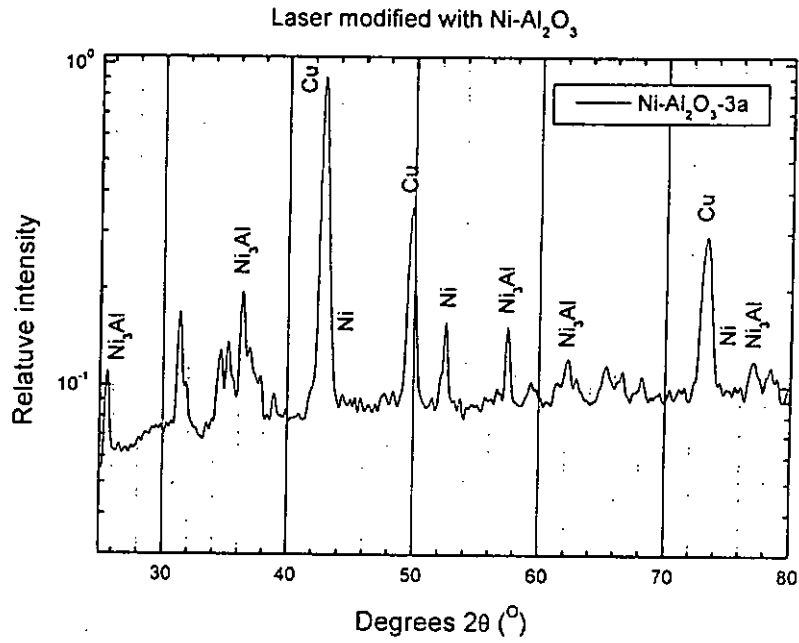
(a)



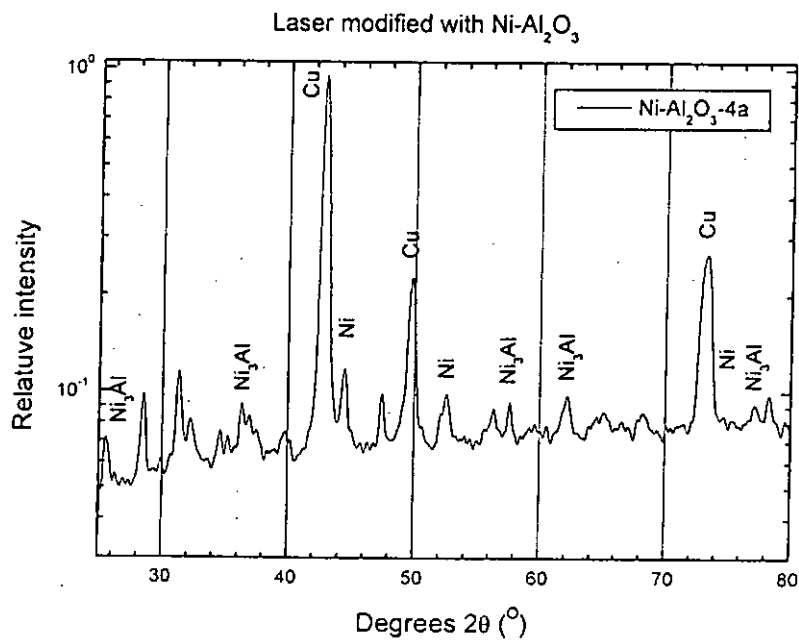
(b)



(c)



(d)



(e)

Figure 5. 4 X-ray diffraction spectra of (a) As-received bronze, (b) Ni-Al<sub>2</sub>O<sub>3</sub>-1, (c) Ni-Al<sub>2</sub>O<sub>3</sub>-2a, (d) Ni-Al<sub>2</sub>O<sub>3</sub>-3a and (e) Ni-Al<sub>2</sub>O<sub>3</sub>-4a

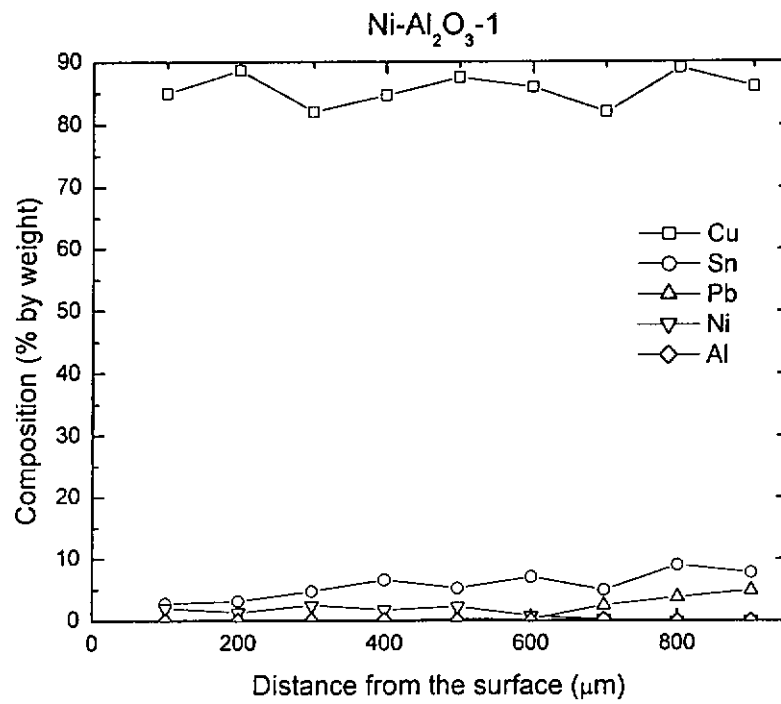


## 5.4 Composition profiles of Ni-Al<sub>2</sub>O<sub>3</sub>/bronze

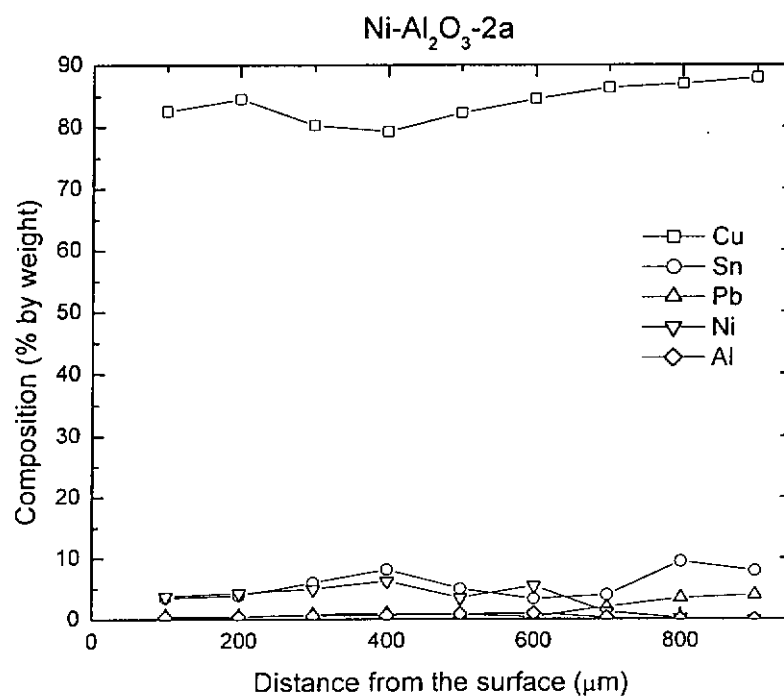
The chemical compositional profiles of specimens laser surface modified with Ni-Al<sub>2</sub>O<sub>3</sub> are shown in Fig. 5. 5. According to the results, the composition of the melt layer was homogeneous. However, the content of nickel was at a very low level. The high dilution ratio of Ni-Al<sub>2</sub>O<sub>3</sub>-2a (DR 59%) and Ni-Al<sub>2</sub>O<sub>3</sub>-3a (DR 65%) was due to the vapourisation of the alloy powder by the high laser power density. Dramatically, the nickel content of the melt layer increased as the power density increased.

It could be observed that as the laser power density increased, the Ni content also increased. This seemingly contradictory result might arise from the fact that more Ni-Al<sub>2</sub>O<sub>3</sub> particles were expelled from the surface at lower power density than at higher power density. At higher power density, the wetting between Al<sub>2</sub>O<sub>3</sub> and Cu might be better than in the case of lower power density. Thus more Ni and Al were present. This was also supported by the fact that more Ni<sub>3</sub>Al was formed at a higher power density. In this respect, the value of the dilution ratio is somewhat misleading in such a situation owing to material loss in laser processing.

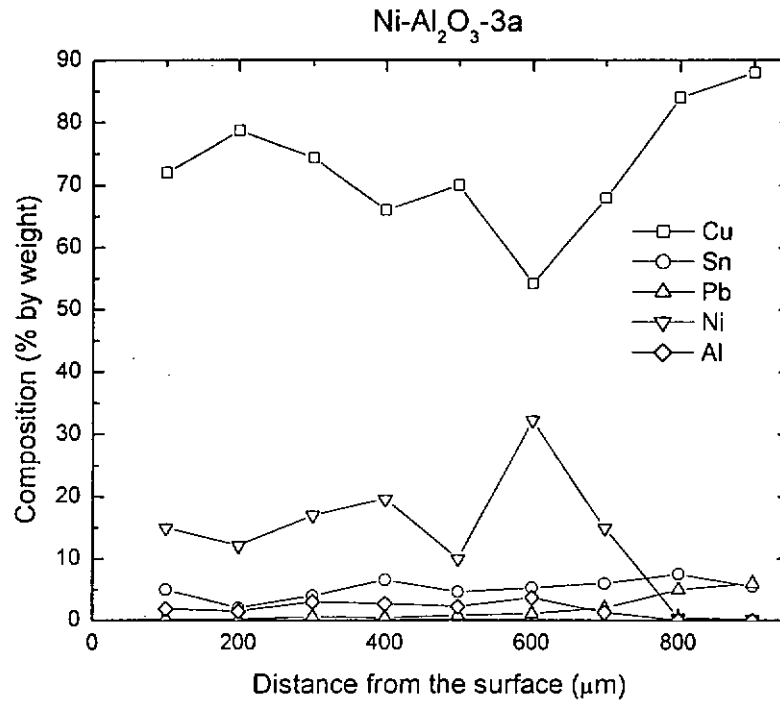
In addition, with a higher power density, more laser energy was absorbed by the sprayed coating and changed the alumina to liquid state, owing to the high interfacial energy between liquid copper and liquid alumina [Shepeleva *et al.*, 2000]. The increasing of the formation of nickel-rich intermetallic phases lead to higher nickel content.



(a)



(b)



(c)

Figure 5.5 Chemical compositional profiles of various laser surface modified specimens (a) Ni-Al<sub>2</sub>O<sub>3</sub>-1, (b) Ni-Al<sub>2</sub>O<sub>3</sub>-2a and (c) Ni-Al<sub>2</sub>O<sub>3</sub>-3a

## 5.5 Hardness profiles of Ni-Al<sub>2</sub>O<sub>3</sub>/bronze

The hardness profiles along the melt depth of tin bronze modified with Ni-Al<sub>2</sub>O<sub>3</sub> are shown in Fig. 5. 6. For specimen Ni-Al<sub>2</sub>O<sub>3</sub>-3a, the hardness was significantly improved by laser surface modification. The average hardness of Ni-Al<sub>2</sub>O<sub>3</sub>-3a was about 208 Hv<sub>0.2</sub> and the maximum hardness was exhibited by the nickel-rich intermetallic phase. The measured hardness of this phase was above 400 Hv<sub>0.2</sub>. For Ni-Al<sub>2</sub>O<sub>3</sub>-1 and Ni-Al<sub>2</sub>O<sub>3</sub>-2a the hardness also increased to 139 Hv<sub>0.2</sub> and 171 Hv<sub>0.2</sub>, respectively. The higher hardness of Ni-Al<sub>2</sub>O<sub>3</sub>-3a was attributed to a higher nickel

content in the matrix, and the formation of the intermetallic precipitates. Moreover, the percentage, size and distribution of the intermetallic phase formed in the modified layer differed in specimens with different laser processing parameters.

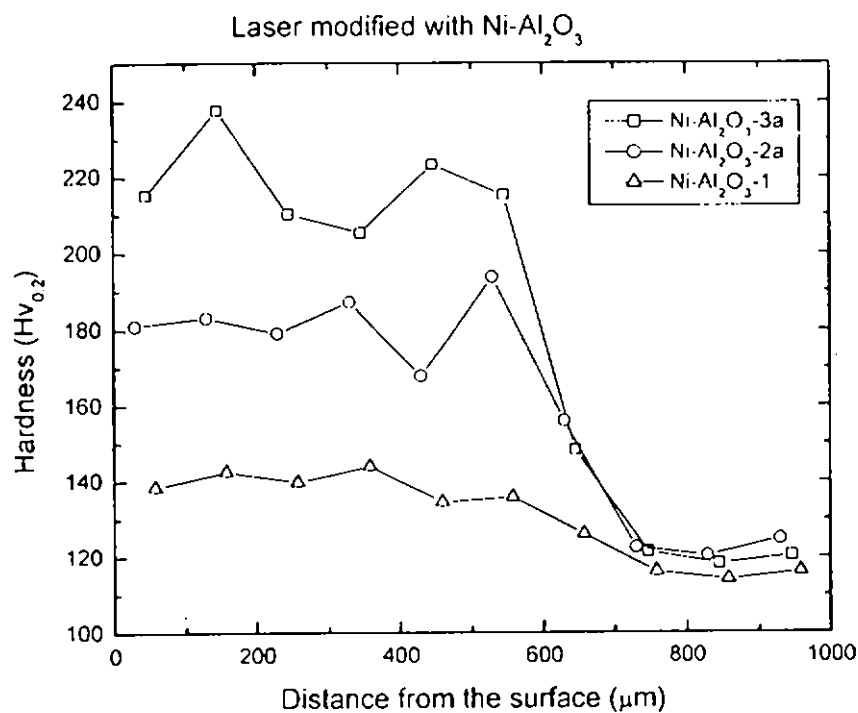


Figure 5. 6 Matrix hardness profiles along the melt depth of the cross section of laser surface modified specimens

## 5.6 Cavitation erosion of Ni-Al<sub>2</sub>O<sub>3</sub>/bronze

The cavitation erosion resistance of all the laser surface modified specimens was improved relative to that of the tin bronze substrate. The graph of the cumulative mean depth of penetration as a function of time for the as-received brass and laser surface modified specimens eroded in 3.5% NaCl solution at 23°C was shown in Fig. 5. 7. For specimen Ni-Al<sub>2</sub>O<sub>3</sub>-3a, the cavitation erosion resistance was 5 times that of the tin bronze substrate. The cavitation erosion resistance of the laser surface modified tin bronze increased as the power density increased, except for the specimen Ni-Al<sub>2</sub>O<sub>3</sub>-4a, which was deliberately not polished before cavitation erosion test. In the as-treated condition, the weight loss in the first 30 min was very rapid, as revealed in Fig. 5. 7. This reduction in cavitation erosion resistance was attributed to the thermally induced crack present in the matrix and the nickel-rich intermetallic phase in the melt layer. The normalized cavitation erosion resistance of modified specimens is shown in Fig. 5. 8.

The improvement in cavitation erosion resistance of laser surface modified coatings was attributed to the formation of the nickel-rich intermetallic phase. The increase in the cavitation erosion resistance depended on the amount of the intermetallic phase present and its distribution in the laser modified layer.

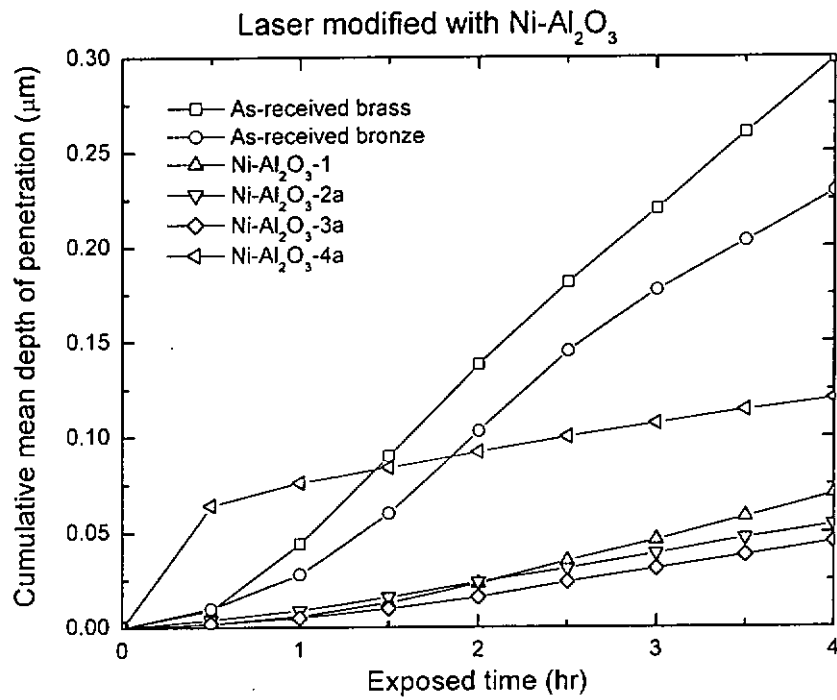


Figure 5.7 Cumulative MDP as a function of time for the as-received and laser surface modified specimens eroded in 3.5% NaCl solution at 23°C

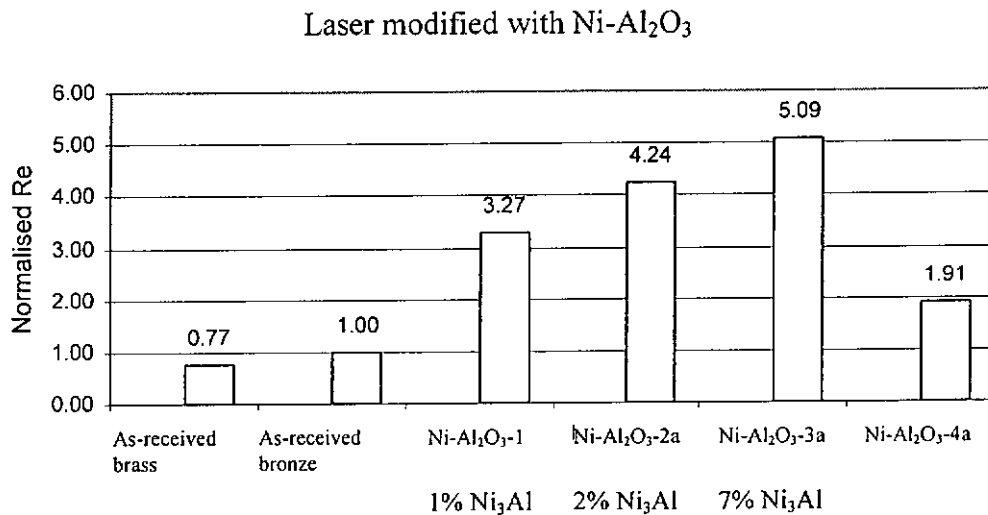
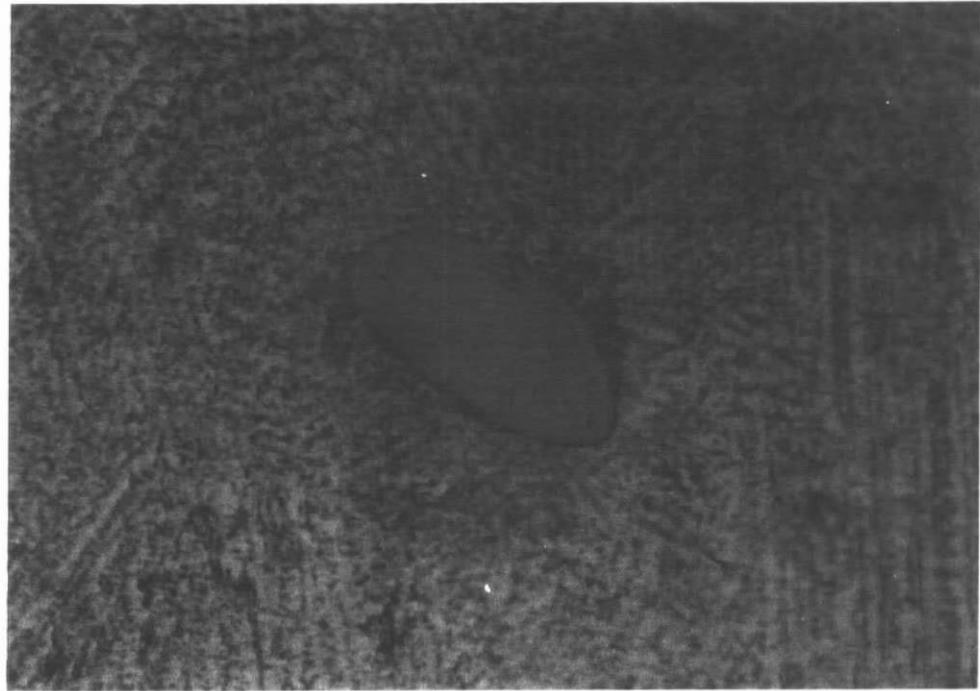


Figure 5.8 Normalised cavitation erosion resistance of the as-received and laser surface modified specimens eroded in 3.5% NaCl solution at 23°C

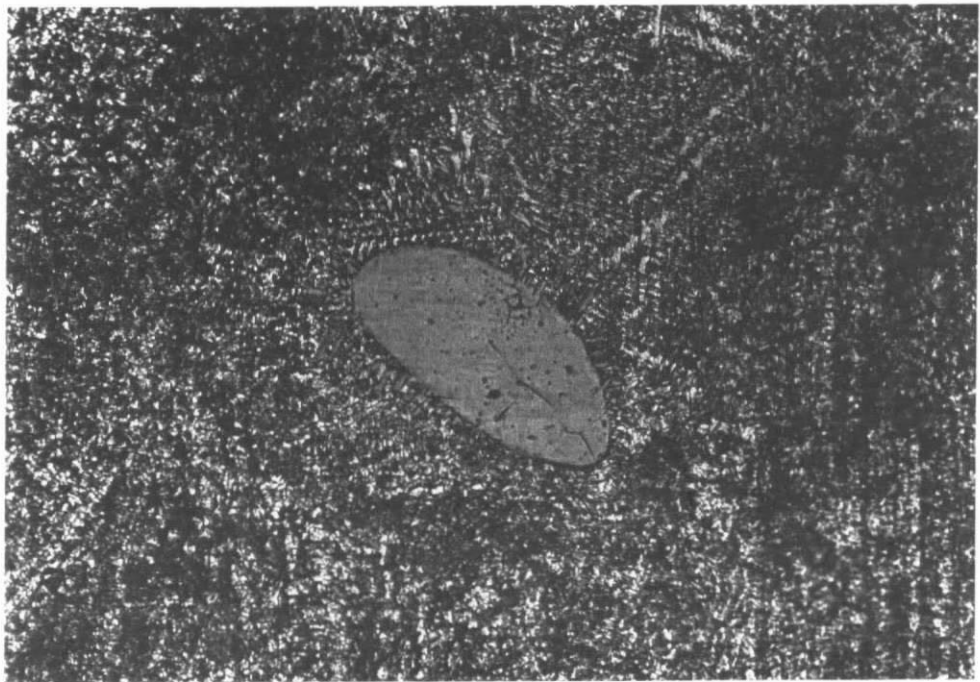
Fig. 5. 9 (a-d) and Fig. 5. 10 (a-d) show the nickel-rich intermetallic phase during 4 hours cavitation erosion test.

(a)



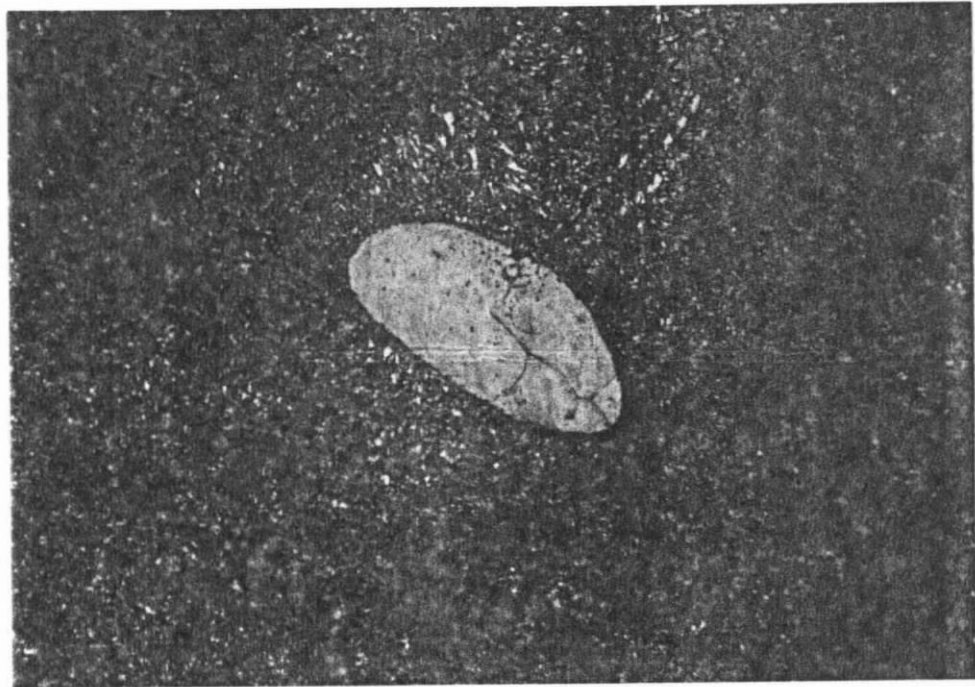
20  $\mu\text{m}$  ———

(b)



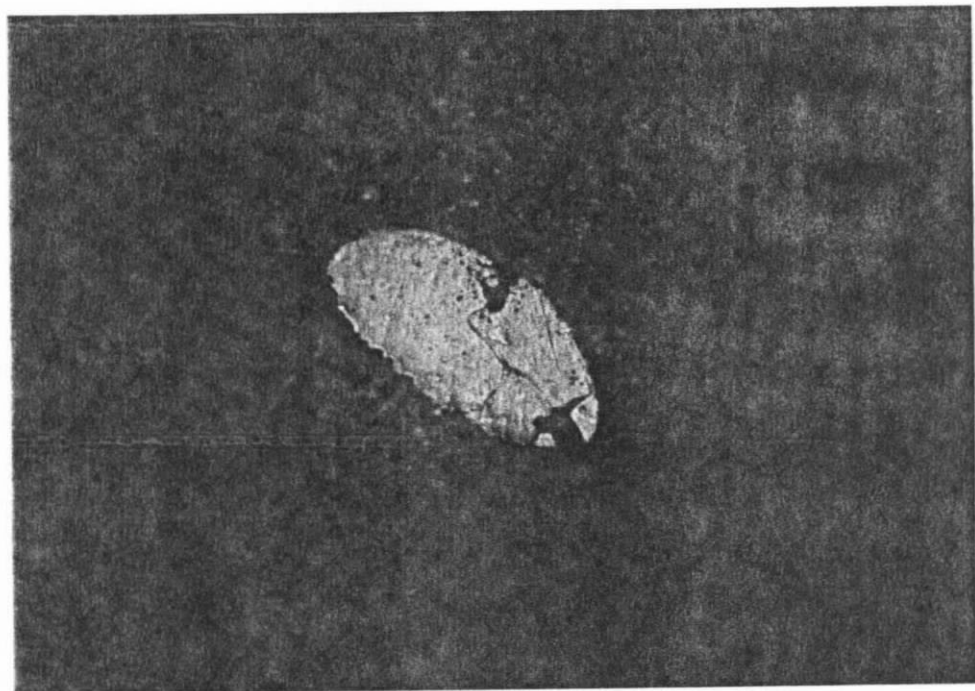
20  $\mu\text{m}$  ———

(c)



20  $\mu$ m

(d)

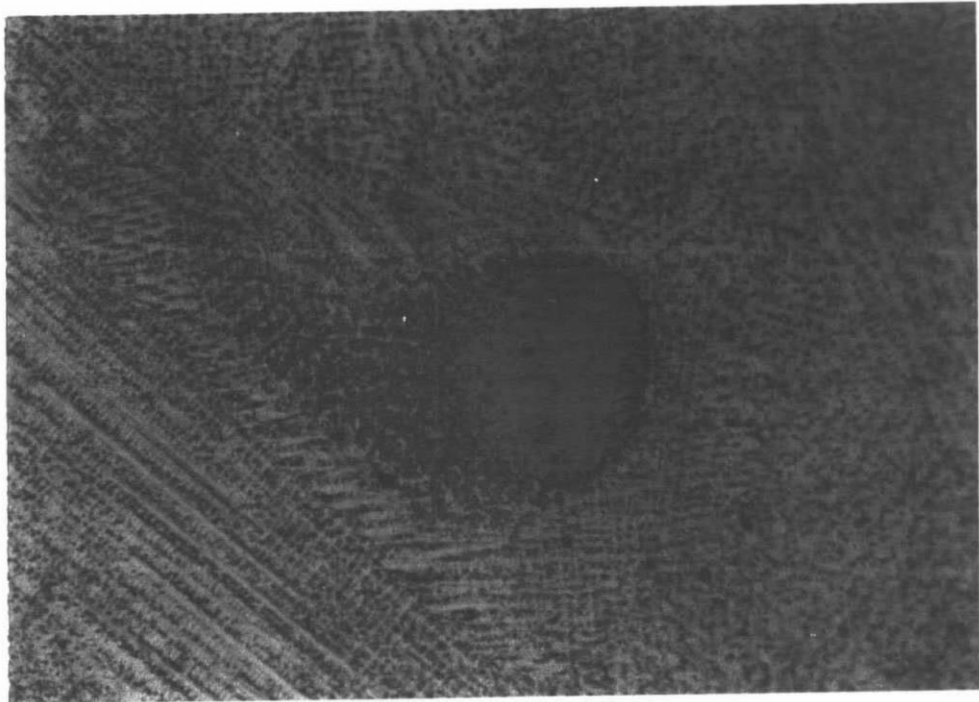



20  $\mu$ m

Figure 5. 9 Appearance of damaged surface of Ni-Al<sub>2</sub>O<sub>3</sub>-I after different exposure times to cavitation erosion. (a) 30 minutes 400 $\times$ , (b) 60 minutes 400 $\times$ , (c) 120 minutes 400 $\times$  and (d) 240 minutes 400 $\times$

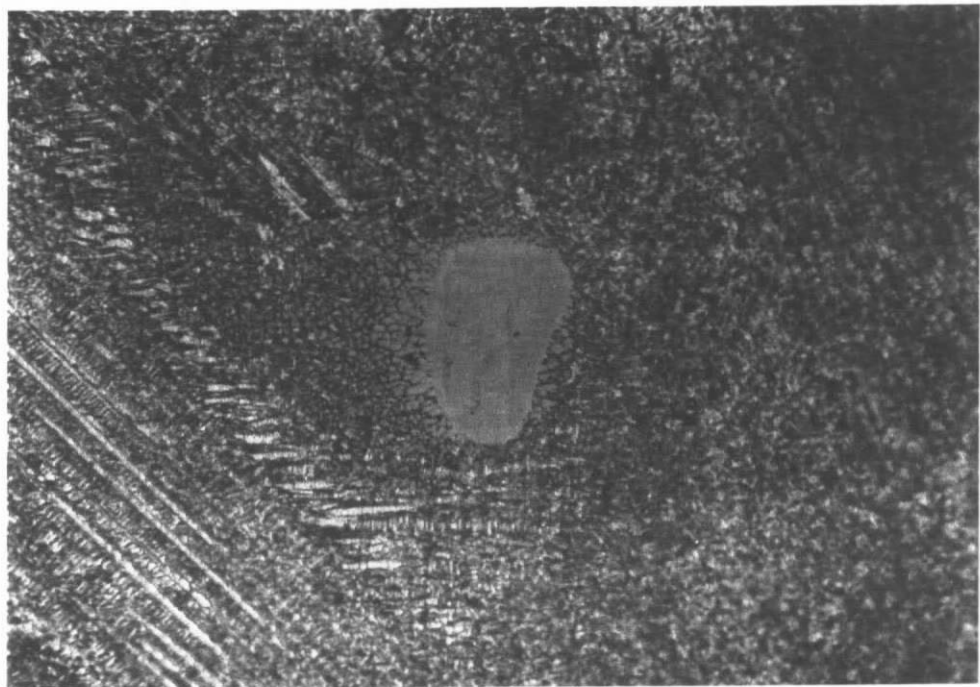


(a)



20  $\mu\text{m}$  

(b)



20  $\mu\text{m}$  

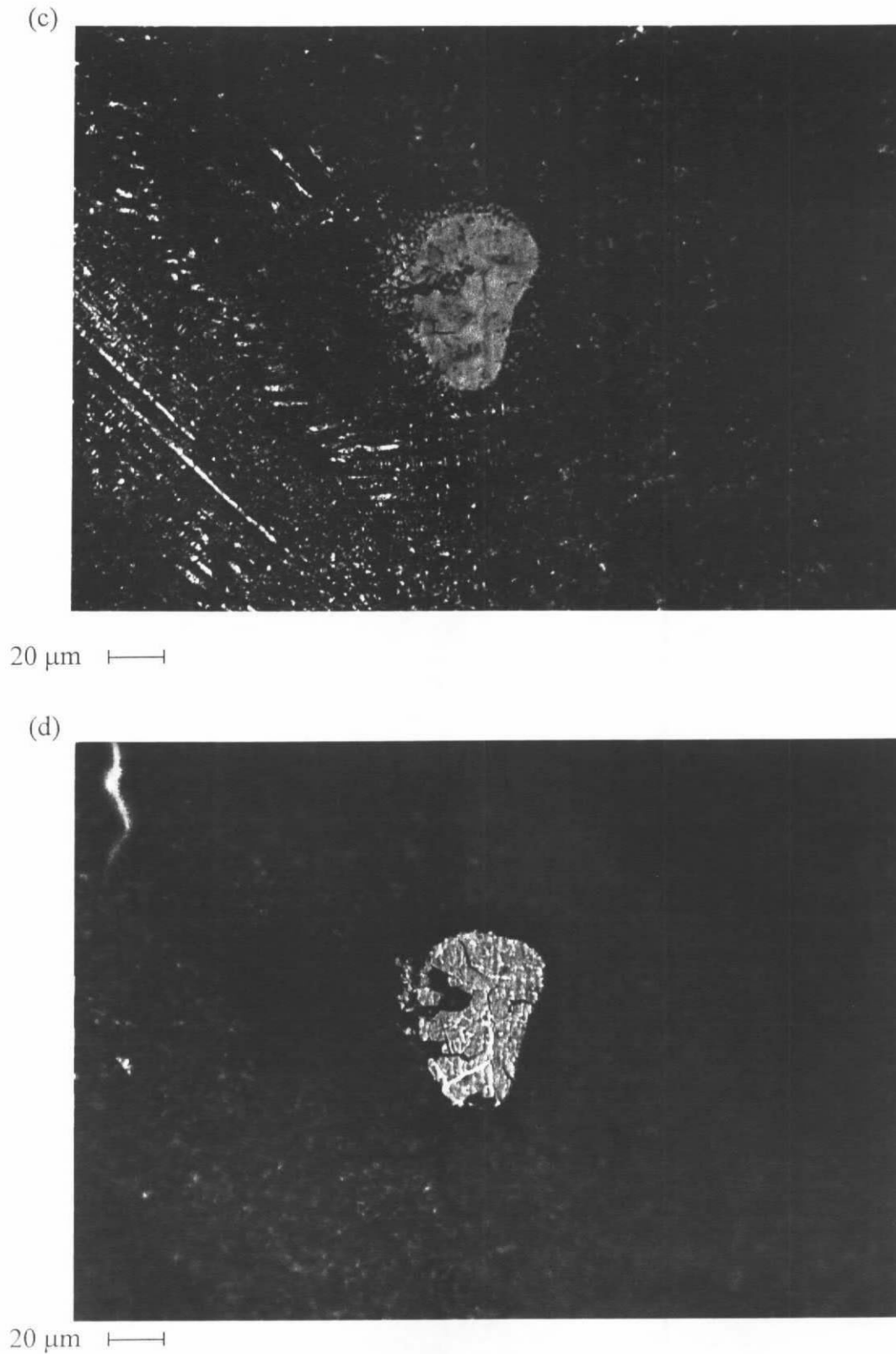


Figure 5. 10 Appearance of damaged surface of Ni-Al<sub>2</sub>O<sub>3</sub>-1 after different exposure times to cavitation erosion. Cavitation eroded the small region and cracked the entire nickel intermetallic phase. (a) 30 minutes 400×, (b) 60 minutes 400×, (c) 120 minutes 400× and (d) 240 minutes 400×

## 5.7 Electrochemical corrosion of Ni-Al<sub>2</sub>O<sub>3</sub>/bronze

All the laser surface modified specimens were polished down to 1  $\mu\text{m}$  surface finish before the polarization test, except Ni-Al<sub>2</sub>O<sub>3</sub>-4a, which was tested with and without polishing prior to test for the sake of comparison. The potentiodynamic polarisation curves of the as-received bronze and the laser modified specimens in 3.5% NaCl solution at 23°C are shown in Fig. 5. 11. According to the graph, the corrosion resistance deteriorated as indicated by the increase in the current density. The corrosion potential  $E_{\text{corr}}$  was slightly higher than that of bronze and brass substrate. Due to the formation of secondary intermetallic phase, the corrosion resistance was not only inferior to bronze, but also to brass.

For specimen Ni-Al<sub>2</sub>O<sub>3</sub>-4a, polishing seemed to have an adverse effect on the corrosion resistance as indicated by the fact that the as-treated specimen had a smaller corrosion current density than the polished one. However, the polished specimen had a higher erosion resistance. Thus it might be concluded that the outer layer in the treated surface was mechanically weak but chemically inert.

The corrosion data of the polarization curves are extracted and summarized in Table 5. 5.

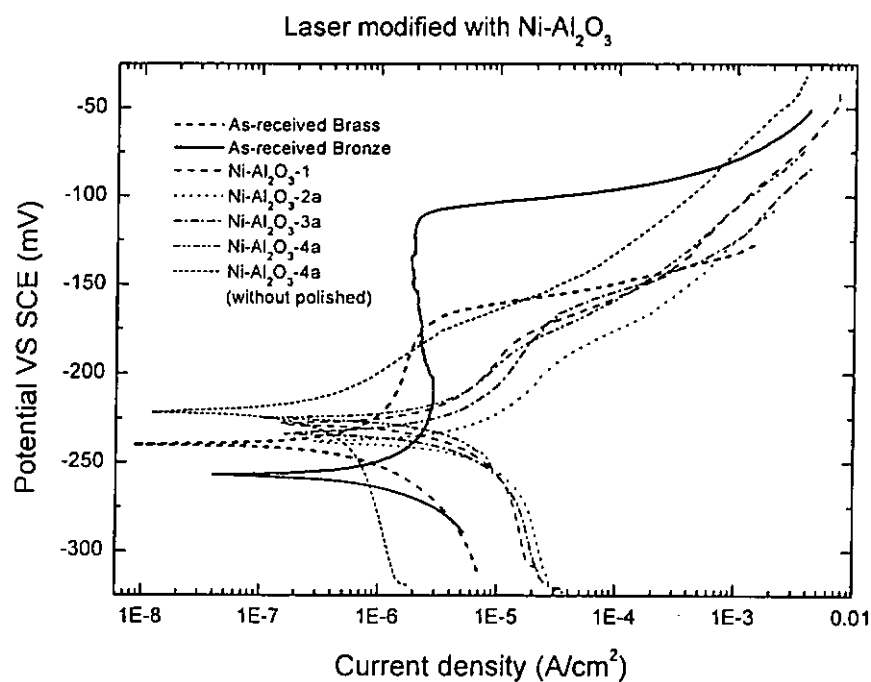


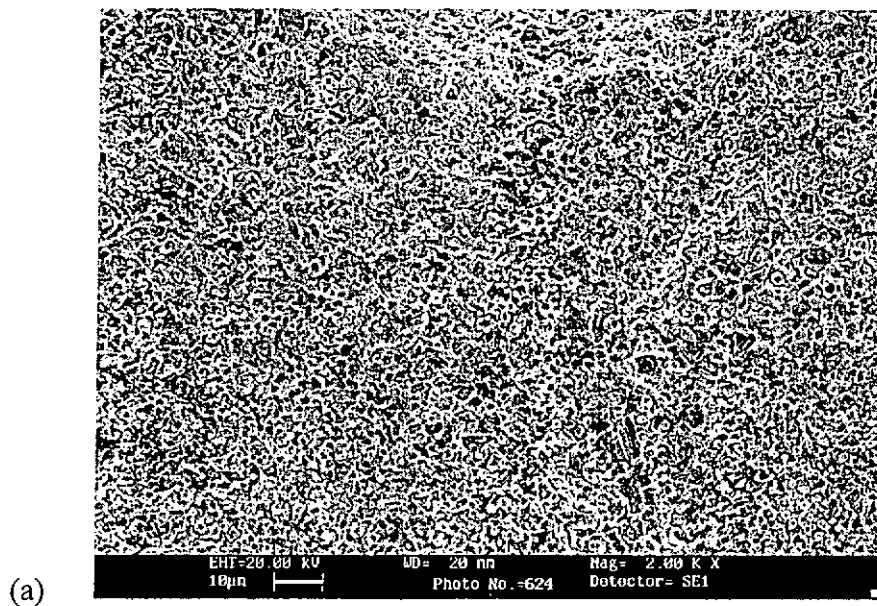
Figure 5. 11 Potentiodynamic polarisation curves of the as-received brass and the laser modified specimens in 3.5% NaCl solution at 23°C

Table 5. 5 The cavitation resistance and corrosion parameters of as-received and laser surface modified specimens

Sample	Ave. Hardness (Hv <sub>0.2</sub> )	Re (hμm <sup>-1</sup> )	Normalised Re	Ecorr (mV)	Icorr (μA/cm <sup>2</sup> )	Epit (mV)
As-received tin bronze	112	17.45	1.00	-263	3.1	-112
Ni-Al <sub>2</sub> O <sub>3</sub> -1	139	57.08	3.27	-229	7.2	-180
Ni-Al <sub>2</sub> O <sub>3</sub> -2a	171	74.00	4.24	-238	13.4	-194
Ni-Al <sub>2</sub> O <sub>3</sub> -3a	208	88.80	5.09	-234	8.8	-173
Ni-Al <sub>2</sub> O <sub>3</sub> -4a	/	33.30	1.19	-225	0.8	-186
As-received brass	117	13.36	0.77	-238.3	1.0	-173
Precipitate	437	/	/	/	/	/

## 5.8 Cavitation damage mechanism of Ni-Al<sub>2</sub>O<sub>3</sub>/bronze

The SEM micrograph of Ni-Al<sub>2</sub>O<sub>3</sub>-3a subjected to cavitation erosion for 4 hours is given in Fig. 5. 12 (a) and (b). The morphology of the cavitated surface revealed that the matrix was severely attacked by the cavitation pressure pulses. According to the SEM micrograph in (a), the erosion of the matrix was accomplished by ductile fracture, as indicated by the roughened surface. For the nickel rich-intermetallic phase, the microcracks were induced and propagated by the cavitation pressure pulses as shown in Fig 5. 9 and Fig 5. 10. There was no selective attack of the boundaries between the nickel-rich intermetallic phase and the matrix (b). Finally, the nickel-rich intermetallic phase was eroded by brittle fracture.



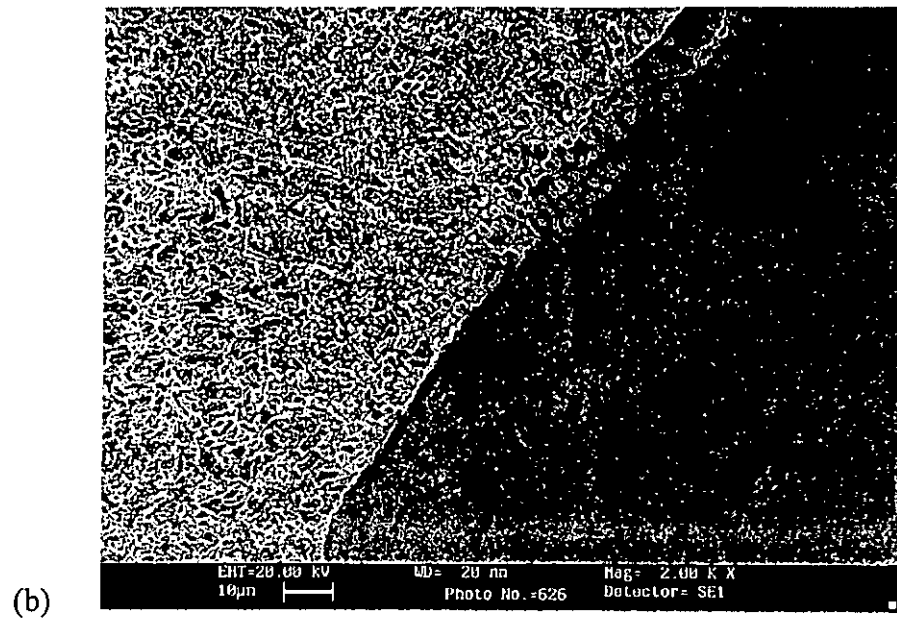


Figure 5. 12 Appearance of the damaged surface of modified specimen Ni-Al<sub>2</sub>O<sub>3</sub>-3a after 4 hours exposure to cavitation erosion

## **6 Results and discussions - Laser surface modification of brass (Cu38%Zn) with Ni-Cr-Al-Mo**

### **6.1 Introduction**

Brasses are by far the most extensively used copper-based alloys. Cu38%Zn has a duplex structure containing both  $\alpha$  (fcc) and  $\beta$  (bcc) phases, therefore also called  $\alpha+\beta$  brass. Laser surface modification gives rise to a rapid solidification, which produces alloy materials with reduced chemical segregation, fine grained microstructures, a uniform distribution of very fine precipitates and extended solid solubility.

Cu-Ni alloys are often used in marine applications for their corrosion resistant properties and good strength. The most important advantage of these materials is a continuous solid solution across the entire composition range. The fine structure of the Cu-Ni results in a lower corrosion rate. Cu-Al alloys are also used in moderately corrosive environments, and provide good strength and ductility. Furthermore, Cu-Cr is one of the few copper binary systems that can be easily strengthened by precipitation hardening. Cavitation erosion corrosion is a complex phenomenon, which combines electrochemical and mechanical actions. The addition of the above alloying elements can improve the resistance to cavitation erosion corrosion. Laser surface modification techniques was employed to achieve the enhancement of the surface properties for cavitation erosion resistance and corrosion resistance.

## 6.2 Materials and laser processing parameters

### 6.2.1 Materials

Brass specimens 30 mm × 15 mm × 8 mm were cut from a plate and sand blasted, degreased and flame sprayed with Ni-Cr-Al-Mo alloy powder. The nominal composition of brass specimen and the Ni-Cr-Al-Mo powder is shown in Table 6. 1. The thickness of the preplaced coating was calculated from the difference in thickness of the specimen before and after flame spraying using a digital micrometer. The coating thickness of the sprayed specimens was range from 170  $\mu\text{m}$  to 350  $\mu\text{m}$ .

Table 6. 1 Nominal composition of brass and Ni-Cr-Al-Mo powder

Material	Cu	Zn	Pb	Ni	Cr	Al	Mo	Fe	B	Particle size
Brass	Bal.	38	1.5							
Ni-Cr-Al-Mo alloy powder				Bal.	10	7	5	5	1	~ -140 to +350 mesh ( < 105 $\mu\text{m}$ and > 40 $\mu\text{m}$ )

### 6.2.2 Laser processing parameters

From preliminary studies of single-track melt profiles, appropriate width to depth ratio of the melt track could be obtained by a laser power density in the neighbourhood of 76  $\text{W}/\text{mm}^2$  and a scanning speed in the neighborhood of 15 mm/s. The metallographic cross section of a single melt track is shown in Fig. 6. 1. For the present study, the laser processing parameters were varied from this setting in order to investigate the characteristics of the specimens with different laser processing parameters and to optimize the power density and scanning speed. The power density was varied from 64  $\text{W}/\text{mm}^2$  to 119  $\text{W}/\text{mm}^2$  with a beam diameter of 4 mm or 5 mm, and scanning speed from 10 mm/s to 35 mm/s. Table 6. 2 summarizes the processing



parameters used laser power density, scanning speed, coating thickness and flow rate of shielding gas.



200μm —

Figure 6. 1 The metallographic of the laser modified track with power density 76 W/mm<sup>2</sup> and scanning speed 15mm/s

Table 6. 2 Summary of laser power density, scanning speed, coating thickness and flow rate of shielding gas

Specimen	Laser power density	Scanning speed	Coating thickness	Shielding gas flow rate
Ni-Cr-Al-Mo-1	80 W/mm <sup>2</sup>	15 mm/s	~ 170 μm	Argon 15 l/min
Ni-Cr-Al-Mo-2	95 W/mm <sup>2</sup>	15 mm/s	~ 170 μm	Argon 15 l/min
Ni-Cr-Al-Mo-3	119 W/mm <sup>2</sup>	15 mm/s	~ 220 μm	Argon 15 l/min
Ni-Cr-Al-Mo-4	76 W/mm <sup>2</sup>	15 mm/s	~ 220 μm	Argon 15 l/min
Ni-Cr-Al-Mo-5	76 W/mm <sup>2</sup>	25 mm/s	~ 230 μm	Argon 15 l/min
Ni-Cr-Al-Mo-6	76 W/mm <sup>2</sup>	35 mm/s	~ 230 μm	Argon 15 l/min
Ni-Cr-Al-Mo-7	64 W/mm <sup>2</sup>	15 mm/s	~ 230 μm	Argon 15 l/min
Ni-Cr-Al-Mo-8	64 W/mm <sup>2</sup>	25 mm/s	~ 230 μm	Argon 15 l/min
Ni-Cr-Al-Mo-9	76 W/mm <sup>2</sup>	15 mm/s	~ 350 μm	Argon 15 l/min
Ni-Cr-Al-Mo-10	76 W/mm <sup>2</sup>	10 mm/s	~ 350 μm	Argon 15 l/min

After laser irradiation, the laser modified specimens were cross sectioned and polished to measure the laser melted depth and calculate the dilution ratio (DR). The calculated DR is listed in Table 6. 3.

Table 6.3 Melt depth and estimated dilution ratio of laser modified specimen

Sample	Coating thickness (t)	Melt depth (d)	Dilution ratio (DR)*
Ni-Cr-Al-Mo-1	~ 170 $\mu\text{m}$	/	/
Ni-Cr-Al-Mo-2	~ 170 $\mu\text{m}$	/	/
Ni-Cr-Al-Mo-3	~ 220 $\mu\text{m}$	/	/
Ni-Cr-Al-Mo-4	~ 220 $\mu\text{m}$	354.5 $\mu\text{m}$	38%
Ni-Cr-Al-Mo-5	~ 230 $\mu\text{m}$	280.5 $\mu\text{m}$	18%
Ni-Cr-Al-Mo-6	~ 230 $\mu\text{m}$	248.5 $\mu\text{m}$	7%
Ni-Cr-Al-Mo-7	~ 230 $\mu\text{m}$	273.3 $\mu\text{m}$	15.6%
Ni-Cr-Al-Mo-8	~ 230 $\mu\text{m}$	242.2 $\mu\text{m}$	5.1%
Ni-Cr-Al-Mo-9	~ 350 $\mu\text{m}$	417.9 $\mu\text{m}$	16.3%
Ni-Cr-Al-Mo-10	~ 350 $\mu\text{m}$	/	/

$$* \text{ Dilution ratio (DR)} = \left( 1 - \frac{t}{d} \right) \times 100\%$$

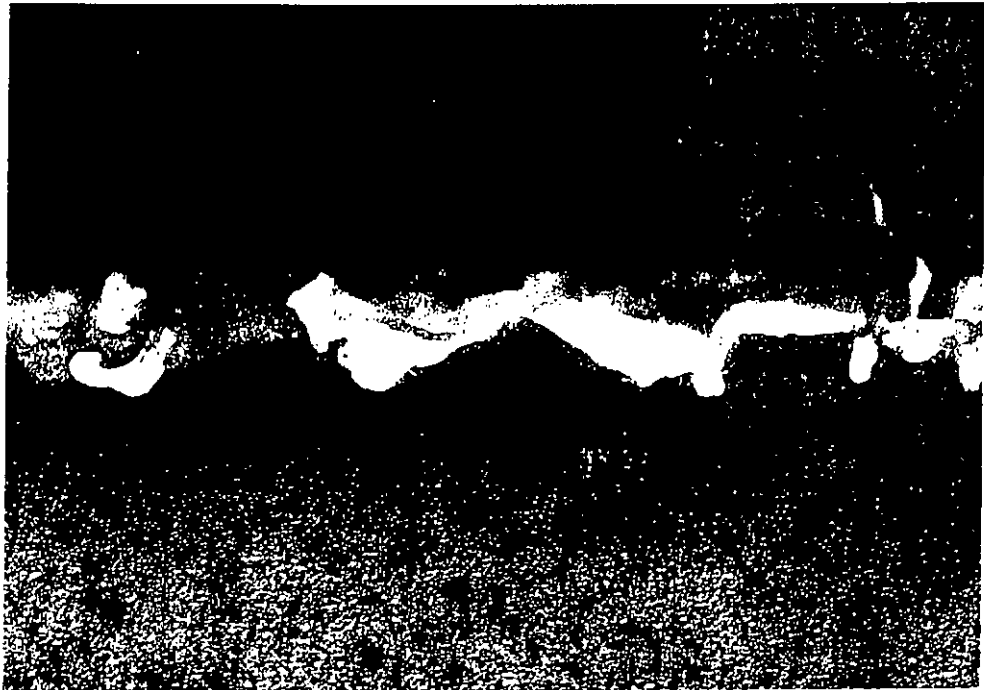
## 6.2 Microstructural and metallographic analysis

The scanning speed significantly affects the microstructure and composition of the laser treated layer since it determines the rate of resolidification and the laser-material interaction time. According to the laser parameters for appropriate width to depth ratio obtain in preliminary studies, the power density was constantly set at 76 W/mm<sup>2</sup> while the scanning speed was varied in the range 15 mm/s to 35 mm/s.

After the remelting of the preplaced Ni-Cr-Al-Mo sprayed layer on brass by laser irradiation, the pores present in the sprayed layer were completely removed, and the remelted layer was bonded to the brass substrate with excellent metallurgical bond. The laser modified specimens Ni-Cr-Al-Mo-4, Ni-Cr-Al-Mo-5, Ni-Cr-Al-Mo-6, Ni-Cr-Al-Mo-7 and Ni-Cr-Al-Mo-8 were cross sectioned, polished and etched. The micrographs are shown in Fig. 6. 2 - Fig. 6. 6, respectively.

From the optical micrograph of Ni-Cr-Al-Mo-4 (Fig. 6. 2), the melt layer could be divided into black regions and white regions. The black regions containing less of alloying elements from EDX analysis, were selective etched, revealing a dendritic microstructure, while the white regions containing more of alloying elements from EDX analysis, were shiny and located near the interface between the melt layer and the brass substrate.

(a)



200  $\mu\text{m}$  ———

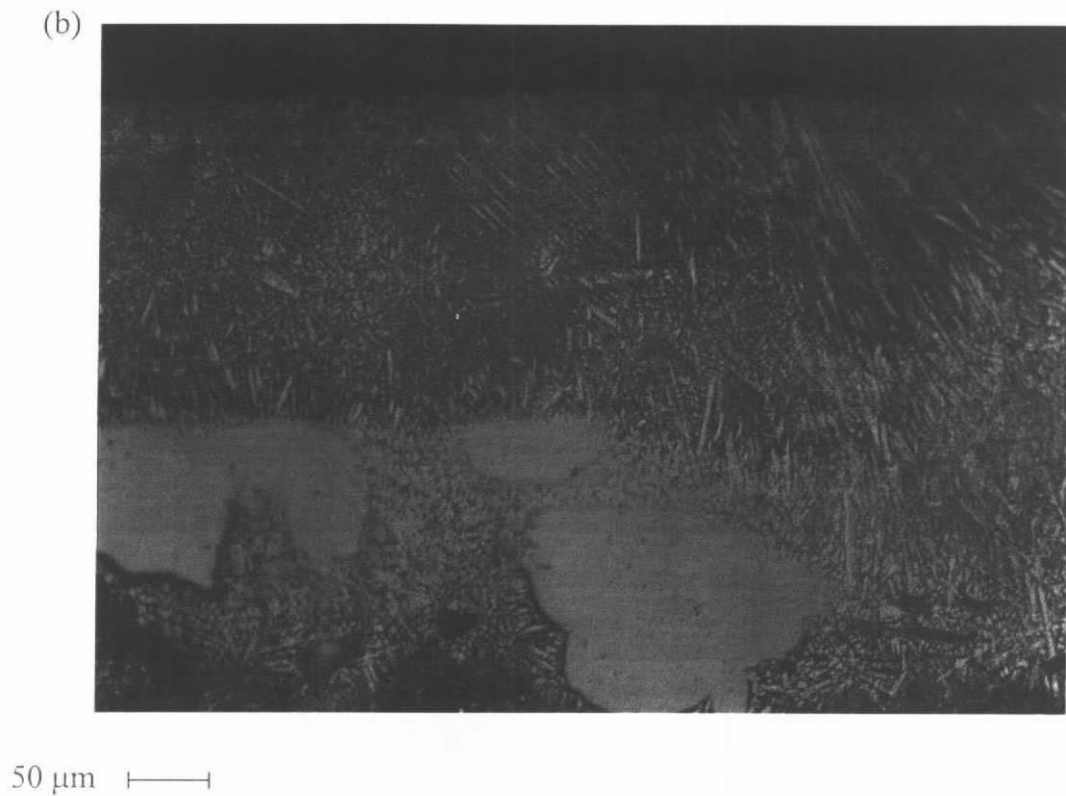


Figure 6. 2 Microstructure of Ni-Cr-Al-Mo-4 (a) melt layer 50 $\times$ , (b) growth of dendritic structure 200 $\times$

For specimen Ni-Cr-Al-Mo-5 (Fig. 6. 3), the melt depth was smaller than specimen Ni-Cr-Al-Mo-4 owing to a higher scanning speed. The dilution ratio of Ni-Cr-Al-Mo-5 was 18 %, while that of Ni-Cr-Al-Mo-4 was 38 %. Moreover, the microstructure of Ni-Cr-Al-Mo-5 was more homogeneous with a higher percentage of alloying elements, as indicated by an increase of the portion of white regions. The black regions in specimen Ni-Cr-Al-Mo-5 had finer dendritic structure than of that in specimen Ni-Cr-Al-Mo-4 due to the higher scanning speed. Consequently, the volume of the melt pool was smaller and resulted in a higher self-quenching rate.

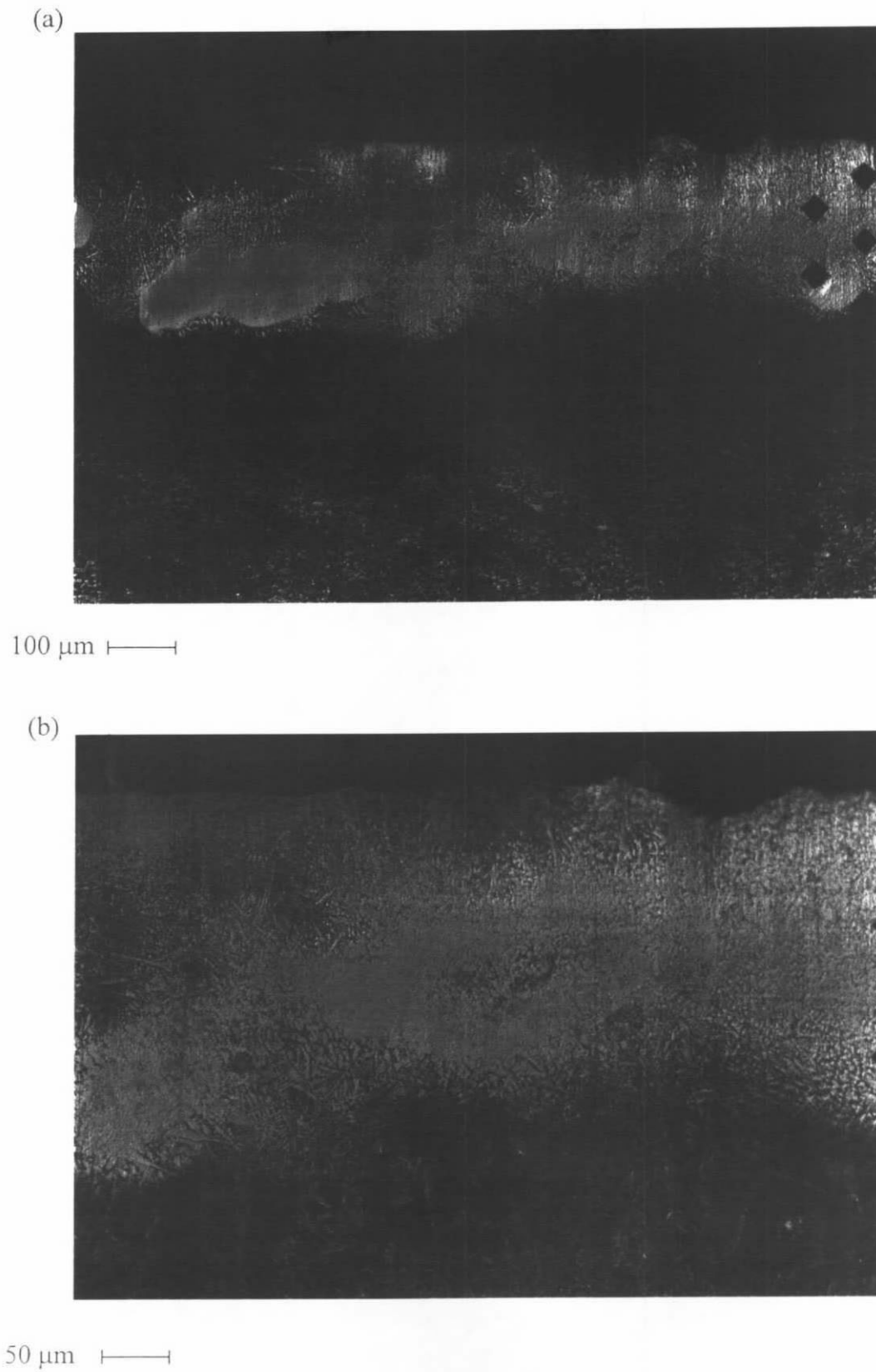
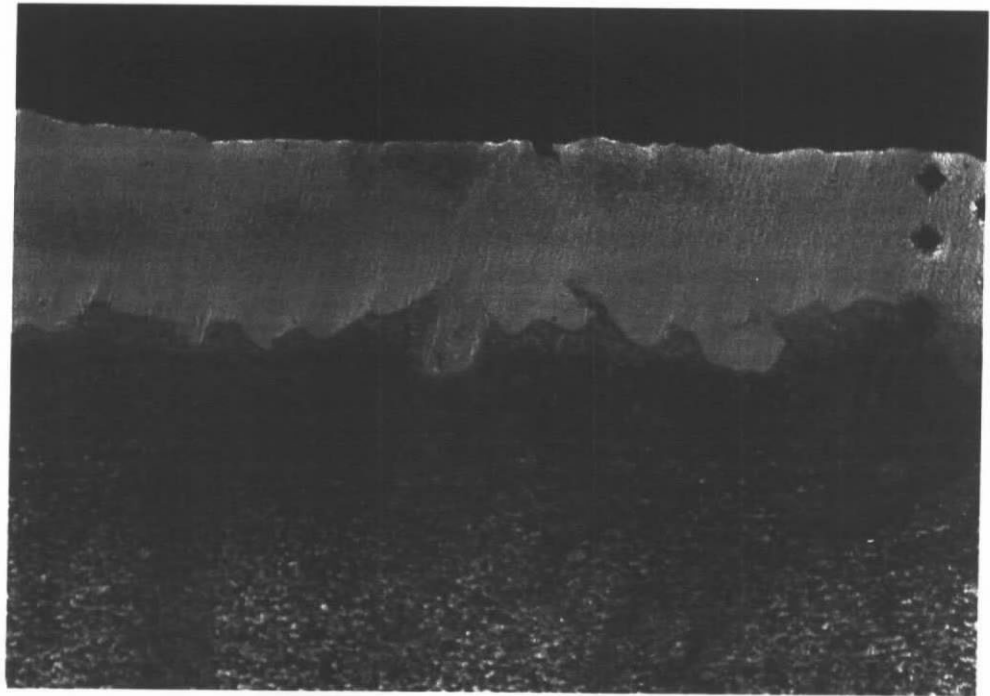


Figure 6. 3 Microstructure of Ni-Cr-Al-Mo-5 (a) melt layer 100 $\times$ , (b) growth of dendritic structure 200 $\times$

Specimen Ni-Cr-Al-Mo-6 (Fig. 6. 4) had a homogeneous microstructure and contained mainly the alloying elements. The scanning speed corresponding to Ni-Cr-Al-Mo-6 was 35 mm/s and was faster than the other two. As a result of the higher self-quenching rate, the melt layer had microcracks, which were induced by thermal stress.

(a)



100 μm

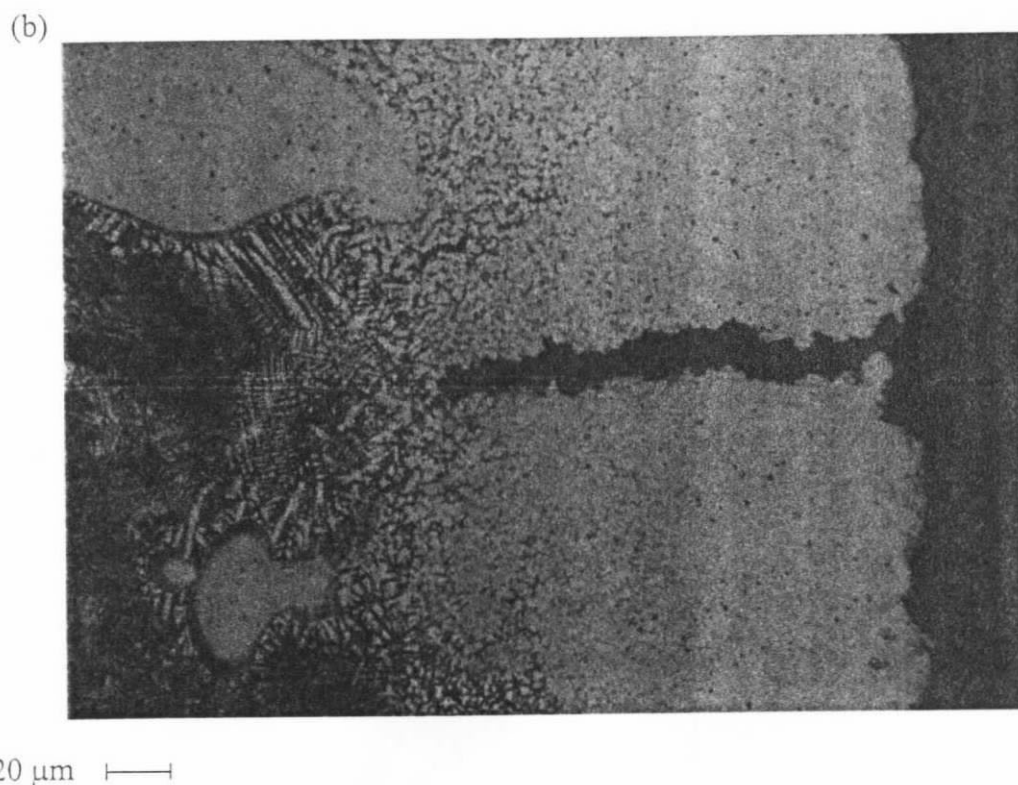


Figure 6. 4 Microstructure of Ni-Cr-Al-Mo-6 (a) melt layer 100 $\times$ , (b) microcrack 400 $\times$

Specimen Ni-Cr-Al-Mo-7 and Ni-Cr-Al-Mo-8 (Fig. 6. 5 and Fig. 6. 6) show a similar structure as the specimen Ni-Cr-Al-Mo-5 and Ni-Cr-Al-Mo-6. They were modified with lower power densities, hence scanning speed was slightly lower, 15 mm/s and 25m/s, respectively. In addition, specimen Ni-Cr-Al-Mo-8 was no microcrack, which was much better than Ni-Cr-Al-Mo-6.



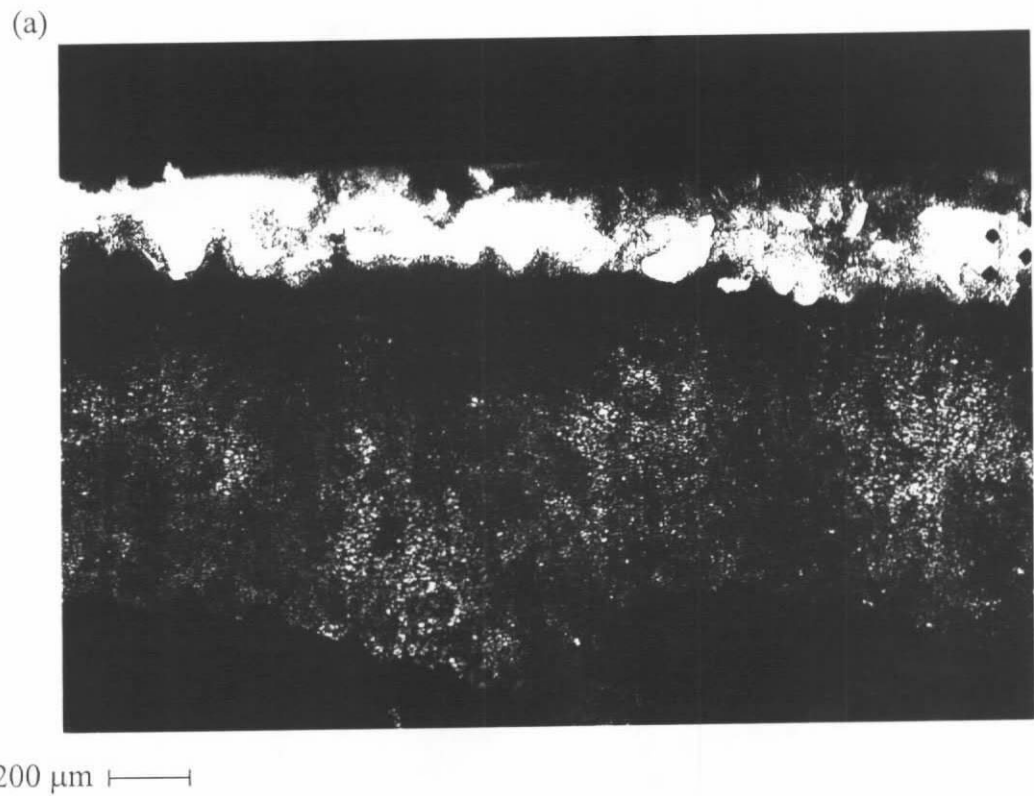
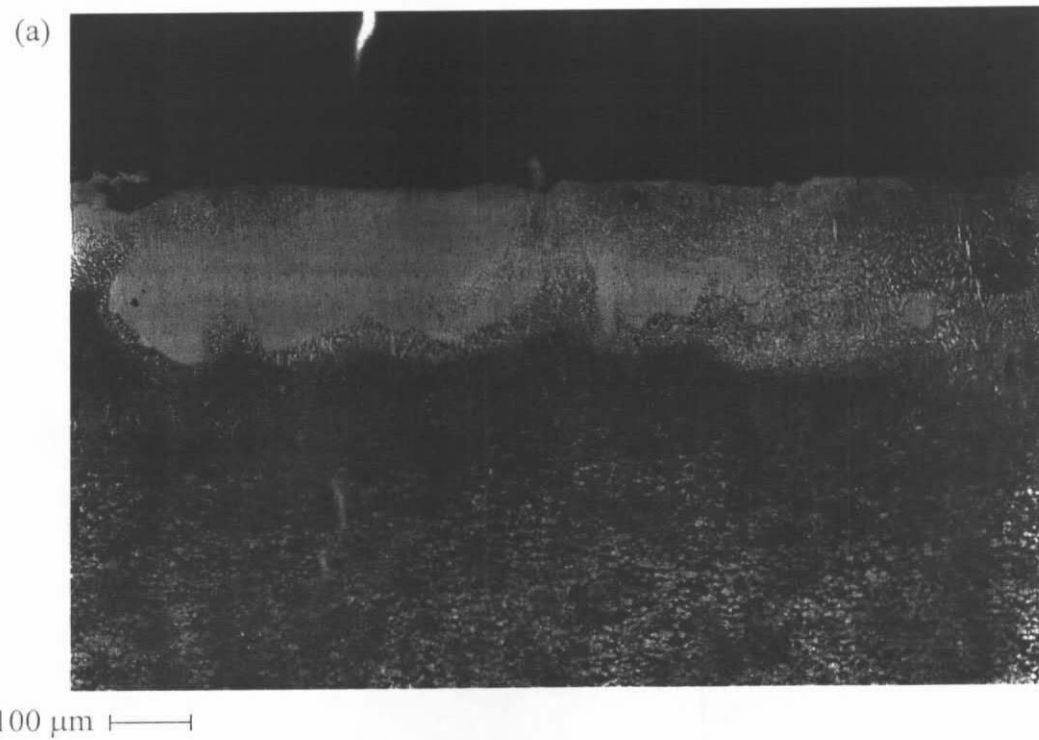


Figure 6. 5 Microstructure of Ni-Cr-Al-Mo-7 (a) melt layer 50×





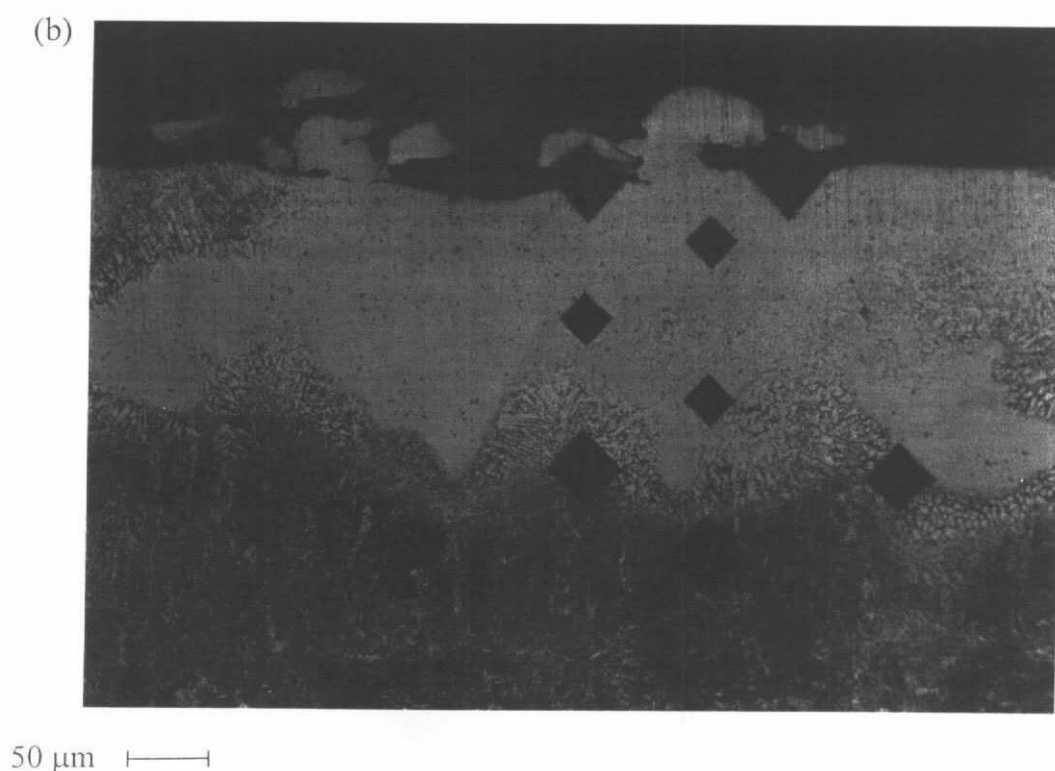
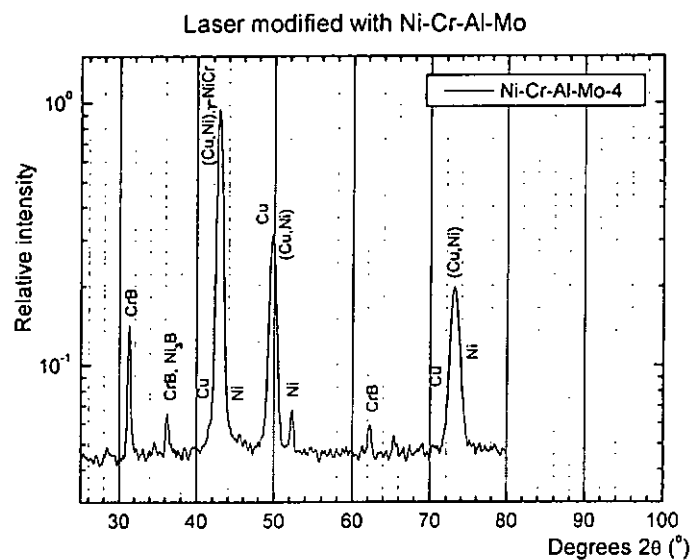


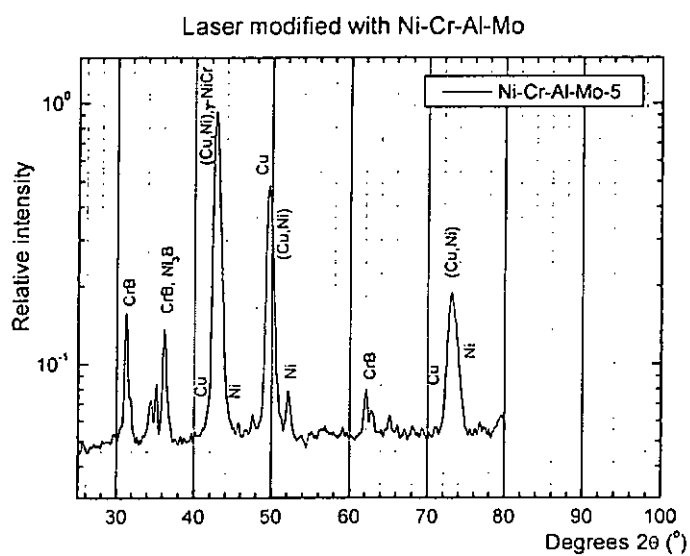
Figure 6. 6 Microstructure of Ni-Cr-Al-Mo-8 (a) melt layer 100 $\times$ , (b) growth of dendritic structure 200 $\times$

### 6.3.1 X-ray diffraction analysis of Ni-Cr-Al-Mo/brass

The corresponding X-ray spectra of the brass substrate and the specimen laser surface modified with Ni-Cr-Al-Mo are shown as Fig. 6. 7 and Fig. 6. 8. All of the laser modified layers were mainly composed of Cu, Ni, (Cu, Ni) and  $\gamma$ -NiCr, and a small amount of secondary phases CrB and Ni<sub>3</sub>B. For the specimen Ni-Cr-Al-Mo-6 and Ni-Cr-Al-Mo-8, the peaks of (Cu,Ni) and  $\gamma$ -NiCr were much stronger in intensity, which resulted from faster scanning speed.



(a)



(b)

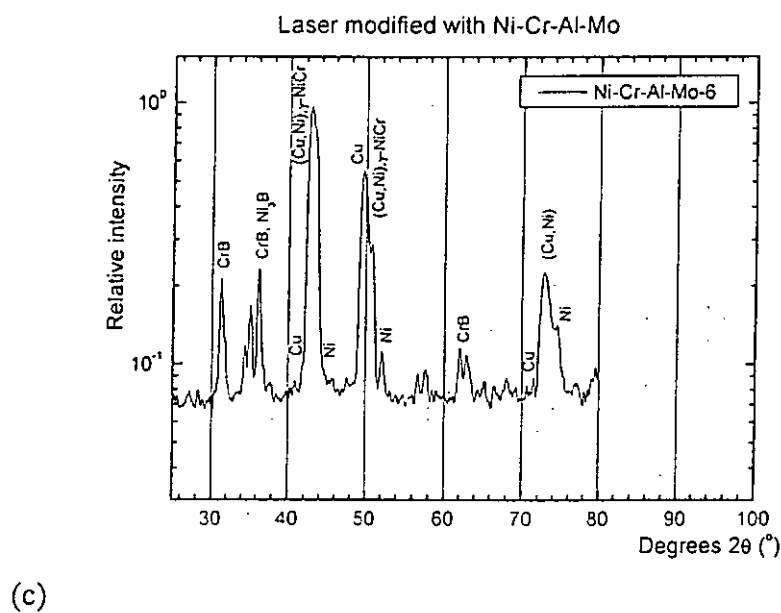
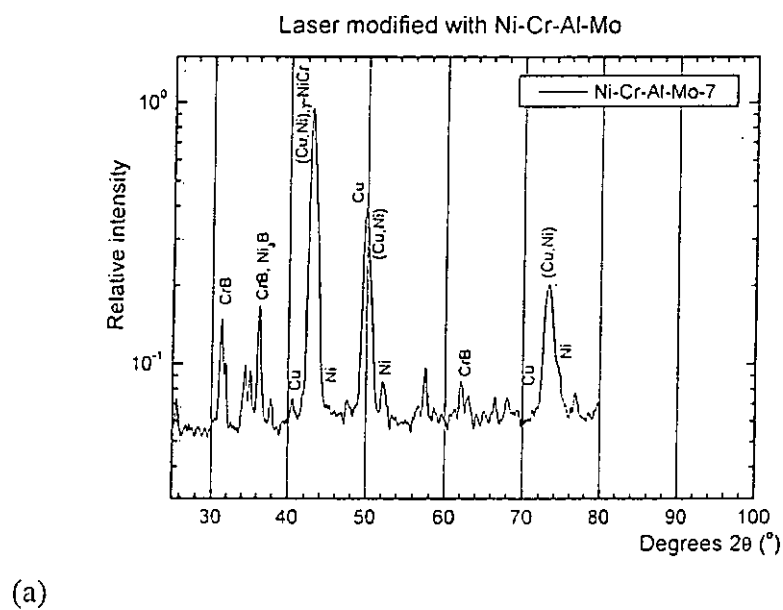
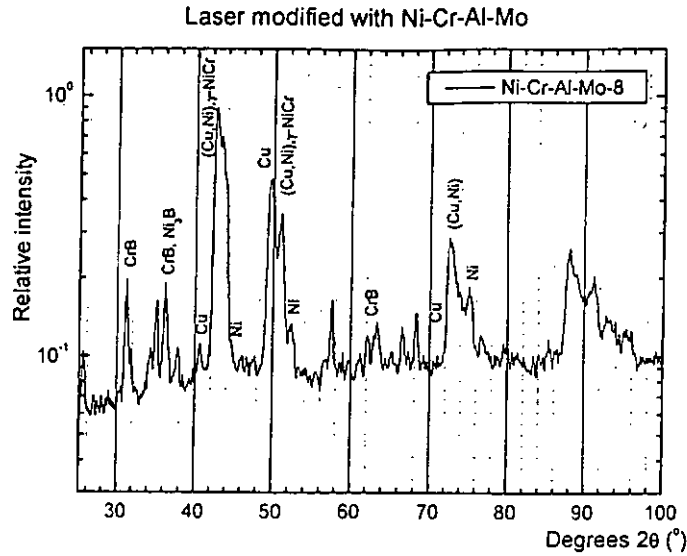


Figure 6. 7 X-ray diffraction spectra of (a) Ni-Cr-Al-Mo-4, (b) Ni-Cr-Al-Mo-5 and (c) Ni-Cr-Al-Mo-6



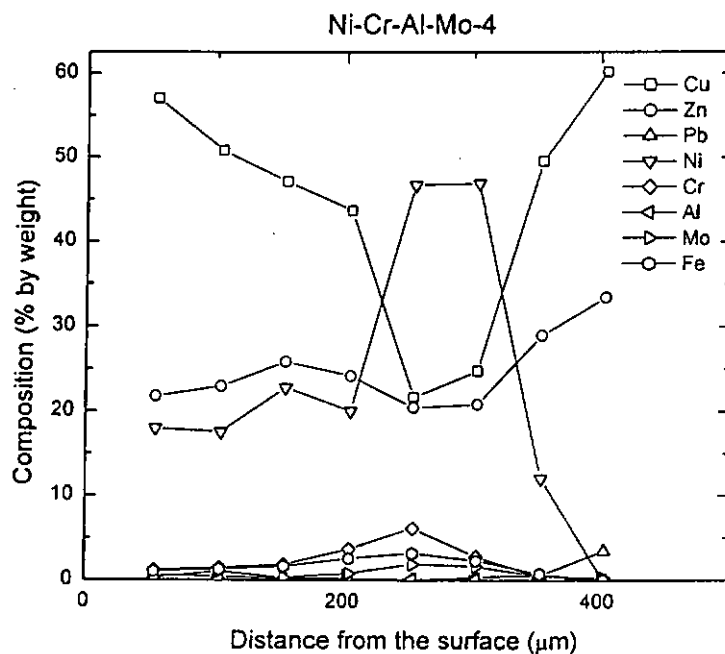


(b)

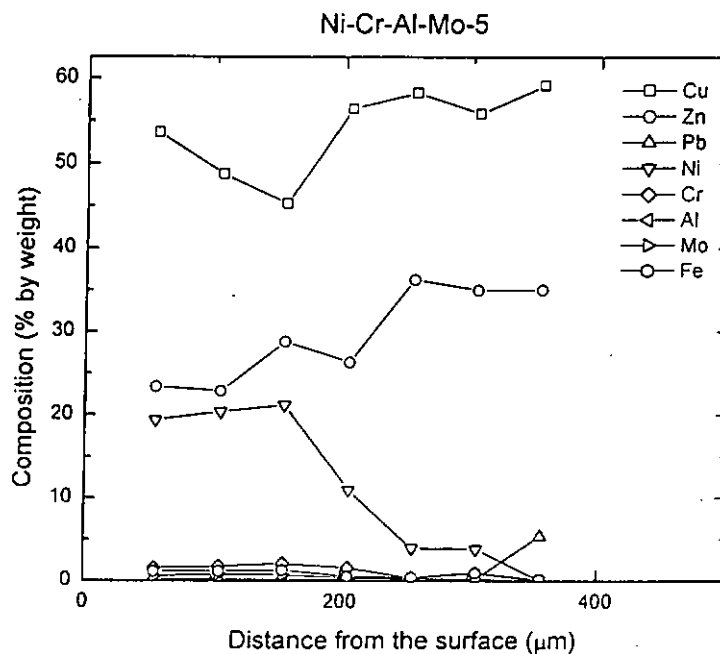
Figure 6. 8 X-ray diffraction spectra of (a) Ni-Cr-Al-Mo-7 and (b) Ni-Cr-Al-Mo-8

## 6.4 Compositional profiles of Ni-Cr-Al-Mo/brass

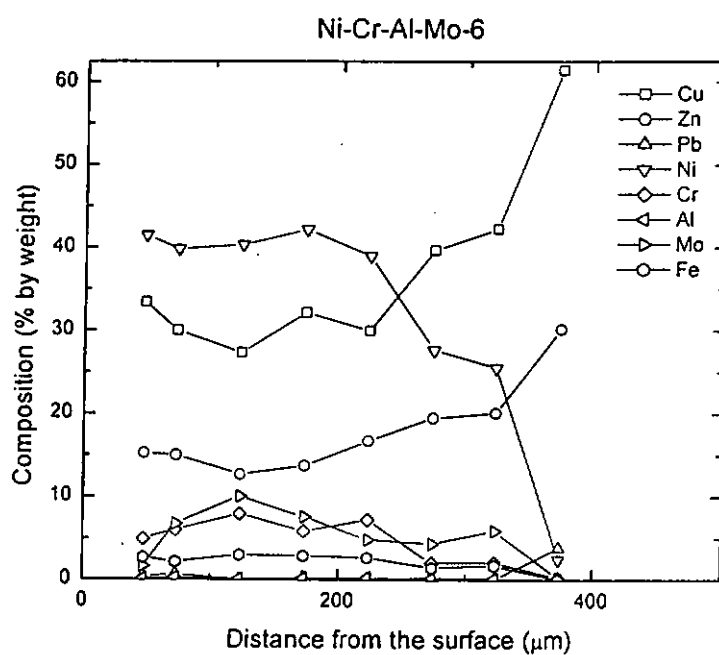
The compositional profiles of the specimens laser surface modified with Ni-Cr-Al-Mo are shown in Fig. 6. 9 and Fig. 6. 10. For specimen Ni-Cr-Al-Mo-4, the alloying elements (mainly of nickel and chromium) were evenly distributed near the surface of the melt layer and rapidly increased to a maximum. It was identified as the white regions revealed in the micrograph. As the scanning speed increased, the compositional profiles showed a relatively more homogenous distribution of the alloying elements. Due to the lower dilution ratio in specimen Ni-Cr-Al-Mo-6 (DR 8%), the melt layer contained a high nickel, chromium, and molybdenum content. This agreed with the micrograph of specimen Ni-Cr-Al-Mo-6 that showed a large proportion of white regions.



(a)



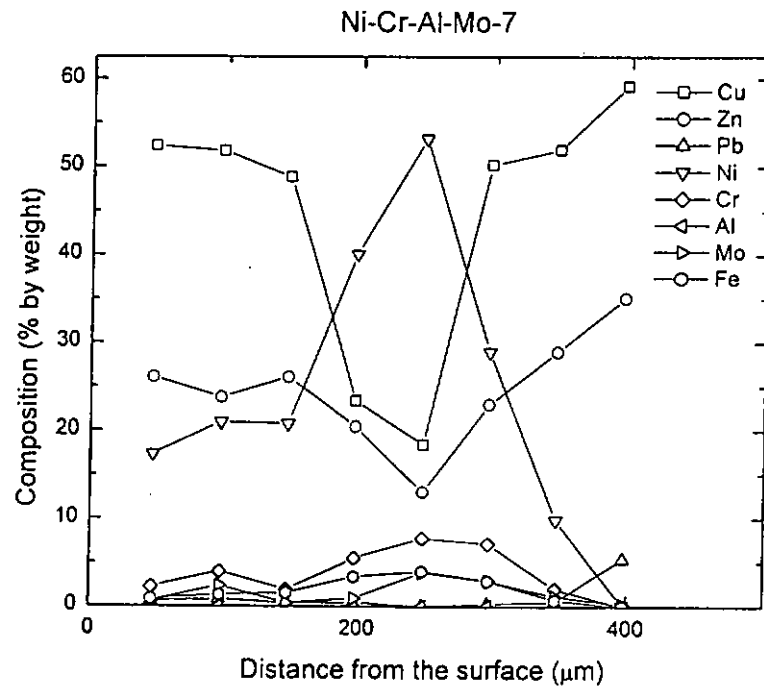
(b)



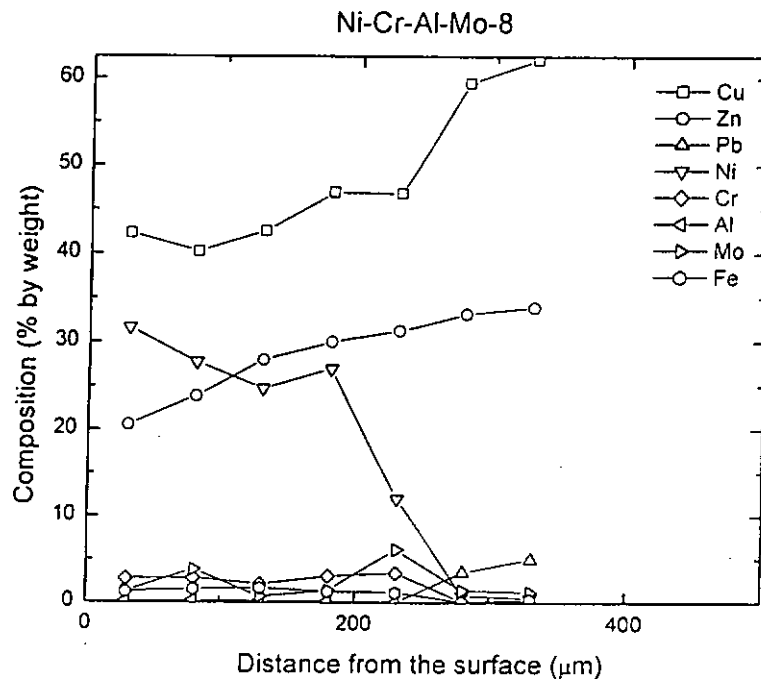
(c)

Figure 6. 9 Chemical compositional profiles of various laser surface modified specimens (a) Ni-Cr-Al-Mo-4, (b) Ni-Cr-Al-Mo-5 and (c) Ni-Cr-Al-Mo-6

The specimen Ni-Cr-Al-Mo-7 shows a similar result as Ni-Cr-Al-Mo-4, the alloying elements were concentrated at the interface between the melt layer and the brass substrate. As the scanning speed increased to 25 mm/s, the melt layer was more homogenous for Ni-Cr-Al-Mo-8.



(a)



(b)

Figure 6. 10 Chemical compositional profiles of various laser surface modified specimens (a) Ni-Cr-Al-Mo-7 and (b) Ni-Cr-Al-Mo-8

## 6.5 Hardness profiles of Ni-Cr-Al-Mo/brass

The hardness profiles along the melt depth of brass modified with Ni-Cr-Al-Mo are shown in Fig. 6. 11, Fig. 6. 12 and Fig. 6. 13. From the graph, it could be observed that the hardness of the modified layers rose to a maximum at a depth of about 150  $\mu\text{m}$  below the surface and then dropped to the hardness of the brass substrate. All of the specimens exhibited a substantial increase in their hardness. In the range of the present study, the hardness achieved was increased with the scanning speed. For specimen Ni-Cr-Al-Mo-4, the average hardness was 152.53  $\text{Hv}_{0.2}$ , which was about 1.5 times that of the hardness of brass substrate. For specimen Ni-Cr-Al-Mo-5 the average hardness increased to 176.52  $\text{Hv}_{0.2}$ . The maximum average hardness 198.35  $\text{Hv}_{0.2}$  was attained by Ni-Cr-Al-Mo-6, which was processed by a high scanning speed of 35 mm/s.

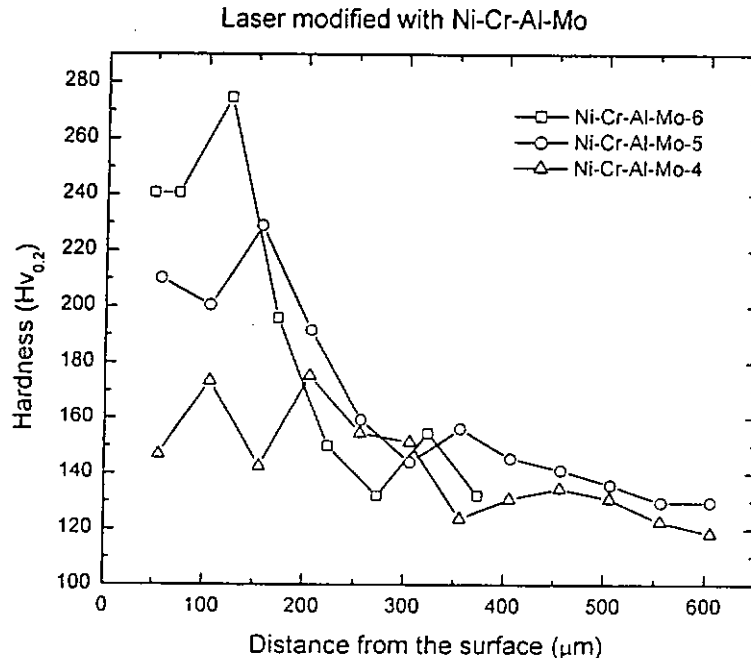


Figure 6. 11 Hardness profiles along the melt depth of the cross section of laser surface modified specimens



As described in the previous paragraph, the hardness was increased as the scanning speed increased. Moreover, the increasing of hardness was due to the decreasing of the laser power density. The average hardness of specimen Ni-Cr-Al-Mo-7 (power density  $64 \text{ W/mm}^2$ , scanning speed  $15 \text{ mm/s}$ ) was  $184.55 \text{ Hv}_{0.2}$  that was higher than the specimen Ni-Cr-Al-Mo-4  $152.53 \text{ Hv}_{0.2}$  (power density  $76 \text{ W/mm}^2$ , scanning speed  $15 \text{ mm/s}$ ). And also, the same result was obtained at the specimen Ni-Cr-Al-Mo-8. The average hardness of specimen Ni-Cr-Al-Mo-8 (power density  $64 \text{ W/mm}^2$ , scanning speed  $25 \text{ mm/s}$ ) was  $256.13 \text{ Hv}_{0.2}$  that was higher than the specimen Ni-Cr-Al-Mo-5  $152.53 \text{ Hv}_{0.2}$  (power density  $76 \text{ W/mm}^2$ , scanning speed  $25 \text{ mm/s}$ ). Although, the specimen Ni-Cr-Al-Mo-6 (power density  $76 \text{ W/mm}^2$ , scanning speed  $35 \text{ mm/s}$ ) proceed by higher scanning speed, the average hardness was lower than the specimen Ni-Cr-Al-Mo-8. The maximum hardness of the specimen Ni-Cr-Al-Mo-8 was revealed by the surface of the melt layer and the measured value was  $335.47 \text{ Hv}_{0.2}$ .

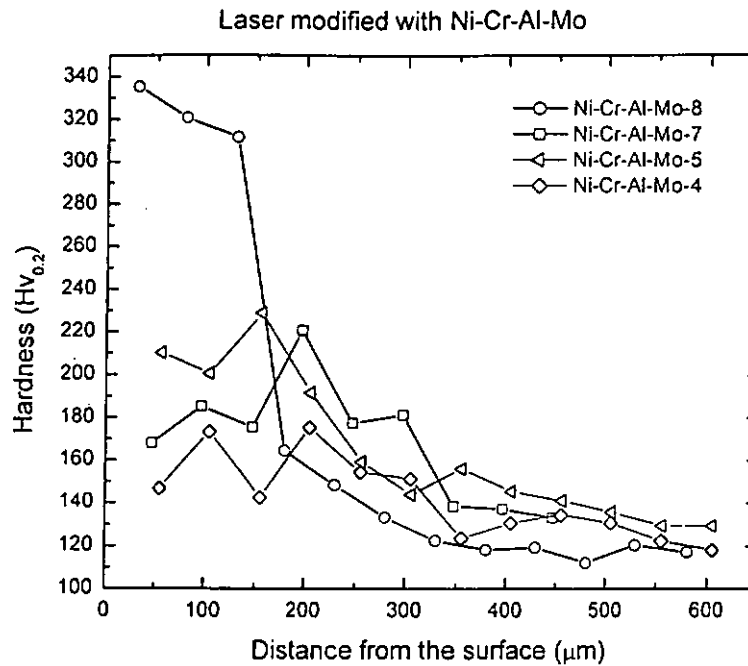


Figure 6. 12 Hardness profiles along the melt depth of the cross section of laser surface modified specimens

Dramatically, the hardness decreased while the preplaced thickness was increased to 350  $\mu\text{m}$  and processed with the same laser processing parameters as Ni-Cr-Al-Mo-9, (laser power density 76  $\text{W}/\text{mm}^2$  and scanning speed 15  $\text{mm}/\text{s}$ ). The hardness profile of specimen Ni-Cr-Al-Mo-9 was in lower level than the hardness profile of the specimen of Ni-Cr-Al-Mo-4. The average hardness of Ni-Cr-Al-Mo-9 was 147.93  $\text{Hv}_{0.2}$ . Moreover, for specimen Ni-Cr-Al-Mo-10, the average hardness dropped when the scanning speed was decreased to 10  $\text{mm}/\text{s}$ . The average hardness was reduced to 125.37  $\text{Hv}_{0.2}$ , very close to the hardness of the brass substrate. The results were similar to the discussion on Ni-Cr-Al-Mo-4 compared with Ni-Cr-Al-Mo-6, and Ni-Cr-Al-Mo-7 compared with Ni-Cr-Al-Mo-8. The hardness of the specimen laser surface modified

with Ni-Cr-Al-Mo was increased as the scanning speed increased and the power density decreased in the range of studies.

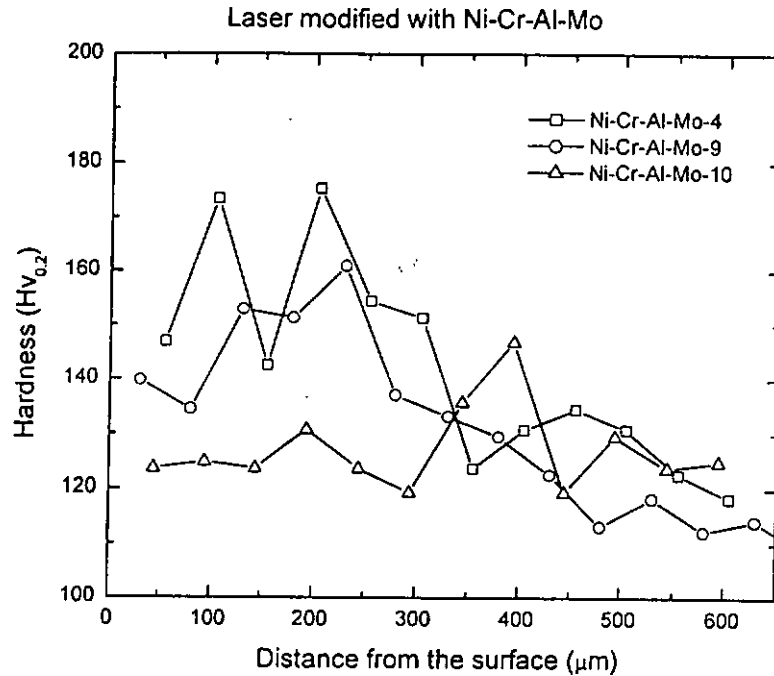


Figure 6. 13 Hardness profiles along the melt depth of the cross section of laser surface modified specimens

## 6.6 Cavitation erosion of Ni-Cr-Al-Mo/brass

Fig. 6. 14 and Fig. 6. 15 show the graph of cumulative mean depth of penetration as a function of time for the as-received and laser surface modified specimens eroded in 3.5% NaCl solution at 23°C. The cavitation erosion resistance of all the laser surface modified specimens was improved relative to that of the brass substrate. The normalised value cavitation erosion resistance  $Re$  of specimens modified with Ni-Cr-Al-Mo is shown in Fig. 6. 16. Those values were relative to that of the brass substrate. The cavitation erosion resistance of the modified specimens increased as the scanning

speed increased and the power density decreased. It was because of its higher hardness and lower dilution ratio.

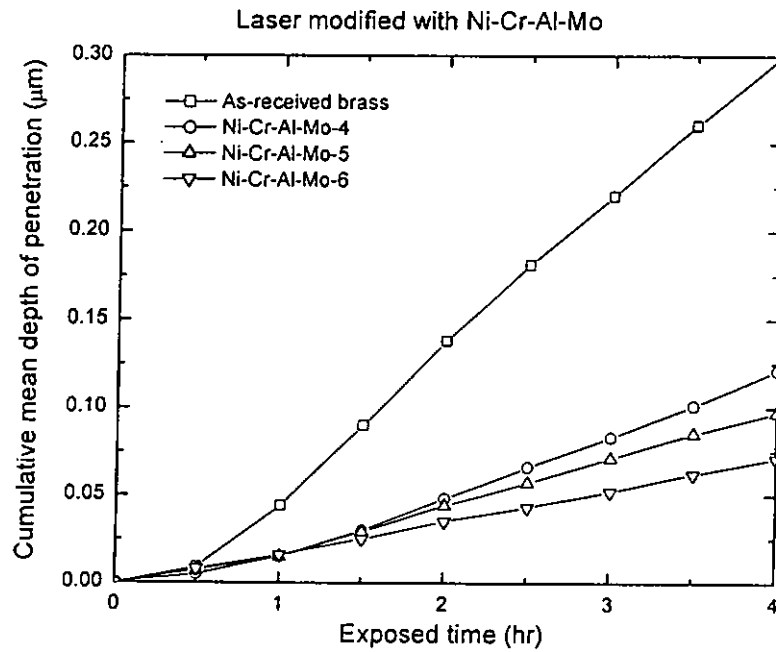


Figure 6. 14 Cumulative MDP as a function of time for the as-received and laser surface modified specimens eroded in 3.5% NaCl solution at 23°C

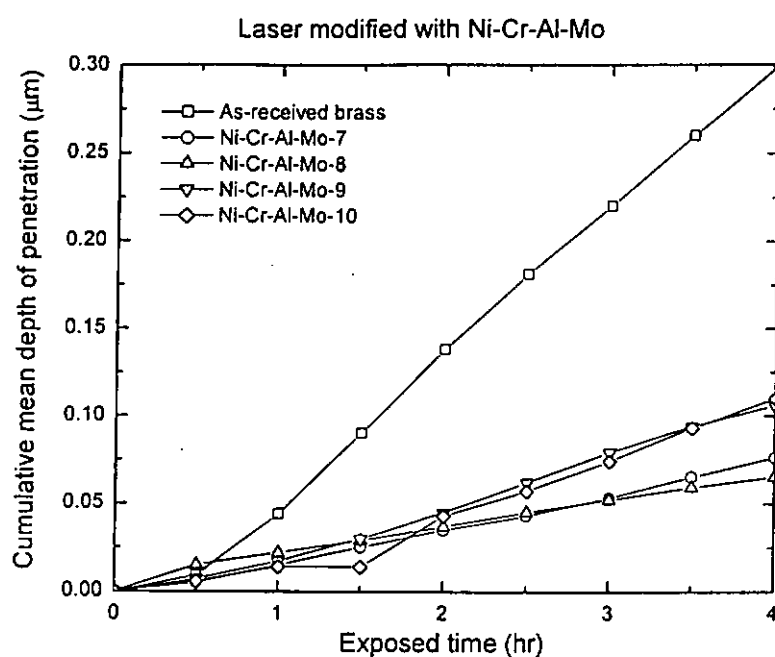


Figure 6. 15 Cumulative MDP as a function of time for the as-received and laser surface modified specimens eroded in 3.5% NaCl solution at 23°C

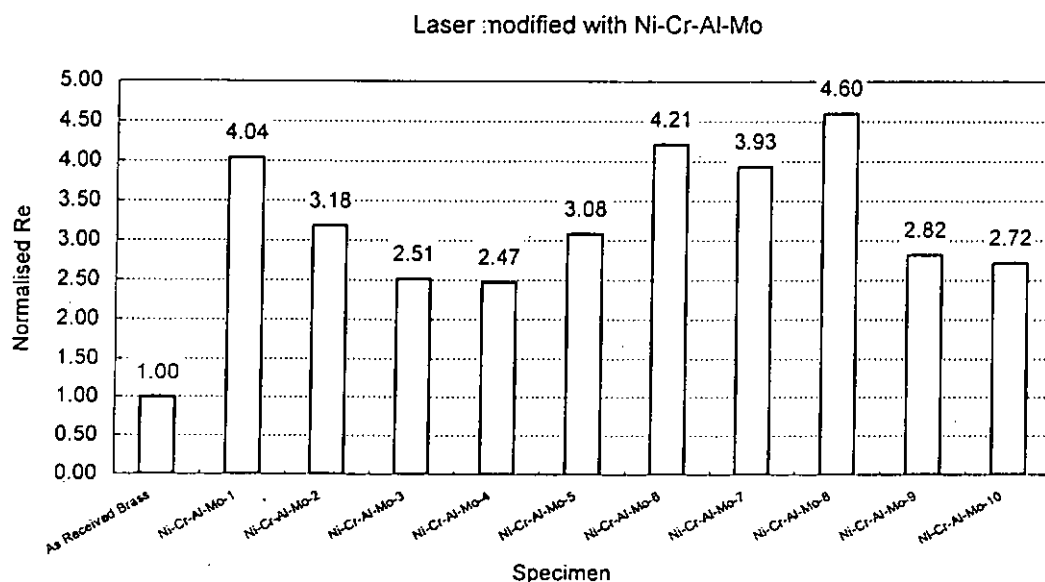


Figure 6. 16 Normalised cavitation erosion resistance for the as-received and laser surface modified specimens eroded in 3.5% NaCl solution at 23°C

## 6.7 Electrochemical corrosion of Ni-Cr-Al-Mo/brass

The potentiodynamic polarization curves of the as-received brass specimen and the specimens laser surface modified with Ni-Cr-Al-Mo in 3.5% NaCl solution at 23°C are shown in Fig. 6. 17 and Fig. 6. 18. The corrosion potential  $E_{corr}$  and the corrosion current density  $I_{corr}$  extracted from the curves are shown in Table 6. 4. The values of the  $E_{corr}$  and  $I_{corr}$  were quite close to those of the as-received specimen. However, it could be observed that there was a shift of the polarization curves towards higher current densities, especially for specimen Ni-Cr-Al-Mo-6, which had cracks in the surface layer. It might thus be concluded that laser surface alloying with Ni-Cr-Al-Mo could not bring an improvement in the corrosion resistance, due to the Cr content was extremely low in the modified layer.

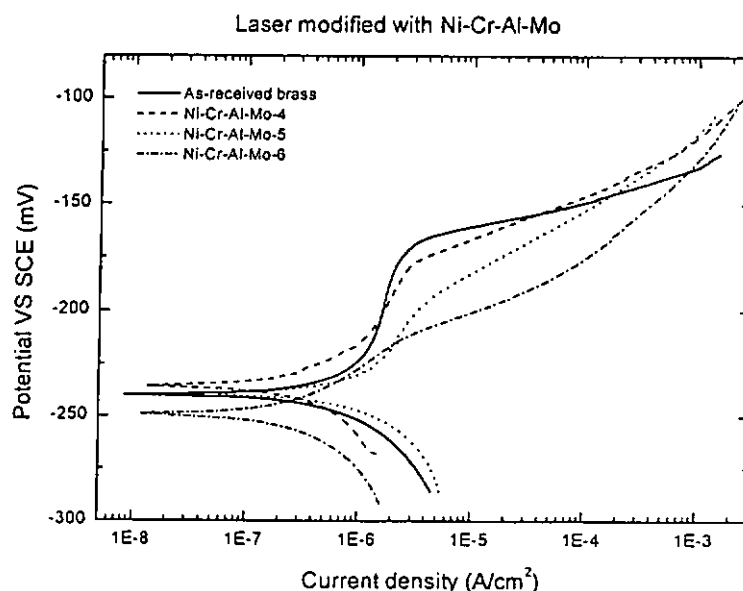


Figure 6. 17 Potentiodynamic polarisation curves of the as-received brass and the laser modified specimens in 3.5% NaCl solution at 23°C

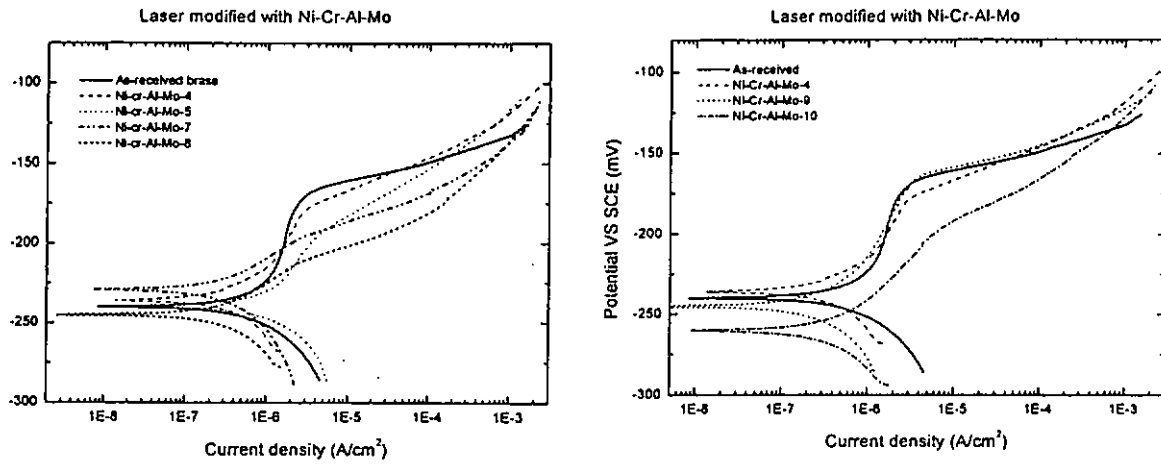


Figure 6. 18 Potentiodynamic polarisation curves of the as-received brass and the laser modified specimens in 3.5% NaCl solution at 23°C

Table 6. 4 The cavitation resistance and corrosion parameters of as-received and laser surface modified specimens

Sample	Ave. Hardness (Hv <sub>0.2</sub> )	Re (hμm <sup>-1</sup> )	Normalised Re	Ecorr (mV)	Icorr (μA/cm <sup>2</sup> )	Epit (mV)
As-received brass	110	13.40	1.00	-238.3	1.0	-173
Ni-Cr-Al-Mo-1	/	54.00	4.04	-472	0.1	-338
Ni-Cr-Al-Mo-2	/	42.51	3.18	/	/	/
Ni-Cr-Al-Mo-3	/	33.58	2.51	-354	0.2	/
Ni-Cr-Al-Mo-4	152.53	33.02	2.47	-236	0.15	-177
Ni-Cr-Al-Mo-5	176.52	41.20	3.08	-239	0.1	-191
Ni-Cr-Al-Mo-6	198.35	56.28	4.21	-249	0.1	-216
Ni-Cr-Al-Mo-7	184.55	52.58	3.93	-229	0.25	-199
Ni-Cr-Al-Mo-8	256.13	61.48	4.60	-245	0.2	-209
Ni-Cr-Al-Mo-9	147.93	37.70	2.82	-245	0.1	-167
Ni-Cr-Al-Mo-10	125.37	36.33	2.72	-260	0.2	-197

Fig. 6. 19 shows the variation of the normalized Re and average hardness with DR.

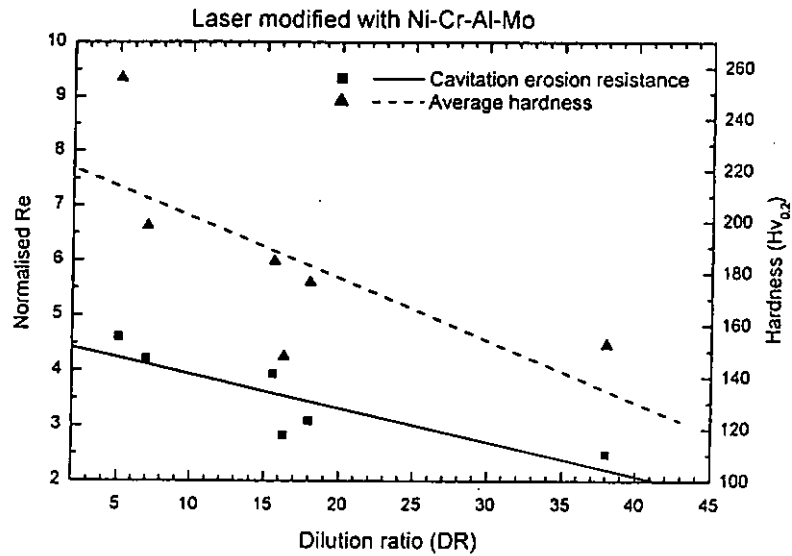
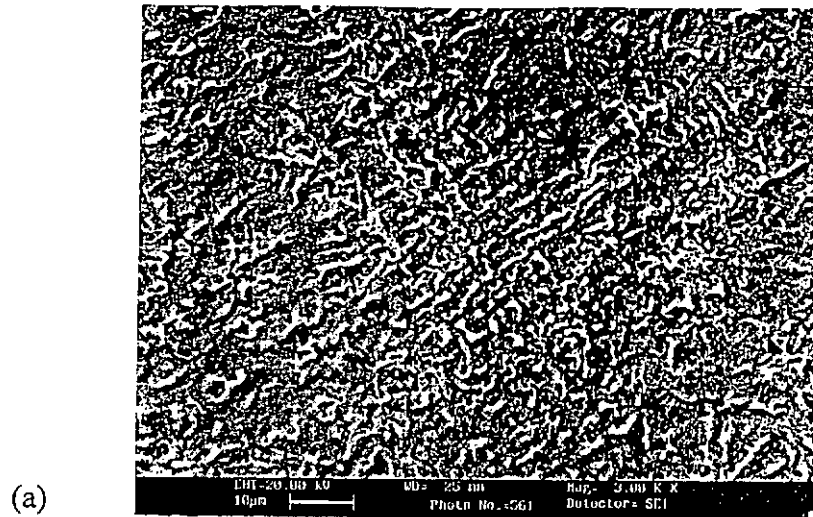


Figure 6. 19 Variation of the normalized Re and average hardness with DR

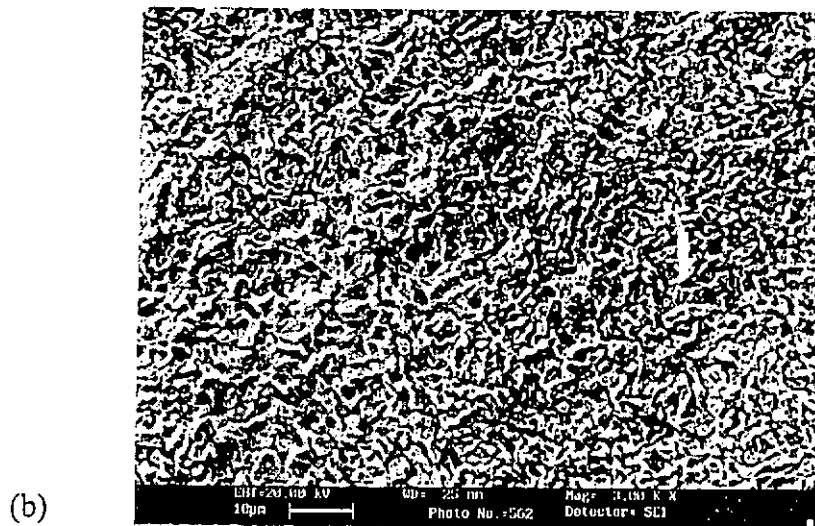
## 6.8 Cavitation damage mechanism of Ni-Cr-Al-Mo/brass

The SEM micrographs of Ni-Cr-Al-Mo-6 subjected to cavitation erosion test for 4 hours are given in Fig. 6. 20. The morphology of the cavitated surface which consisted of undulations and craters indicated that the damage mechanism of the surface was ductile fracture. The SEM picture of the nickel-rich region is shown in Fig. 6. 20 (a) and that of the copper-rich region is shown in Fig. 6. 20 (b). The copper-rich region obviously was more severely damaged.





	Cu	Zn	Ni	Cr	Al	Mo	Fe
wt %	6.45	2.65	74.8	8.43	0.55	3.71	4.59



	Cu	Zn	Ni	Cr	Al	Mo	Fe
wt %	57.29	34.96	6.23	0.54	0	0.48	0.38

Figure 6. 20 Microstructure of brass laser surface modified with Ni-Cr-Al-Mo (Ni-Cr-Al-Mo-6) (a) nickel-rich region (SEM), (b) copper-rich region (SEM)

## **7 Results and discussions –**

### **Laser surface modification of brass (Cu38%Zn) with Ni-Cr-Si-B**

#### **7.1 Introduction**

Ni-Cr-Si-B is a well-known self-fluxing alloying material for hardfacing because of its relatively low melting point, good mechanical and corrosion properties, and maintains high hardness at evaluated temperature. The content of Si and B were used for lowering the melting point of the alloy. Moreover, Si and B react with metal oxides to form boron / silicon salt on the top surface of the alloy layer as dirt during the surfacing process. Therefore, the modified layer is free from pores and metal oxides. Laser surface modification of various engineering materials with Ni-Cr-Si-B for enhancing the surface properties were studied by few researchers [Qian *et al.*, 1997, 1998] [Chizhskaya *et al.*, 1997] [Kwok *et al.*, 1998] [Vannes, 1998] [Dehm, 1999]. The effect of adding alloying element Cr, Fe, B into cupro-nickel were studied by Wang *et al.* [Wang *et al.*, 1998]. It is the aim of the present chapter to laser modify brass with Ni-Cr-Si-B for enhancing the cavitation erosion resistance and corrosion resistance.

#### **7.2 Materials and laser processing parameters**

The nominal composition of Ni-Cr-Si-B alloy powder is shown in Table 7. 1, which was preplaced on brass substrates to a thickness of ~ 200  $\mu\text{m}$  - ~ 600  $\mu\text{m}$  by flame spraying followed by laser irradiation. The flame sprayed coatings were uneven and porous as shown in Fig. 7. 1. Moreover, the as-sprayed coating was not contributive to improving the cavitation erosion and corrosion resistance of the substrate

because of the presence of pores. There were three sprayed specimens with coating thickness  $\sim 350 \mu\text{m}$  treated with different power density  $141 \text{ W/mm}^2$ ,  $184 \text{ W/mm}^2$ , and  $212 \text{ W/mm}^2$ , and constant scanning speed  $5 \text{ mm/s}$ , while the beam spot size was  $3 \text{ mm}$  diameter. The other two sprayed specimens with coating thickness  $\sim 200 \mu\text{m}$  and  $\sim 600 \mu\text{m}$  were modified with laser intensity  $141 \text{ W/mm}^2$ , scanning speed  $5 \text{ mm/s}$  and beam spot diameter  $3 \text{ mm}$ . During the laser processing, argon was used as shielding gas to prevent oxidation. The summary of laser processing parameters and the preplaced coating thickness for brass are shown in Table 7. 2.

Table 7. 1 Nominal composition of Ni-Cr-Si-B powder

Material	Ni	Cr	Si	Fe	B	C	Particle size (mesh)
Ni-Cr-Si-B	Bal.	16.5	3.5	15.5	3.8	<1	$\sim -140$ to $+350$ mesh ( $< 105 \mu\text{m}$ and $> 40 \mu\text{m}$ )



Figure 7. 1 As-sprayed Ni-Cr-Si-B on the brass substrate

Table 7.2 Laser processing parameters of brass surface modified with Ni-Cr-Si-B alloy powder

Specimen	Laser power density	Scanning speed	Coating thickness	Shielding gas flow rate
Ni-Cr-Si-B-1	212 W/mm <sup>2</sup>	5 mm/s	~ 350 μm	Argon 15 l/min
Ni-Cr-Si-B-2	184 W/mm <sup>2</sup>	5 mm/s	~ 350 μm	Argon 15 l/min
Ni-Cr-Si-B-3	141 W/mm <sup>2</sup>	5 mm/s	~ 350 μm	Argon 15 l/min
Ni-Cr-Si-B-4	141 W/mm <sup>2</sup>	5 mm/s	~ 200 μm	Argon 15 l/min
Ni-Cr-Si-B-5	141 W/mm <sup>2</sup>	5 mm/s	~ 600 μm	Argon 15 l/min

After laser irradiation, the modified specimens were cross-sectioned, polished and etched to measure the laser melt depth and calculate the dilution ratio (DR). The melt depth and DR are summarized in Table 7.3.

Table 7.3 Summary of the melt depth and estimated dilution ratio

Specimen	Coating thickness (t)	Melt depth (d)	Dilution ratio* (DR)
Ni-Cr-Si-B-1	~ 350 μm	527 μm	34%
Ni-Cr-Si-B-2	~ 350 μm	452 μm	23%
Ni-Cr-Si-B-3	~ 350 μm	448 μm	22%
Ni-Cr-Si-B-4	~ 200 μm	236.8 μm	16%
Ni-Cr-Si-B-5	~ 600 μm	704.7 μm	15%

$$\text{*Dilution ratio (DR)} = \left( 1 - \frac{t}{d} \right) \times 100\%$$

## 7.3 Effect of power density

### 7.3.1 Microstructural and micrograph analysis

Ni-Cr-Si-B-1, Ni-Cr-Si-B-2 and Ni-Cr-Si-B-3 were treated with different power densities, same scanning speed 5 mm/s and coating thickness ~ 350 μm in order to investigate the effect of power density. During laser irradiation, the Ni-Cr-Si-B powder and the surface of the brass substrate were melted and intermixed, and rapidly solidified

to form a surface layer. This alloyed layer was free from pores and cracks, and bonded to the brass substrate by metallurgical fusion bonding. However, the interface between the laser melted region and the brass substrate was uneven. The cross-sectional view of the laser surface modified specimens is shown in Fig. 7. 2, Fig. 7. 3 and Fig. 7. 4.

For specimens Ni-Cr-Si-B-1 and Ni-Cr-Si-B-2, the micrographs revealed dendritic structure along the modified layer in the former, while the latter showed the dendritic structure only near the surface of the modified layer. A quite different microstructure was observed in specimen Ni-Cr-Si-B-3, which could be divided into three zones, including the surface region, the central region (relatively dark area) and the interface between the modified layer and the brass substrate.





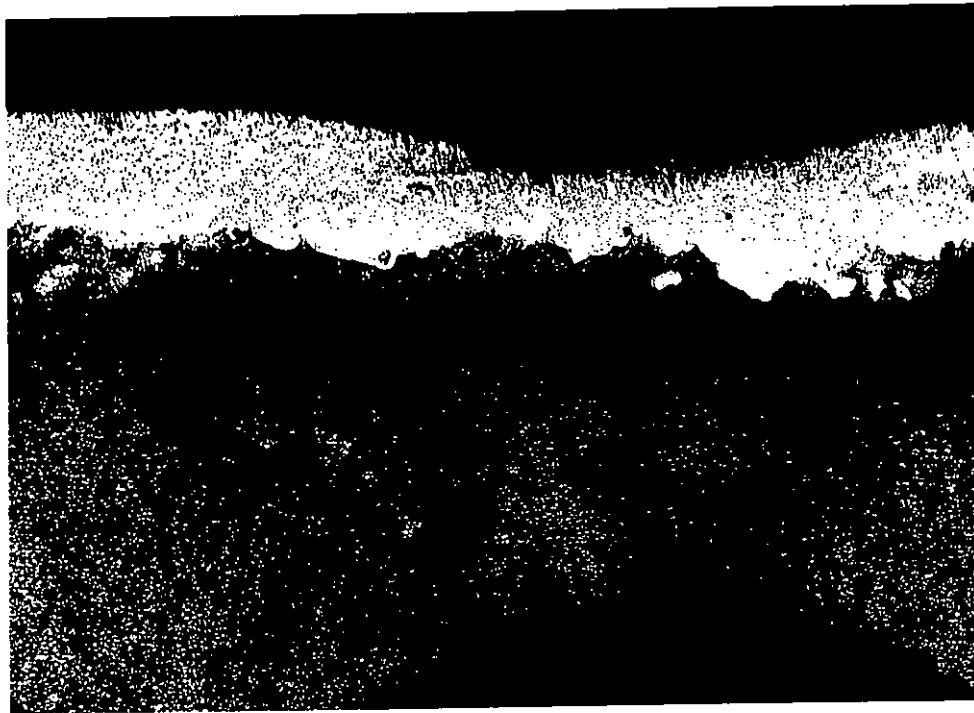
100  $\mu\text{m}$  ———



50  $\mu\text{m}$  ———

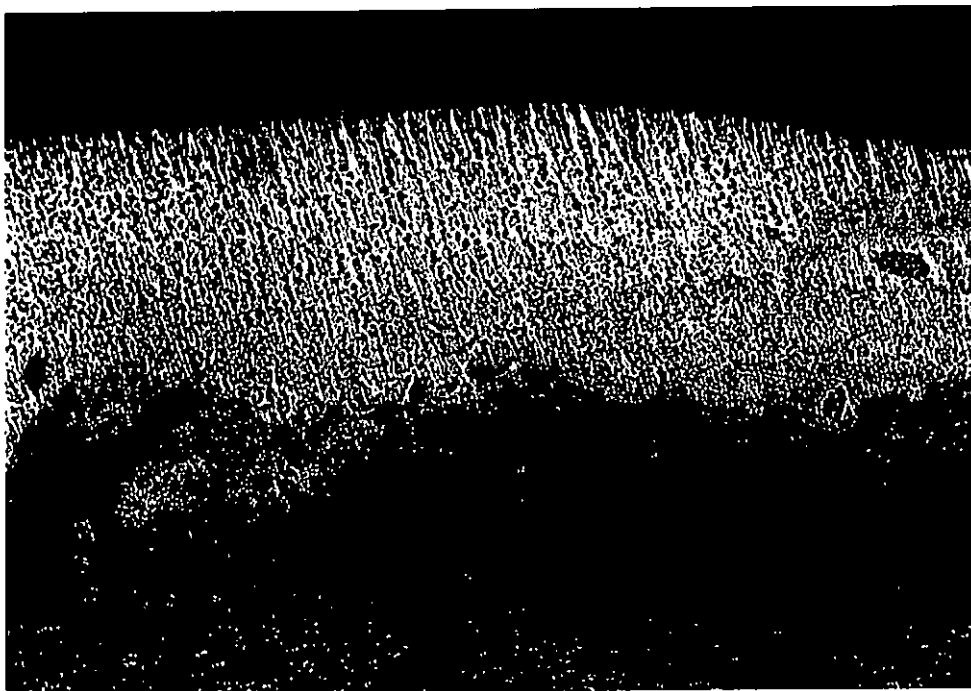
Figure 7. 2 Microstructure of Ni-Cr-Si-B-1 (a) melt layer 50 $\times$ , (b) 100 $\times$  and (c) 200 $\times$

(a)

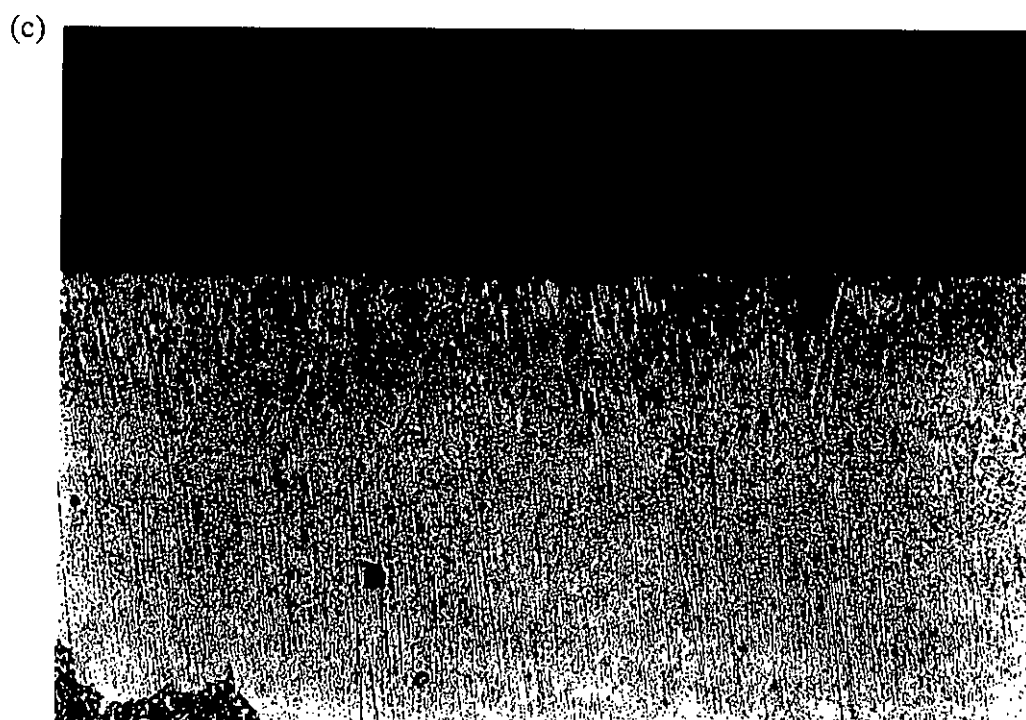


200  $\mu\text{m}$  ———

(b)

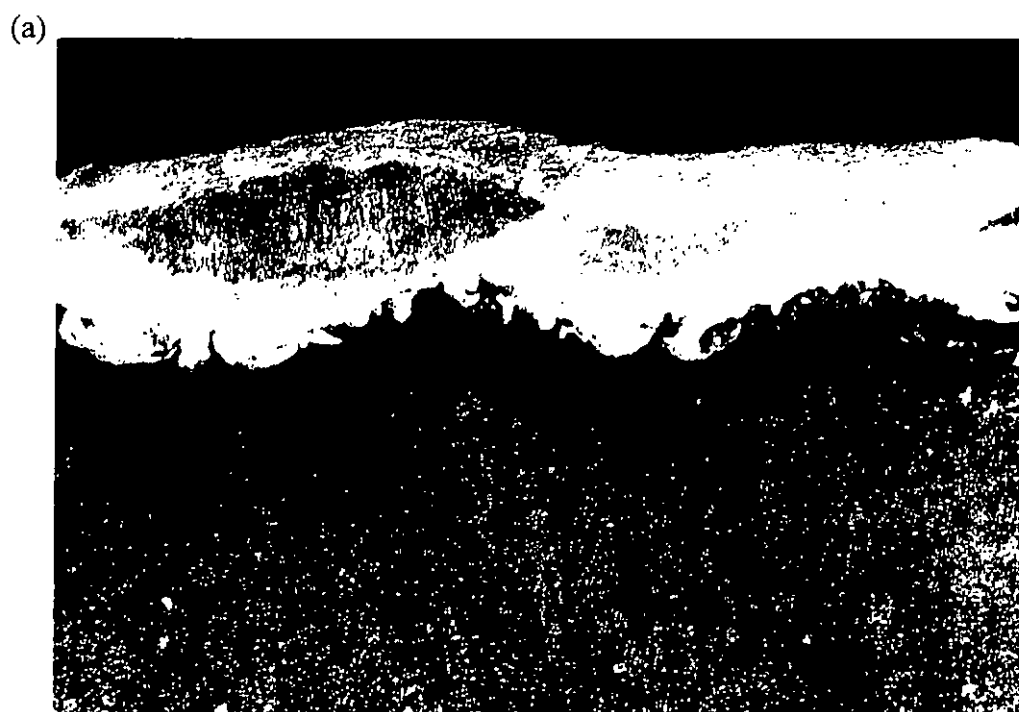


100  $\mu\text{m}$  ———



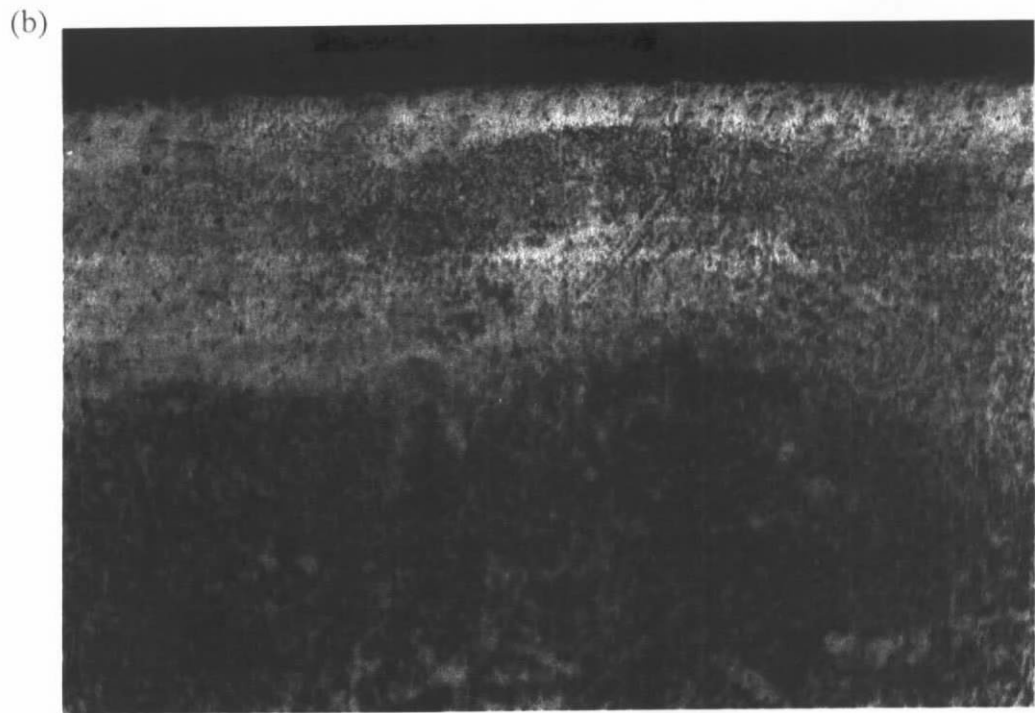
50  $\mu\text{m}$  ———

Figure 7.3 Microstructure of Ni-Cr-Si-B-2 (a) melt layer 50 $\times$ , (b) 100 $\times$  and (c) 200 $\times$



200  $\mu\text{m}$  ———





20  $\mu\text{m}$  —|—



10  $\mu\text{m}$  —|—

Figure 7. 4 Microstructure of Ni-Cr-Si-B-3 (a) melt layer 50 $\times$ , (b) 400 $\times$  and (c) 800 $\times$

### 7.3.2 X-ray diffraction analysis of Ni-Cr-Si-B/brass

The X-ray spectra of the as-sprayed Ni-Cr-Si-B coating and the laser surface modified specimens are shown in Fig. 7. 5. According to the spectra, the as-sprayed coating was mainly fcc  $\gamma$ -NiCr with small amounts of secondary phases such as, chromium boride (CrB), nickel boride ( $\text{Ni}_3\text{B}$ ), and carboboride  $\text{M}_7(\text{CB})_3$ . For the laser surface modified specimens Ni-Cr-Si-B-1, Ni-Cr-Si-B-2 and Ni-Cr-Si-B-3, fcc  $\gamma$ -NiCr, which was the main phase in the as-sprayed coating was not present. Instead, the main phases present were Cu, Ni and (Cu,Ni), together with several secondary phases such as, CrB,  $\text{Ni}_3\text{B}$  and  $\text{M}_7(\text{CB})_3$  similar to those in the as-sprayed coating.

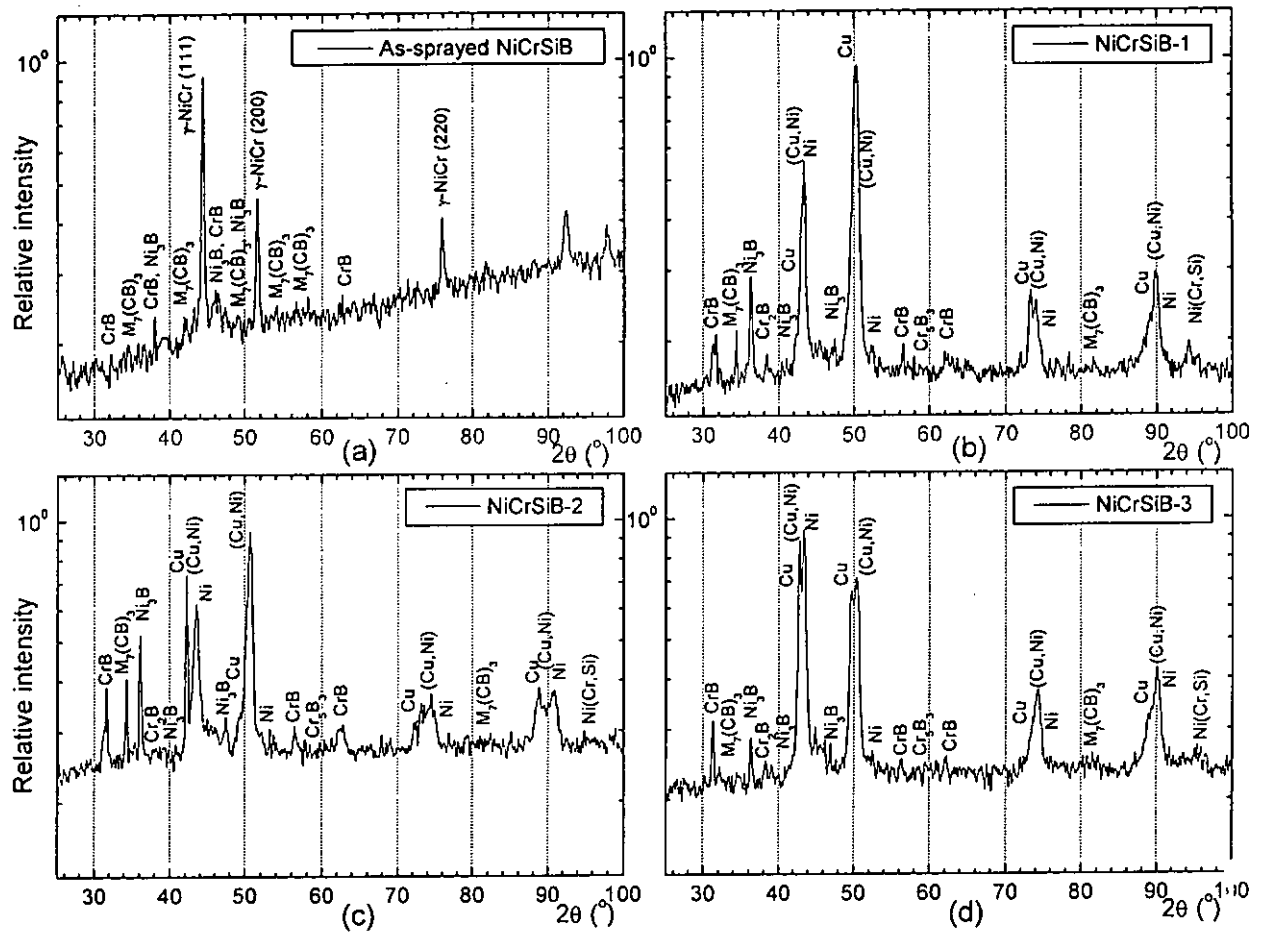


Figure 7.5 X-ray diffraction spectra of (a) as-sprayed Ni-Cr-Si-B, (b) Ni-Cr-Si-B-1, (c) Ni-Cr-Si-B-2, (d) Ni-Cr-Si-B-3

### 7.3.3 Hardness profiles of Ni-Cr-Si-B/brass

The hardness profiles from the surface of the laser modified region to the substrate of the specimen are shown in Fig. 7. 6. The hardness rises from the treated surface to a maximum and then falls to the value of the substrate at the interface between the treated layer and the substrate. The corresponding average value of the hardness is shown in Table 7. 4.

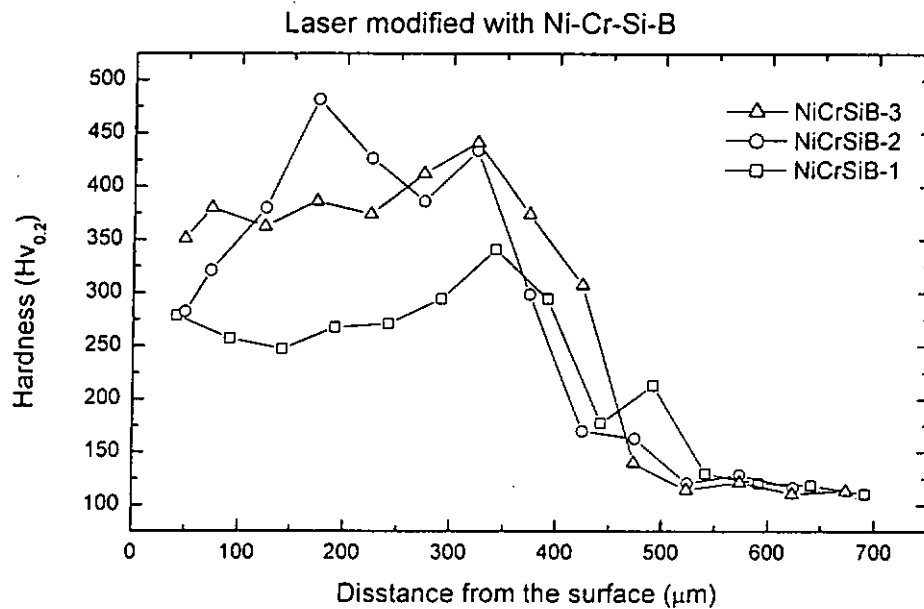


Figure 7. 6 Hardness profiles along the melt depth of the cross section of laser surface modified specimens

#### 7.3.4 Composition profiles of Ni-Cr-Si-B/brass

The compositional profiles of the laser surface modified zone are shown in Fig. 7. It can be observed that in specimen Ni-Cr-Si-B-3, where a lower powder density was used, the composition was homogeneous, while in specimens Ni-Cr-Si-B-1, where a higher power density was used, the dilution ratio was high and the layer contained excessive Cu. This was also reflected in the low hardness shown in Table 7. 4. At intermediate power density in specimen Ni-Cr-Si-B-2, the distribution of the elements was not homogeneous.

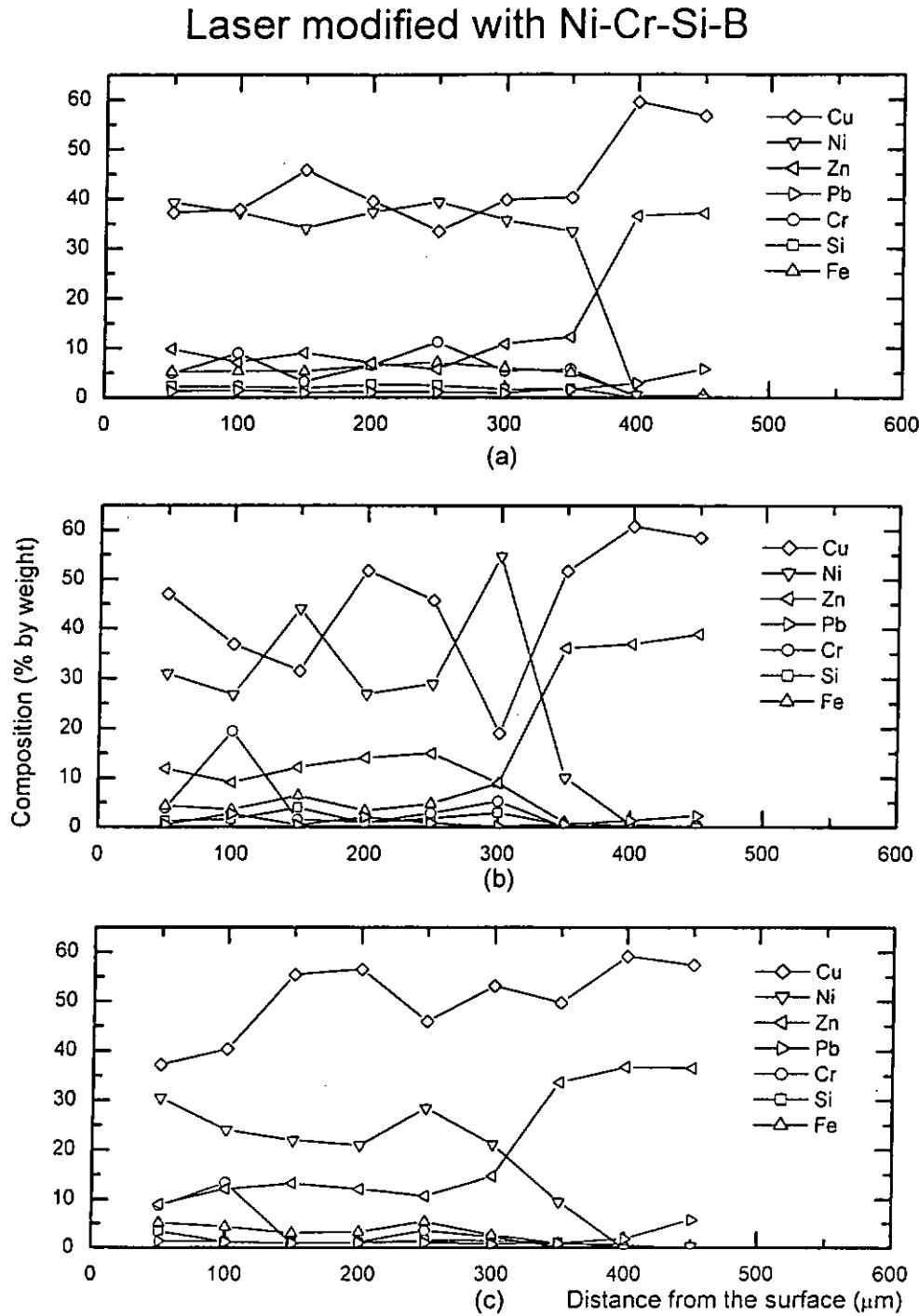


Figure 7. 7 Chemical compositional profiles of various laser surface modified specimens (a) Ni-Cr-Si-B-3, (b) Ni-Cr-Si-B-2 and (c) Ni-Cr-Si-B-1

### 7.3.5 Cavitation erosion of Ni-Cr-Si-B /brass

The cumulative MDP of the as-received brass and laser surface modified specimens cavitared in 3.5% NaCl solution at 23°C is plotted against time in Fig. 7. 8. The cavitation erosion resistance  $R_e$  values of the various laser alloyed specimens are normalised with respect to that the as-received brass and shown in Table 7. 4. The  $R_e$  value increased as the laser power decreased in the range studied. The  $R_e$  of specimen Ni-Cr-Si-B-3 was improved by about 7 times as compared with that of the as-received brass.

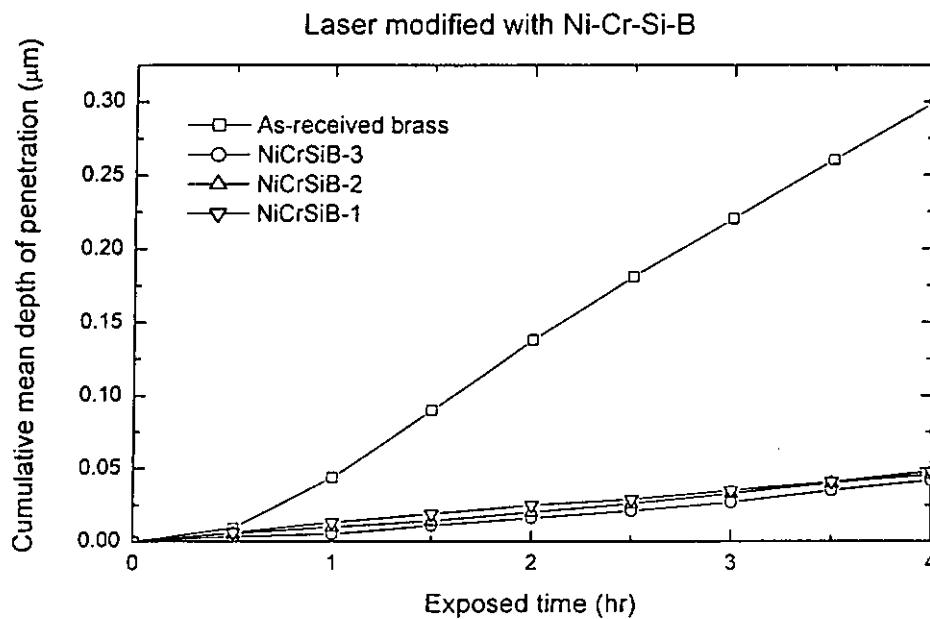


Figure 7. 8 Cumulative MDP as a function of time for the as-received and laser surface modified specimens eroded in 3.5% NaCl solution at 23°C

### 7.3.6 Electrochemical corrosion of Ni-Cr-Si-B /brass

Fig. 7. 9 shows the potentiodynamic polarisation curves of the as-received brass and the various laser surface modified specimens in 3.5% NaCl solution at 23°C. The corrosion potentials of the various specimens were very close to the value of as-received brass. On the other hand, the pitting potential, which indicates resistance to pitting corrosion, was improved in all the laser surface modified specimens. In addition, the corrosion current density was reduced. For specimen Ni-Cr-Si-B-3, the pitting potential was shifted in the noble direction by an amount of about 61mV (from -173mV to -112mV), while the current density was at least an order lower than that of the as-received brass. The corresponding corrosion parameters of the various specimens are summarized in Table 7. 4.

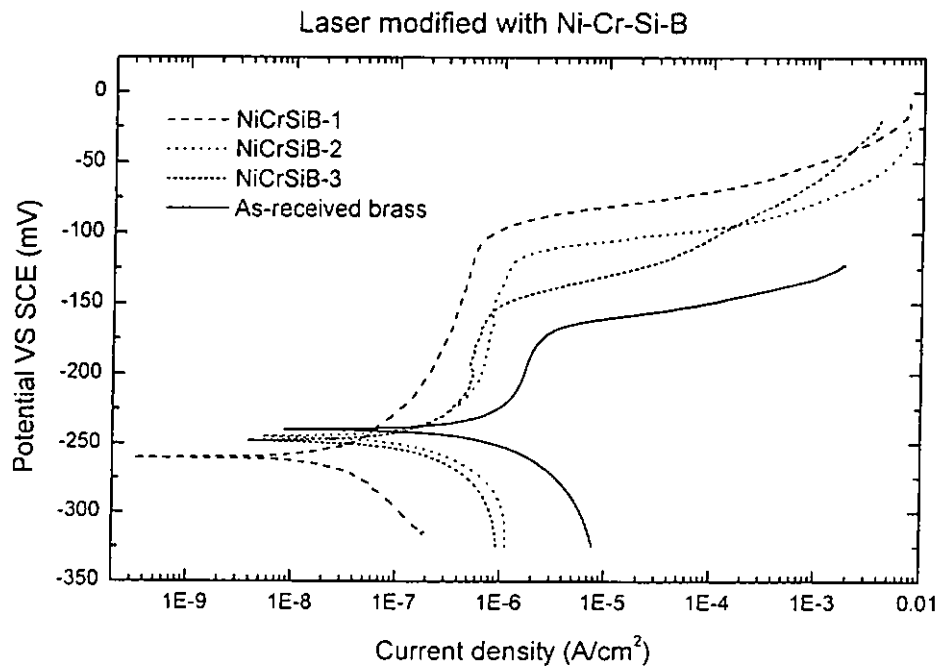


Figure 7. 9 Potentiodynamic polarisation curves of the as-received brass and the laser modified specimens in 3.5% NaCl solution at 23°C



Table 7.4 The average hardness, cavitation erosion resistance and corrosion parameters of as-received and laser surface modified specimens

Specimens	Ave. Hardness (H <sub>V0.2</sub> )	Re (hμm <sup>-1</sup> )	Normalised Re	E <sub>corr</sub> (mV)	I <sub>corr</sub> (μA/cm <sup>2</sup> )	E <sub>pit</sub> (mV)
As-received brass	110	13.4	1.00	-238.3	1.0	-173
Ni-Cr-Si-B-3	378	95.1	7.12	-262.0	0.09	-112
Ni-Cr-Si-B-2	376	86.9	6.50	-244.1	0.5	-128
Ni-Cr-Si-B-1	281	81.5	6.10	-250.0	0.4	-168

### 7.3.7 Cavitation damage mechanism of Ni-Cr-Si-B/brass

The appearance of the damaged surface of specimen Ni-Cr-Si-B-3 after 4 hours of cavitation test is shown in Fig. 7. 10. The surface was roughened after the 4-hour test, indicating that material was eroded from the surface by ductile fracture, similar to the results of one of our previous works [Kwok *et al.*, 1998]. The eroded loss was mainly the copper-rich phases as evidenced by the X-ray diffraction spectra shown in Fig. 7. 11.

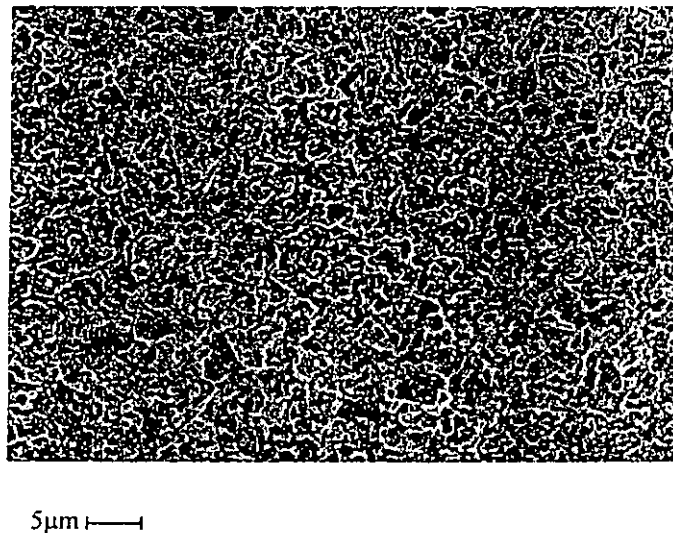


Figure 7. 10 Appearance of the damaged surface of modified specimen Ni-Cr-Si-B-3 after 4 hours exposure to cavitation erosion

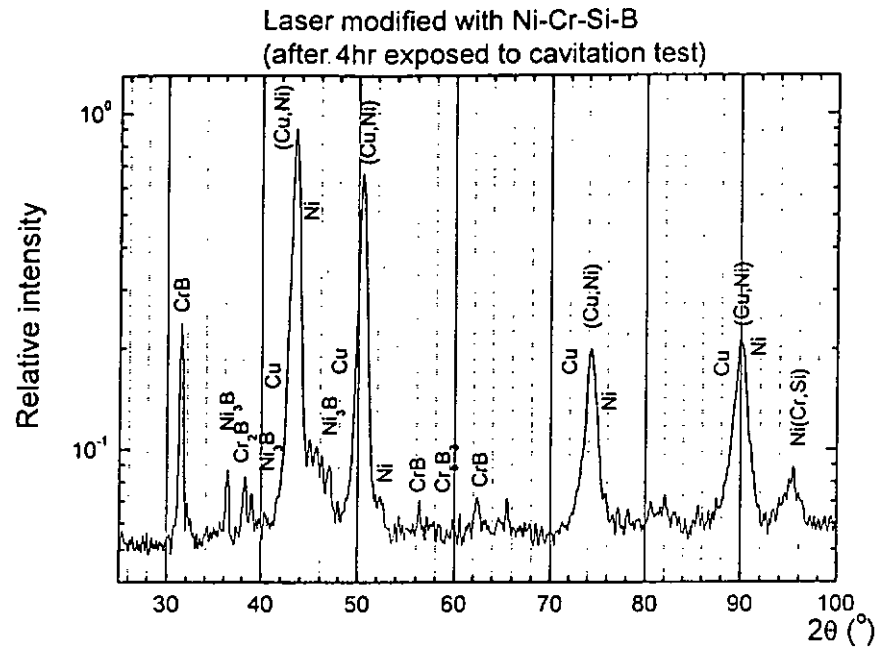


Figure 7. 11 X-Ray diffraction spectra of Ni-Cr-Si-B-3 after 4 hours exposed to cavitation erosion test

## 7.4 Effect of coating thickness

The amount of the preplaced coating significantly affected the melted depth, which in turn affected the dilution ratio and the compositional profile along the treated zone. The laser processing parameters were kept unchanged, (laser power density  $141 \text{ W/mm}^2$  and scanning speed  $10 \text{ mm/s}$ , respectively, which is the most appropriate laser processing parameter discussed in the previous section 7.3). Three brass specimens were preplaced with different coating thickness of  $\sim 200 \text{ }\mu\text{m}$ ,  $\sim 350 \text{ }\mu\text{m}$  and  $\sim 600 \text{ }\mu\text{m}$ . The results showed that the characteristics of the modified layer with different preplaced coating thickness were quite different.

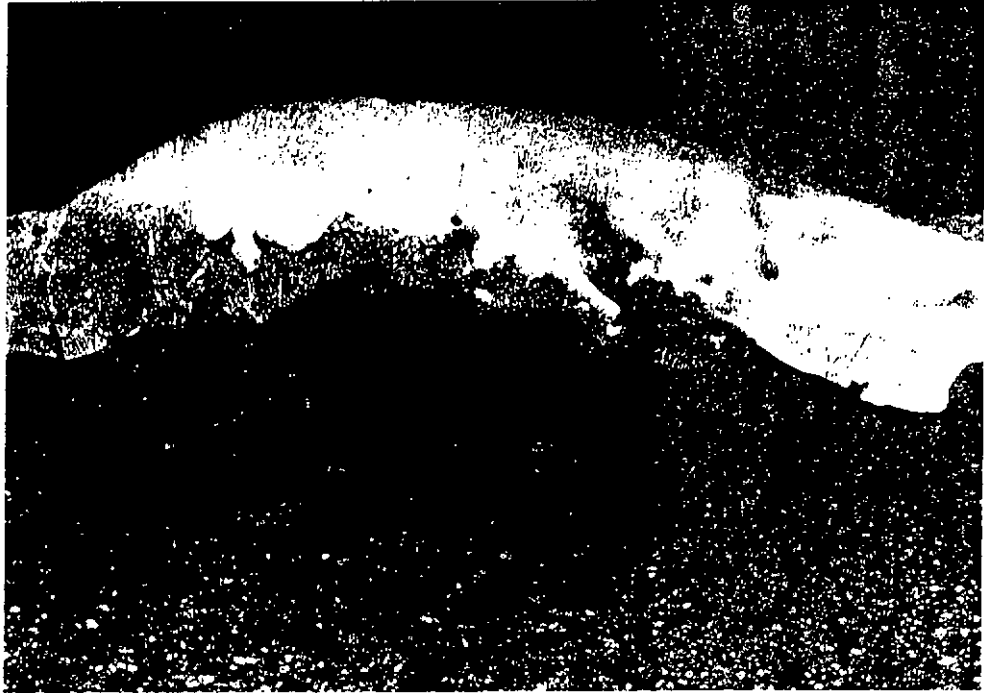
#### 7.4.1 Microstructural and micrograph analysis

The microstructure of specimen Ni-Cr-Si-B-4 was not homogeneous along the modified layer as shown in Fig. 7.12. The modified surface showed a peak-and-valley profile in the direction perpendicular to the laser melted tracks. For specimen Ni-Cr-Si-B-5, the cross sectional view exposed a homogenous microstructure and precipitates were evenly distributed inside the modified layer. In addition, the Ni-Cr-Si-B layer was bonded to the substrate by the metallurgical fusion bonding. However, there were pores in specimen Ni-Cr-Si-B-5. It may be due to the air trapped in the thick section of the melt pool and / or insufficient coverage of shielding gas during the laser surface processing. The cross-sectional view of the laser surface modified specimens is shown in Fig. 7. 12 and Fig. 7. 13.



200  $\mu\text{m}$  ———

(b)



100  $\mu\text{m}$  ———

(c)



20  $\mu\text{m}$  ———

Figure 7. 12 Microstructure of Ni-Cr-Si-B-4 (a) melt layer 50 $\times$ , (b) 100 $\times$  and (c) 400 $\times$



Figure 7. 13 Microstructure of Ni-Cr-Si-B-5 melt layer 100×

#### 7.4.2 X-ray diffraction analysis of Ni-Cr-Si-B/brass

According to the spectra, the results were similar with discussed in the Section 7.3.2. The melt layer was mainly composed with Cu, Ni and (Cu, Ni), and accompanied with CrB, Ni<sub>3</sub>B and M<sub>7</sub>(CB)<sub>3</sub> secondary phases. Fig. 7. 14 shows the X-ray diffraction spectra of the modified specimens with Ni-Cr-Si-B alloy powder.

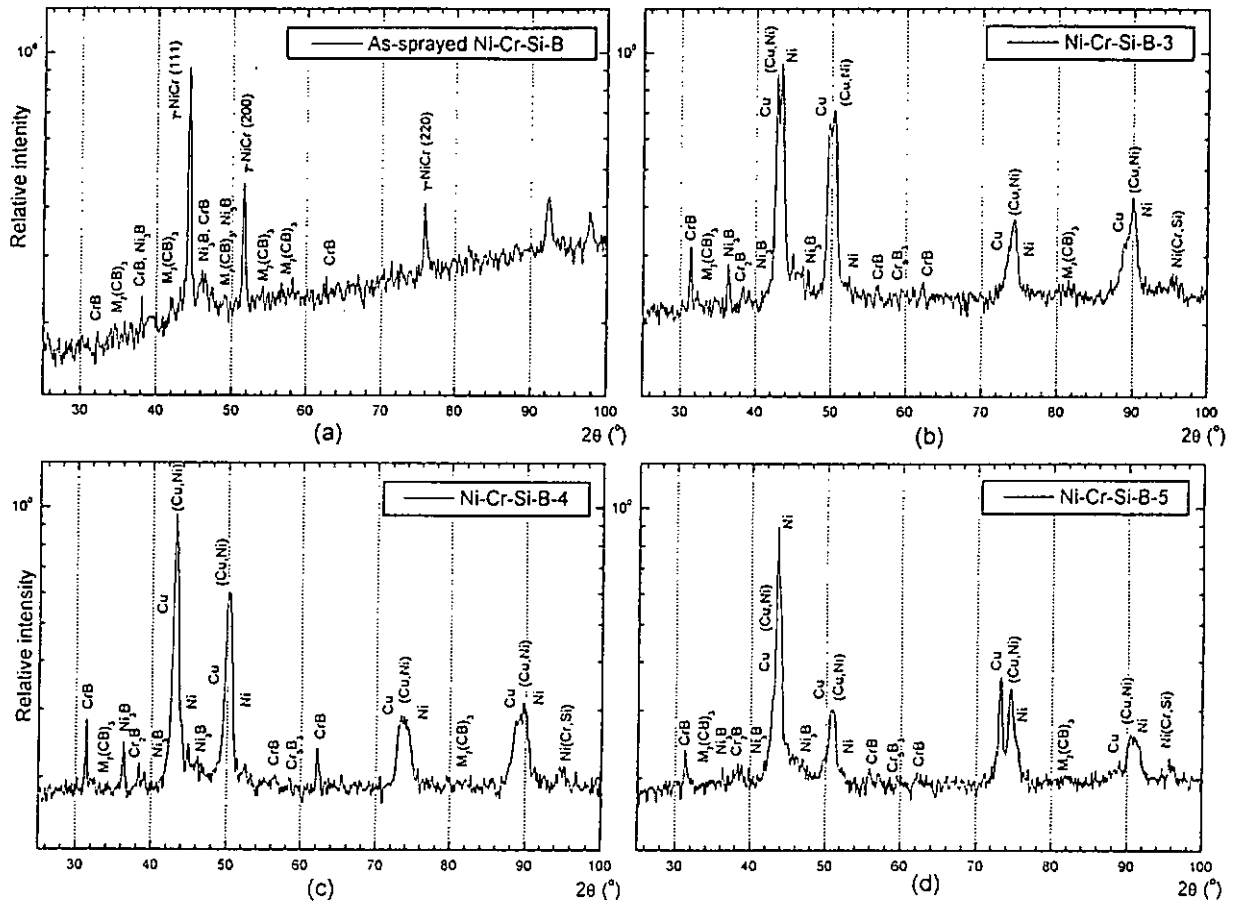


Figure 7.14 X-ray diffraction spectra of (a) as-sprayed Ni-Cr-Si-B, (b) Ni-Cr-Si-B-3, (c) Ni-Cr-Si-B-4, (d) Ni-Cr-Si-B-5

### 7.4.3 Hardness profiles of Ni-Cr-Si-B/brass

Fig. 7.15 shows the hardness profile along the melt depth of the modified layer of the specimens with different preplaced coating thickness,  $\sim 200\ \mu\text{m}$ ,  $\sim 350\ \mu\text{m}$  and  $\sim 600\ \mu\text{m}$ . The hardness profiles of those three modified layer were uniform across the melted zone and reduced to the value of the substrate at the interface between the alloyed layer and the substrate. For the case of Ni-Cr-Si-B-3 and Ni-Cr-Si-B-5, the hardness was slightly raised from the surface of the modified layer to the maximum value, near the intermediate region. The highest hardness was found in Ni-Cr-Si-B-5,

which was attributed to a higher Cr content, as revealed by the compositional profile shown in Fig. 7. 16.

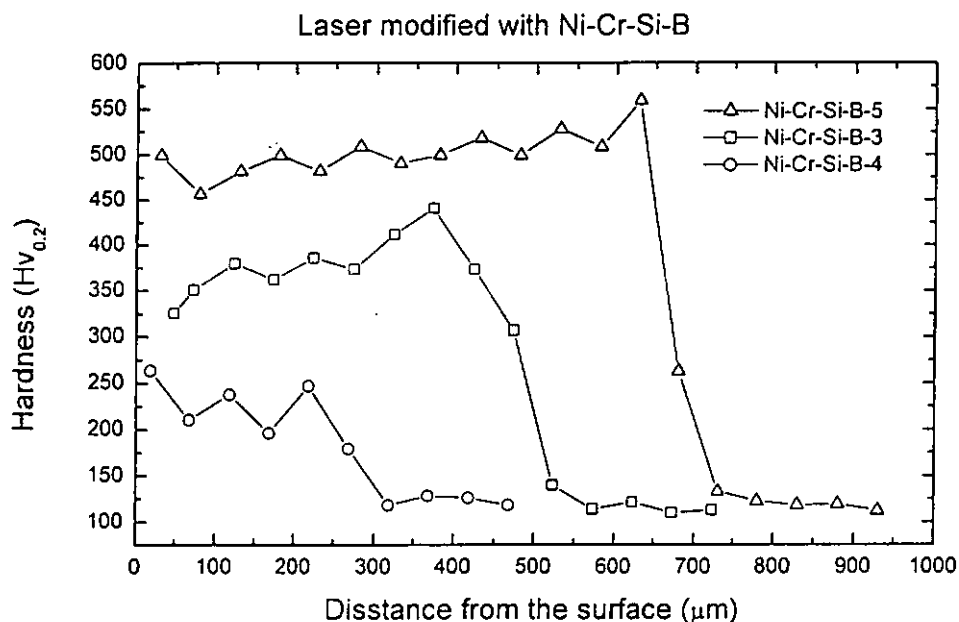


Figure 7. 15 Hardness profiles along the melt depth of the cross section of laser surface modified specimens

#### 7.4.4 Composition profiles of Ni-Cr-Si-B/brass

The compositional profiles along the depth of the melted layer of the modified specimens with different preplaced coating thickness was shown in Fig. 7. 16. Copper and nickel were the main elements and were homogeneously distributed along the depth of the melted region, except in the case of Ni-Cr-Si-B-4. This heterogeneous structure was due to the less preplaced coating on the brass substrate. The laser energy was mainly absorbed by the preplaced coating and the thickness of the preplaced coating

affected the absorption of the laser energy, thinner preplaced coating expected to lesser energy absorbed and penetrated to melt the brass substrate. Therefore, the melted depth of the laser surface modification effected layer is limited. Consequently, the total solidification time was shorter when compared with the other case, due to the lower energy absorbed and smaller alloying region by faster quenching rate with overhead flowing Ar shielding gas and bulk brass substrate. The alloying elements cannot evenly distributed in the laser modified layer in this short interaction time. Moreover, the inhomogeneity of the elements in the melt pool could be attributed to the unfavorable depth to width ratio. The ratio of depth to width ( $d/h$ ) has been reported to affect the homogeneity of the constituents of the melt pool in the alloying of a medium carbon steel with Cr, because  $d/h$  affects the convection currents in the pool.

The chromium content fluctuated in all the three cases. In traditional alloying process, the solubility of Cr in Cu solid solution was about 0.89 atomic wt % at 1350 K [Massalski (Ed), 1990]. Cr content can be increased up to 40% [Galantucci *et al.*, 1989] by laser processing because of the nonequilibrium nature of the process. Moreover, the Cr particles were dispersed in the melted layer. As a result, the concentration of the Cr content varied along the depth of the melted layer.



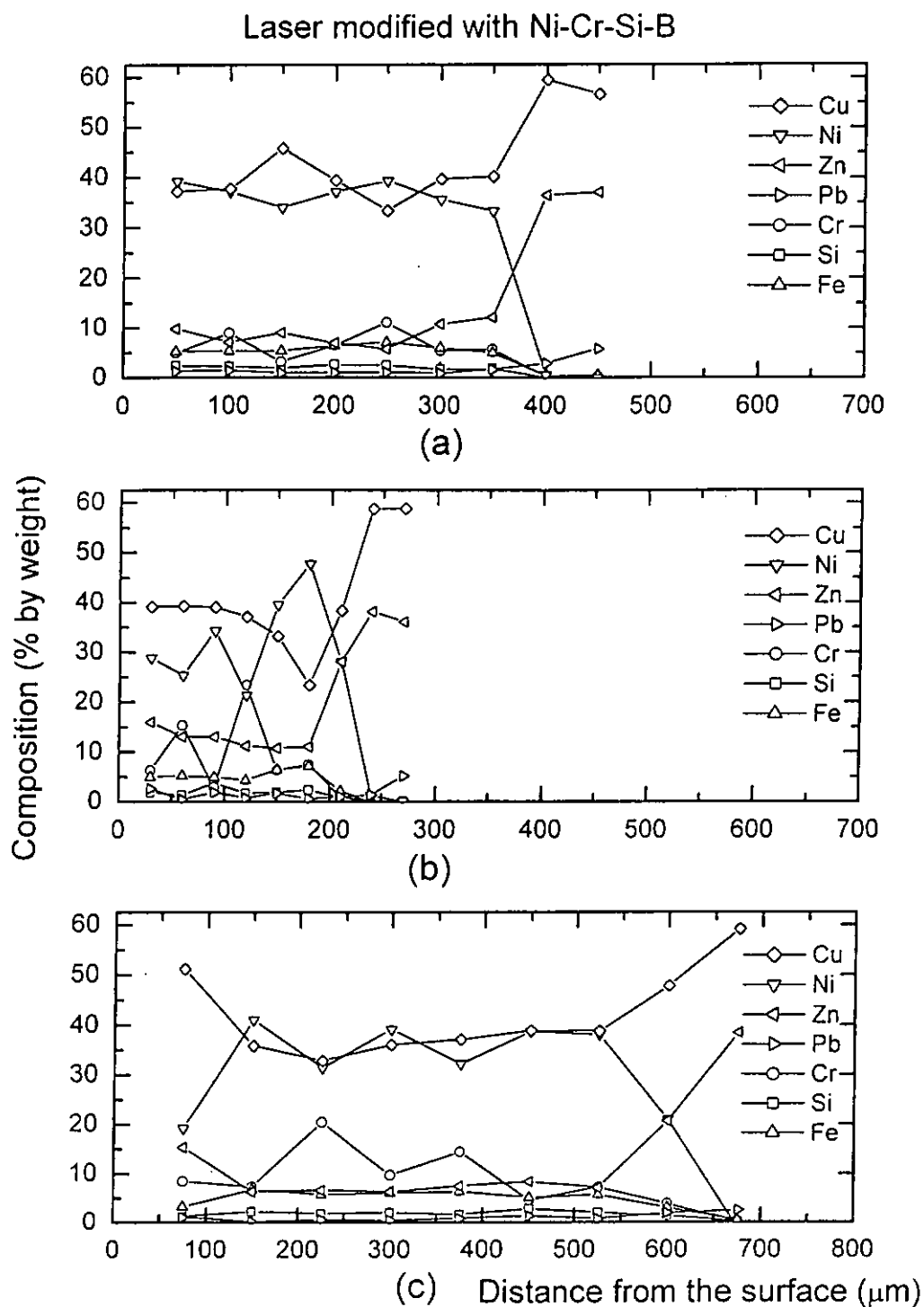


Figure 7. 16 Chemical compositional profiles of various laser surface modified specimens (a) Ni-Cr-Si-B-3, (b) Ni-Cr-Si-B-4 and (c) Ni-Cr-Si-B-5

#### 7.4.5 Cavitation erosion of Ni-Cr-Si-B/brass

Fig. 7. 17, the graph of the cumulative mean depth of penetration (MDP) as a function of time for the as-received brass and modified specimens with different coating thickness, eroded in 3.5% NaCl solution at 23°C. The values of  $R_e$  for the laser surface modified specimen were normalized with respected to the as-received brass as shown in Table 7. 5.

The  $R_e$  of the laser surface modified specimen increased as the preplaced coating thickness increased. The  $R_e$  of specimen Ni-Cr-Si-B-4 was improved about 6 times as compared with that of the as-received brass. For the case of Ni-Cr-Si-B-5 (~ 600 $\mu$ m preplaced coating thickness), the  $R_e$  was improved by 9 times as compared with that of the as-received brass. Fig. 7. 18 is the graph of the normalized value of cavitation erosion resistance  $R_e$  with respect to that of the brass substrate.

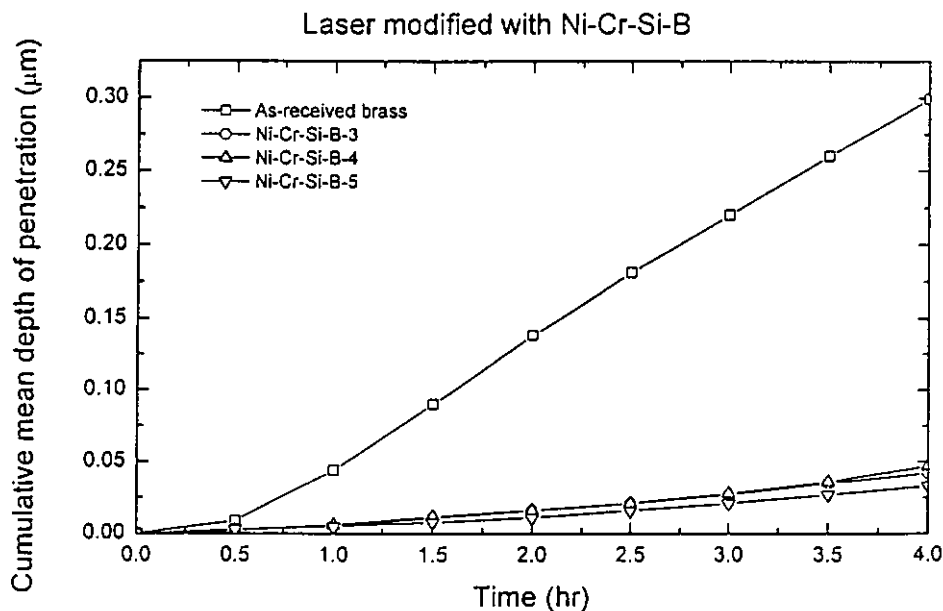


Figure 7. 17 Cumulative MDP as a function of time for the as-received and laser surface modified specimens eroded in 3.5% NaCl solution at 23°C

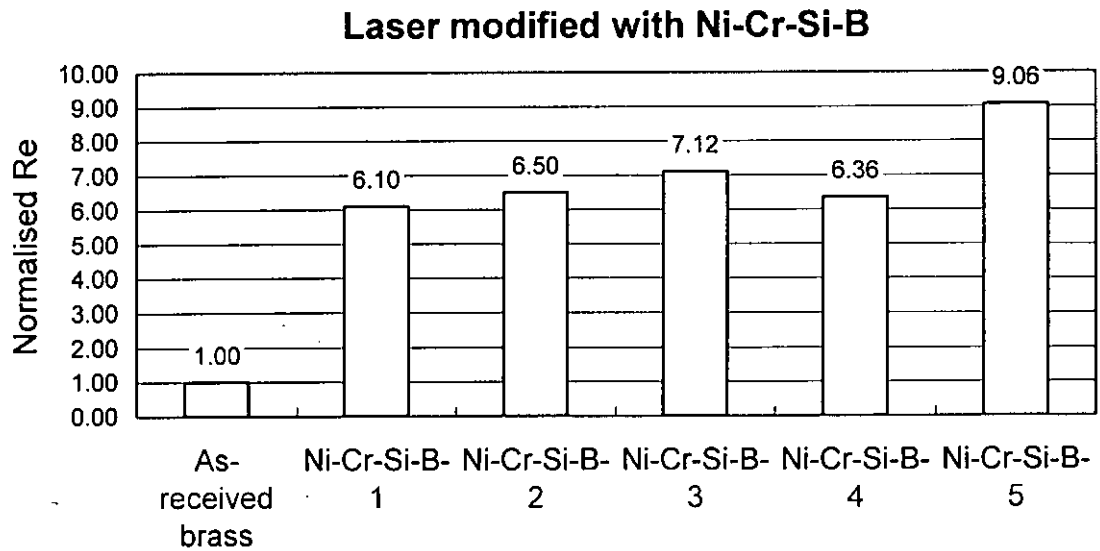


Figure 7. 18 Normalised cavitation erosion resistance of the as-received and laser surface modified specimens with Ni-Cr-Si-B eroded in 3.5% NaCl solution at 23°C

#### 7.4.6 Electrochemical corrosion of Ni-Cr-Si-B/brass

Fig. 7. 19 shows the potentiodynamic polarisation curves of the as-received brass and the various laser surface modified specimens in 3.5% NaCl solution at 23°C. The corrosion potentials of the various specimens were very close to the value of as-received brass. All of the laser surface modified specimens were improved in the pitting corrosion resistance as indicated by shift of the pitting potential in the noble direction. (Table 7.5)

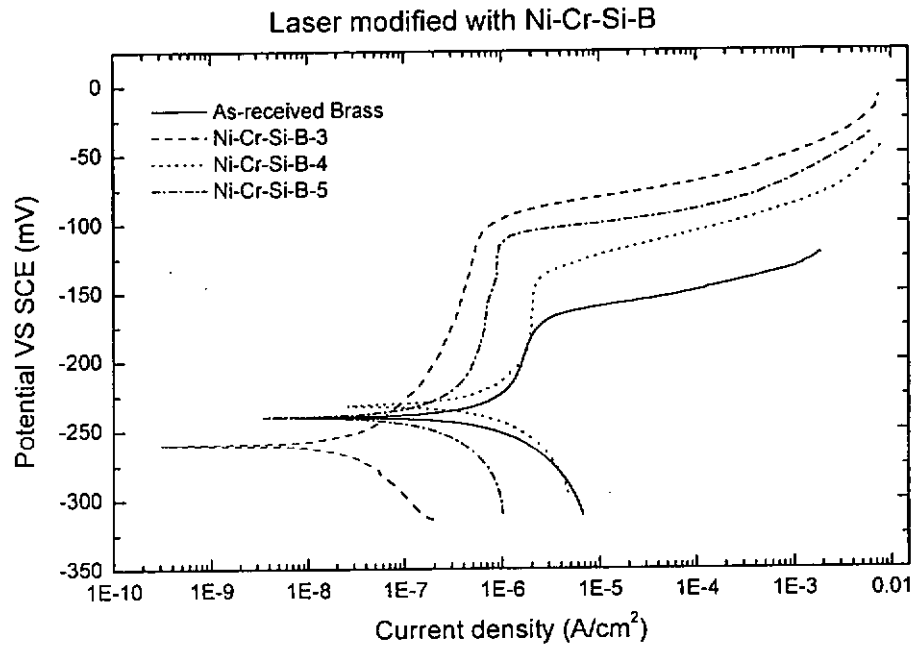


Figure 7.19 Potentiodynamic polarisation curves of the as-received brass and the laser modified specimens in 3.5% NaCl solution at 23°C

The reduction of pitting potential of Ni-Cr-Si-B-5 is due to higher content of Ni, Cr and evenly distributed in the modified layer. The higher amount of Cr content will produce a lot of precipitates, thus reducing the corrosion resistance, while increasing the microhardness and cavitation erosion resistance.

Table 7.5 The average hardness, cavitation resistance and corrosion parameters of as-received and laser surface modified specimens

Specimens	Ave. Hardness (Hv <sub>0.2</sub> )	Re (hμm <sup>-1</sup> )	Normalised Re	Ecorr (mV)	Icorr (μA/cm <sup>2</sup> )	Epit (mV)
As-received brass	110	13.4	1.00	-238.3	1.0	-173
Ni-Cr-Si-B-3	378	95.1	7.12	-262.0	0.09	-112
Ni-Cr-Si-B-4	222	85.0	6.36	-232.0	0.15	-142
Ni-Cr-Si-B-5	502	121.1	9.06	-240.0	0.8	-115

Fig. 7. 20 shows the variation of the normalized  $R_e$  and average hardness with DR.

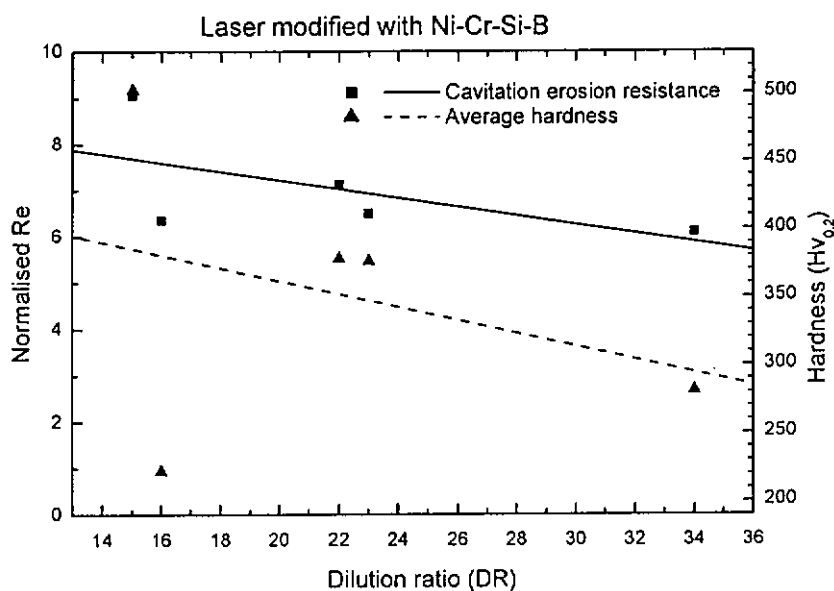


Figure 7.20 Variation of the normalized  $R_e$  and average hardness with DR

## **8 Results and discussions –**

### **Laser surface modification of brass (Cu38%Zn) with Ni-Cr-Si-B-35%WC and Ni-Cr-Fe-20%WC**

#### **8.1 Introduction**

Tungsten carbide (WC) combines high hardness, a low coefficient of thermal expansion, a certain amount of plasticity and good wettability by molten metals. Thus WC is used for producing metal matrix composite containing various volume fraction of WC, for the purpose of improving surface properties by conventional hardfacing techniques such as plasma spraying and thermal spraying etc. The sprayed coating is usually to some extent porous. Although this can be very small with high velocity techniques, it does not provide sufficient bonding to the substrate in many applications because the interfacial bond is formed between a substrate and a liquid droplet.

With the development of high power lasers, the laser surface modification process has been well developed, and can eliminate the disadvantages of the conventional hardfacing processes. Laser surface modification with tungsten carbide metal composite powder has shown high potentiality for enhancing surface properties. For the high energy input of laser surface modification processes, the level of dilution, carbide and precipitation of the brittle phases must be taken into account for consideration of processing parameters. The dissolved WC particles precipitate either as WC in the nickel based alloy or cobalt based alloy melt with a high carbon concentration, or as  $W_2C$  or  $\eta$  phase complex carbides in the melt with a low carbon concentration. Both

W<sub>2</sub>C or  $\eta$  phase carbides are very brittle, and their chemical corrosion resistance and wear resistance are also inferior to that of WC.

## 8.2 Brass (Cu38%Zn) laser surface modified with Ni-Cr-Si-B-35%WC

### 8.2.1 Materials and laser processing parameters

The composition of the coating in the Ni-Cr-Si-B-WC powder was the same as Ni-Cr-Si-B powder used in the Chapter 7 and the composite powder consisted of 30 - 35 wt % of tungsten carbide WC. The coating thickness on brass specimens ranged from ~ 200  $\mu\text{m}$  - ~ 650  $\mu\text{m}$ . The laser power density was varied from 79.5 W/mm<sup>2</sup> - 240.5 W/mm<sup>2</sup> and the scanning speed was set constant at 5 mm/s. The laser surface modification was carried out using a beam diameter of 3 mm or 4 mm. During the laser processing, argon was used as shielding gas to avoid oxidation. The summary of laser processing parameter, the preplaced coating thickness and, the laser treated parameters for brass are shown in Table 8. 1.

Table 8. 1 Laser processing parameters of laser modified brass with Ni-Cr-Si-B-WC alloy powder

Sample	Power density W/mm <sup>2</sup>	Scanning speed mm/s	Coated thickness ( $\mu\text{m}$ )	Shielding Gas (l/min)	Beam Diameter (mm)
Ni-Cr-Si-B-WC-1	141	5	~ 200	15	3
Ni-Cr-Si-B-WC-2	141	5	~ 400	15	3
Ni-Cr-Si-B-WC-3	212	5	~ 300	15	3
Ni-Cr-Si-B-WC-4	212	5	~ 650	15	3
Ni-Cr-Si-B-WC-5	240.5	5	~ 300	15	3
Ni-Cr-Si-B-WC-6	79.5	5	~ 200	15	4
Ni-Cr-Si-B-WC-7	111	5	~ 200	15	4
Ni-Cr-Si-B-WC-8	143	5	~ 200	15	4

### 8.2.2 Microstructural and metallographic analysis

The melt depth and the estimated dilution ratio of the modified specimens are shown in Table 8. 2. The cross-sectional view of the laser surface modified specimens with 3 mm beam diameter are shown in Fig. 8. 1 - Fig. 8. 4.

Ni-Cr-Si-B-WC-1 and Ni-Cr-Si-B-WC-2 were laser modified with same parameters with different coated thickness ( $\sim 200\ \mu\text{m}$  and  $\sim 400\ \mu\text{m}$ ). As shown in Fig. 8. 1 and Fig. 8. 2, the tungsten carbide particles were more evenly distributed in the modified layer of Ni-Cr-Si-B-WC-2, but were concentrated at the bottom of the modified layer in Ni-Cr-Si-B-WC-1. Moreover, the interface of Ni-Cr-Si-B-WC-1 and Ni-Cr-Si-B-WC-2 showed a different contrast (white region) with melt layer. For specimen Ni-Cr-Si-B-WC-3, the microstructure was homogeneous, and revealed a network-like structure in the modified layer in Fig. 8. 3b. The microstructure of Ni-Cr-Si-B-WC-5 was dendritic at the top of the modified layer. In Fig. 8. 4c, the network-like structure was on the right side as in Ni-Cr-Si-B-WC-3 and the tungsten carbides were partially dissociated and combined with alloying element to form the mixed carbide,  $(\text{W}, \text{Cr}, \text{Ni}, \text{Fe})_x\text{C}_y$  in the metal matrix.

For the specimens treated with 4 mm beam diameter, the melt depth increased as the laser power densities increased. The cross-sectional view of specimen Ni-Cr-Si-B-WC-6 and Ni-Cr-Si-B-WC-7 are shown in Fig. 8. 5 and Fig. 8. 6, respectively.

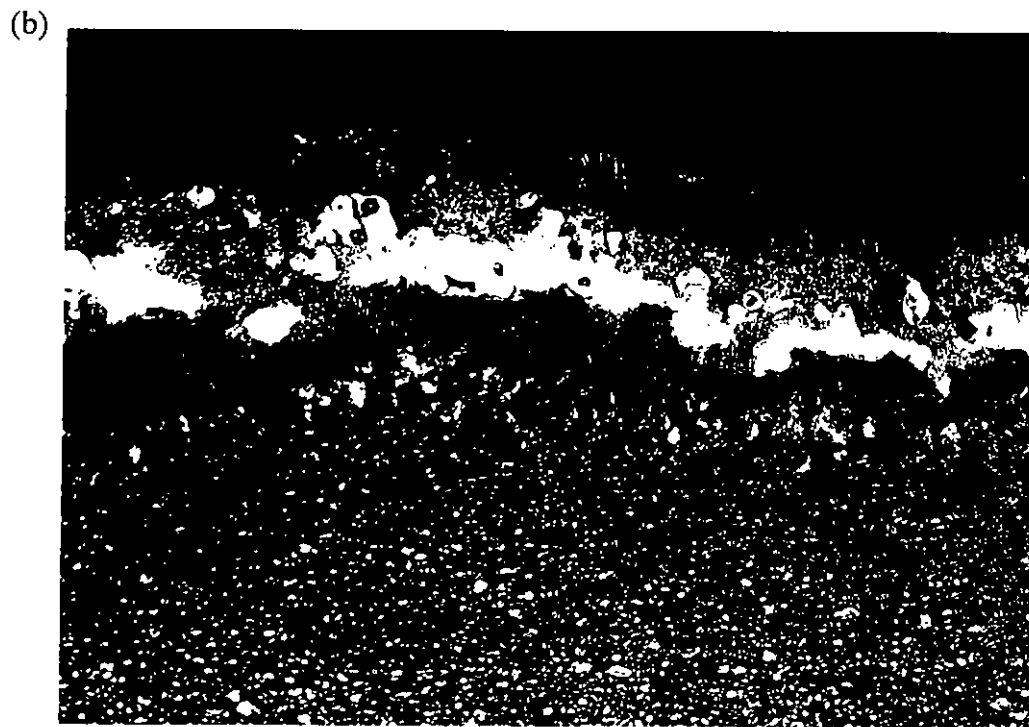


Table 8.2 Summary of coating thickness, melt depth and estimated dilution ratio of brass specimens laser surface modified with Ni-Cr-Si-B-WC

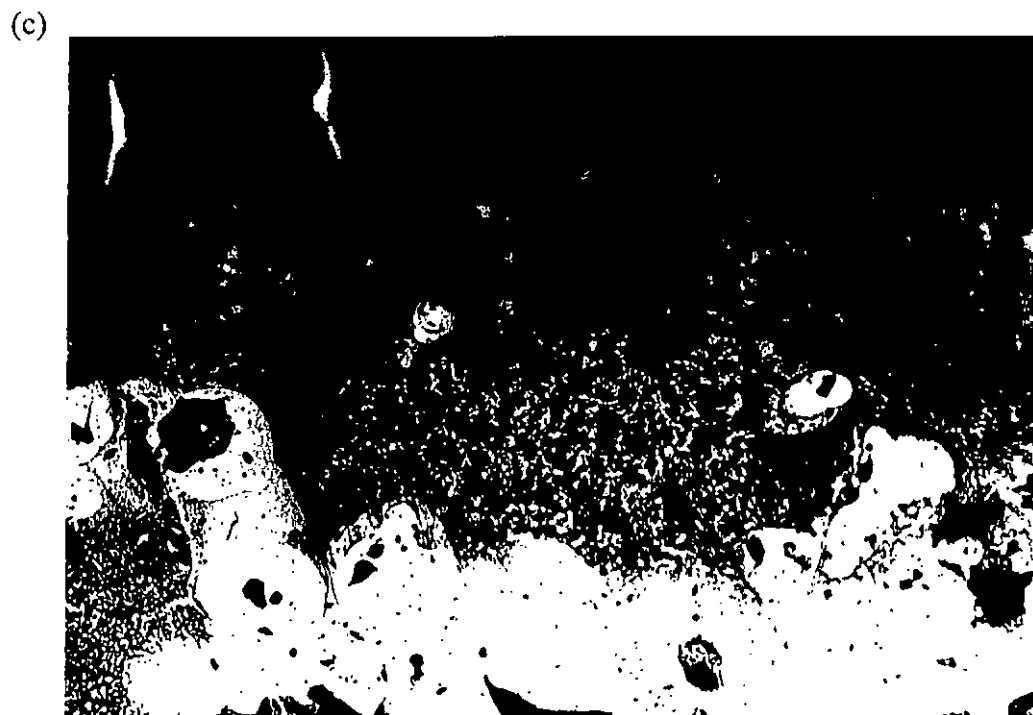
Specimen	Coated thickness	Melt depth	Dilution ratio (DR)
Ni-Cr-Si-B-WC-1	~ 200 $\mu\text{m}$	234.5 $\mu\text{m}$	14.7%
Ni-Cr-Si-B-WC-2	~ 400 $\mu\text{m}$	459.2 $\mu\text{m}$	12.9%
Ni-Cr-Si-B-WC-3	~ 300 $\mu\text{m}$	340.9 $\mu\text{m}$	12%
Ni-Cr-Si-B-WC-4	~ 650 $\mu\text{m}$	718.2 $\mu\text{m}$	9.5%
Ni-Cr-Si-B-WC-5	~ 300 $\mu\text{m}$	355.9 $\mu\text{m}$	15.7%
Ni-Cr-Si-B-WC-6	~ 200 $\mu\text{m}$	200.8 $\mu\text{m}$	0.4%
Ni-Cr-Si-B-WC-7	~ 200 $\mu\text{m}$	243.5 $\mu\text{m}$	17.9%
Ni-Cr-Si-B-WC-8	~ 200 $\mu\text{m}$	412.9 $\mu\text{m}$	52.6%



200  $\mu\text{m}$  ———



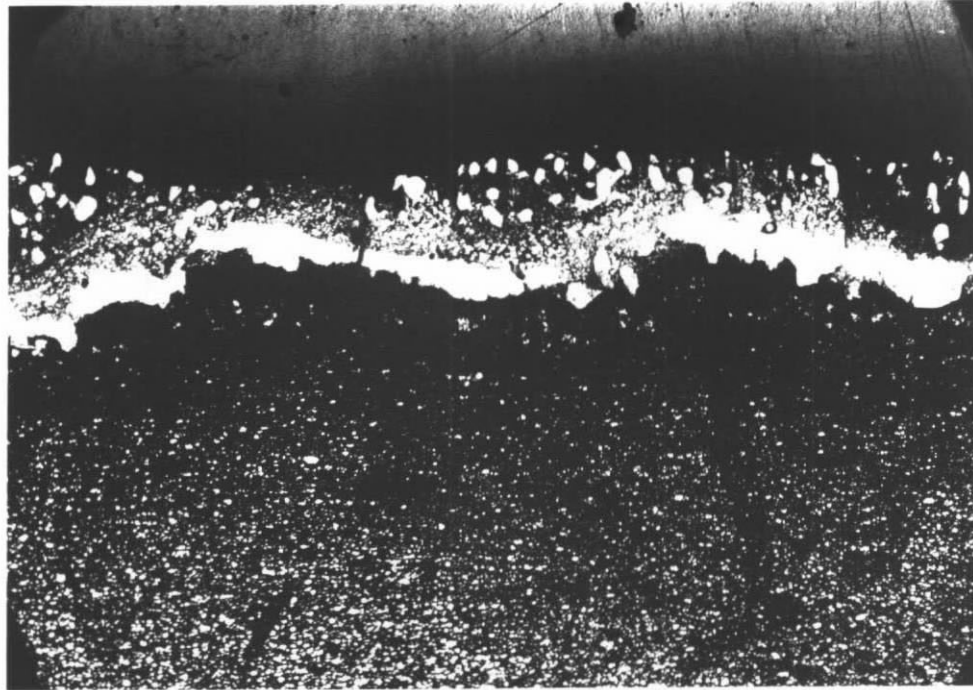
100  $\mu\text{m}$  ———



20  $\mu\text{m}$  ———

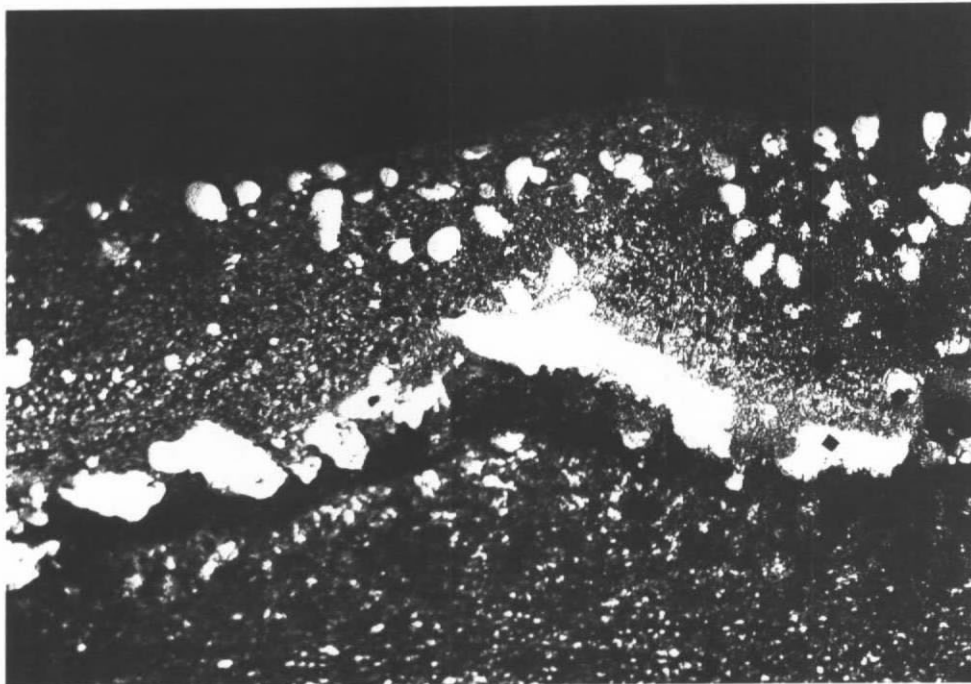
Figure 8. 1 Microstructure of Ni-Cr-Si-B-WC-1 (a) melt layer 50 $\times$ , (b) 100 $\times$  and (c) 400 $\times$

(a)



200  $\mu\text{m}$  ———

(b)



100  $\mu\text{m}$  ———

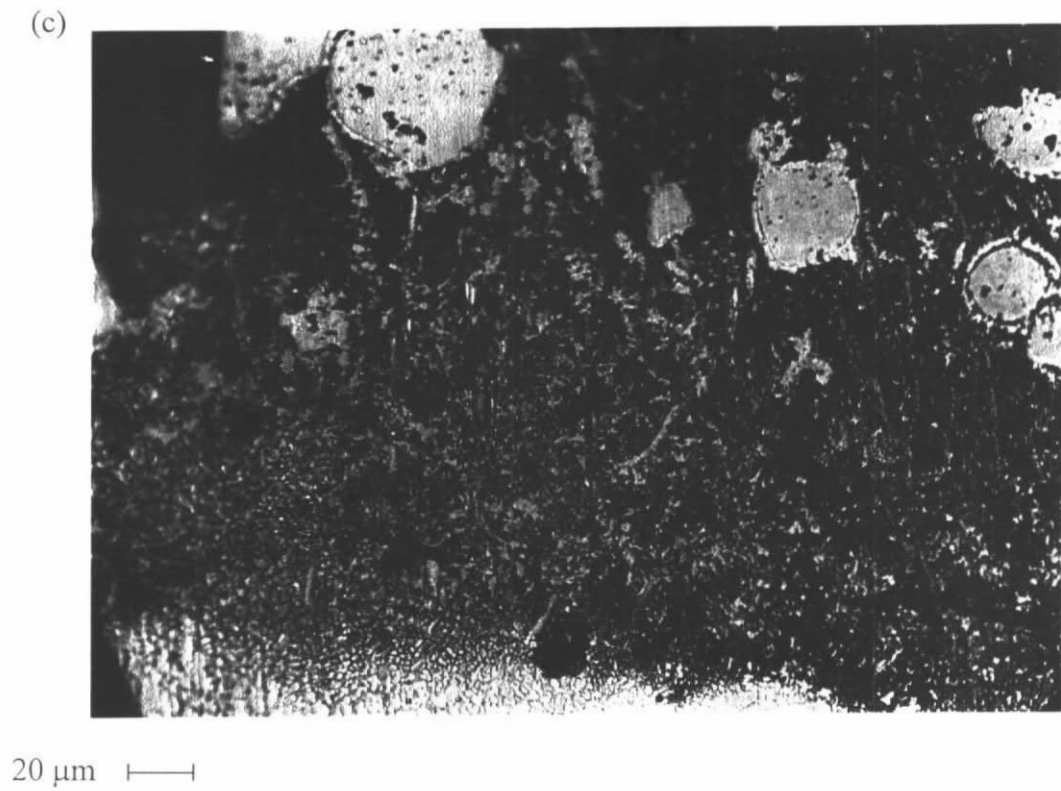
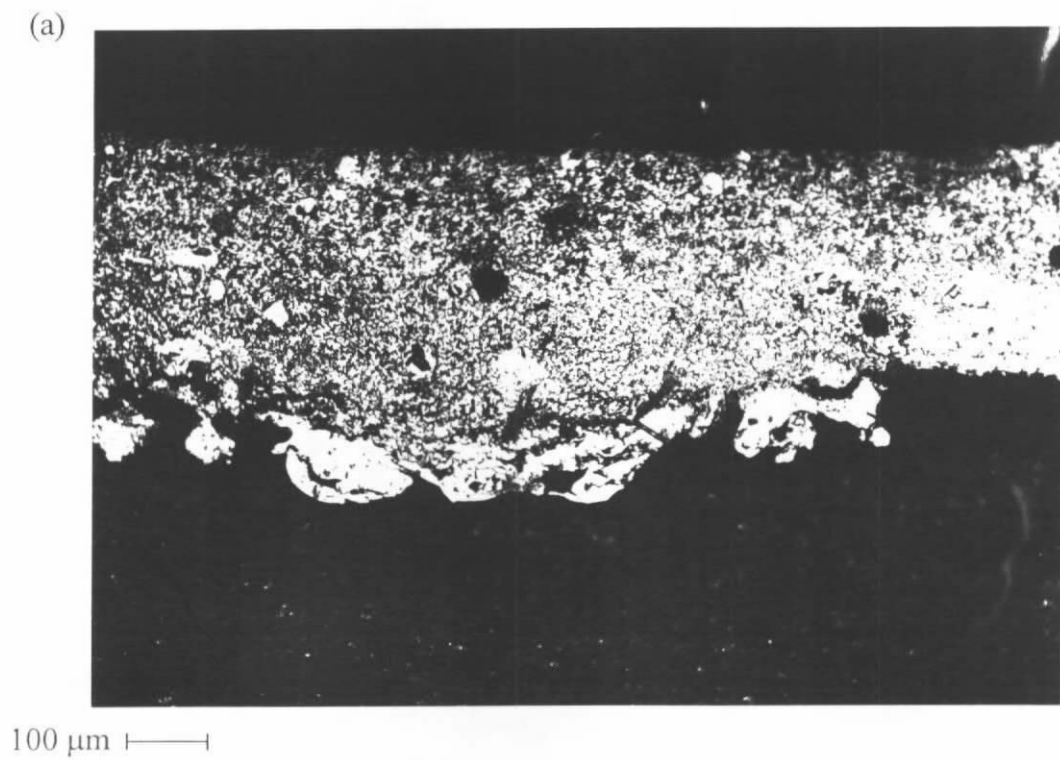
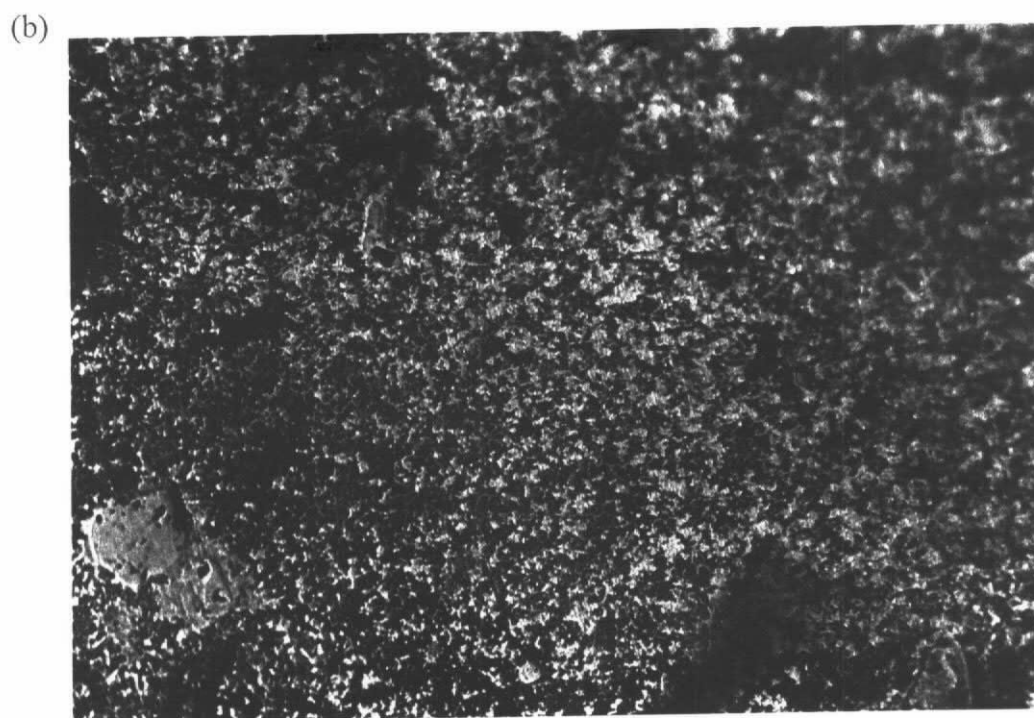


Figure 8. 2 Microstructure of Ni-Cr-Si-B-WC-2 (a) melt layer 50 $\times$ , (b) 100 $\times$  and (c) 400 $\times$

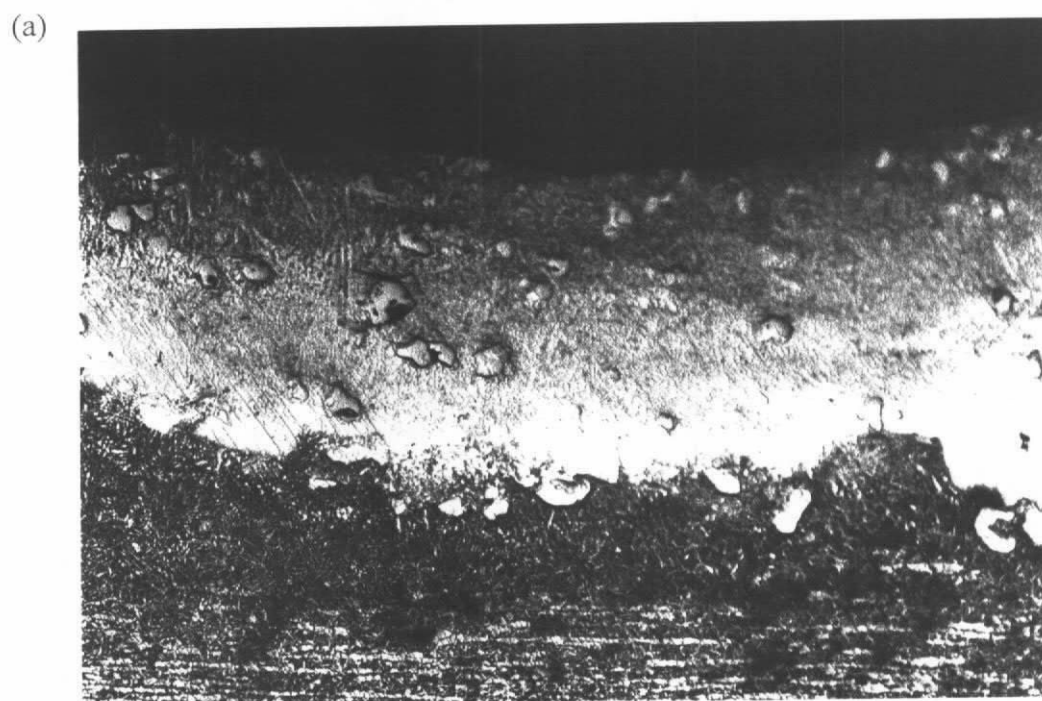






20  $\mu\text{m}$  —|—

Figure 8. 3 Microstructure of Ni-Cr-Si-B-WC-3 (a) melt layer 100 $\times$  and (b) 400 $\times$



100  $\mu\text{m}$  —|—

(b)



20  $\mu\text{m}$  

(c)



20  $\mu\text{m}$  

Figure 8. 4 Microstructure of Ni-Cr-Si-B-WC-5 (a) melt layer 100 $\times$  (b) 400 $\times$  and (c) 400 $\times$

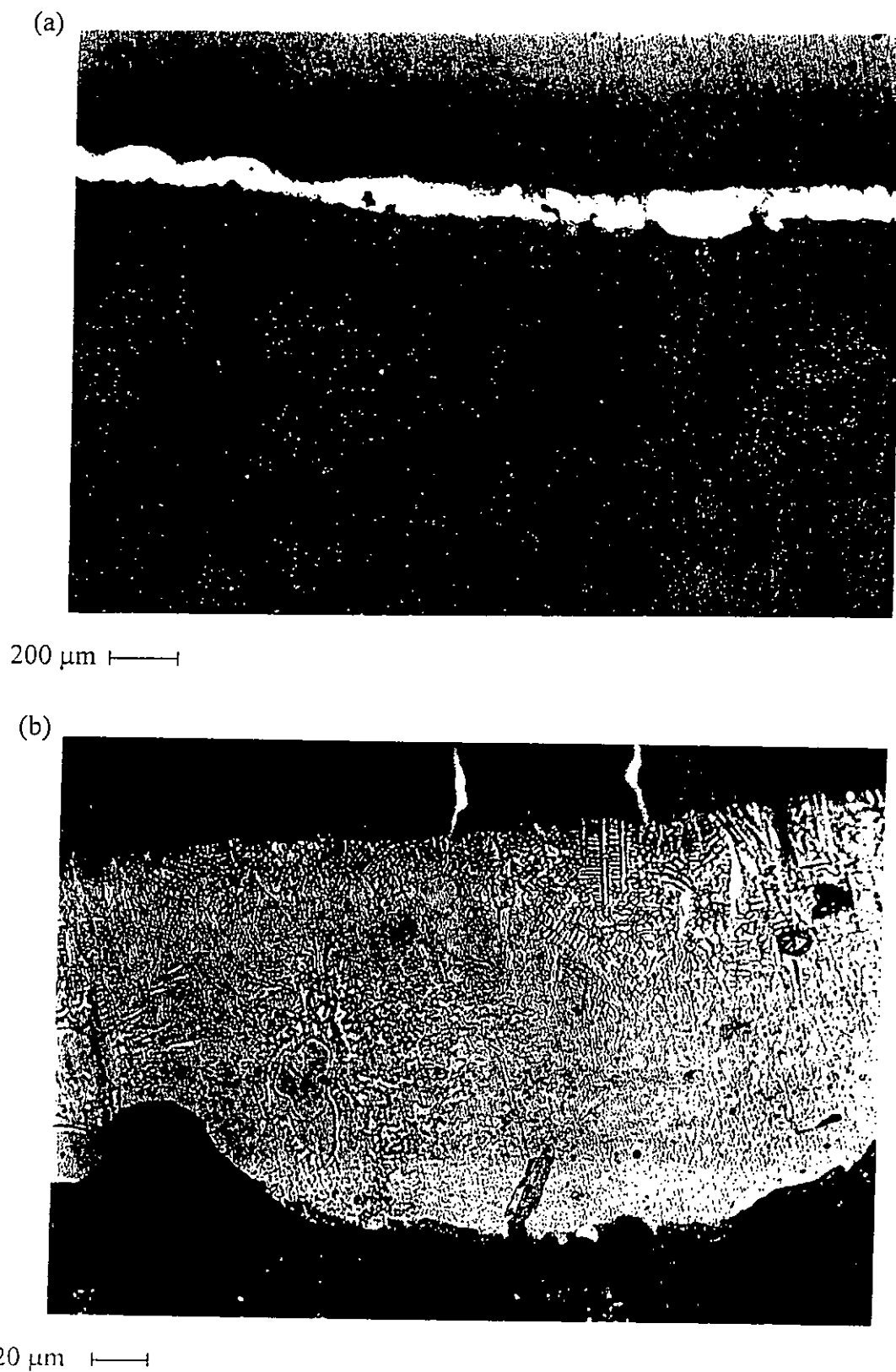


Figure 8. 5 Microstructure of Ni-Cr-Si-B-WC-6 (a) melt layer 50 $\times$  and (b) 400 $\times$



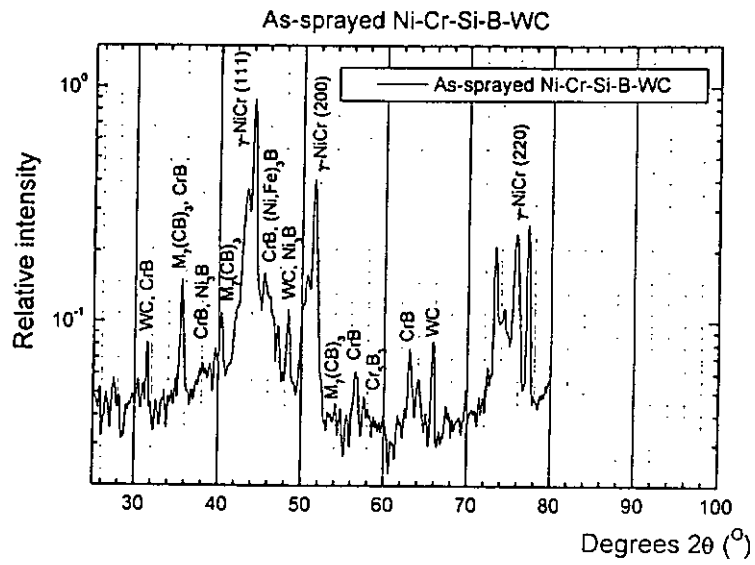
Figure 8. 6 Microstructure of Ni-Cr-Si-B-WC-7 (a) melt layer 50×

### 8.2.3 X-ray diffraction analysis of Ni-Cr-Si-B-WC/brass

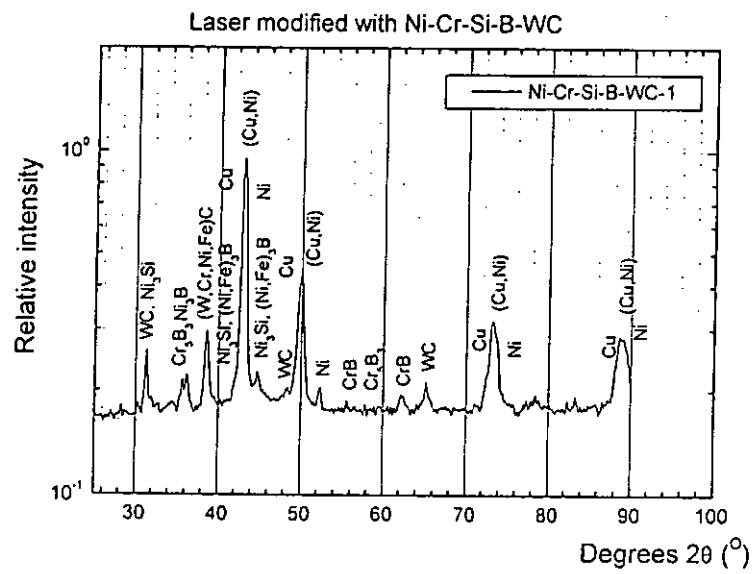
The X-ray spectrum of the as-sprayed Ni-Cr-Si-B-WC coating and the laser surface modified specimens are shown in Fig. 8. 7. According to the spectra, the as-sprayed coating was similar as the Ni-Cr-Si-B alloy powder discuss in Chapter 7, together with WC.

The specimens laser surface modified with Ni-Cr-Si-B-WC were mainly composed of Cu, Ni and (Cu,Ni), retained WC and (W, Cr, Ni, Fe)C, and several secondary phases such as,  $\text{Ni}_3\text{B}$ ,  $\text{Ni}_3\text{Si}$ ,  $\text{Fe}_3\text{B}$ ,  $\text{CrB}$ ,  $\text{Cr}_5\text{B}_3$ .

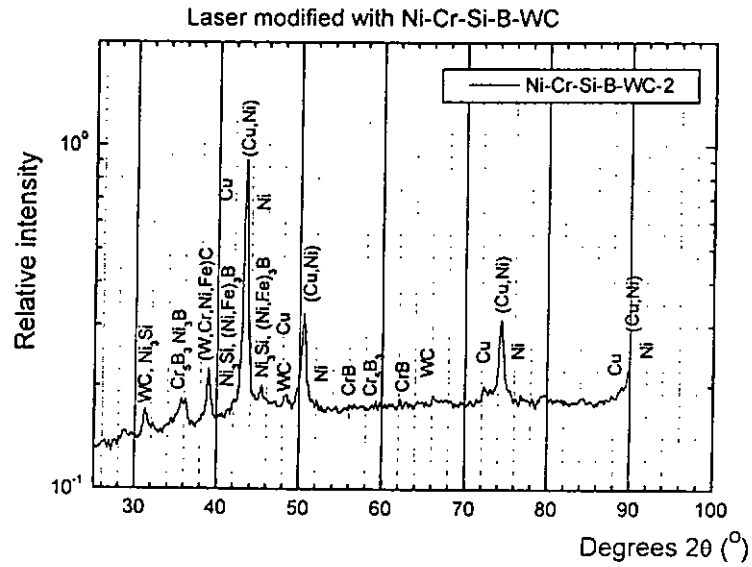




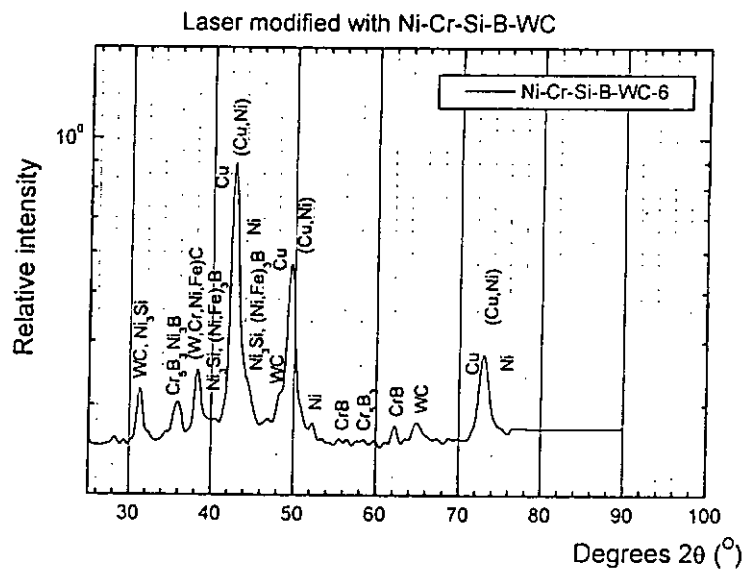
(a)



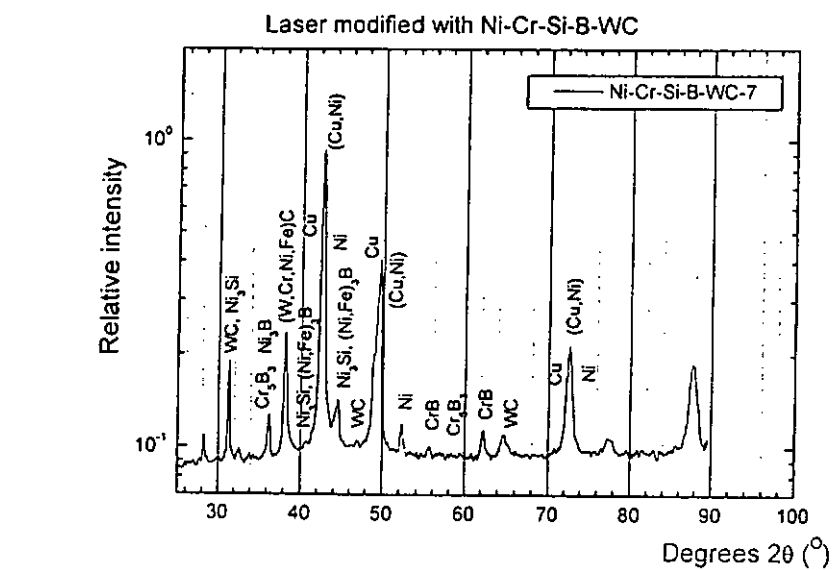
(b)



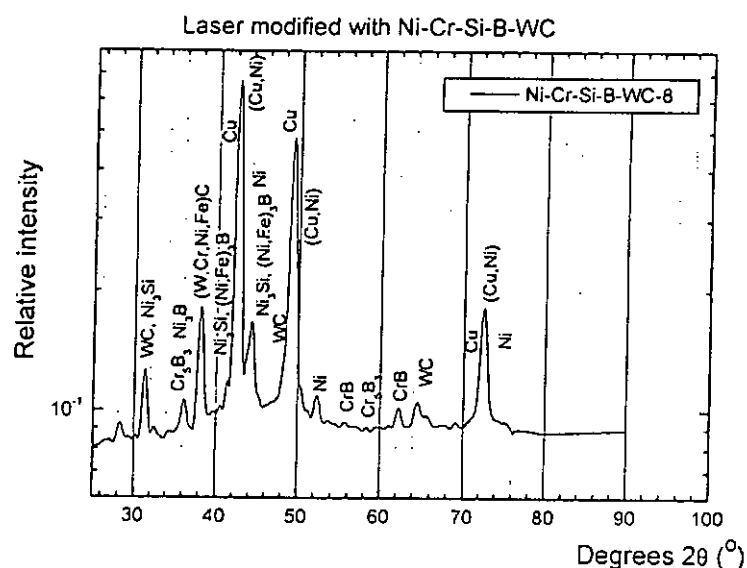
(c)



(d)



(e)



(f)

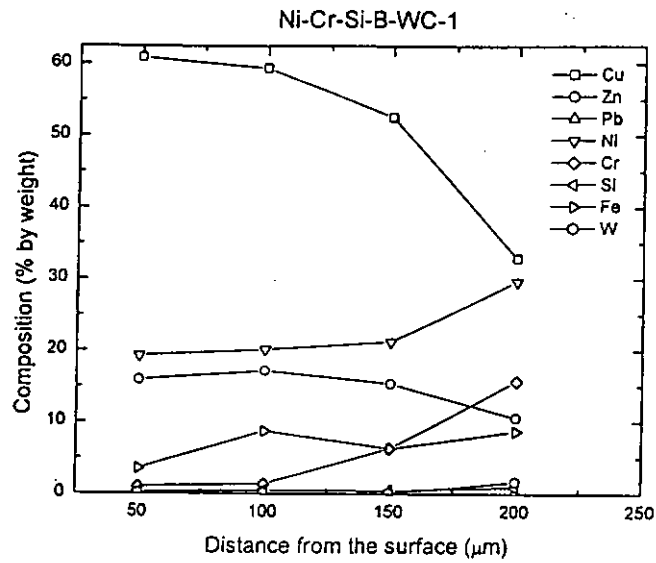
Figure 8. 7 X-ray diffraction spectra of (a) as-sprayed Ni-Cr-Si-B-WC, (b) Ni-Cr-Si-B-WC-1, (c) Ni-Cr-Si-B-WC-2, (d) Ni-Cr-Si-B-WC-6, (e) Ni-Cr-Si-B-WC-7 and (f) Ni-Cr-Si-B-WC-8

#### 8.2.4 Compositional profiles of Ni-Cr-Si-B-WC/brass

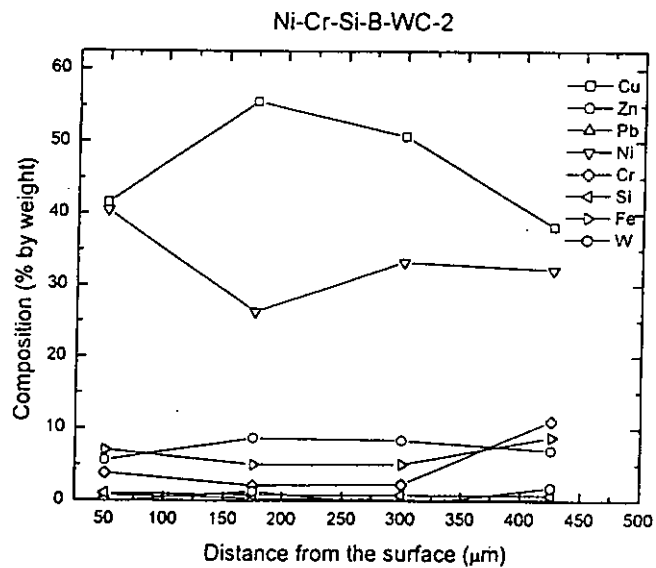
The compositional profiles of the specimens modified with Ni-Cr-Si-B-WC along the depth are shown in Fig. 8. 8. For specimens Ni-Cr-Si-B-WC-1 and Ni-Cr-Si-B-WC-2, the composition along the depth was homogeneous and the nickel content increased as the preplaced coating thickness increased. However, the chromium content rose from the surface to a maximum value at the interface between the melt layer and the brass substrate (transition zone).

According to the results, specimens Ni-Cr-Si-B-WC-3 and Ni-Cr-Si-B-WC-4 were mainly nickel with a high chromium content. Ni-Cr-Si-B-WC-4 was more homogeneous, and also the chromium content was concentrated at the transition zone as in Ni-Cr-Si-B-WC-1 and Ni-Cr-Si-B-WC-2. The compositional profile of specimen Ni-Cr-Si-B-WC-5 was similar to that of Ni-Cr-Si-B-WC-2.

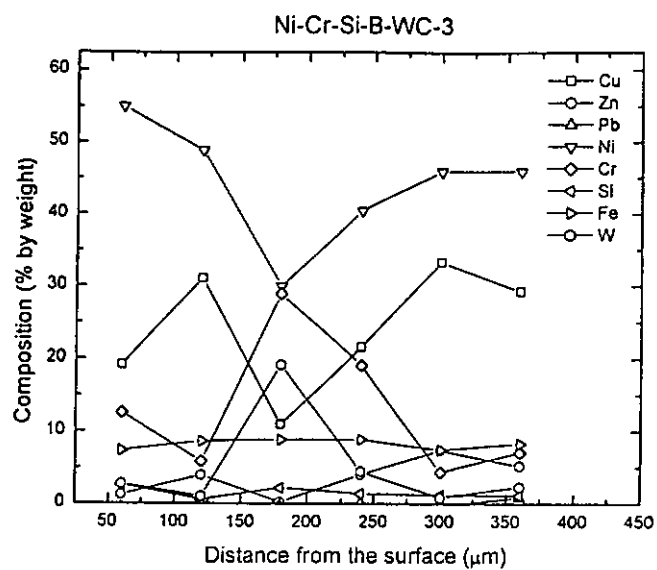
At lower power density in specimens Ni-Cr-Si-B-WC-6, Ni-Cr-Si-B-WC-7 and Ni-Cr-Si-B-WC-8, the distribution of the elements was not homogeneous, also with high chromium content in the transition zone.



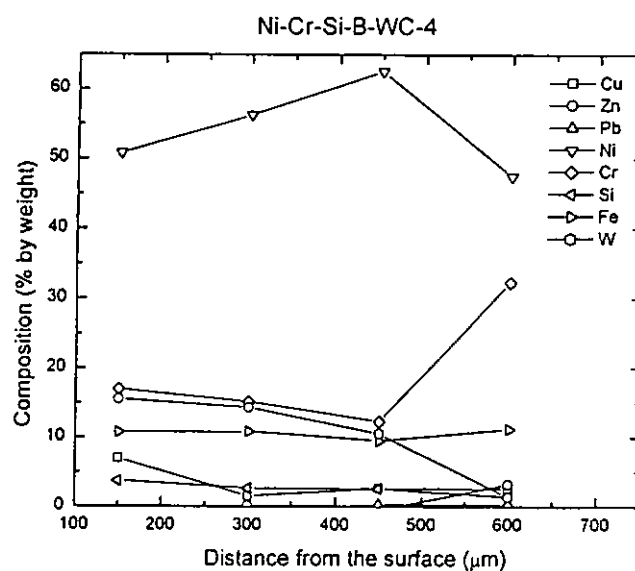
(a)



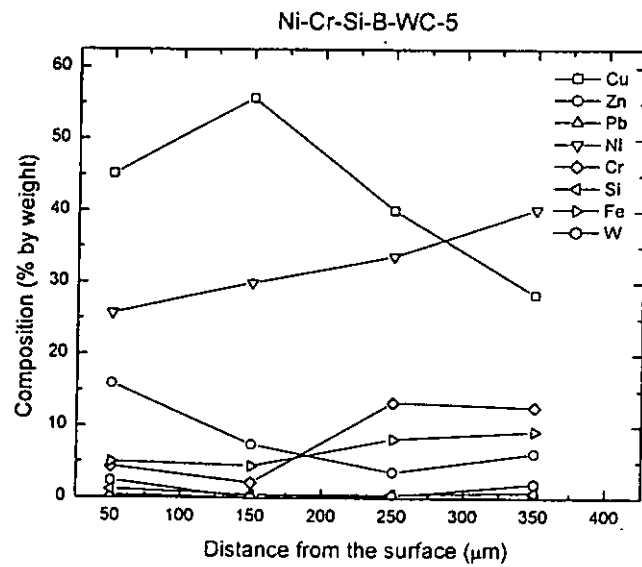
(b)



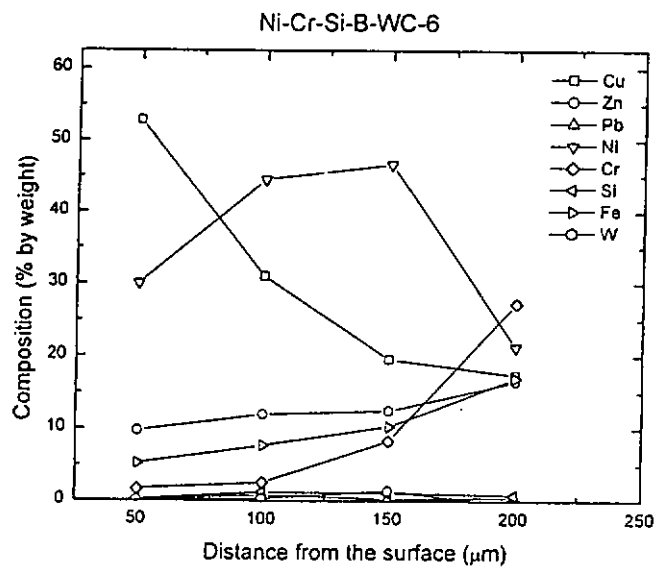
(c)



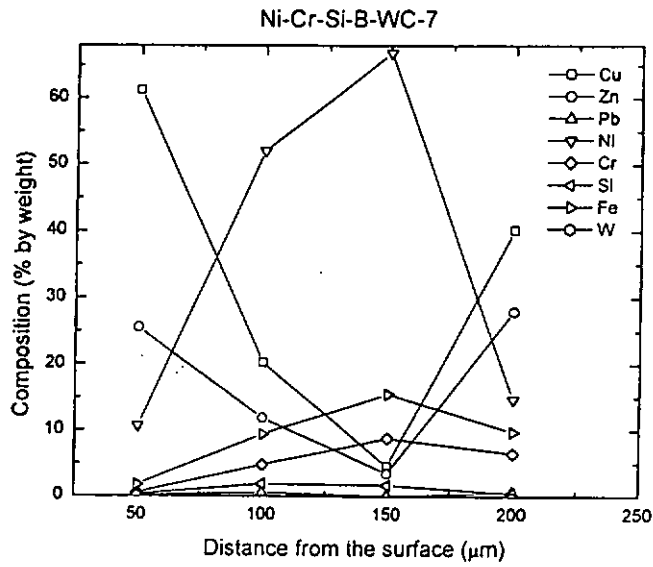
(d)



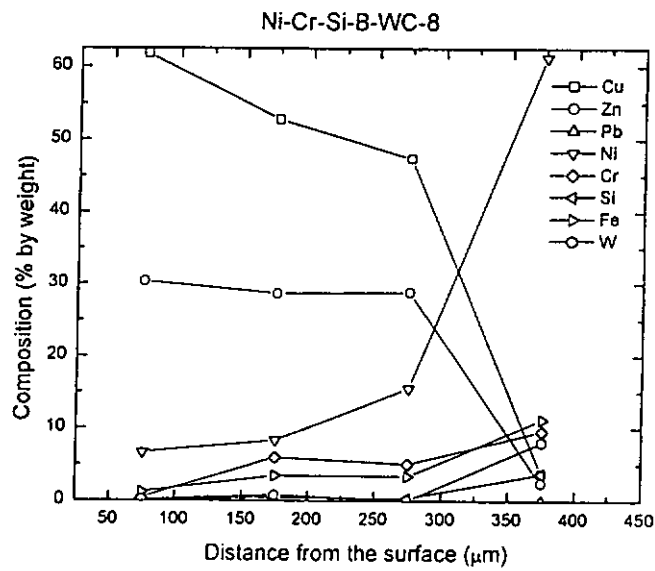
(e)



(f)



(g)



(h)

Figure 8. 8 Chemical compositional profiles of various laser surface modified specimens (a) Ni-Cr-Si-B-WC-1, (b) Ni-Cr-Si-B-WC-2, (c) Ni-Cr-Si-B-WC-3, (d) Ni-Cr-Si-B-WC-4, (e) Ni-Cr-Si-B-WC-5, (f) Ni-Cr-Si-B-WC-6, (g) Ni-Cr-Si-B-WC-7 and (h) Ni-Cr-Si-B-WC-8



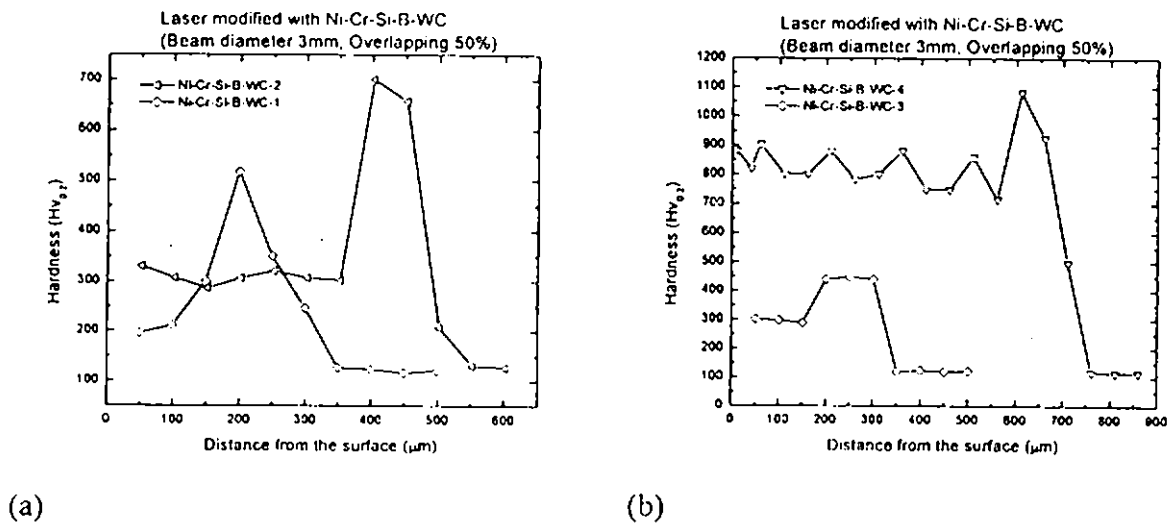
### 8.2.5 Hardness profiles of Ni-Cr-Si-B-WC/brass

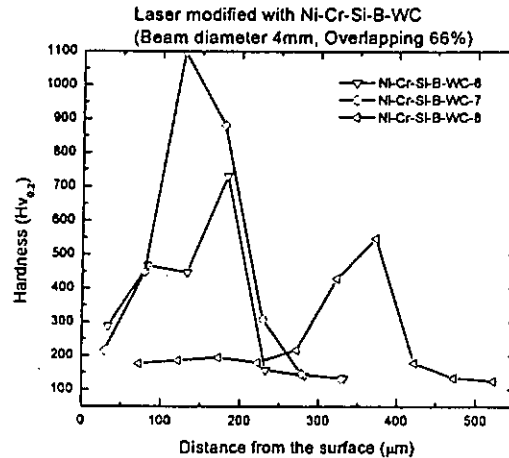
The hardness profiles in brass specimens laser modified with Ni-Cr-Si-B-WC are shown in Fig. 8. 9. The hardness rose from the treated surface to a maximum, which was near to the interface between the melt region and the brass substrate. The irregular hardness in specimen Ni-Cr-Si-B-WC-4 was due to the indentation positioned on the tungsten carbide particle. The microstructure of the transition zone (white region) was definitely different with the microstructure of surface region (black region) and also the brass substrate. Below the transition zone, the hardness fell to the value of the brass substrate. According to the result of the compositional profiles of the specimen modified with Ni-Cr-Si-B-WC, the higher hardness in the transition region was attributed to the higher chromium there.

Specimens Ni-Cr-Si-B-WC-1 and Ni-Cr-Si-B-WC-2, which were treated with the same laser processing parameters, (the laser power density  $141 \text{ W/mm}^2$  and the scanning speed  $5 \text{ mm/s}$ ), but with different preplaced coating thickness ( $\sim 200 \text{ }\mu\text{m}$  and  $\sim 400 \text{ }\mu\text{m}$ , respectively). The hardness of Ni-Cr-Si-B-WC-2 was higher than that of Ni-Cr-Si-B-WC-1 in both the surface and the transition region, by about  $100 \text{ Hv}_{0.2}$ , probably due to a smaller dilution ratio.

In addition, specimen Ni-Cr-Si-B-WC-3 and Ni-Cr-Si-B-WC-4 had also different preplaced coating thickness, ( $\sim 300 \text{ }\mu\text{m}$  and  $\sim 650 \text{ }\mu\text{m}$ , respectively). The result was the same as the Ni-Cr-Si-B-WC-1 and Ni-Cr-Si-B-WC-2. The hardness increased as the dilution ratio decreased. The highest hardness was obtained by Ni-Cr-Si-B-WC-4 and with least fluctuation.

The laser power densities were varied from 79.5 to 143 W/mm<sup>2</sup>, with constant scanning speed 5mm/s and beam diameter 4 mm, in treating Ni-Cr-Si-B-WC-6, Ni-Cr-Si-B-WC-7 and Ni-Cr-Si-B-WC-8. All of the specimens were preplaced with about 200  $\mu$ m coating thickness. According to the result, the hardness profiles of Ni-Cr-Si-B-WC-6 and Ni-Cr-Si-B-WC-7 were similar (the point of highest hardness of Ni-Cr-Si-B-WC-7 was positioned on tungsten carbide particle). For specimen Ni-Cr-Si-B-WC-8, the hardness profile was reduced to a relatively low level due to the highest dilution ratio in the range of present study. The result of the average hardness for all specimens modified with Ni-Cr-Si-B-WC is shown in Table 8. 3.





(c)

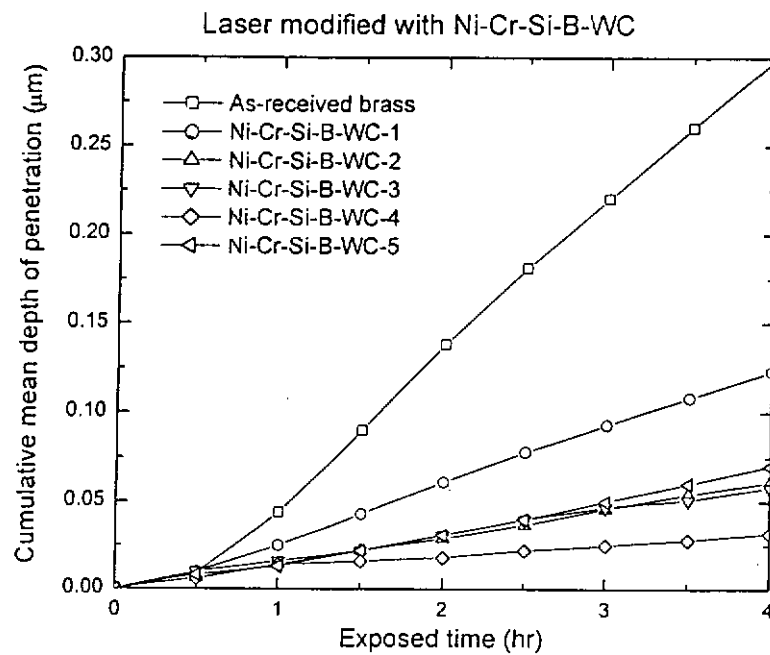
Figure 8.9 Hardness profiles along the melt depth of the cross section of laser surface modified specimens

#### 8.2.6 Cavitation erosion of Ni-Cr-Si-B-WC/brass

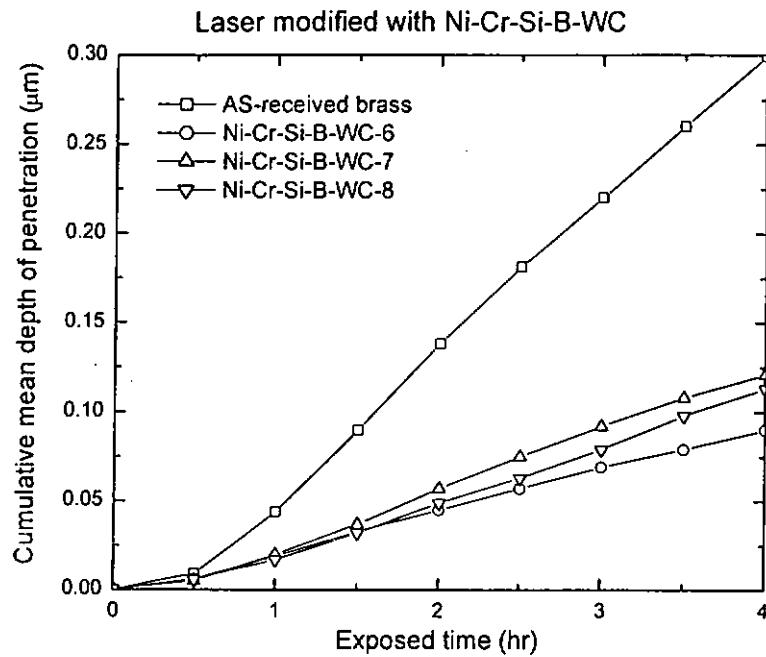
The cumulative mean depth of penetration of the as-received brass and specimens laser modified with Ni-Cr-Si-B-WC cavitared in 3.5% NaCl solution at 23°C is plotted against time in Fig. 8. 10 (a) and (b). The cavitation erosion resistance of all the laser modified specimen was improved by at least 2 times as compared with that of the brass substrate.

For the pairs of specimens Ni-Cr-Si-B-WC-1 and Ni-Cr-Si-B-WC-2, Ni-Cr-Si-B-WC-3 and Ni-Cr-Si-B-WC-4, the cavitation erosion resistance doubled that of the counterpart under the same laser processing parameters. The normalised cavitation erosion resistance of these specimens was 2.4 and 4.9, 5.2 and 9.3, respectively. The improvement of the cavitation erosion resistance was attributed to the hardness of the modified layer.

Ni-Cr-Si-B-WC-2, Ni-Cr-Si-B-WC-3 and Ni-Cr-Si-B-WC-5 were treated with different power densities at same scanning speed (coating thickness  $\sim 300 \mu\text{m}$ ). According to the results, there was no significant effect on the cavitation erosion resistance of the modified specimens in the range studied. Moreover, specimen Ni-Cr-Si-B-WC-6, Ni-Cr-Si-B-WC-7 and Ni-Cr-Si-B-WC-8 had similar results. The  $R_e$  of specimens Ni-Cr-Si-B-WC was improved by about 3.3, 2.5 and 2.6 times as compared with that of the as-received brass substrate. The  $R_e$  values of the various laser alloyed specimens are normalised with respect to that the as-received brass and shown in Fig. 8. 11 and Table 8. 3.



(a)



(b)

Figure 8. 10 Cumulative MDP as a function of time for the as-received and laser surface modified specimens eroded in 3.5% NaCl solution at 23°C

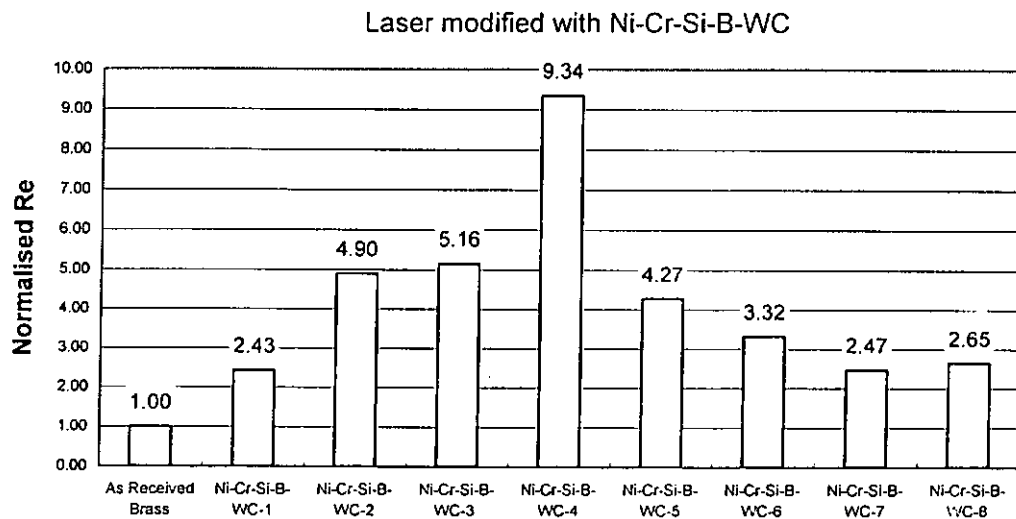


Figure 8. 11 Normalised cavitation erosion resistance of the as-received brass and laser surface modified specimens eroded in 3.5% NaCl solution at 23°C

### 8.2.7 Electrochemical corrosion of Ni-Cr-Si-B-WC/brass

The potentiodynamic polarisation curves of the as-received brass and the various specimens laser modified with Ni-Cr-Si-B-WC in 3.5% NaCl solution at 23°C are shown in Fig. 8. 12. The corrosion potentials of the various specimens were very close to the value of as-received brass. The corrosion resistance of the modified specimens deteriorated as indicated by the increase in the current density. For specimen Ni-Cr-Si-B-WC-3, the polarization curve was close to that of the brass substrate. The pitting potential was -188 mV, which was slightly lower than that of brass. On the other hand, the pitting potential of specimen Ni-Cr-Si-B-WC-5 was increased significantly, to a value of -152 mV, indicating that it was more resistant to pitting corrosion. Moreover, the corrosion current density was reduced by about an order compared with that of the as-received brass. Thus Ni-Cr-Si-B-WC-5 had the highest corrosion resistance among the specimens studied in this chapter. The corresponding corrosion parameters of the various specimens are summarized in Table 8. 3.

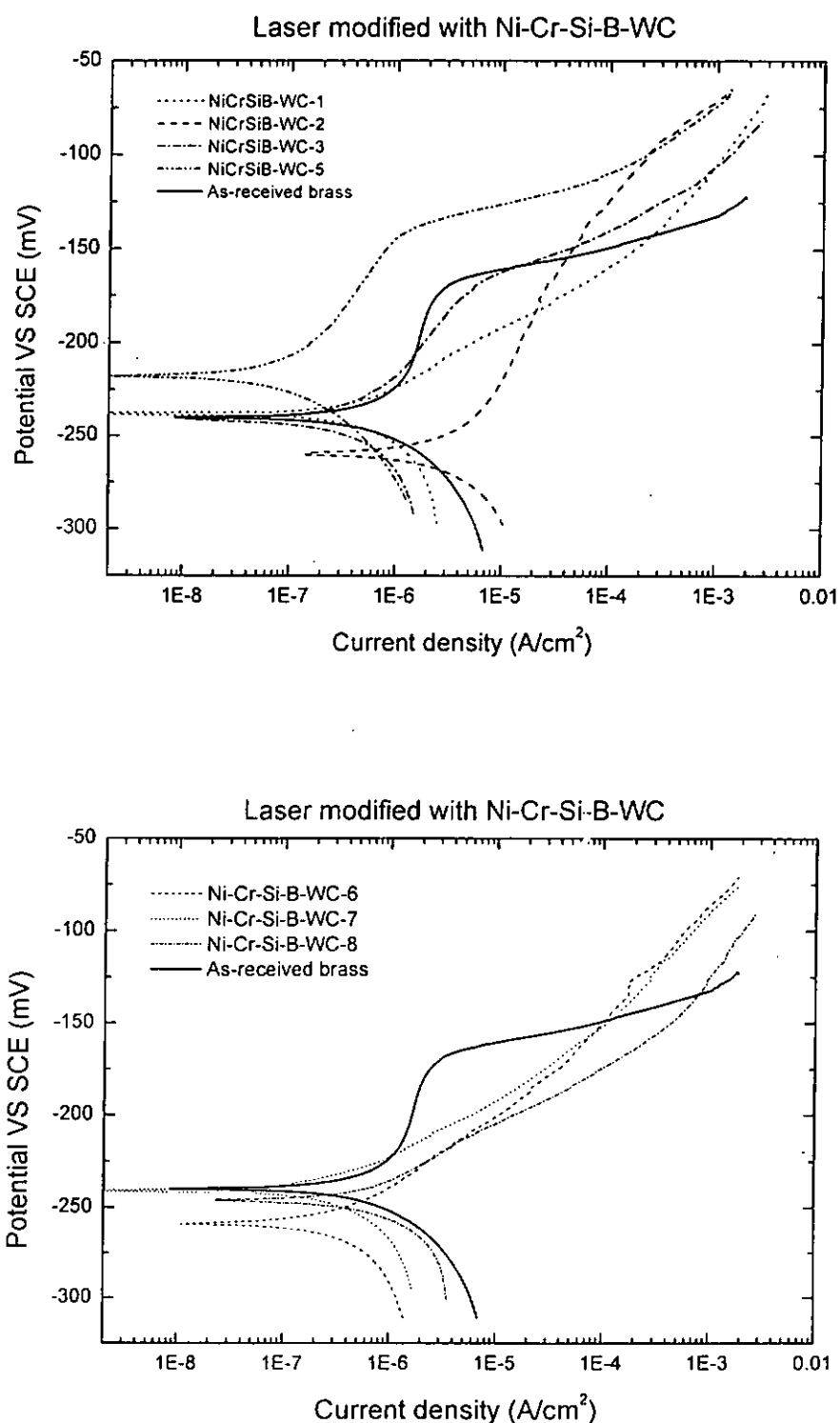


Figure 8. 12 Potentiodynamic polarisation curves of the as-received brass and the laser modified specimens in 3.5% NaCl solution at 23°C

Table 8.3 The average hardness, cavitation erosion resistance and corrosion parameters of as-received and laser surface modified specimens

Specimen	Ave. hardness (Hv <sub>0.2</sub> )	R <sub>e</sub> (h/μm)	Normalised R <sub>e</sub>	E <sub>corr</sub> (mV)	I <sub>corr</sub> (μA/cm <sup>2</sup> )	E <sub>pit</sub> (mV)
As-received brass	110.00	13.4	1.00	-238.3	1.0	-173
Ni-Cr-Si-B-WC-1	315.51	32.48	2.4	-238	12.5	/
Ni-Cr-Si-B-WC-2	372.80	65.51	4.9	-259	0.35	-159
Ni-Cr-Si-B-WC-3	/	68.90	5.2	-241	0.3	-188
Ni-Cr-Si-B-WC-4	780.60	124.87	9.3	/	/	/
Ni-Cr-Si-B-WC-5	334.80	57.08	4.3	-218	0.09	-152
Ni-Cr-Si-B-WC-6	419.20	44.40	3.3	-259	0.25	/
Ni-Cr-Si-B-WC-7	590.87	33.02	2.5	-241	0.2	/
Ni-Cr-Si-B-WC-8	264.65	35.36	2.6	-246	0.45	/

Fig. 8. 13 shows the variation of the normalised R<sub>e</sub> and average hardness with DR.

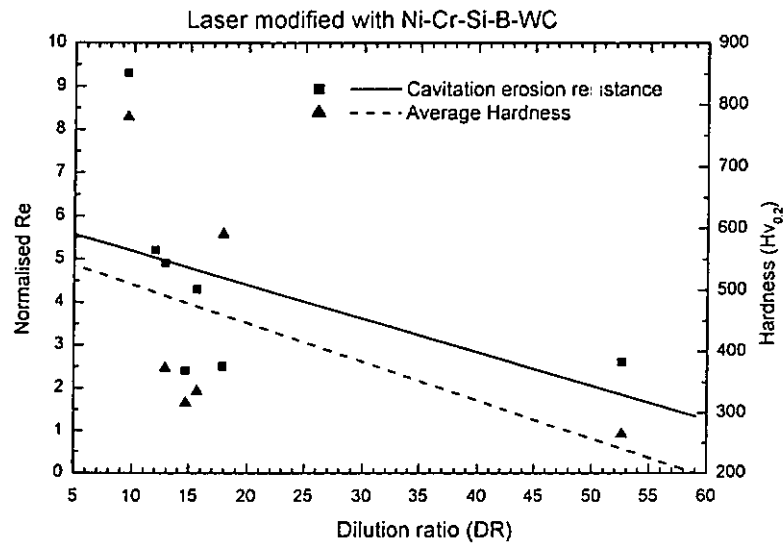


Figure 8. 13 Variation of the normalized R<sub>e</sub> and average hardness with DR



### 8.2.8 Cavitation damage mechanism of Ni-Cr-Si-B-WC/brass

Fig. 8. 14 and Fig. 8. 15 shows the appearance of the damaged surface of specimen Ni-Cr-Si-B-WC-2 and Ni-Cr-Si-B-WC-5 after 4 hours of cavitation test. The surface was roughened after the 4-hour test, indicating that the matrix was eroded from the surface by ductile fracture. Microcracks were induced in the tungsten carbide particles by cavitation pressure pulses. The crack propagated and the tungsten carbides were fragmented by brittle fracture under continuous attack. From the SEM micrograph, the tungsten carbide seemed to be forced into the metal matrix as indicated by lipping of the surrounding matrix.

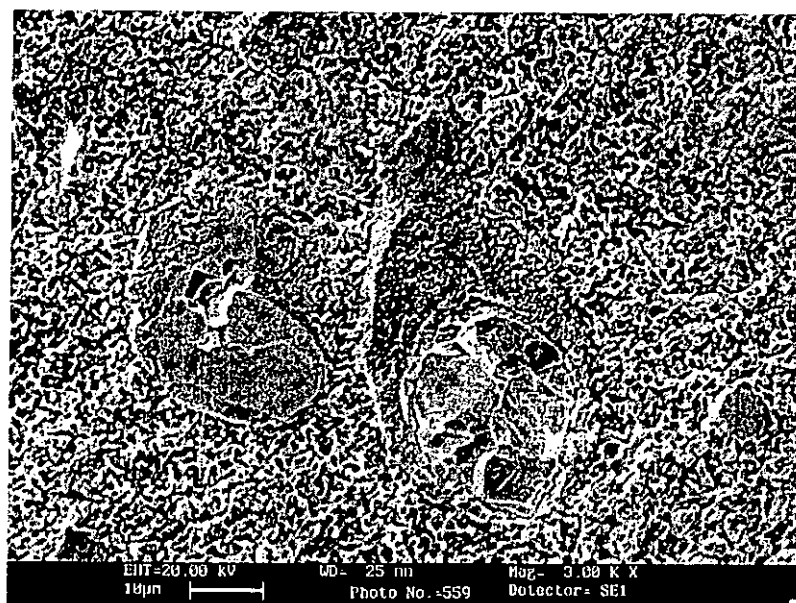


Figure 8. 14 Appearance of the damaged surface of specimen Ni-Cr-Si-B-WC-2 after 4 hours exposure to cavitation erosion

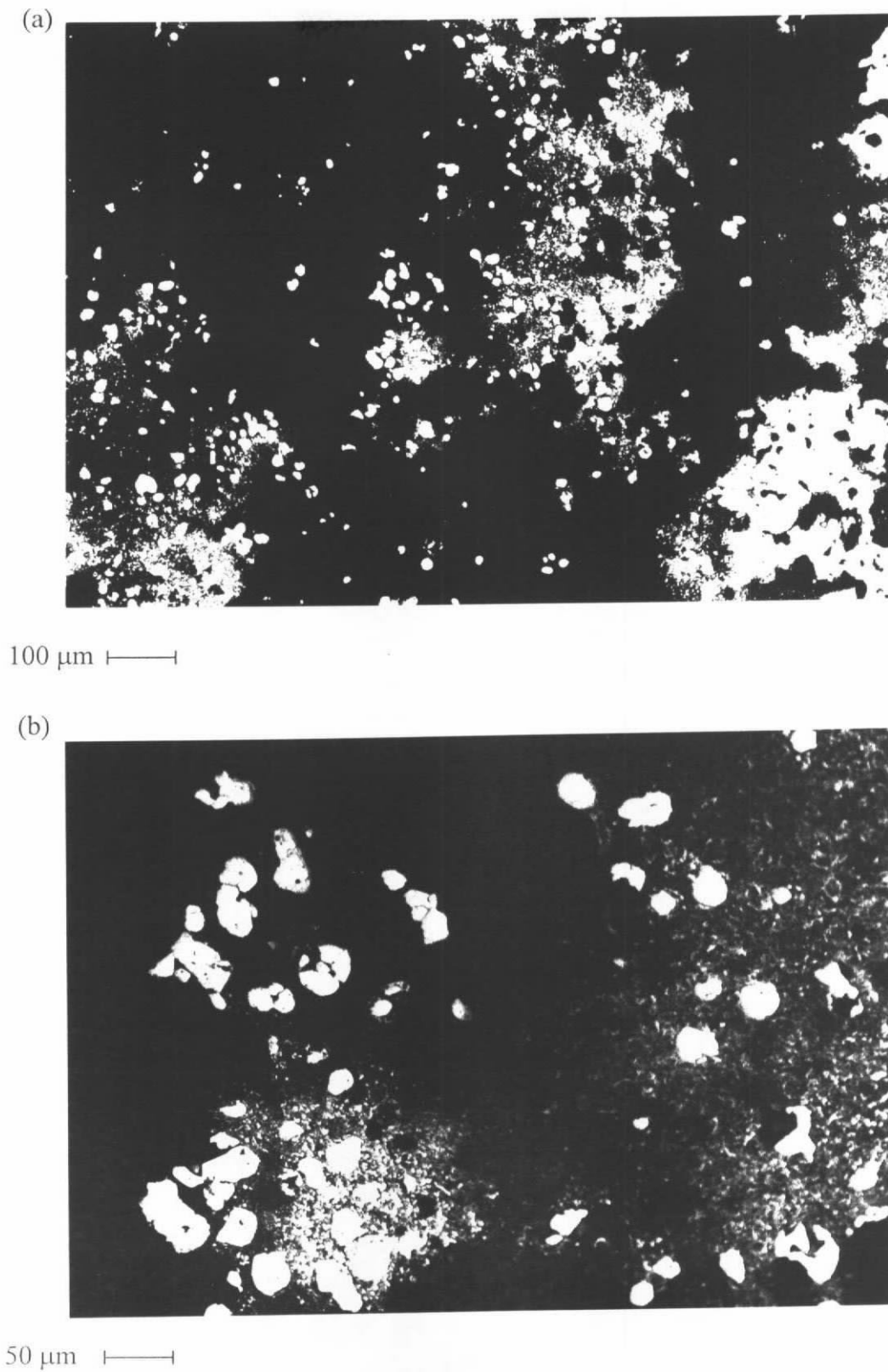


Figure 8. 15 Appearance of the damaged surface of specimen Ni-Cr-Si-B-WC-5 after 4 hours exposure to cavitation erosion (a) 100 $\times$  and (b) 200 $\times$

## 8.3 Brass (Cu38%Zn) laser surface modified with Ni-Cr-Fe-20%WC

### 8.3.1 Materials and laser processing parameters

The alloy powder was a Ni-Cr based alloy power. This alloy powder was similar in composition to the alloy powder used in Chapter 6, with additional tungsten carbide (WC) particle which is in about 15 - 20 wt %. The nominal composition of the Ni-Cr-Fe-WC powder is shown in Table 8. 5.

Table 8. 5 Nominal compositions (wt %) of Ni-Cr-Fe-WC power

Material	Ni	Cr	Fe	WC	Particle size
Ni-Cr-Fe-WC	Bal.	10	10	15-20	~ -140 to +350 mesh ( $< 105 \mu\text{m}$ and $> 40 \mu\text{m}$ )

From preliminary studies of the melt profiles in single-track process, the laser processing parameters were selected and summarized as shown in Table 8. 6

Table 8. 6 Laser processing parameters of brass laser modified with Ni-Cr-Fe-WC alloy powder

Specimen	Power density $\text{W/mm}^2$	Scanning speed $\text{mm/s}$	Coating thickness $(\mu\text{m})$	Overlapping ratio (%)	Shielding gas $(\text{l/min})$
Ni-Cr-Fe-WC-1	95.5	10	~ 150	50	15
Ni-Cr-Fe-WC-2	103.5	5	~ 150	50	15
Ni-Cr-Fe-WC-3	119.4	5	~ 150	50	15
Ni-Cr-Fe-WC-4	119.4	10	~ 400	0	15
Ni-Cr-Fe-WC-5	119.4	10	~ 400	5	15
Ni-Cr-Fe-WC-6	119.4	5	~ 400	0	15
Ni-Cr-Fe-WC-7	212.2	10	~ 400	40	15

### 8.3.2 Microstructural and metallographic analysis

The melt depth and the estimated dilution ratio of the modified specimens are shown in Table 8. 7

Table 8. 7 Summary of coating thickness, melt depth and estimated dilution ratio of brass specimens laser surface modified with Ni-Cr-Fe-WC

Specimen	Coating thickness	Melt depth	Dilution ratio (DR)
Ni-Cr-Fe-WC-1	~ 150 $\mu\text{m}$	/	/
Ni-Cr-Fe-WC-2	~ 150 $\mu\text{m}$	183.6 $\mu\text{m}$	18.29%
Ni-Cr-Fe-WC-3	~ 150 $\mu\text{m}$	192.6 $\mu\text{m}$	22.11%
Ni-Cr-Fe-WC-4	~ 400 $\mu\text{m}$	407.6 $\mu\text{m}$	1.87%
Ni-Cr-Fe-WC-5	~ 400 $\mu\text{m}$	412.4 $\mu\text{m}$	3.01%
Ni-Cr-Fe-WC-6	~ 400 $\mu\text{m}$	435.6 $\mu\text{m}$	8.18%
Ni-Cr-Fe-WC-7	~ 400 $\mu\text{m}$	431.0 $\mu\text{m}$	7.20%

The cross-sectional views of the laser surface modified specimens are shown in Fig. 8. 16 - Fig. 8. 21, respectively. For specimen Ni-Cr-Fe-WC-2 and Ni-Cr-Fe-WC-3 the modified layer bonded to the brass substrate with metallurgical fusion bonding with uniformly distributed tungsten carbides in the melt zone. The dendritic structure of heat affected brass substrate in Ni-Cr-Fe-WC-3 (Fig. 8. 17a) was much coarser than in Ni-Cr-Fe-WC-2 (Fig. 8. 16a), when the power densities decreased from 119.4 W/mm<sup>2</sup> to 103.5 W/mm<sup>2</sup>. Ni-Cr-Fe-WC-4 (Fig. 8. 18), Ni-Cr-Fe-WC-5 (Fig. 8. 19), Ni-Cr-Fe-WC-6 (Fig. 8. 20) and Ni-Cr-Fe-WC-7 (Fig. 8. 21) were modified by laser surface cladding. All of the specimens were not entirely metallurgical bonded to with the brass substrate and pores at the root of the laser clad layer. Tungsten carbides were partially dissociated and combined with alloying element to form mixed carbide, (W, Cr, Ni, Fe)<sub>x</sub>C<sub>y</sub> in the metal matrix.

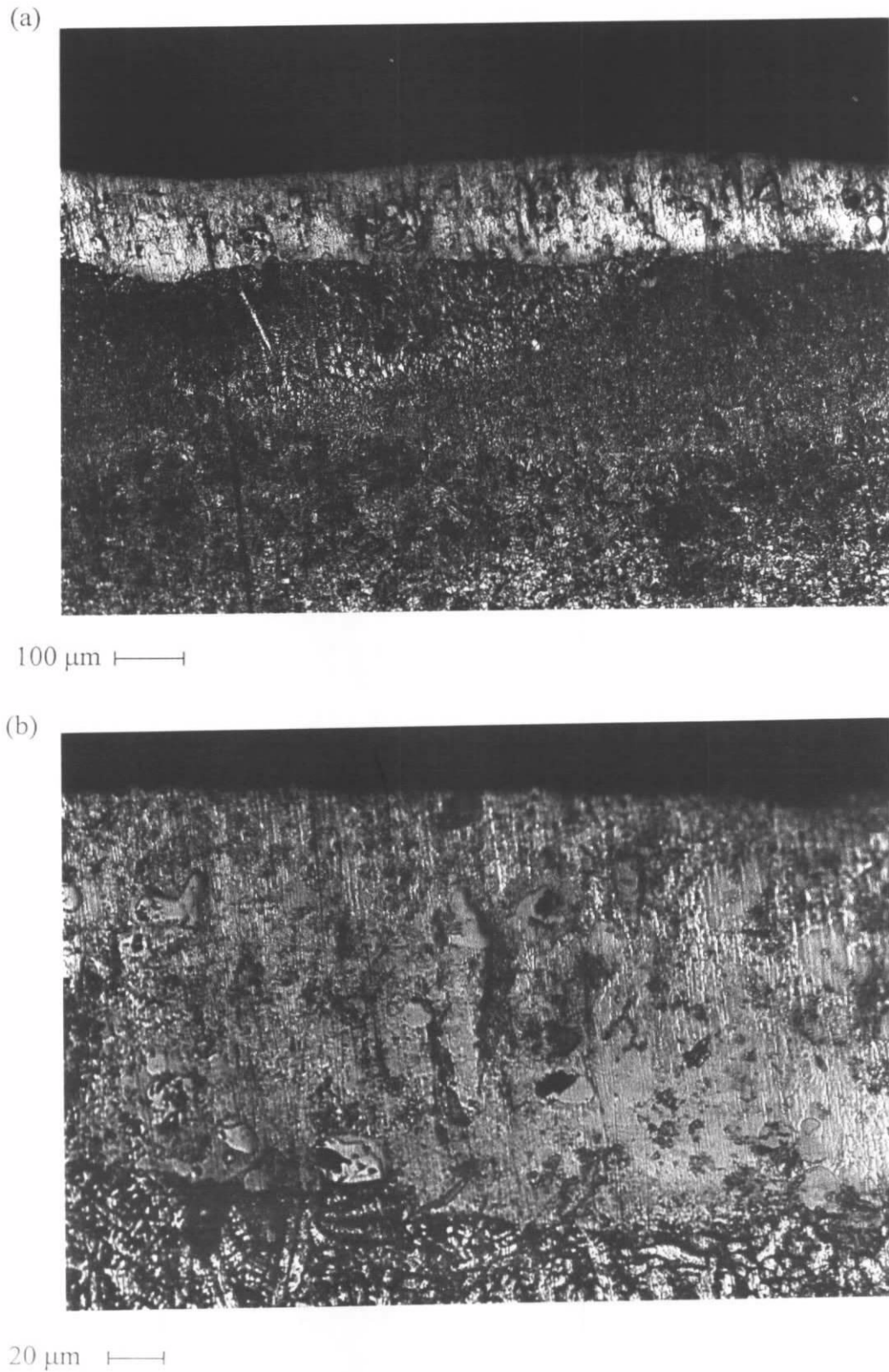


Figure 8. 16 Microstructure of Ni-Cr-Fe-WC-2 (a) melt layer 100 $\times$ , (b) 400 $\times$



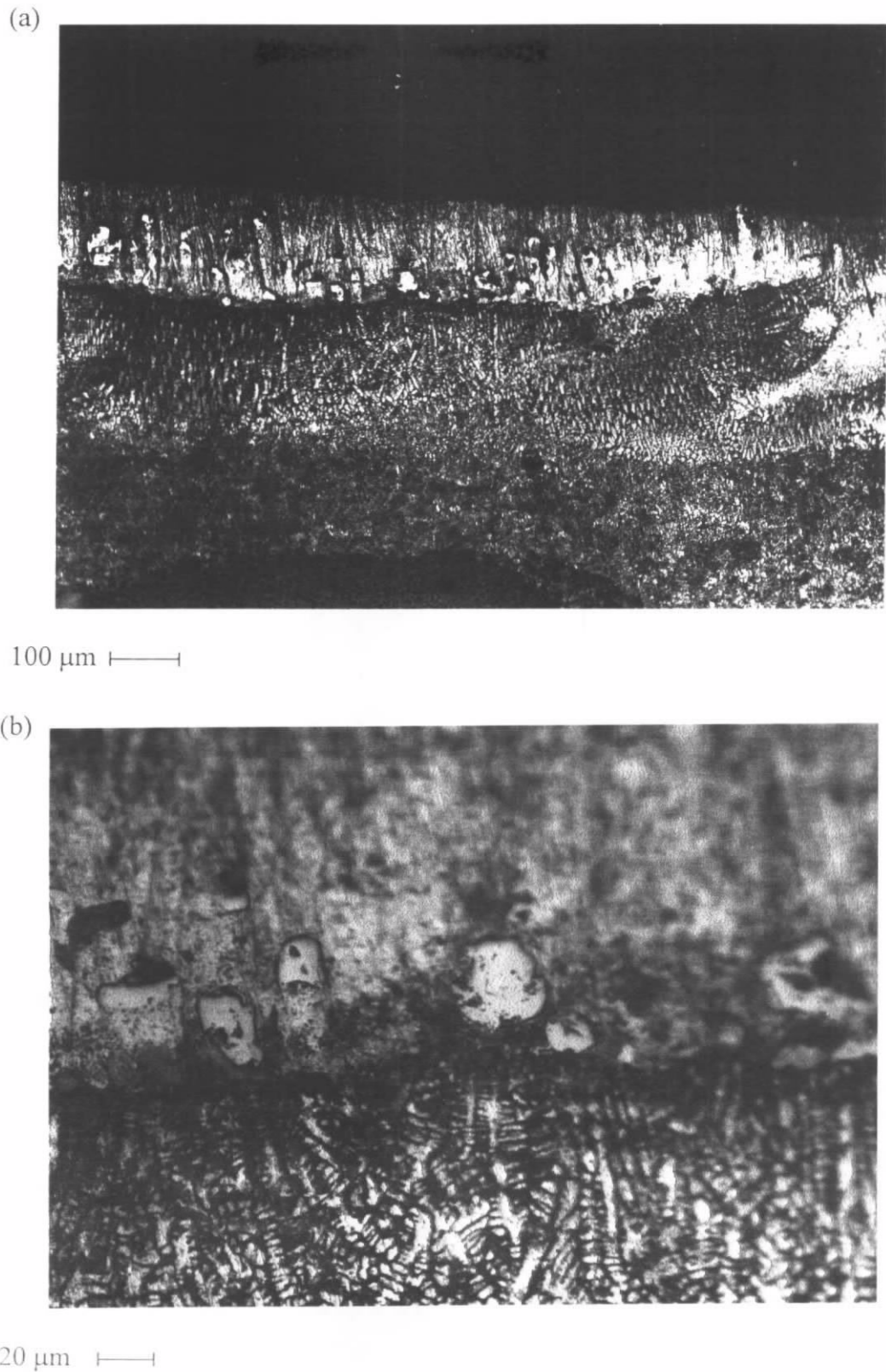
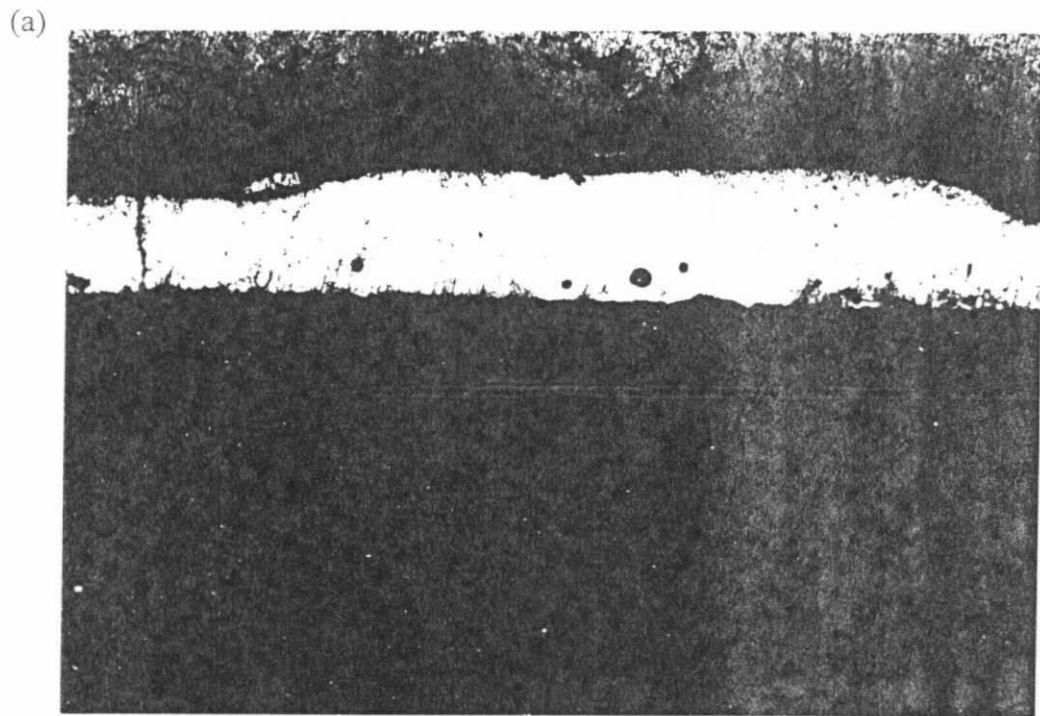
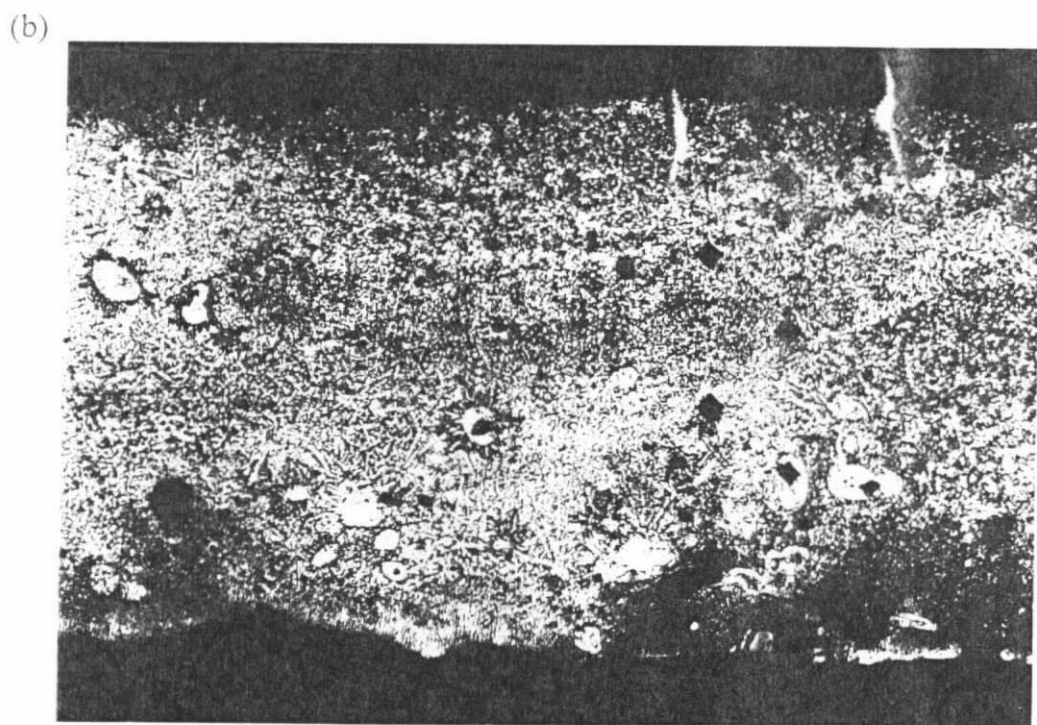


Figure 8. 17 Microstructure of Ni-Cr-Fe-WC-3 (a) melt layer 100×, (b) 400×

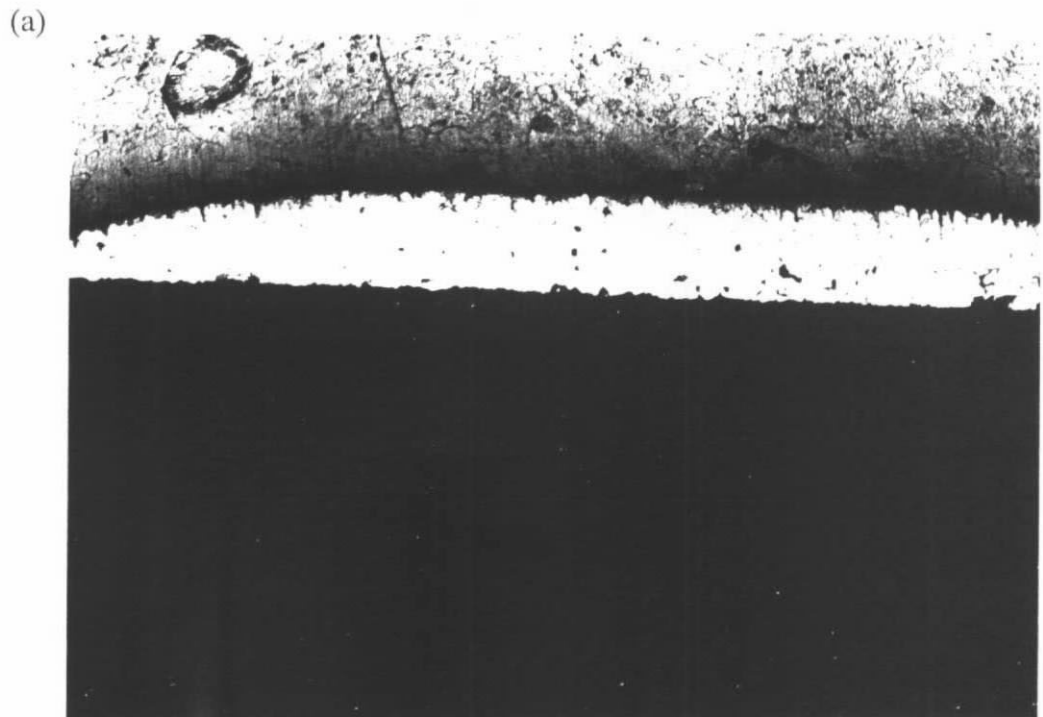


200  $\mu\text{m}$  ———



50  $\mu\text{m}$  ———

Figure 8. 18 Microstructure of Ni-Cr-Fe-WC-4 (a) melt layer 50 $\times$ , (b) 200 $\times$



200  $\mu\text{m}$  ———

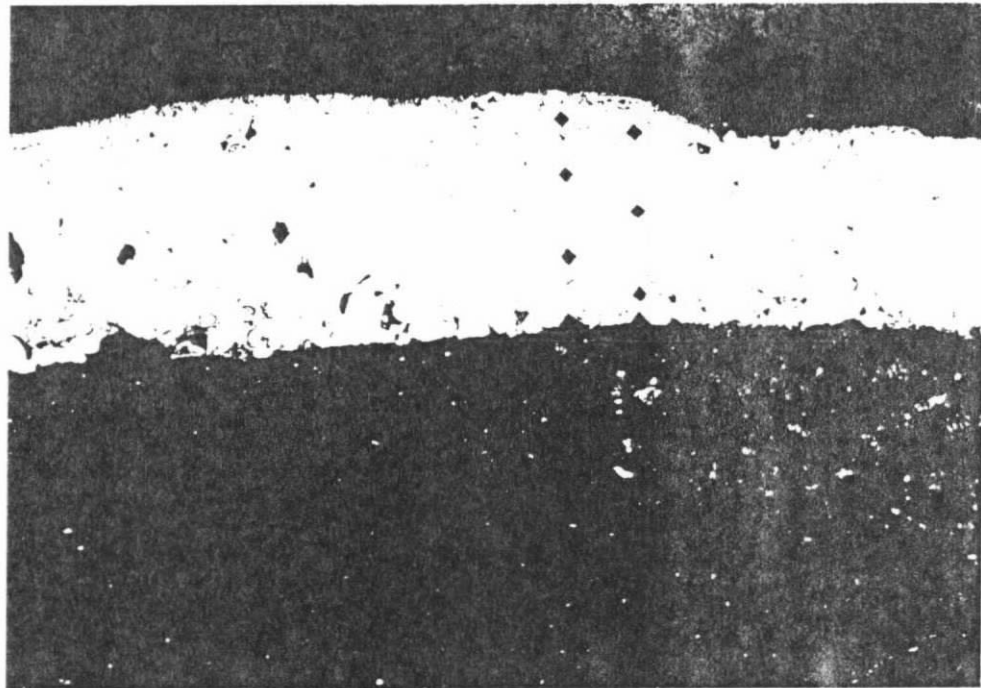


20  $\mu\text{m}$  ———

Figure 8. 19 Microstructure of Ni-Cr-Fe-WC-5 (a) melt layer 50 $\times$ , (b) 400 $\times$



(a)



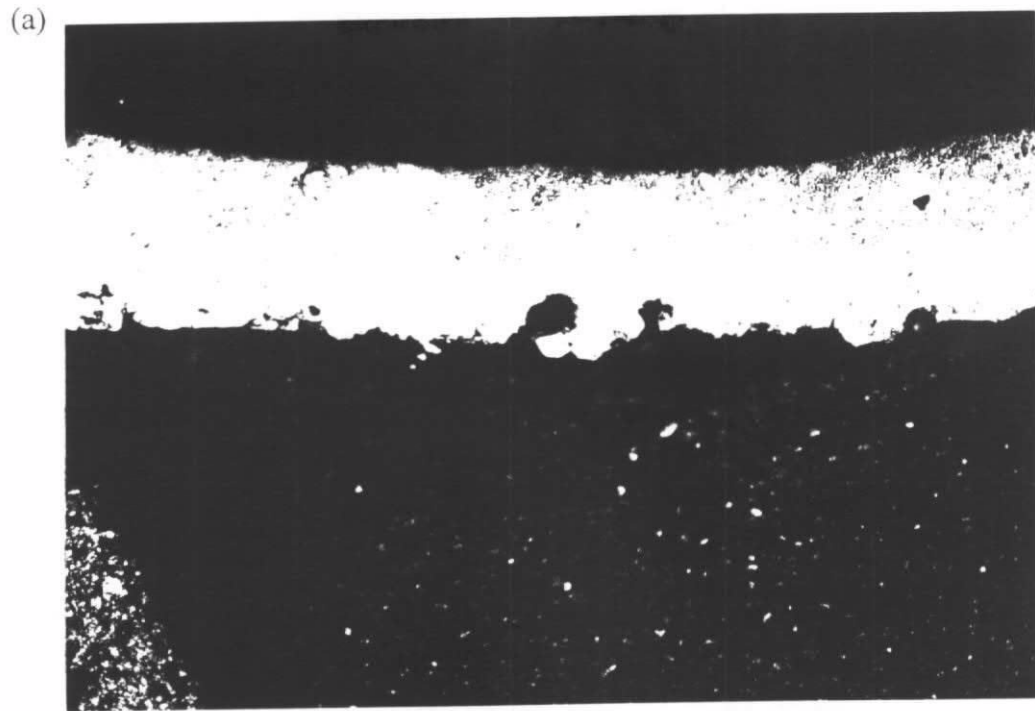
100 μm

(b)

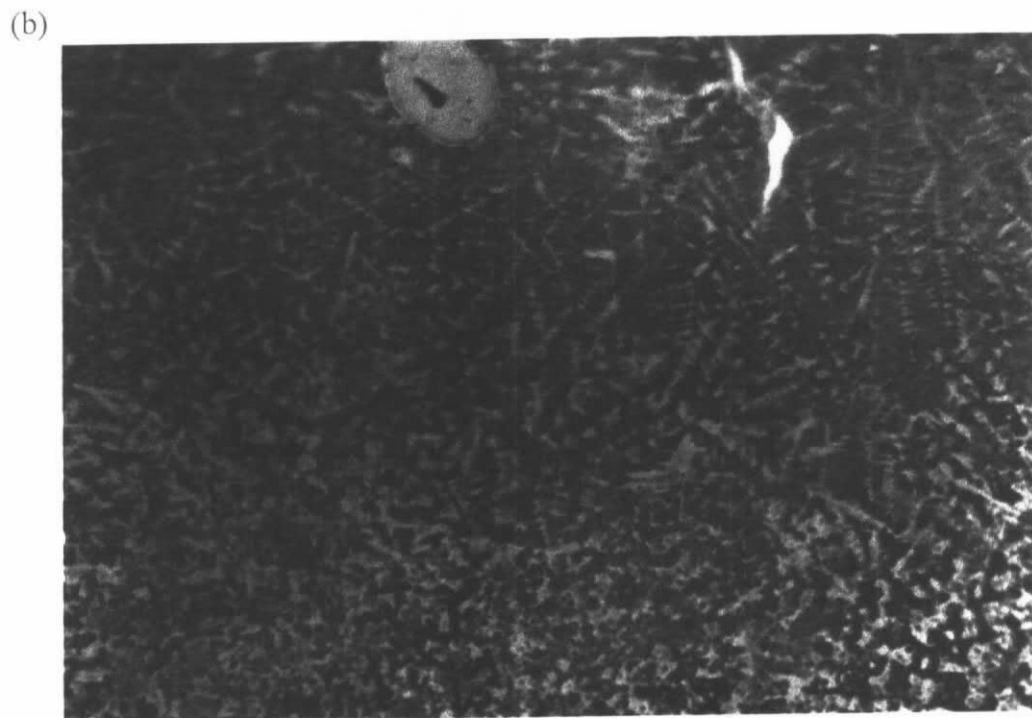


20 μm

Figure 8. 20 Microstructure of Ni-Cr-Fe-WC-6 (a) melt layer 100×, (b) 400×



100  $\mu\text{m}$  ———



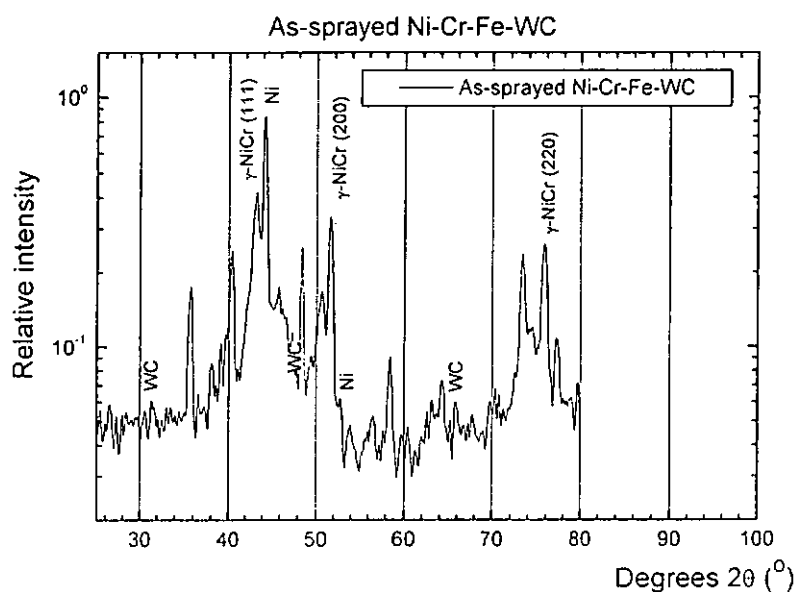
10  $\mu\text{m}$  ———

Figure 8. 21 Microstructure of Ni-Cr-Fe-WC-7 (a) melt layer 100 $\times$ , (b) 800 $\times$

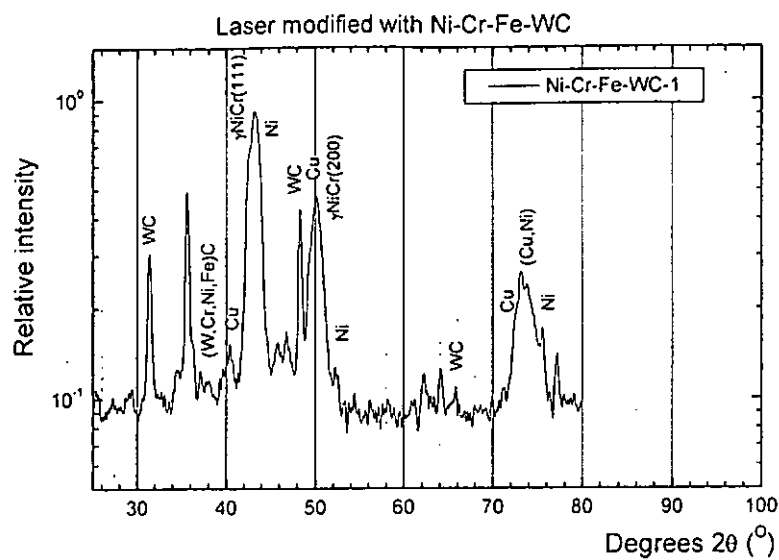
### 8.3.3 X-ray diffraction analysis of Ni-Cr-Fe-WC/brass

The X-ray spectra of the as-sprayed Ni-Cr-Fe-WC coating and the laser surface modified specimens are shown in Fig. 8. 22. According to the spectra, the as-sprayed coating was composed mainly of  $\gamma$ -NiCr and WC.

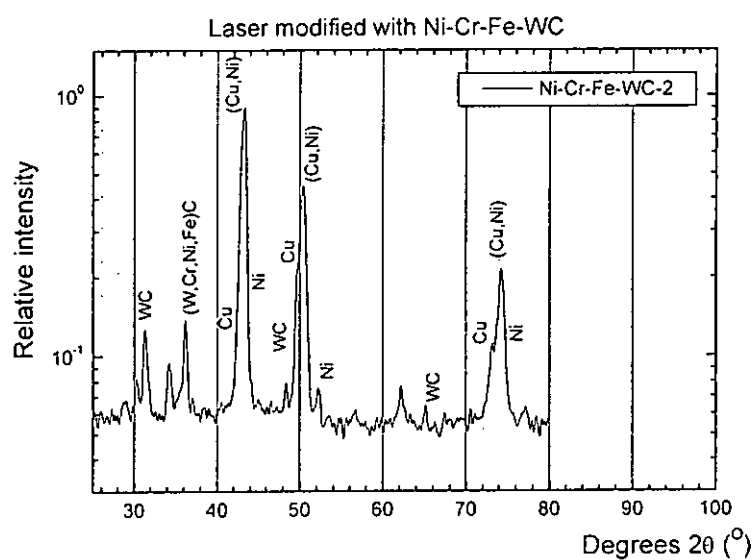
Referring to the result of the dilution ratio, specimens Ni-Cr-Fe-WC-1, Ni-Cr-Fe-WC-2 and Ni-Cr-Fe-WC-3 were mainly composed of Cu, Ni and (Cu,Ni), retained WC and  $(W, Cr, Ni, Fe)_x C_y$ . For specimens Ni-Cr-Fe-WC-4, Ni-Cr-Fe-WC-5, Ni-Cr-Fe-WC-6 and Ni-Cr-Fe-WC-7, the spectra were quite different from the previous three due to their low dilution ratios. These specimens mainly contained  $\gamma$ -NiCr, WC and a small amount of  $(W, Cr, Ni, Fe)_x C_y$ .



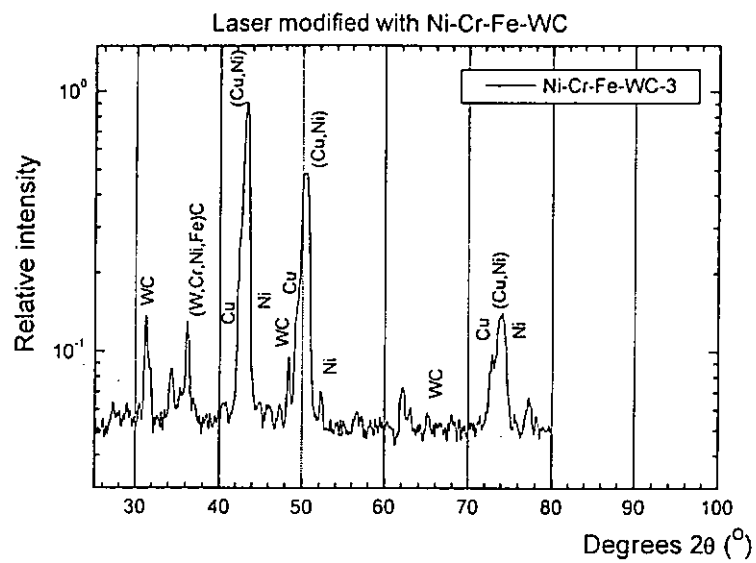
(a)



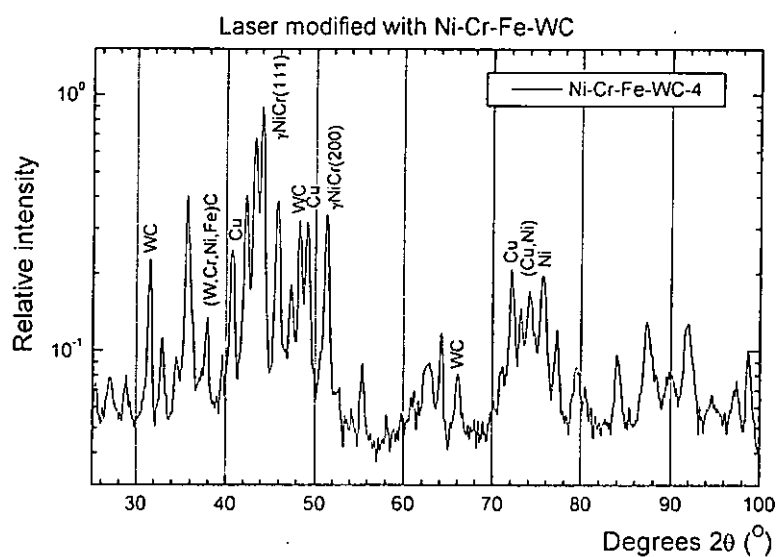
(b)



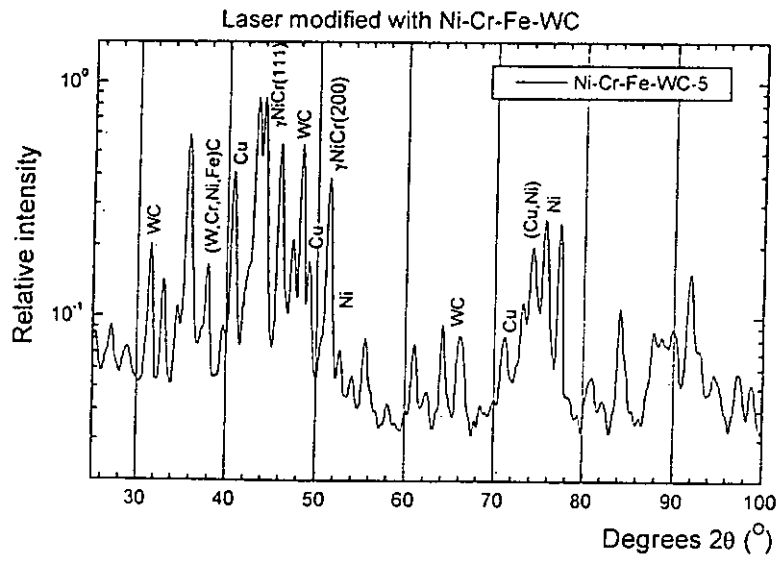
(c)



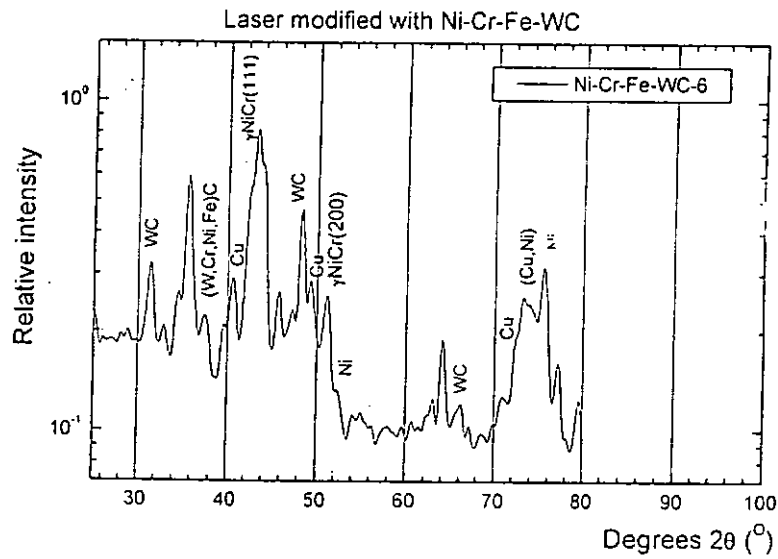
(d)



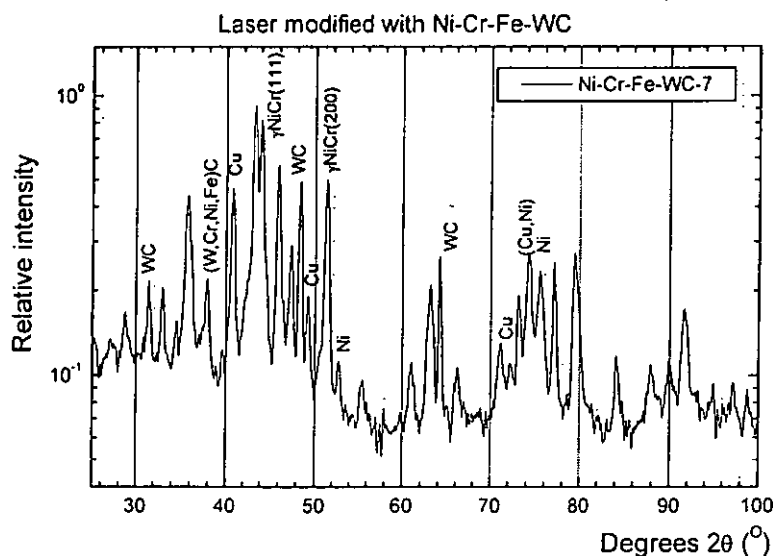
(e)



(f)



(g)



(h)

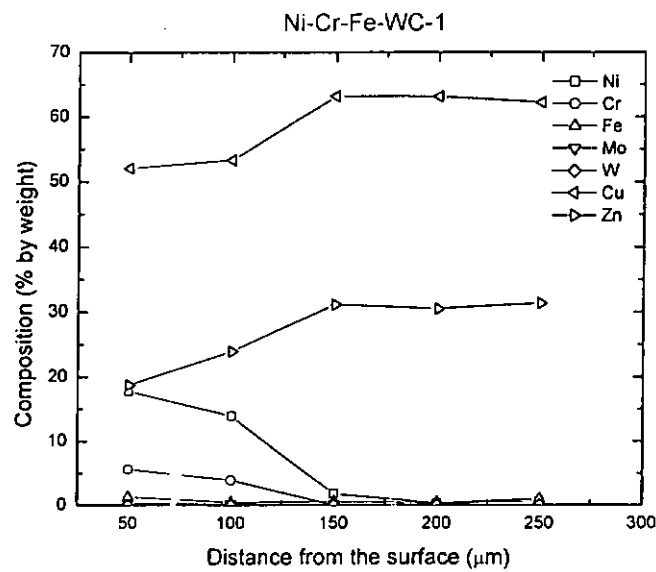
Figure 8. 22 X-ray diffraction spectra of (a) as-sprayed Ni-Cr-Fe-WC, (b) Ni-Cr-Fe-WC-1, (c) Ni-Cr-Fe-WC-2, (d) Ni-Cr-Fe-WC-3, (e) Ni-Cr-Fe-WC-4, (f) Ni-Cr-Fe-WC-5, (g) Ni-Cr-Fe-WC-6 and (h) Ni-Cr-Fe-WC-7

### 8.3.4 Composition profiles of Ni-Cr-Fe-WC/brass

The compositional profiles of the specimens along the modified layer are shown in Fig. 8. 23. For specimen Ni-Cr-Fe-WC-1 and Ni-Cr-Fe-WC-2, the composition along the modified layer was homogeneous and high in copper content due to the high dilution ratio. Ni-Cr-Fe-WC-3 was not homogeneous and more tungsten was found in the matrix, because a higher power density was used. The presence of tungsten was attributed to the dissociation of tungsten carbide.

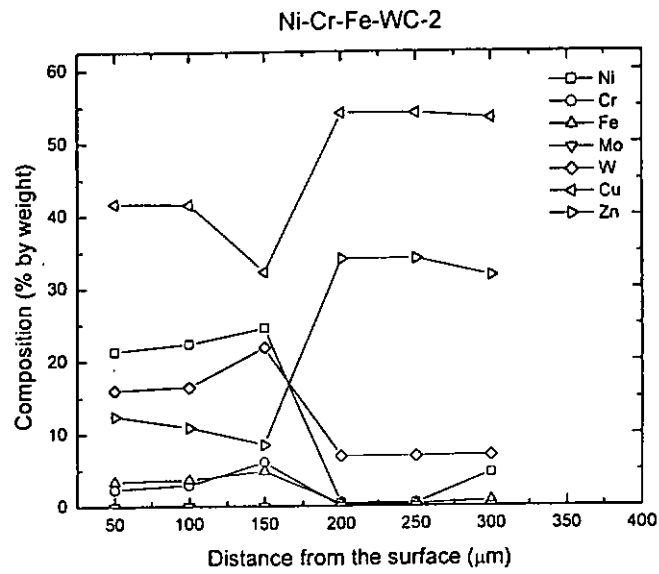
For specimens Ni-Cr-Fe-WC-4, Ni-Cr-Fe-WC-5, Ni-Cr-Fe-WC-6 and Ni-Cr-Fe-WC-7, the melt layer was mainly composed of nickel and chromium, and homogenous along the melt layer. Except Ni-Cr-Fe-WC-6, the nickel content raise from the surface

to a maximum value near the interface and then reduced. In addition, the tungsten content was found very high near the surface and reduced in the center of the melt layer. Ni-Cr-Fe-WC-6 was process with slower scanning speed, hence the interaction time was relatively longer and more laser energy absorbed. Therefore, more tungsten carbides dissociated and found at the surface of the modified layer.

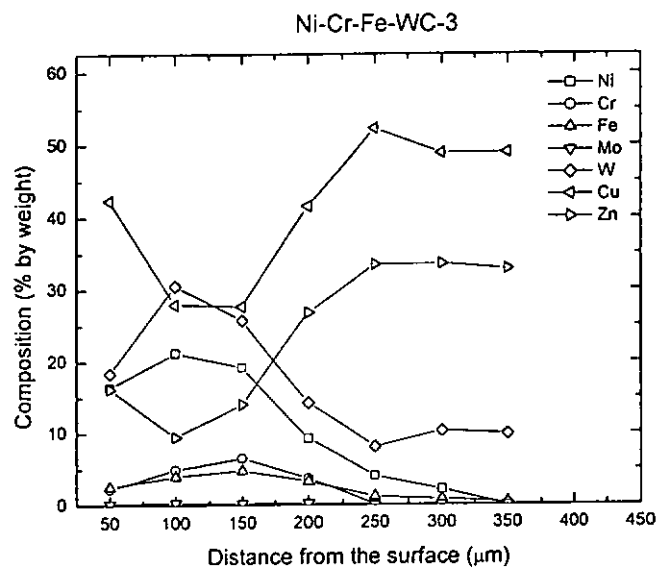


(a)

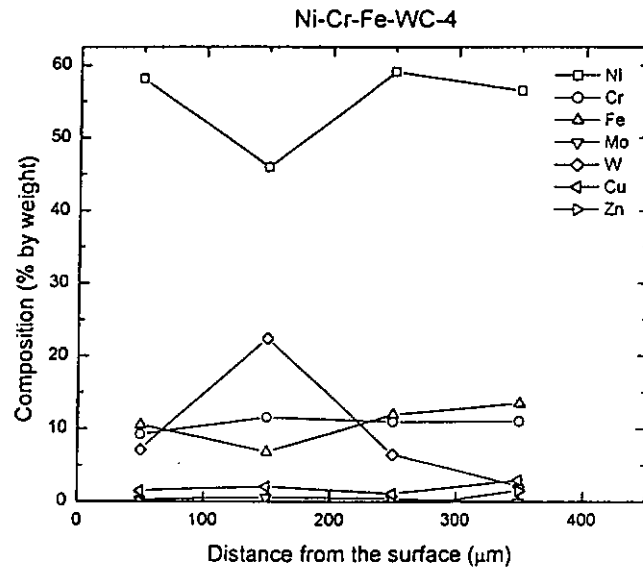




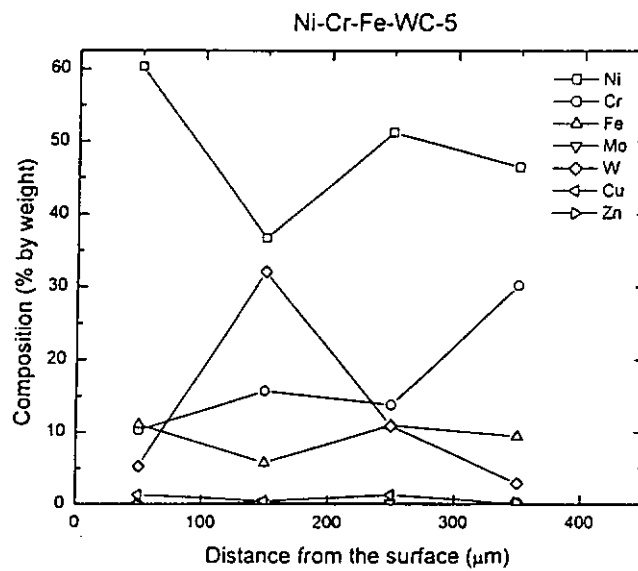
(b)



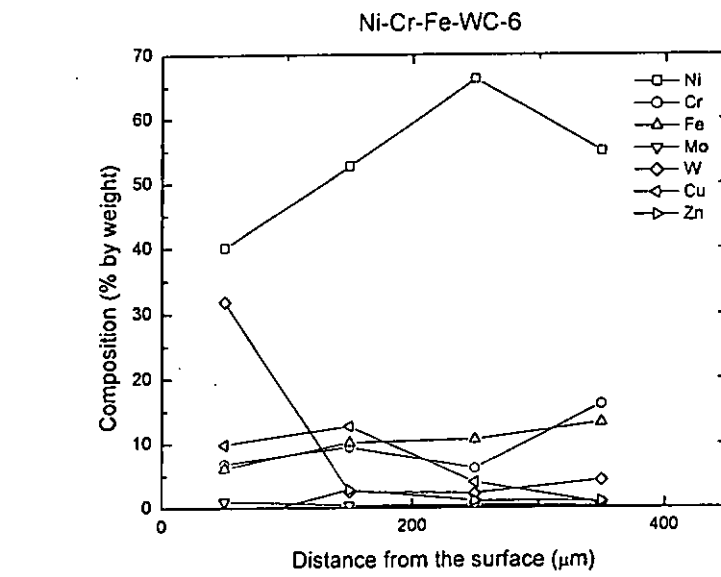
(c)



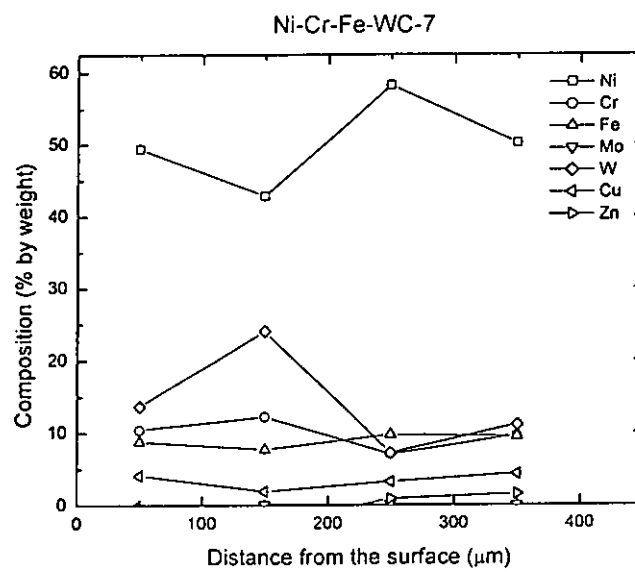
(d)



(e)



(f)



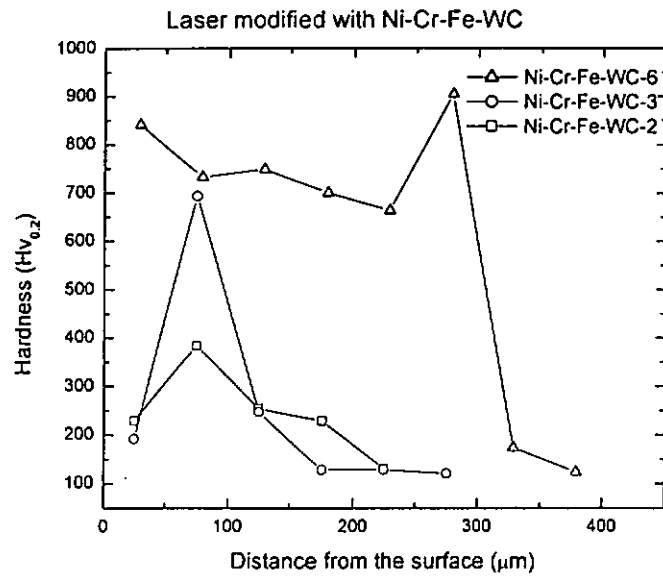
(g)

Figure 8. 23 Chemical compositional profiles of various laser surface modified specimens (a) Ni-Cr-Fe-WC-1, (b) Ni-Cr-Fe-WC-2, (c) Ni-Cr-Fe-WC-3, (d) Ni-Cr-Fe-WC-4, (e) Ni-Cr-Fe-WC-5, (f) Ni-Cr-Fe-WC-6 and (g) Ni-Cr-Fe-WC-7

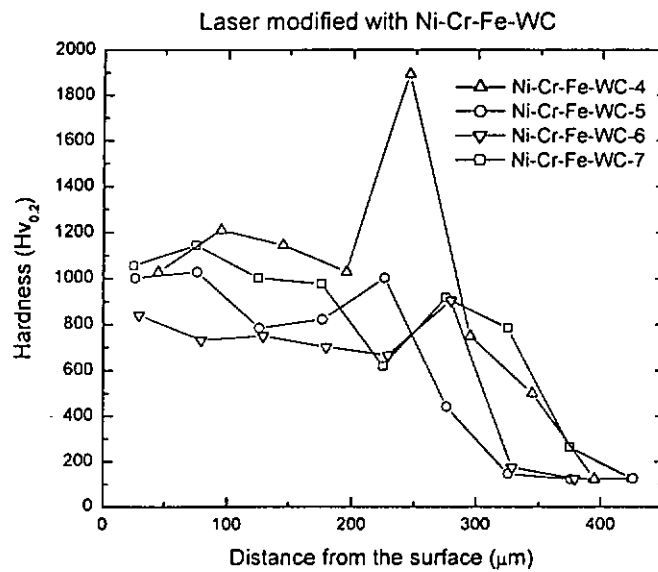
### 8.3.5 Hardness profiles of Ni-Cr-Fe-WC/brass

The hardness profiles from the surface of the laser modified (with Ni-Cr-Fe-WC) region to the substrate of the varies specimen are shown in Fig. 8. 24. The hardness of specimen Ni-Cr-Fe-WC-2 and Ni-Cr-Fe-WC-3 increased from the treated surface to a maximum at the center of the melt layer and fall to the value of that of the brass substrate. The highest hardness of the Ni-Cr-Fe-WC-3 was attributed to the high content of tungsten as shown in the compositional profile. This point was similar to the hardness profile of Ni-Cr-Fe-WC-6, in which the tungsten content near the surface was the same as Ni-Cr-Fe-WC-3 (about 30 wt%). The hardness value of Ni-Cr-Fe-WC-6 reduced as the melt depth increased because of the reduction of tungsten content. Near the interface, the hardness increased due to the higher concentration of nickel and chromium.

The hardness profile of the specimen Ni-Cr-Fe-WC-4, Ni-Cr-Fe-WC-5 and Ni-Cr-Fe-WC-7 was uniform along the melt layer. The sudden increase of hardness in Ni-Cr-Fe-WC-4 was due to indentation at tungsten carbide. Corresponding to the lower scanning speed of the Ni-Cr-Fe-WC-6, the hardness was lower.



(a)



(b)

Figure 8. 24 Hardness profiles along the melt depth of the cross section of laser surface modified specimens

### 8.3.6 Cavitation erosion of Ni-Cr-Fe-WC/brass

The cumulative mean depth of penetration of the as-received brass and laser modified specimens cavitated in 3.5% NaCl solution at 23°C is plotted against time in

Fig. 8. 25. Referring to the results of specimen Ni-Cr-Fe-WC-2 and Ni-Cr-Fe-WC-3, the cavitation erosion resistance increased as the power densities decreased, owing to the decrease in dilution ratio. For specimen Ni-Cr-Fe-WC-1, the cavitation erosion resistance was significantly improved by a factor of 6.5 as compared that of the brass substrate.

The rapid weight loss of specimen Ni-Cr-Fe-WC-4 for the first 30 minutes could be explained by the loose particles between successive melt tracks. The cavitation erosion resistance of specimen Ni-Cr-Fe-WC-5 with on, overlapping of 5%, was substantially improved. The highest cavitation resistance was achieved in specimen Ni-Cr-Fe-WC-7. The value of  $R_e$  was 9 times that of the as-received brass substrate, which was due to the homogeneous composition and high Ni, Cr and W content as indicated in the compositional profile. The normalised cavitation erosion resistance of the modified specimens is shown in Fig. 8. 26.

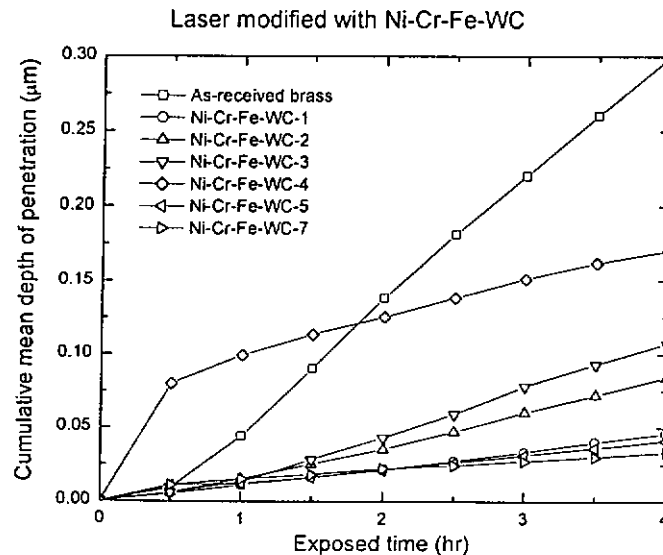


Figure 8. 25 Cumulative MDP as a function of time for the as-received and laser surface modified specimens eroded in 3.5% NaCl solution at 23°C

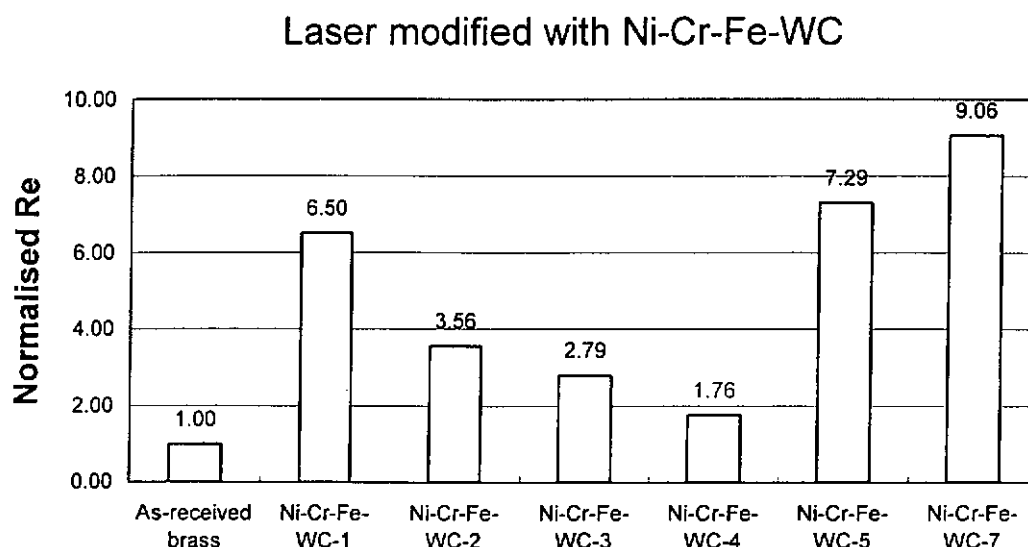


Figure 8. 26 Normalised cavitation erosion resistance of the as-received and laser surface modified specimens eroded in 3.5% NaCl solution at 23°C

### 8.3.7 Electrochemical corrosion of Ni-Cr-Fe-WC/brass

The potentiodynamic polarization curves of the modified specimen Ni-Cr-Fe-WC-2 and Ni-Cr-Fe-WC-3 are shown in Fig. 8. 27. The corrosion resistance was lower than the brass substrate, as indicated by an active shift of the corrosion potential to, -245 mV and -258 mV, respectively. In addition no passive region was present in the graph, indicating that specimens Ni-Cr-Fe-WC-2 and Ni-Cr-Fe-WC-3 did not passivate in NaCl solution.

Fig. 8. 28 shows the potentiodynamic polarization curves of the laser clad single-track specimen, and Ni-Cr-Fe-WC-4, Ni-Cr-Fe-WC-5 and Ni-Cr-Fe-WC-6. The corrosion potentials were reduced to -301 mV, -357 mV, -337 mV and -298 mV,

respectively. The pitting potential of Ni-Cr-Fe-WC-single-track specimen was substantially increased by 304 mV (from -173 mV to +131 mV) as compared with the as-received brass substrate. Moreover, for specimen Ni-Cr-Fe-WC-4, the resistance to pitting corrosion was also improved by a noble shift of the pitting potential (from -173 mV to -107 mV). For specimen Ni-Cr-Fe-WC-6, the pitting potential to -169 mV was slightly higher than the brass substrate. The corrosion data extracted from the graph, including corrosion potential  $E_{corr}$ , current density  $I_{corr}$  and pitting potential  $E_{pit}$ , were summarised in Table 8. 8.

The inclusion of the single-track specimen in the polarization study revealed a common and important problem encountered in laser surfacing by overlapping of melt tracks it could be seen from Fig. 8. 28 that the corrosion resistance of the single-track specimen for excelled that of the multi-track-surfaced specimens. Overlapping inevitably led to deterioration of the surface layer due to the geometrical heterogeneity introduced the remelting and heating effect on adjacent tracks. The success of single-track specimen only indicates the feasibility of modification in terms of alloying, cladding, microstructure and adhesion, while the minimization of multi-track influence is an important and difficult problem to tackle for successful surfacing.



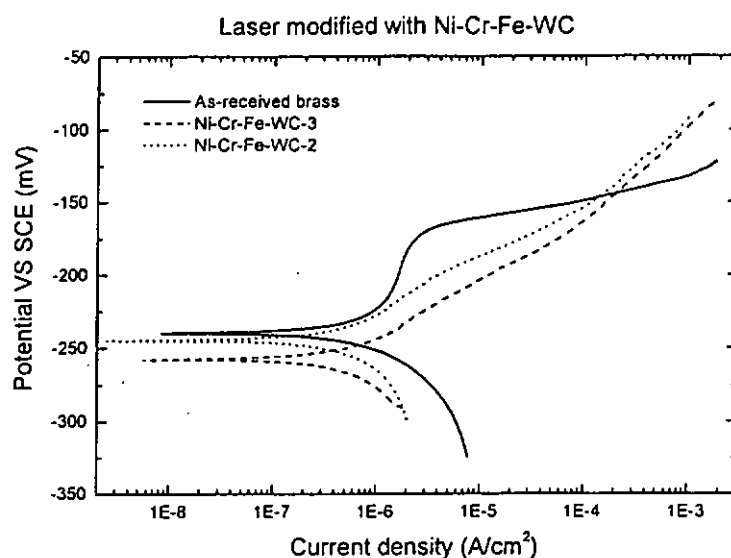


Figure 8. 27 Potentiodynamic polarisation curves of the as-received brass and the laser modified specimens in 3.5% NaCl solution at 23°C

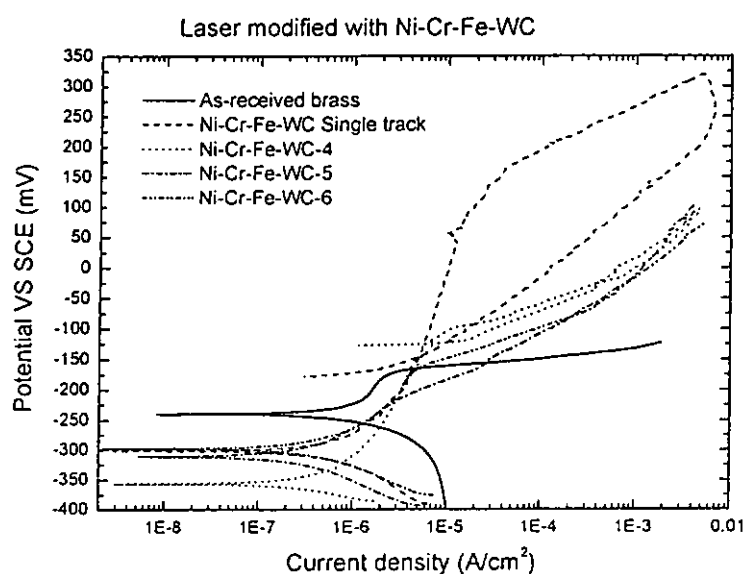


Figure 8. 28 Potentiodynamic polarisation curves of the as-received brass, Ni-Cr-Fe-WC-single-track and the laser modified specimens in 3.5% NaCl solution at 23°C

Table 8.8 The average hardness, cavitation erosion resistance and corrosion parameters of as-received and laser surface modified specimens

Specimen	Ave. hardness (Hv <sub>0.2</sub> )	R <sub>c</sub> (h/μm)	Normalised R <sub>c</sub>	E <sub>corr</sub> (mV)	I <sub>corr</sub> (μA/cm <sup>2</sup> )	Epit (mV)
As Received Brass	110.00	13.4	1.00	-238.3	1.0	-173
Ni-Cr-Fe-WC-1	/	86.87	6.50	/	/	/
Ni-Cr-Fe-WC-2	273.55	47.57	3.56	-245	0.4/	/
Ni-Cr-Fe-WC-3	315.12	37.35	2.79	-258	0.4	/
Ni-Cr-Fe-WC-4	1078.76	23.51	1.76	-357	0.4	-107
Ni-Cr-Fe-WC-5	745.83	97.46	7.29	-311	0.35	-213
Ni-Cr-Fe-WC-6	680.88	/	/	-298	0.5	-169
Ni-Cr-Fe-WC-7	844.65	121.09	9.06	/	/	/
Ni-Cr-Si-B-WC- single-track	/	/	/	-357	0.5	131

Fig. 8.29 shows the variation of the normalised R<sub>c</sub> and average hardness with DR.

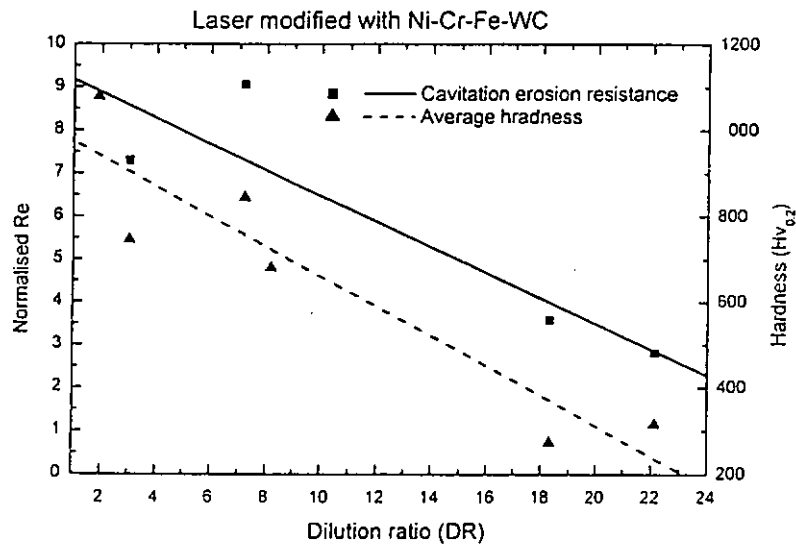
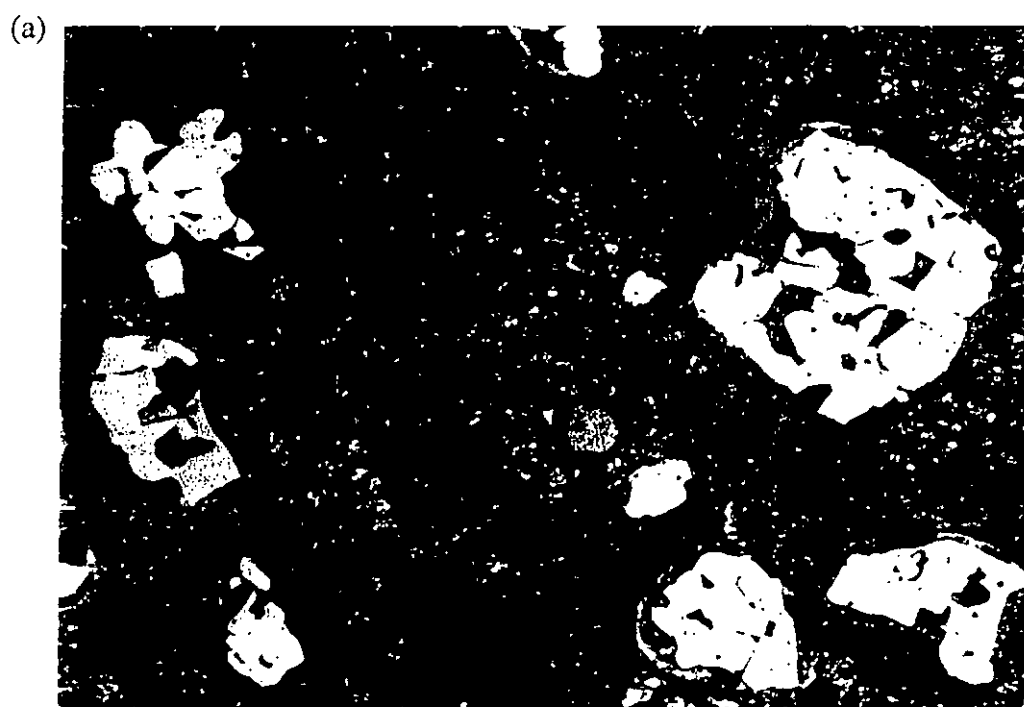


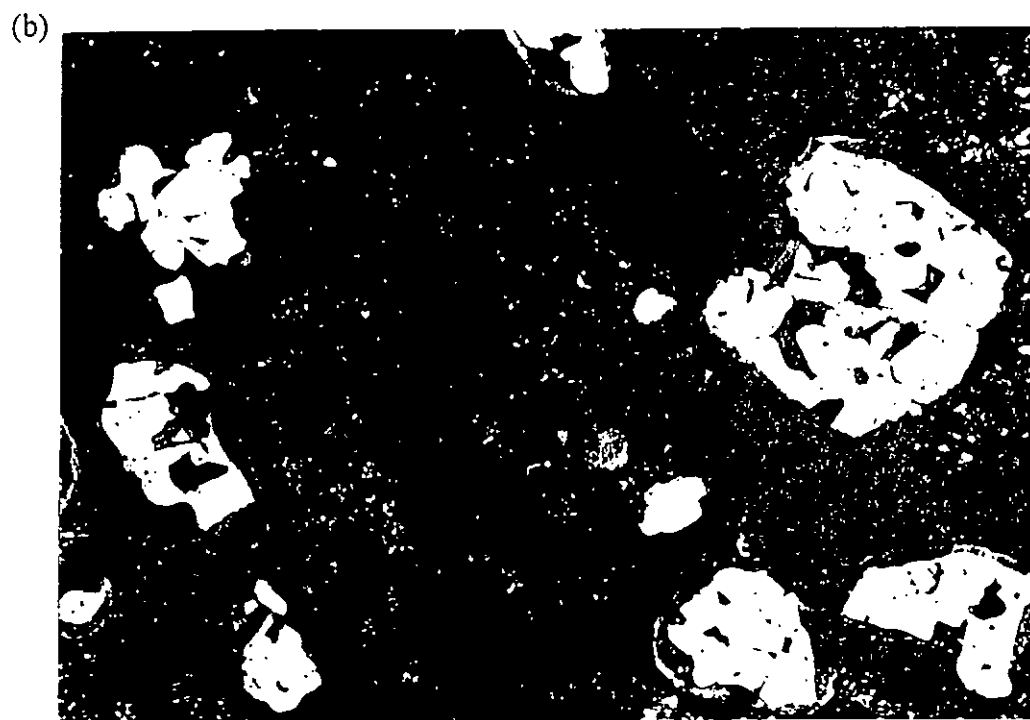
Figure 8.29 Variation of the normalised R<sub>c</sub> and average hardness with DR.

### 8.3.8 Cavitation damage mechanism of Ni-Cr-Fe-WC/brass

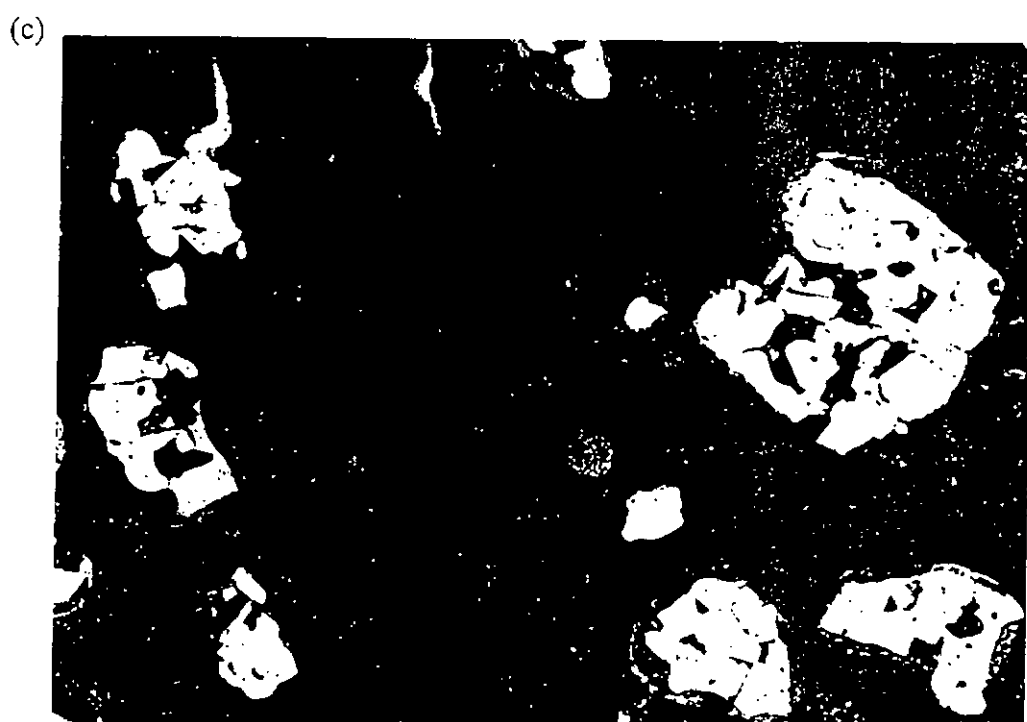
The SEM micrograph of Ni-Cr-Fe-WC-4 subjected to cavitation erosion for 4 hours is given in Fig. 8. 31. The morphology of the cavitated surface revealed that the matrix was not severely attacked by the cavitation pressure pulses. The matrix remained flat as shown in the SEM micrograph. The eroded weight loss was mainly coming from the fragmentation of the tungsten carbide particles. The microcracks were induced and propagated in the tungsten carbide particles by the cavitation pressure pulses. On further attack, the fragmented tungsten carbides were eroded by brittle fracture.



20 μm ———

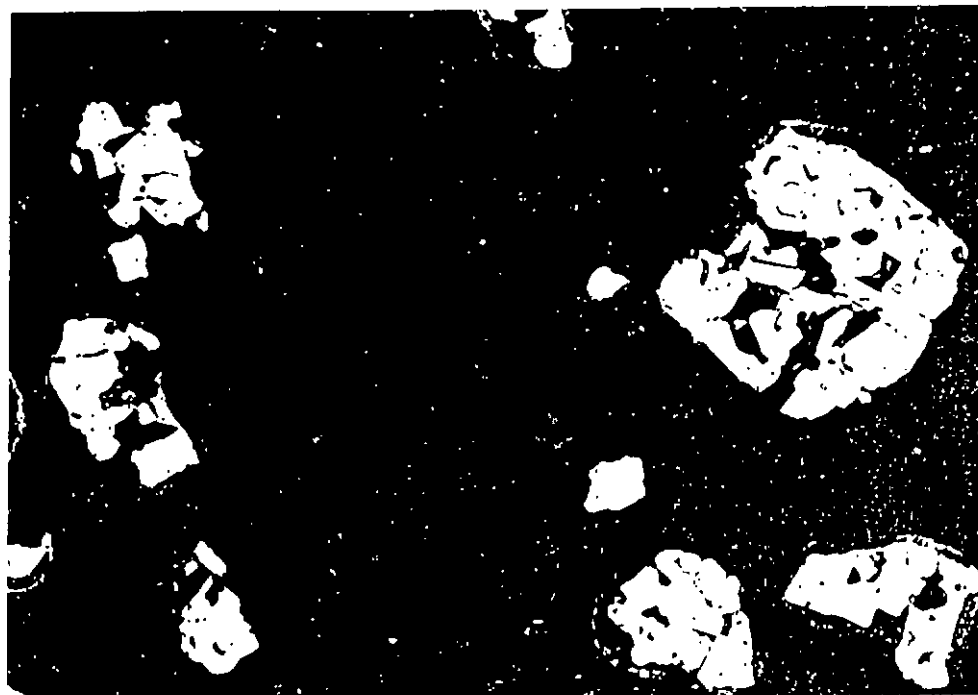


20  $\mu\text{m}$  —|—



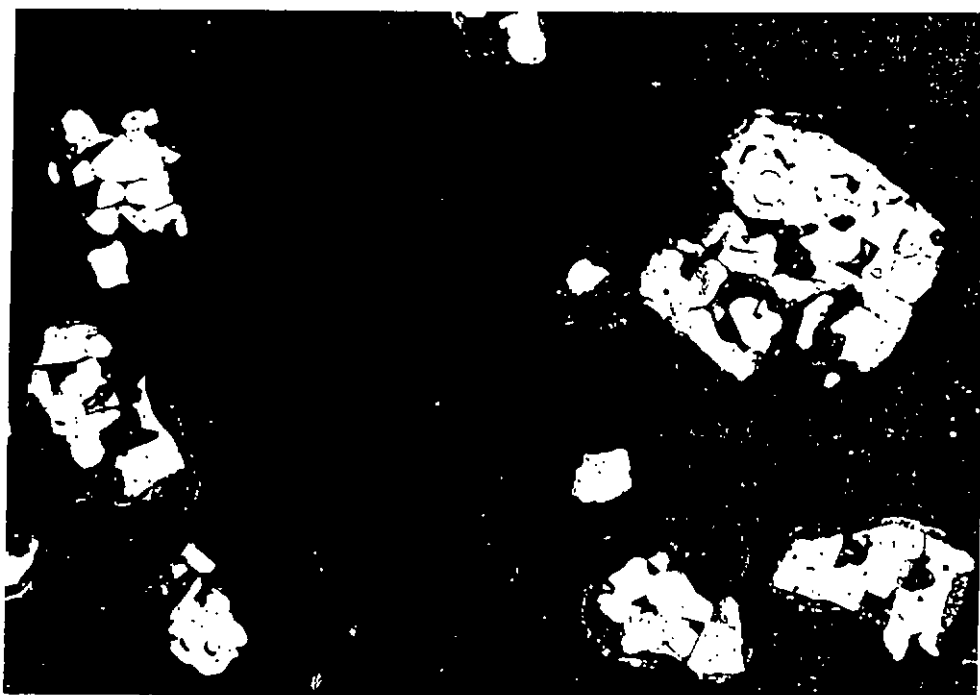
20  $\mu\text{m}$  —|—

(d)



20  $\mu\text{m}$  —

(e)



20  $\mu\text{m}$  —

Figure 8. 30 Appearance of the damaged surface of modified specimen Ni-Cr-Fe-WC-3 exposure to cavitation erosion (a) 90 min 400 $\times$ , (b) 120 min 400 $\times$ , (c) 150 min 400 $\times$ , (d) 180 min 400 $\times$  and (e) 240 min 400 $\times$

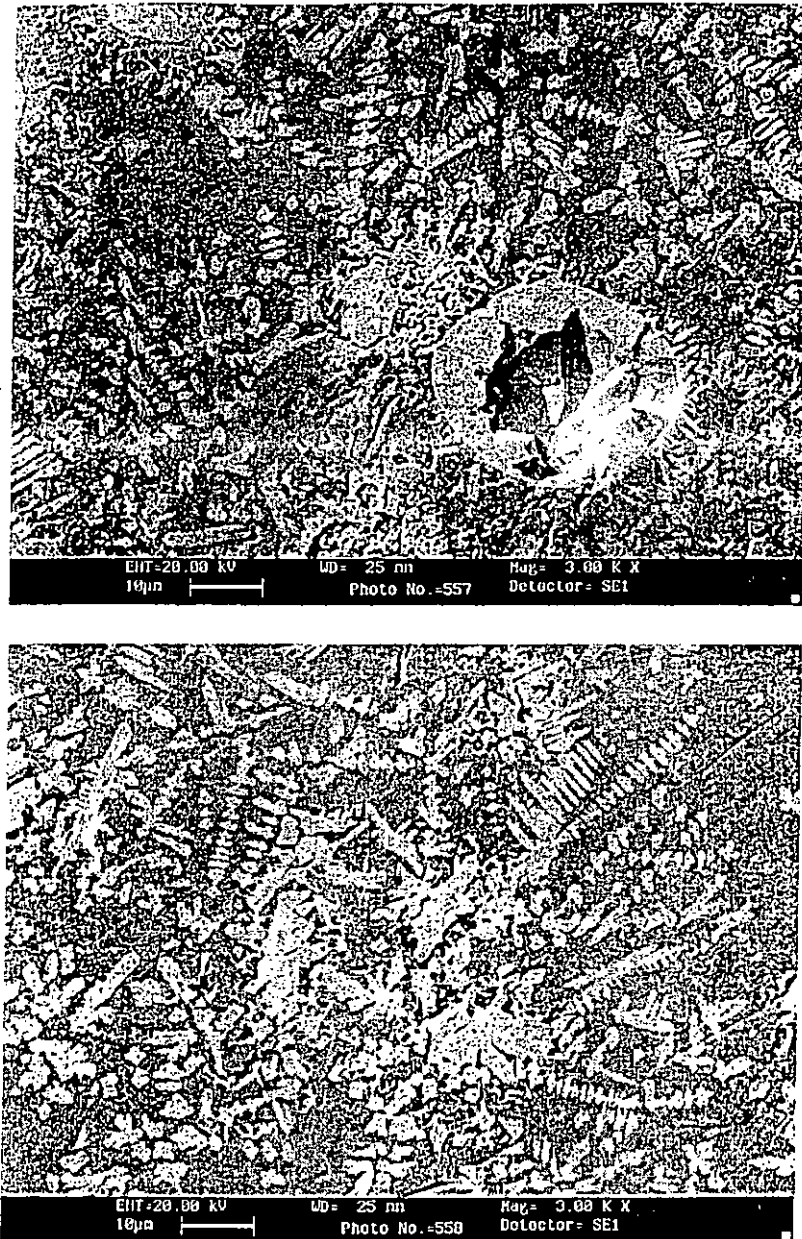


Figure 8. 31 Appearance of the damaged surface of modified specimen Ni-Cr-Fe-WC-4 after 4 hours exposure to cavitation erosion

## 9 Conclusions

### 9.1 Concluding remarks

The present study is devoted to an investigation of the laser surface modification of brass and bronze. From the results of the present study, the following concluding remarks could be made.

1. (a.) Improvement in the cavitation erosion resistance  $Re$  was found in all the bronze specimens modified with  $Ni-Al_2O_3$  and the resistance increased as the power density increased up to  $111\text{ W/mm}^2$ , at which  $Re$  was about 5 times that of bronze.
1. (b.) The improvement was attributed to the formation of a hard nickel-rich intermetallic phase ( $Ni_3Al$ ,  $437\text{ Hv}_{0.2}$ ) resulting from the decomposition of  $Al_2O_3$ .
1. (c.) For power density higher than  $111\text{ W/mm}^2$ , microcracks were induced in the matrix and in the precipitated nickel-rich intermetallic phase. As a result, the cavitation erosion resistance was reduced.
1. (d.) The corrosion resistance was not only inferior to bronze, but also brass due to the formation of secondary intermetallic phases.
2. (a.) The cavitation erosion resistance of the brass specimens modified with  $Ni-Cr-Al-Mo$  alloy was improved by a factor of 2.47 - 4.06 times that of the brass substrate. The improvement was attributed to the formation of nickel-rich phase.
2. (b.) The cavitation erosion resistance increased when the laser scanning speed increased and laser power density decreased in the range studied.

2. (c) The laser surface modification of brass with Ni-Cr-Al-Mo could not bring an improvement to the corrosion resistance.
3. (a.) The improvement of cavitation erosion resistance of brass modified with Ni-Cr-Si-B ranged from 6.1 to 7.12 times that of the brass substrate for a preplaced coating thickness of  $\sim 350 \mu\text{m}$ . As the preplaced coating thickness increased to  $600 \mu\text{m}$ , Re increased to 9.06.
3. (b.) The modified layer was strengthened by the formation of (Cu, Ni) and secondary hard phases such as, CrB,  $\text{Ni}_3\text{B}$  and  $\text{M}_7(\text{CB})_3$ .
3. (c.) The corrosion resistance of the modified specimens was significantly improved as indicated by a shift of the pitting potential in the noble direction. The maximum improvement was achieved in specimen Ni-Cr-Si-B-3 (power density  $141 \text{ W/mm}^2$ , scanning speed  $5 \text{ mm/s}$ ), with a shift of the pitting potential by an amount of about 61 mV (from -173 to -112 mV).
4. (a.) For the specimens modified with Ni-Cr-Si-B-35%WC, the Re of Ni-Cr-Si-B-WC-1 and Ni-Cr-Si-B-WC-3 was improved by 2.43 and 5.16 times respectively. With the preplaced coating thickness increased to  $\sim 400 \mu\text{m}$  the Re of Ni-Cr-Si-B-WC-2 increased to 4.90. For specimen Ni-Cr-Si-B-WC-4, the Re similarly increased to almost two times that of Ni-Cr-Si-B-WC-3. As compared with the specimens modified with Ni-Cr-Si-B, the Re was slightly decreased, except for specimen Ni-Cr-Si-B-WC-4.
4. (b.) According to the polarization curves, the corrosion resistance deteriorated due to the tungsten carbide in the matrix which acted as



active sites for corrosion in a chloride environment. Exceptionally, the resistance to pitting corrosion of Ni-Cr-Si-B-WC-5 was improved as indicated by a shift of the pitting potential to -152 mV and a reduction in the current density by an order of magnitude at the same potential.

- 5. (a) Improvement of cavitation erosion resistance was achieved in all the specimens modified with Ni-Cr-Fe-WC, with a factor of 1.76 to 9.06 times that of the brass substrate.
- 5. (b) The corrosion resistance was also substantially increased. For specimen Ni-Cr-Fe-WC-single-track, the pitting potential shifted nobly by 304 mV (from -173 mV to +131 mV).
- 5. (c) Overlapping of the adjacent tracks during laser surfacing significantly lowered the pitting corrosion resistance. The pitting potential of specimen Ni-Cr-Fe-WC-4 and Ni-Cr-Fe-WC-6 was reduced to -107 mV and -169 mV, respectively due to overlapping, though still more noble than the brass substrate (-173 mV).

The cavitation erosion resistance of various laser modified specimens eroded in 3.5% NaCl solution at 23°C was normalized with respect to as-received brass and summarized in Fig. 9. 1

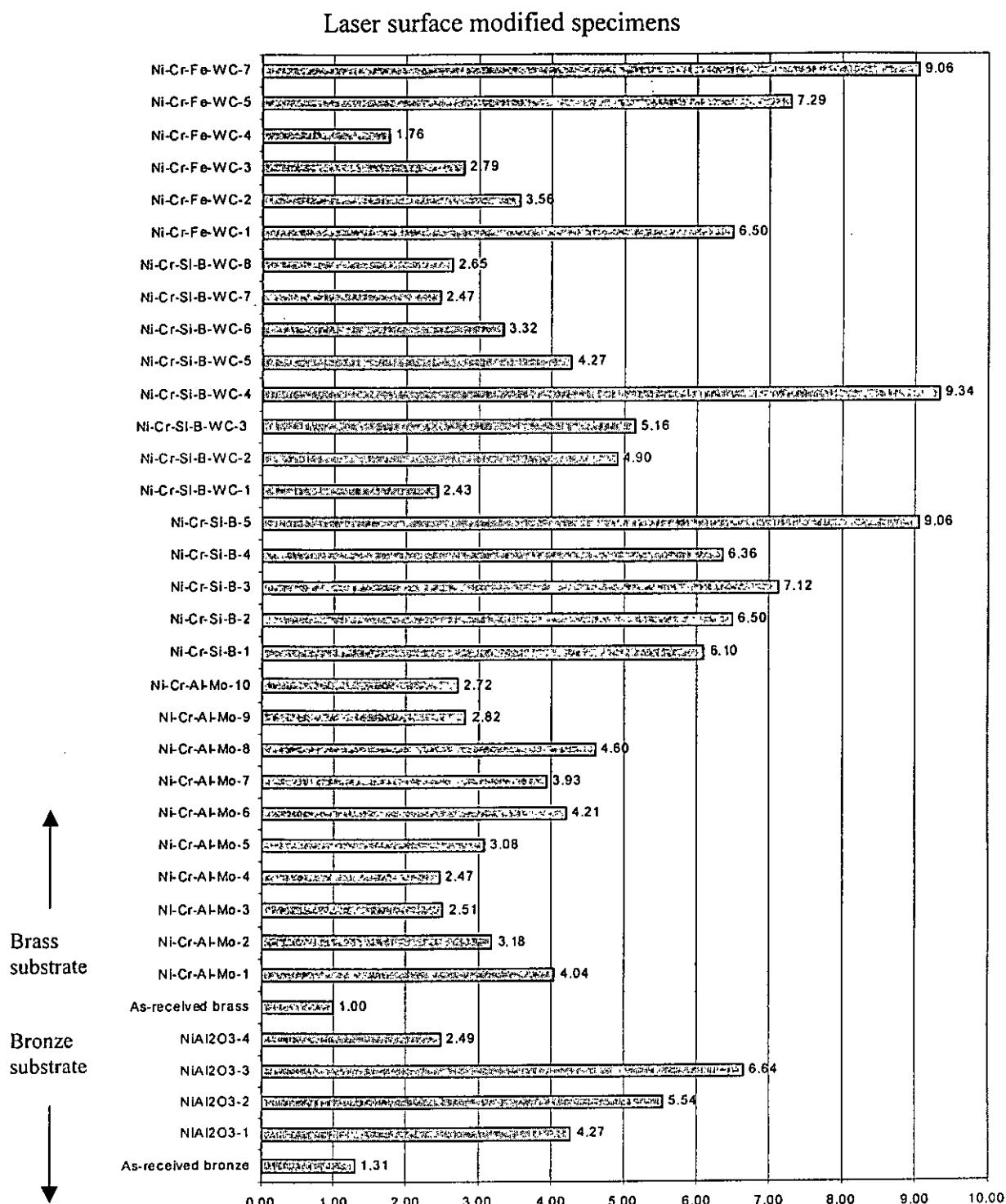


Figure 9.1 Normalized cavitation erosion resistance (with respect to as-received brass) for various laser surface modified specimens eroded in 3.5% NaCl solution at 23°C

## 9.2 Limitations of the present study and suggestions for further work

It is well known that laser surface modification of copper and copper alloys presents a certain degree of difficulty because of high reflectivity and high thermal conductivity. The present study is a preliminary attempt to investigate such a feasibility with an aim to improve the cavitation erosion and corrosion resistance. For further research work, the following investigations may be carried out, in view of the limitations of the present study:

1. As liquid copper has poor wetting property with ceramic particles, copper-based MMCs are more efficiently produced by in-situ processes [Tjong and Lau, 2000] [Ma and Tjong, 2000]. Thus an attempt to include such an in-situ process in the laser surface modification of copper alloys is attractive, since ceramic particles produced in-situ might have a better bonding strength with the matrix.
2. The overlapping of laser melt tracks to obtain a modified surface usually degrades the properties obtained in a single melt track. The degree of overlapping for optimal effect in the copper alloy system is another important problem to tackle.
3. The homogeneity of the elements in the melt layer is another point of concern, as it affects the quality of the modified layer. The homogeneity is in turn determined by the convection in the melt pool and the interaction time. These are affected by the geometry of the melt pool and the laser scanning speed, which should be optimized for a homogeneous

distribution of the elements. Moreover, the alloying elements were found to be more concentrated at the bottom of the layer for unknown reasons. The identification of the cause would shed light on producing a more homogeneous layer.

4. The alloying or cladding powder in the present project was preplaced on the substrate by thermal spraying. As laser heating of the preplaced layer is essentially adiabatic, it is difficult to achieve a low dilution ratio and good fusion bonding simultaneously [Steen, 1998]. Thus it would be meaningful to modify the process by using powder feeding in a one-step process. Although the latter process involves more processing variables, it would produce clad layers of better quality.
5. In the calculation of the depth of penetration, one needs to know the density of the laser processed layer. In the present study, the density of the modified layer was estimated from the composition, which could involve a substantial error. Thus a more reliable way would be to determine the density directly by absolute measurement. A method has to be devised to remove the layer, which is usually of the order of a hundred microns, from the substrate.
6. Similarly, the dilution ratio in the present study, as in most others reported in the literature, was obtained from the coating thickness and the melt depth. This could induce a substantial error because of two reasons. First, the preplaced layer is not compact. Second, there might be material loss during laser processing. Thus a better way of determining the

dilution ratio has to be devised if such a factor is to be used as a variable in the study of laser materials processing.

7. With respect to performance, only cavitation erosion test and polarisation test, both carried out in 3.5% NaCl solution, have been employed in the present study. Some other tests might also be included for a more in-depth assessment. These might include (a) test of adhesion strength between the clad layer and the substrate, (b) the synergistic effect between erosion and corrosion, (c) other corrosion tests such as salt spray test and immersion tests, (d) tests in other environments, such as acidic or sulfur-containing environments.
8. The incorporation of ceramic particles has only been superficially touched in the present study. Further studies to elucidate the effect of the type of ceramic, the volume fraction, and the particle size on the cavitation erosion resistance of the modified layer would be very meaningful.
9. Finally, the results of the present study indicate that it is difficult to improve the cavitation erosion resistance and the corrosion resistance simultaneously. This difficulty might be solved by a careful selection of the cladding / alloying material and a proper choice the processing parameters.

## References

- Abd El-Rehim, S.S., Assaf, F.H., El-Sayed, A. and Zaky, A.M. "Cyclic voltammetric behaviour of copper rich brasses in NaCl solution". *British Corrosion Journal*, Vol. 30, No. 4, pp. 297-301 (1995)
- Al-Hashem, A., Caceres, P.G., Riad, W.T. and Shalaby, H.M. "Cavitation corrosion behaviour of cast nickel-aluminum bronze in seawater". *Corrosion*, Vol. 51, No. 5, pp. 331-342 (1995)
- ASTM G32-92, *Annual Book of ASTM Standards*, Vol. 03.02, ASTM, Philadelphia, PA (1994)
- ASTM G5-94, *Annual Book of ASTM Standards*, Vol. 03.02, ASTM, Philadelphia, PA (1994)
- ASTM G73-93, "Standard practice for liquid impingement erosion testing". *Annual Book of ASTM Standards*, Vol. 03.02, ASTM, Philadelphia, PA (1992)
- Auret, J.G., Damm, O.F.R.A., Wright G.J. and Robinson, F.P.A. "Influence of cathodic and anodic currents on cavitation erosion". *Corrosion*, Vol. 49, No. 11, pp. 910-920 (1993)
- Beach, D.P., Shotwell, A. and Essue, P. *Applications of Lasers and Laser Systems*. A Simon & Schuster, New York, pp. 271 (1993)
- Bjorndahl, W. D. and Nobe, K. "Copper corrosion in chloride media : effect of oxygen". *Corrosion*, Vol. 40, pp. 82-87 (1984)
- Chizhskaya, T. G., Khaskin, V. YU. and Nakvas,. "Laser surfacing the looy powders of Ni-Cr-B-Si system at copper and its alloys". *Avtomaticheskaya Svarka*, Vol. V.9, pp. 45-47 (1997).
- Dehm, G., Medres, B., Shepeleva, L., Scheu, C., Bamberger, M., Mordike, B.L., Mordike, S, Ryk, G., Halperin, G. and Etsion, I. "Microstructure and tribological properties of Ni-based claddings on Cu substrates". *Wear*, Vols. 225-229, pp. 18-26 (1999)
- Draper, C.W. "Laser surface melting of Fe--Al bronzes". *High Temp. Mater. Process*, Vol. 6, Nos. 3-4, pp. 213-224 (1984)
- Draper, C.W. "The use of laser surface melting to homogenize Fe--Al bronzes". *Journal of Materials Science*, Vol. 16, No. 10, pp. 2774-2780 (1981)
- Draper, C.W. and Ewing, C.A. "Laser surface alloying: a bibliography". *Journal of Materials Science*, Vol. 19, pp. 3815-3825 (1984)

- Draper, C.W. and Sharma, S.P. "The effect of laser surface melting on tin-modified Cu-Ni". *Thin Solid Films*, Vol. 84, pp. 333-340 (1981)
- Draper, C.W., Franey, J.P. and Gibson, J.M. "Microstructure and behavior of laser-mixed Cr/Ni films on copper alloys". *Journal of Materials Research*, Vol. 2, No. 1, pp. 35-45 (1987)
- Draper, C.W., Sharma, S.P., Yeh, J. I. and Bernasek, S.I. "Examination of elemental nonuniformities in laser surface melted ternary copper alloys". *Surf. Interface Anal.*, Vol. 2, No.5, pp. 179-182 (1980)
- Draper, C.W., Vandenberg, J.M, Preece, C.M. and Clayton, C.R. "Characterization and properties of laser quenched aluminum bronzes". In Kear, B.H., Giessen, B.C. and Cohen, M., eds., *Rapidly Solidified Amorphous and Crystalline Alloys*, Elsevier Science Publishing Co., pp. 529-533 (1982)
- Draper, C.W., Woods, R.E. and Meyer, L.S. "Enhanced corrosion resistance of laser surface melted aluminum bronze D (CDA-614)". *Corrosion*, Vol. 36, No. 8, pp. 405-408 (1980)
- Fontana, M. G. *Corrosion Engineering*, 3<sup>rd</sup> edition, McGraw-Hill, New York, 556pp. (1988)
- Galantucci, L.M., Ruta, G. and Magnanelli, S. "An experimental study on Co2 500W laser surface alloying of Chromium on copper". pp. 57-73
- Galantucci, L.M., Ruta, G. and Magnanelli, S. "An experimental study on CO sub 2 500 W laser surface alloying of chromium on copper". In Niku-Lari, A. and Mordike, B.L., eds., *High Power Lasers*, Pergamon Press plc, Headington Hill Hall, Oxford, pp. 57-74 (1989)
- Gnanamuthu, D.S. "Laser surface treatments". *Proceedings of the Conference on Applications of Lasers in Materials Processing*, Washington DC, USA, 18-20 April, 1979, pp. 177-211 (1979)
- Gurkovsky, S. and Stoychev, D. "Surface modification of electrochemical copper coatings with a CW CO2 laser". *Journal of Materials Science Letters*, Vol. 13, No. 13, pp. 985-988 (1994)
- Haferkamp, H., Lois, H., Tai, P.T. and Wehlage, T. "Detection and evaluation of cavitation damage by roughness measurements in their early stages". *Proceedings of the Seventh International Conference on Erosion by Solid and Liquid Impact*, Cavendish Laboratory, University of Cambridge, pp. 33-1 - 33-8 (1987)
- Hammit, F.G. *Cavitation and Multiphase Flow Phenomena*. McGraw-Hill, NY, p.222 (1980)

- Han, S.C. and Zhao, J.Y. *Corrosion and Corrosion Control for Offshore and Marine Construction*, Xiamen, China, pp. 451-457 (1988)
- Hidouci, A., Pelletier, J.M. Ducoin, F., Dezert, D., El Guerjouma, R. "Microstructural and mechanical characteristics of laser coatings". *Surface and Coatings Technology*, Vol. 123, pp. 17-23 (2000)
- Hirose, A. and Kobayashi, K.F. "Surface alloying of copper with chromium by CO<sub>2</sub> laser". *Materials Science and Engineering*, Vol. A174, No. 2, pp. 199-206 (1994)
- Hyatt, C.V. and Mackay, K.D. "Characterization of defects in laser treated copper alloys". In Singh, J. and Copley, S.M., eds., *Proceedings of the symposium on International Conference on Beam Processing of Advanced Materials*, Chicago, Illinois, 2-5 November, 1992, pp. 247-258 (1993)
- Hyatt, C.V., Magee, K.H. and Betancourt, T. "The effect of heat input on the microstructure and properties of nickel aluminum bronze laser clad with a consumable of composition Cu-9.0Al-4.6Ni-3.9Fe-1.2Mn". *Metallurgical and Materials Transactions A*, Vol. 29A, pp. 1677-1690 (1998)
- Javadpour, J., Clayton, C. R. and Draper, C. W. "The electrochemical corrosion behavior of laser quenched iron--aluminum bronze". *Corrosion of Metals Processed by Directed Energy Beams*, Metallurgical Society/AIME, pp. 135-145 (1982)
- Johnson, M., Mikkola, D.E. and Wright, R.N. "Influences of alloying on abrasive wear and cavitation erosion behaviour of Fe<sub>3</sub>Al-based alloy". In Schneibel, J.H. and Crimp, M.A., eds., *Processing, Properties, and Applications of Iron Aluminides*, Minerals, Metal & Materials Society (1994)
- Johnson, M., Mikkola, D.E., March, P.A. and Wright, R.N. "The resistance of Nickel and Iron Aluminides to cavitation erosion and abrasive wear", *Wear*, Vol. 140, pp. 279-289 (1990)
- Jones, D. A. *Principle and prevention of corrosion*, 2<sup>nd</sup> edition, Prentice Hall, USA, 572pp. (1996)
- Karimi, A. and Martin, J.L. "Cavitation erosion of materials". *International Metals Reviews*, Vol. 31, No. 1, pp. 1-26 (1986)
- Karimi, A., Maamouri, M. and Martin, J.I. "Cavitation-erosion-induced microstructures in copper single crystals". *Materials Science and Engineering*, Vol. A113, pp. 287-296 (1989)
- Kikuchi, K. and Hammitt, F.G. "Effect of separation distance on the cavitation erosion of vibratory and stationary specimens in a vibratory facility". *Wear*, Vol. 102, (3), pp. 211-225 (1985)



- Kinsman, G. and Duley, W.W. "Enhancing the 10.6 $\mu$ m absorptivity of copper and aluminium using excimer laser radiation". *Applied Physics Letter*, Vol. 54, No. 1, pp. 7-9 (1989)
- Koch, M. and Ebersbach, U. "Experimental study of chromium PVD coatings on brass substrates for the watch industry". *Surface Engineering*, Vol. 13, No. 2, pp. 157-164 (1997)
- Kwok, C.T., Man, H.C. and Cheng, F.T. "Cavitation erosion and damage mechanisms of alloys with duplex structure", *Materials Science and Engineering*, Vol. A242, pp. 108-120 (1998)
- La, Peiqing, Bai, Mingwu, Xue, Qunji and Liu Weimin "A study of Ni<sub>3</sub>Al coating on carbon steel surface via the SHS casting route". *Surface and Coatings Technology*, Vol. 113, Issues 1-2, pp 44-51 (1999)
- Li, Q., Lei, T.C. and Chen, W.Z. "Microstructural characterization of laser-clad TiCp-reinforced Ni-Cr-B-Si-C composite coatings on steel". *Surface and Coatings Technology*, Vol. 114, pp. 278-284 (1999)
- Li, Q., Lei, T.C. and Chen, W.Z. "Microstructural characterization of WCp reinforced Ni-Cr-B-Si-C composite coatings". *Surface and Coatings Technology*, Vol. 114, pp. 285-291 (1999)
- Lim, L.C., Qian, M. and Chen, Z.D. "Microstructure of laser-clad nickel-based hardfacing alloys". *Surface & Coatings Technology*, Vol. 106, pp. 183-192 (1998)
- Lindner, H, Bergmann, H.W. and Endres, T.H. "Remelting and alloying of Al-Si alloys". *Proceedings of the Third European Conference on Laser Treatment of Materials*, Germany (1990)
- Luperi, S., Bertamini, L. Valente, T. and De Cristofaro, N. "Electrochemical behaviour of NiCrBSi/Mo air plasma sprayed composite coatings in chloride containing solutions". *Materials Science Forum*, Vols. 289-292, pp. 707-718 (1998)
- Ma, Z. Y. and Tjong, S. C. "High temperature creep behavior of in-situ TiB<sub>2</sub> particulate reinforced copper-based composite". *Materials Science and Engineering A*, Vol. 284, pp. 70-76 (2000)
- Man, H.C., Kwok, C.T. and Cheng F.T. "Cavitation erosion-corrosion behaviour of various engineering alloys in 3.5% NaCl solution", *Proceedings of the International Symposium on Ship-building & Ship-repairing, ISSS'97*, pp.81-89 (1997)
- Manna, I., Majumdar, J.D., Chatterjee, U.K. and Nath, A.K. "Laser surface engineering of copper with chromium for enhanced wear resistance". *Scripta Materialia*, Vol. 35, No. 3, pp. 405-410 (1996)

Megaw, J. H. P. C. *Laser Surface Treatments*. pp. 23

Milosev, I. and Metikos, M. "Factors influencing the breakdown susceptibility of the passive film on Cu-Ni alloy". *Corrosion*, Vol. 48, pp. 185-193 (1992)

Ming, Q., Lim, L.C. and Chen, Z.D. "Laser cladding of nickel-based hardfacing alloys". *Surface and Coatings Technology*, Vol. 106, pp. 174-182 (1998)

Nakata, K., Tomoto, K. and Matsuda, F. "Laser boronizing of copper alloy". *Transactions of the Japan Welding Research Institute*, Vol. 25, No. 1, pp. 37-41 (1996)

Nakata, K., Tomoto, K. and Matsuda, F. "Surface hardening of copper alloy by laser boronizing". In Sudarshan, T.S. and Jeandin, M., eds., *Proceedings of the Eighth International Conference on Surface Modification Technologies*, Nice, France, 26-28 September, 1994, pp. 383-388 (1995)

Palumbo, G., Lassau, R.T. and Kilp, T. "Laser treatment of Al-Bronze. Final Report". *Government Research Announcements and Index*, pp. 133 (1989)

Panagopoulos, C. and Michaelides, A. "Laser surface treatment of copper". *Journal of Materials Science*, Vol. 27, No. 5, pp. 1280-1284 (1992)

Pelletier, J.M., Issa, A. and Sallamand, P. "Laser surface alloying on copper base alloys". *Lasers in Engineering*, Vol. 2, pp. 81-92 (1993)

Preece, C.M., editor, *Erosion treatise on materials science and technology*, Vol. 16, Academic Press, New York, (1979)

Preece, C.M., Vaidya S. and Dakshinamoorthy, S. *Erosion: Prevention and Useful Application*, ASTM (1979)

Pynn, S.I. and Chun, Y.G. "Role of alloying elements, tin and aluminium in anodic behaviour of homogenous copper-based alloys in 3.5 wt % NaCl solution". *British Corrosion Journal*, Vol. 31, pp. 147-152 (1996)

Qian, M., Lim, L.C., Chen, Z.D. and Chen, W.L. "Parametric studies of laser cladding processes". *Journal of Materials Processing Technology*, Vol. 63, pp. 590-593 (1997)

Qian, M., Lim, L.C. and Chen, Z.D. "Laser cladding of nickel-based hardfacing alloys". *Surface & Coatings Technology*, Vol. 106, pp. 174-182 (1998)

Rao, B.C.S. and Buckley, D.H. "Deformation and erosion of F.C.C. metals and alloys under cavitation attack". *Materials Science and Engineering*, Vol. 67, pp. 55-67 (1984)

- Sang, K. and Li, Y. "Cavitation erosion of flame spray weld coating of nickel-base alloy powder". *Wear*, Vol. 189, pp. 20-24 (1995)
- Selvan, J.S., Subramanian, K., Nath, A.K., Kumar, H., Ramachandra, C. and Ravindranathan, S.P. "Laser bronising of Ti-6Al-4V as a result of laser alloying with pre-placed BN". *Materials Science and Engineering*, Vol. A260, pp. 178-187 (1999)
- Selvan, J. S., Soundararajan, G. and Subramanian, K. "Laser alloying of aluminium with electrodeposited nickel : optimisation of plating thickness and processing parameters". *Surface and Coatings Technology*, Vol. 124, pp. 117-127 (2000)
- Sequeira, C.A.C. "Inorganic, physicochemical, and microbial aspects of copper corrosion: literature survey". *British Corrosion Journal*, Vol. 30, No. 2, pp. 137-153 (1995)
- Shalaby, H.M., Al-Hashem, A., Al-Mazcedi, H. and Abdullah, A. "Field and laboratory study of cavitation corrosion nickel aluminium bronze in sea water". *British Corrosion Journal*, Vol. 30, (1), pp. 63-70 (1995)
- Shalaby, H.M., *Paper no. 497, Corrosion/96*, Colorado, USA. 1996 (1996)
- Shepeleva, L., Medres, B., Kaplan, W.D., Bamberger, M., McCay, M.H., McCay, T.D. and Sharp M. "Laser induced Cu/alumina bonding : Microstructure and bond mechanism". *Surface and Coatings Technology*, Vol. 125, pp 40-44 (2000)
- Steen, *Laser material processing*, 2<sup>nd</sup> edition, Springer Verlag, (1998)
- Steen, W.M. "Laser surface cladding". *Proceedings of the NATO Advanced Study Institute on Laser Surface Treatment of Metals*, San Miniato, Italy, 2-13 September, 1985, pp. 369- (1986)
- Stern, G. "Absorptivity of CW CO<sub>2</sub>, CO and YAG-laser beams by different metallic alloys". *ECLAT'90*, pp. 25-35 (1990)
- Tjong, S. C. and Lau, K. C. "abrasive wear behaviour of TiB<sub>2</sub> particle-reinforced copper matrix composites". *Materials Science and Engineering A*, Vol. 282, pp. 183-186 (2000)
- Tjong, S. C. and Ma, Z. Y. "Microstructural and mechanical characteristics of in-situ metal matrix composites". *Materials Science and Engineering R*, Vol. 29, pp. 49-113 (2000)
- Toivanen, R.O. and Hirvonen, J-P. "Selective corrosion of excimer laser melted brass surface". In Was, G.S. and Grabowski, K.S., eds., *Proceedings of the symposium on Environmental Degradation of Ion and Laser Beam Treated Surfaces*, Chicago, Illinois, 26-29 September, 1988, pp. 247-258 (1989)

- Tomlinson, W.J. and Talks, M.G. "Erosion and corrosion of cast iron under cavitation condition". *Tribology International*, Vol. 24, (2), pp. 67-75 (1991)
- Tomlinson, W.J., Moule, R.T. and Blount, G.N. "Cavitation erosion of pure iron in distilled water containing chloride and chromates". *Tribology International*, Vol. 21, (1), pp. 21-25 (1988)
- Trethewey, K.R., Haley, T.J. and Clark, C.C., "Effect of ultrasonically induced cavitation on corrosion behaviour of a copper-manganese-aluminium alloy". *British Corrosion Journal*, Vol. 23, (1), pp. 55-60 (1988)
- Vandenberg, J.M. and Draper, C.W. "An X-Ray diffraction study on the microstructure of laser surface melted Cu--Al--Fe alloys. (Retroactive Coverage)". *Materials Letters*, Vol. 2, No. 5A, pp. 386-392 (1984)
- Vannes, A.B., Malau, V. and Pelletier, J.M. "Laser remelting and laser cladding: determination of the mechanical behaviour of the treated layers". In Sudarshan, T.S., Jeandin, M. and Khor, K.A., eds., *Proceedings of the Eleventh International Conference on Surface Modification Technologies*, Paris, France, 8-10 September, 1997, pp. 568-580 (1998)
- Vyas, B. and Hansson, I. L. H. "The cavitation erosion-corrosion of stainless steel". *Corrosion science*, Vol. 30, (8-9) pp. 261-270 (1990)
- Wang, J., Jaing, X. and Li, S. "Development of new erosion-corrosion resistant cupronickel alloys". *Trans. Nonferrous Metals Society of China*, Vol. 8, No. 1, pp. 73-77 (1998).
- Weisheit, A. and Mordike, B.L. "In situ formation of a new wear resistant Cu-Fe-Al alloy by laser cladding". *Proceedings of EUROMAT 97: 5th European Conference on Advanced Materials and Processes and Applications. Vol. 3. Surface Engineering and Functional Materials*, Maastricht, Netherlands, 1997, pp. 127-130 (1997)
- Wigren, J. "Grit-blasting as surface preparation before plasma spraying". In Houck, D.L., ed., *Thermal spray: advances in coatings technology: proceedings of the National Thermal Spray Conference*, Orlando, Florida, USA, 14-17 September, 1987, pp. 99-104 (1988)
- Wojtas, H. and Boehni, H. "Corrosion and electrochemical characterization of rapidly solidified Cu-B, Cu-Al-B, Cu-Cr-Zr alloys". *Materials Science and Engineering*, Vol. A134, pp. 1065-1069 (1991)